EFFECT OF NANO-GRAPHITE COATING ON SMALL DI DIESEL ENGINE PERFORMANCE

Ph.D. THESIS

by

HIMANSHU PANJIAR

**DEPARTMENT OF METALLURGICAL AND MATERIALS ENGINEERING
INDIAN INSTITUTE OF TECHNOLOGY ROORKEE
ROORKEE-247 667 (INDIA)
JUNE, 2016**

EFFECT OF NANO-GRAPHITE COATING ON SMALL DI DIESEL ENGINE PERFORMANCE

A THESIS

*Submitted in partial fulfilment of the
requirements for the award of the degree
of*

DOCTOR OF PHILOSOPHY
in

METALLURGICAL AND MATERIALS ENGINEERING

by

HIMANSHU PANJIAR

**DEPARTMENT OF METALLURGICAL AND MATERIALS ENGINEERING
INDIAN INSTITUTE OF TECHNOLOGY ROORKEE
ROORKEE-247 667 (INDIA)
JUNE, 2016**

INDIAN INSTITUTE OF TECHNOLOGY ROORKEE
ROORKEE

CANDIDATE'S DECLARATION

I hereby certify that the work which is being presented in the thesis entitled "**EFFECT OF NANO-GRAPHITE COATING ON SMALL DI DIESEL ENGINE PERFORMANCE**" in partial fulfilment of the requirements for the award of Degree of Doctor of Philosophy and submitted in the Department of Metallurgical and Materials Engineering of the Indian Institute of Technology Roorkee, Roorkee is an authentic record of my own work carried out during a period from July, 2010 to June, 2016 under the supervision of Dr. B.S.S. Daniel, Professor, Department of Metallurgical and Materials Engineering, and Dr. R.P. Gakkhar, Professor, Department of Mechanical and Industrial Engineering, Indian Institute of Technology Roorkee, Roorkee.

The matter presented in the thesis has not been submitted by me for the award of any other degree of this or any other Institute.

(Himanshu Panjiar)

This is to certify that the above statement made by the candidate is correct to the best of our knowledge.

(B.S.S. Daniel)   (R.P. Gakkhar)
  Supervisor   Supervisor

Date: , 2016

ABSTRACT

Energy efficient systems are always in demand due to the ever widening supply demand gap. Oil import bill of India consumes about one-third of its total expenditure. A large proportion of the oil is consumed by the automobile sector which is a huge burden on our country's economy. Among the different categories of automobiles, small transport utility vehicles sector is the fastest growing sector. To control fuel consumption and pollution, it is necessary to improve the engine technology to provide more efficient vehicles in terms of their engine performance. Therefore use of technological advancements to reduce engine power losses is of vital importance, which directly improves the engine performance. Amongst the engine power losses, friction is one of the major contributors. It is therefore desirable to make an attempt to minimize friction in the engine.

Internal combustion engine is the heart of the automobile as it is the sole power source which runs the vehicle. Its performance plays a major role and recently nanotechnology solutions are being explored for engine development technology. This is a modern challenge and a successful real-scale application of suitable nanomaterial-coating could lead to significant engine performance enhancements. In order to improve performance of IC engine, its combustion chamber would be coated with appropriate nanomaterials and then tested for its performance in terms of friction, mechanical efficiency, fuel consumption, and emissions. In the present work, an attempt is made to enhance performance of the engine with the application of nanomaterials coating on the inner surface of small direct injection (DI) diesel engine's cylinder. The coating in engine component raises expectation of engine performance enhancement which includes increase in fuel economy as well as mechanical efficiency and reduced friction, emission and smoke.

In the present investigation, the engine component selected for coating is the engine cylinder alone. As it is well known that, a major proportion of frictional loss in internal combustion engine occurs due to piston-cylinder system. Piston-cylinder system involves piston, piston rings and engine cylinder. And engine cylinder is found to be a common part against which the rubbing action of piston and piston rings takes place. Graphite is the material of choice in the present study because of compatibility considerations and favorable economics.

Artificial Neural Network (ANN) modeling was carried out to understand the graphite bulk particle reduction until nanoparticle formation during mechanical milling. Such an exercise was necessary to optimize the particle size reduction process such that cumbersome intermediate particle size sampling and over-milling can be avoided. The milling experiment was conducted at

two different speeds 200 rpm and 250 rpm for various hours of run with same initial particle size of graphite. The data was used to develop an ANN model to predict the average particle size as a function of milling time. The ANN model was developed in MATLAB environment (version 8). The best performance of training was found with a single hidden layer comprising of 12 nodes. Based on the ANN model, trial runs were carried out for 70 hrs of milling at jar rotation speed of 200 rpm for synthesis of graphite nanoparticle with less contamination. It had been noticed that on continuous running of jar at higher rotation speed affirm higher amount of contamination while the contamination level is lower in case of lower rotational speed of jar during milling. Contamination level can be further reduced by interrupting the milling at frequent intervals.

Electrophoretic deposition process was found to be the most suitable method for coating. The electrophoretic coatings were performed on small coupons of engine cylinder material. After confirming all the coating parameters by several hit and trial outcome, it had been decided to coat the original engine block used in a commercial vehicle. In current coating method electrophoretic electro-chemical cell supplied with a dc voltage of 45-50 V resulted in better graphite nanoparticles (GNPs) thin film deposition. Coated samples did not have enough adhesive strength between substrate and coating particles (GNPs) after removal of external potential. To improve bonding, heat treatment process was adapted based on component working environment as well as nanoparticles behaviour at component working environment. During heat treatment, polymer used during coating evaporates and the distance between graphite nanoparticle layer and the cast iron substrate is minimized which provides an easy path for: (1) interface bonding between carbon atoms of graphitic basal plane and iron atoms of BCC iron in cast iron substrate, and (2) the diffusion of carbon atoms from graphite nanoparticles into the cast iron coupon.

Physical appearance of coating on coated sample confirmed the properness of coating, which was also verified at microscopic level. XRD characterization tool is used to check the surface chemical analysis of uncoated and coated sample in different stages. From XRD analysis it is found that the coated sample before and after heat treatment possess GNPs on the surface. The average roughness of the cylinder sample is found to be 0.63 µm. After coating and heat treatment, the sample surface roughness increased to ~0.97 µm. On the other hand, after cleaning the coated sample with engine oil which removed decomposed polymer residue and weakly bonded GNPs, the average surface roughness found to be 0.21 µm. From hardness measurement carried out on coated coupons, it was found that the hardness is higher than that of uncoated sample. The rise in hardness of the coated sample is due to (1) interfacial bonding between GNPs and iron matrix of cast iron substrate, and (2) the diffusion of carbon into iron matrix of cast iron substrate.

Understanding wear behavior of the engine cylinder is an important characteristic of its life and performance characteristic. Therefore, scratch test was performed to find the coefficient of friction of uncoated and coated samples. The scratch length of 2 mm was chosen with the travel speed of 0.5 mm/min for both the conditions. From test it was confirmed that the coating have positive effect on coefficient of friction reduction. As the coating is found to be uneven in nature, EDS line-scan analysis at various points was used to measure the coating thickness in-situ. The average coating thickness is found to be ~5.6 µm for 10 min of coating time.

After successful coating on cast-iron sample coupons, coating on engine cylinder (originally used in commercial vehicle) was performed with same line of action using a unique design of counter electrode. And entire engine block was placed in a customized furnace with enclosed chamber for maintaining inert atmosphere during heat treatment. After completion of heat treatment the sample was taken out from external furnace chamber and cleaned with engine oil. The coated engine block was installed and underwent testing in a small DI compression-ignition engine test rig. Engine performance testing of small DI compression-ignition engine was conducted in new engines for two cases (1) uncoated engine cylinder and (2) coated engine cylinder in the engine test rig. Engine testing experiments were conducted with three engine parameters (speed, load, coolant flow rate). And it was based on the full factorial design approach and hence one parameter was varied according to its step size while keeping other parameters fixed during the experiments.

The experiments are conducted in two phases, firstly to check the engine performance at high speed limit and then at higher loading condition. As both the conditions can not be tested in a single experimental design, so the experiments are divided in two phases. The considered engine performance parameters are brake specific fuel consumption (BSFC), friction power, mechanical efficiency, specific emissions (*sCO, sHC, sNO*) with respect to indicated power and smoke opacity.

The characteristics of the engine are found to be quite similar in both the experimental design, which are as follows: BSFC was found to decrease with increasing load. The fuel consumption measured for the coated cylinder was found to be 5.6 to 12.5 % less compared to uncoated engine. The friction power was found to be 14 % high for uncoated engine block as compared to that for coated engine block. As the load increases mechanical efficiency of the engine was found to increase. The trend is same for coated and uncoated engine, while it was observed that there is some difference between uncoated and coated engine block with regard to

mechanical efficiency. For coated engine block it was observed that there is 7.5 to 13.5 % enhancement in mechanical efficiency as compared to the uncoated engine.

The specific emission of CO, *sCO* was observed to decrease as the load increases. And this trend is similar for both uncoated and coated engine blocks. At low load the increase in *sCO* observed for coated engine block while difference at higher loads was found to be negligible. Even for *sHC* similar trend was observed. In case of sNO, the decrease in *sNO* was observed with increase in load. This trend is similar for both uncoated and coated engine blocks with almost constant difference. The specific emission of NO, *sNO,* for coated engine block was observed to be about 10 % lower. Smoke opacity, was observed to increase as the load increases. This trend has been found to be similar for both uncoated and coated engine blocks. It was observed that the smoke opacity was 5.7 % lower for coated engine block.

Optimization of the performance parameters namely BSFC, friction power, mechanical efficiency, *sCO, sHC, sNO* and smoke opacity was performed for engine performance enhancement. Taguchi and response surface methodology – genetic algorithm (RSM-GA) methods were used for optimization. For Taguchi analysis, experimentations were conducted with L_{32} $(2^1 x4^9)$ orthogonal array. The effect of various input factors (engine cylinder, speed, load, and coolant flow rate) on specific engine output parameters were described with the help of factor response plot. The optimization of specific engine output parameters are performed based on their requirement. The coated-block engine have positive impact on BSFC, Friction power, Mechanical efficiency, sNO and smoke opacity while slight negative impact on sCO and sHC. The negative impact is slightly higher at low loading condition only while at higher loading condition there is negligible variation found between coated engine and uncoated engine regarding sCO and sHC. For seven different responses there are seven sets of input, obtained for providing optimal values of each response. So to address the optimization issue properly further multi objective optimization conducted using RSM-GA method.

The experimental matrix opted for RSM-GA optimization method was based on Box-Behnken design with three input parameters (speed, load and coolant flow rate) for both uncoated and coated engine cylinder. From optimization results of uncoated engine block and coated engine block it was found that the predicted value of speed is similar for both the cases, while predicted load is higher for the coated engine block, and the coolant flow rate is similar for both the cases. The optimized results were validated using experimentation at the optimized setting value generated through optimization procedure. The variation (in % error) in the experimental and predicted value is found to be less than 10% in both the cases.

The thesis is organized in six chapters. Chapter 1 provides introductory details of all the matter related to present investigation with outlook on the use of nanotechnology in automotive industry. The literature review is presented in Chapter 2 which gives a state-of-art overview of graphite at nanoscale, nanomaterials coating on IC engine, diesel engine performance studies and lastly, problem formulation. Chapter 3 describes the materials, experimental set-up and methodologies adapted in present study. Chapter 4 includes the synthesis of GNPs and thin film coating of GNPs on the engine cylinder. The details of synthesis of GNPs are followed by the description of coating of GNPs on the engine cylinder. Chapter 5 details the real time testing of coated engine cylinder/block in small DI compression-ignition engine test rig. Finally, the conclusions and recommendations drawn from the present work are contained in Chapter 6.

ACKNOWLEDGEMENT

support in laboratory), Mr. N. K. Sharma (for non technical support) and Mr. S. M. Giri (for technical support in machining laboratory) without their supports and helping hand this work would have never completed. I am also expressing my sincere thanks to Mr. Kalyan (IC Engine Laboratory, Department of Mechanical and Industrial Engineering, Indian Institute of Technology Roorkee) for being very helpful in solving the issues when setting up the IC engine test rig for experiments.

I express my sincere thanks to M/s. Greaves Cotton Limited, Pune for providing back support of test engine used in the investigation, M/s. AVL India Pvt. Ltd, Gurgaon for engine measurement system support.

I record my heartfelt thanks to Mr. Harjeet Singh whose invaluable help, consistent cooperation and technical discussion encouraged me to accomplish my research work as well as I am thankful to Mr. Shejale Kiran Prakash for providing some characterization details of required samples related to this research work. I convey my special thanks to IC engine laboratory mates Mr. Rajesh Kumar and Miss. Veena Chaudhary for their kind cooperation and technical discussion about engine testing made the way to complete this project work. I am thankful to all the non technical staffs, master's students and research scholars at Department of Metallurgical and Materials Engineering, Department of Mechanical and Industrial Engineering, Institute Instrumentation Centre, Chemistry Department and Centre of Nanotechnology for their timely cooperation and needful help. I would like to thank all the persons of this institute and outside this institute who directly or indirectly helped me in completion of my project work.

Finally my very special thanks must go to my family members mainly Sri. R. V. Panjiar (Father), Smt. Radhika Devi (Mother), Nitu (Wife) and Rakesh Kumar (Brother) for their sacrifice, support, love and affection enabled me to complete this work.

Himanshu Panjiar

Table of Contents

List of Figures

List of Tables

Nomenclature

$\dot{m}_{CO}$	-	Mass flow rate of CO
$\dot{m}_a$	-	Mass flow rate of air
$\dot{m}_e$	-	Exhaust gas mass flow rate
$\dot{m}_f$	-	Mass flow rate of fuel
$\dot{m}_s$	-	Mass flow rate of emission species
f_s	-	Mass fraction of emission species
3-D	-	Three dimensional
95% C.I.	-	95% confidence interval
Å	-	Angstrom (unit of length; $1\ \text{Å} = 10^{-10}\text{m}$)
A	-	Cross section area of orifice
A1	-	Level 1 input factor A
A2	-	Level 2 input factor A
AFM	-	Atomic Force Microscope
AISI	-	American Iron and Steel Institute
ALD	-	Atomic layer deposition
ANN	-	Artificial Neural Network
ANOVA	-	Analysis of variance
ASTM	-	American society for testing and materials
B1	-	Level 1 input factor B
B2	-	Level 2 input factor B
B3	-	Level 3 input factor B
B4	-	Level 4 input factor B
BCC	-	Body centred cubic
BHN	-	Brinell hardness number
BIS	-	Bureau of Indian standards
BLU	-	Backlight unit
BP	-	Brake power
BPR	-	Ball-to-powder weight ratio
BSE	-	Back scattered electron
BSFC	-	Brake specific fuel consumption
C1	-	Level 1 input factor C

C2	-	Level 2 input factor C
C3	-	Level 3 input factor C
C4	-	Level 4 input factor C
CBD	-	Chemical bath deposition
CCD	-	Chemical composite design
c_d	-	Coefficient of discharge
CFR	-	Coolant flow rate
CI	-	Compression ignition
CNT	-	Carbon Nanotube
CO	-	Carbon monoxide
CO_2	-	Carbon dioxide
COF	-	Coefficient of friction
CRT	-	Cathode Ray Tube
CSD	-	Chemical solution deposition
CTF	-	Current transformation function
CVD	-	Chemical vapour deposition
D1	-	Level 1 input factor D
D2	-	Level 2 input factor D
D3	-	Level 3 input factor D
D4	-	Level 4 input factor D
DC	-	Direct current
DI	-	Direct injection
DOE	-	Design of experiments
DTA	-	Differential thermal analysis
EDS	-	Energy Dispersive X-ray Spectrometry
EMI	-	Electromagnetic Interference
ESD	-	Electrostatic discharge
FED	-	Field emission display
FP	-	Friction power
FSO	-	Full scale output
FWHM	-	Full width at half maximum
g	-	Acceleration due to gravity
GA	-	Genetic algorithm

GC	-	Gas chromatography
GD	-	Gradient Descent
GMR	-	Giant Magnetoresistance
GNP	-	Graphite nanoparticle
GPa	-	Giga Pascal
h	-	Manometer head
H_2	-	Hydrogen
H_2O	-	Water in the form of vapor
HA	-	Hydroxy-apatite
HC	-	Unburned hydrocarbon
HEBM	-	High energy ball milling
HVOF	-	High velocity oxygen fuel spraying
IC	-	Internal combustion
$imep$	-	Indicated mean effective pressure
IP	-	Indicated power
ISO	-	International organization for standardization
kPa	-	kilo Pascal (unit of pressure)
LCD	-	Liquid Crystal Display
MDS	-	Modular diagnostic system
MSD	-	Mean squared deviation
N	-	Speed
n_i	-	Number of crank revolutions
NO	-	Nitric oxide
NO_2	-	Nitrogen dioxide
NOx	-	Oxides of nitrogen
O_2	-	Oxygen
OA	-	Orthogonal Arrays
P	-	Power
PECVD	-	Plasma enhanced Chemical vapour deposition
P-T	-	Pressure and Temperature
PV	-	Pressure-Volume
PVD	-	Physical vapour deposition
QHT	-	Quartz-Homeo-Type

R1	-	Response 1
R2	-	Response 2
R3	-	Response 3
R4	-	Response 4
R5	-	Response 5
R6	-	Response 6
R7	-	Response 7
Ra	-	Surface roughness
RSM	-	Response surface methodology
RSM-GA	-	Response Surface Methodology – Genetic Algorithm
S/N	-	Signal-to-Noise ratio
SAE	-	Society of Automotive Engineers
sCO	-	Specific emission CO
SEM	-	Scanning electron microscope
sHC	-	Specific emission HC
sNO	-	Specific emission NO
SS	-	Stainless steel
STM	-	Scanning Tunnelling Microscope
t	-	Time for fuel consumption
T	-	Torque
TBAB	-	Tetra-butyl ammonium bromide
TBC	-	Thermal barrier coating
TCD	-	Thermal conductivity detector
TDC	-	Top dead centre
TEM	-	Transmission electron microscopy
TGA	-	Thermo gravimetric analysis
THF	-	Tetrahydrofuran
TOAB	-	Tetra-octyl ammonium bromide
V	-	Volt (unit of potential)
v	-	Volume of fuel
v_a	-	Volume flow rate of air
VCD	-	Video Compact Disc

v_f	-	Volume flow rate of fuel
$\hat{w}$	-	Mole fraction
W_i	-	Indicated work per cycle
xGnP	-	Exfoliated graphite nano-platelets
XRD	-	X-ray diffraction

CHAPTER 1
Introduction

Nanotechnology has played a significant role in improving various material properties and opening up new opportunities in various sectors. Nanotechnology in automobile sector can be used to change mechanical properties such as hardness, friction, tribological effect and braking resistance of the engine components. The engine is considered as the soul of the automotive vehicle and its performance plays a major role towards engine functionality and durability. Recently nanotechnology has come up with modern solutions in various fields, which are also being explored for engine development technology. A successful real-scale application of suitable nanomaterial-coating could lead to significant engine performance enhancements. With this aspiration the present investigation attempts at exploiting nanotechnology for compression ignition engine performance enhancement. In this chapter a brief introduction to the performance of diesel engines, nanoscale materials, nanomaterials role in automotive sector, and the basis of material selection is provided.

1.1 Diesel engine

The diesel engine is an internal combustion (IC) engine in which ignition of the injected fuel into the combustion chamber is initiated by the high temperature of gas when compressed greatly. Diesel engine also known as the Compression Ignition (CI) engine is an important power source for both mobile and stationary equipment for over a century. A heavy petroleum fraction is used as fuel in diesel engines because of huge number of diesel operated vehicles world-wide. As among the different categories of automobiles, diesel based small transport utility vehicles sector is the fastest growing sector. So addressing its engine technology improvement is always necessary to provide more efficient vehicles in terms of their engine performance. Therefore use of technological advancements to reduce engine power losses is of vital importance, which directly improves the engine performance. Amongst the engine power losses, friction is one of the major contributors. It is therefore desirable to make an attempt to minimize friction in the engine.

1.1.1 Performance of diesel engine

The performance parameters of IC diesel engine are several and can be referred to in the literature [69,134,51,176,111]. The considered parameters in the present investigation are based on the effect of coating, which are brake specific fuel consumption, friction power, mechanical efficiency, specific emissions with respect to indicated power and smoke opacity, whose details can be referred in Chapter 3. With the ideal coating, it is expected that the power loss due to

friction may be minimized, and due to that, other collateral effects may come into picture whose elaborated study presented in chapter 5. An overview of friction in the engine is presented below.

1.1.2 Friction – cause of wear in diesel engine

Wear in general is the removal of material from its derivative on a solid surface performed by the action of another surface. And it is directly proportional to coefficient of friction of either or both surface involved in mating or sliding contact. While wear in diesel engine core parts is the deformation and removal of material on a surface as a result of mechanical action of the opposite surface which occurs frequently during engine running condition, it can be considered by taking account of multiple interacting surfaces mainly cylinder liner, piston and piston rings. The critical components prone to wear during engine operations are shown in Fig 1-1, with an addition of coating surface which is one of the performance enhancement techniques usually opted for long functional life of the components.
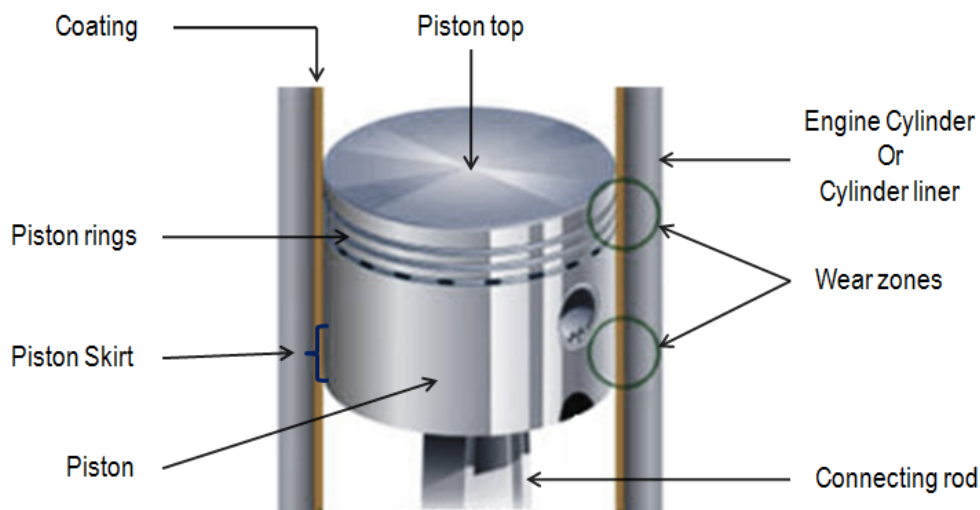
Fig 1-1 Interaction of core engine components

Examples of wear in diesel engine are shown in Fig 1-2 for highlighting the components conditions when not maintained properly during their past functioning period. Improper vehicle operation often causes excessive engine wear, in addition momentary poor lubrication also plays a major role. Failure to observe scheduled change of consumable parts and maintenance fluids e.g. oil filter or air filter, oil also contributes chiefly to engine wear.

Dry operation of the engine results in friction and reduces heat transfer which causes wear of other drive unit parts subjected to friction. Cooling fluid's low level or cooling system poor performance (e.g. very often following winter season poor operation of thermostat or failure of radiator fan may follow) may result in engine overheating and serious failures and consequently expensive repairs.
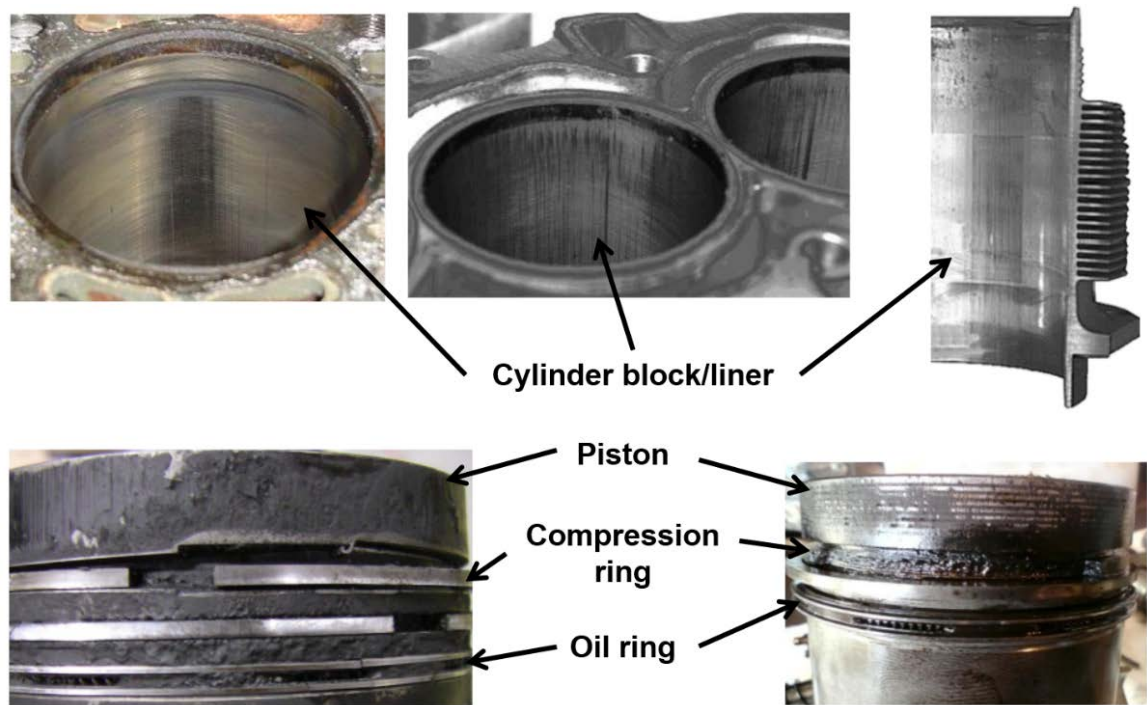
Fig 1-2 Showing wear in diesel engine core components

Engine performance plays a major role and recently nanotechnology based solutions are being explored for engine development technology. This is a contemporary challenge and a successful real-scale application of suitable nanomaterial-coating could lead to significant engine performance enhancements.

1.2 Nanoscale materials and its coating

Nanoscale materials are described as materials with at least one dimension in the nanoscale, i.e. 1-100 nanometres (10^{-9} meter). The use of nanomaterials in any application is termed as nanoscale technology, and it covers a broad cross-disciplinary area of science, engineering and medicine [107]. Few potential applications include high-density data storage devices, flat screen displays, energy storage, fuel cells, sensors, actuators, detectors, nanorobots, molecular electronic devices, nanoimprints, adhesives, fabrics and textiles, catalysts, coatings etc. It also includes materials surface property modification associated with surface phenomena such as adhesion, corrosion, sintering, electrochemistry, etc. and utilizing those phenomena in applications, for example coating, energetic materials, compact disks, environmental monitoring of pollutants, optical coating, etc. As per the current trend in automotive and aerospace industries, nanomaterials (in the form of additive nanoparticles and nanofilms) are finding effective use as catalysts, electrodes, lubricants and advanced antimicrobial, scratch and corrosion resistant coatings. How nanomaterials are converted into useful products is summarized in Fig 1-3. Therefore, nanotechnology is likely to emerge as future key technology in automobile

manufacture, especially in developing new and improved materials to replace existing ones.

Table 1-1 highlights existing product segment with future scopes [107].
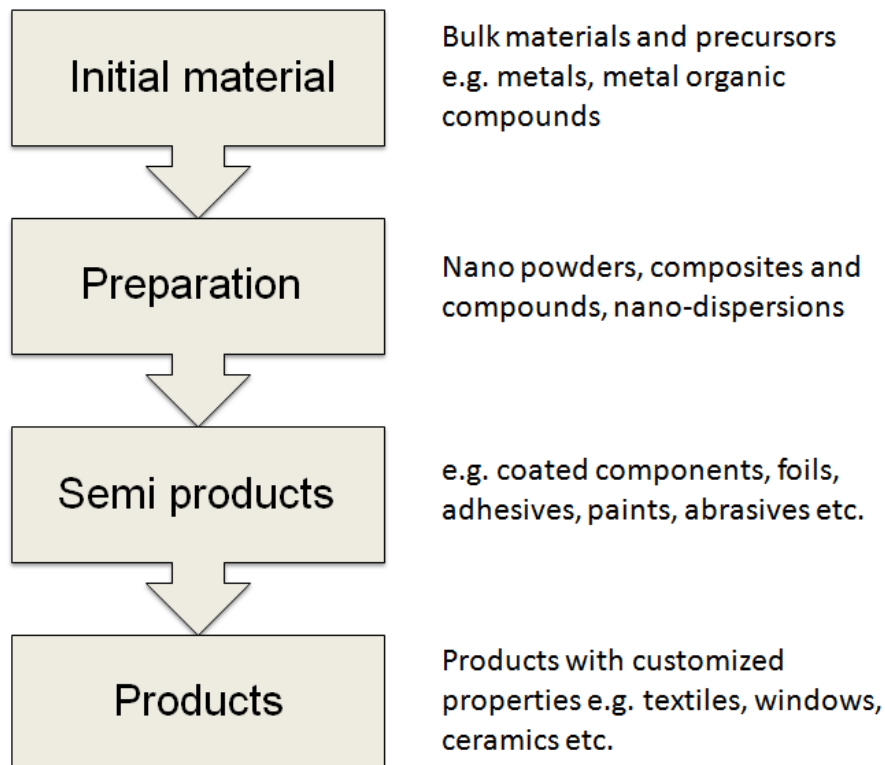
Fig 1-3 Production steps for nanomaterials based products

Table 1-1 Applications of nanotechnologies in automobile

Effects	Functionalities	Existing applications	Future applications
Chemical	Reactivity, surface properties	Corrosion protection, dirt protection, catalysts, fuel additives	Fragrance in the vehicle cabin
Mechanical	Hardness, friction, tribological properties, breaking resistance	Nano varnish, carbon black in tyres	Nano steels, low friction aggregate components
Electronic/Magnetic	Size dependent electronic and magnetic properties	GMR Sensors, piezo injectors	Switchable materials, solar cells
Optical	Colour, fluorescence, transparency	Ultra thin layers, anti glare coatings	Electro chromatic layers
Geometric	Large surface-to-volume ratio	Nano filter	Gecko effect

1.2.1 Coating of nanomaterials

Coating is one of the principal modes incorporating nanomaterials usage in several applications.

A brief overview of coating technology is given below.

Coating is an overlaying process that is applied to the surface of the substrate. The intention of applying the coating is to protect the substrate which may be used for decorative, functional, or both purposes. Functional coatings may be applied to change the surface properties of the substrate, while decorative coatings are performed from aesthetic point of view. The coating may be partially or completely performed based on specific requirement using any of the following processes:

1. Vapour deposition
    a. Chemical vapour deposition
    b. Physical vapour deposition
2. Chemical and electrochemical techniques
3. Spraying
4. Roll-to-roll coating processes
5. Other coating processes

Various functions can be accomplished through coating are changing adhesion properties, altering optical properties, improving magnetic properties, amending catalytic properties, varying electrical or electronics properties, modifying mechanical properties, etc. When the thickness for the coating goes below few micrometers, then it usually referred as thin film coating. Thin film is a layer of material whose thickness ranging from fractions of a nanometer (monolayer) to several micrometers. Generally, thin film deposition technique are classified into two broad categories based on whether the process is primarily chemical or physical. These techniques are explained briefly below:

1. In a chemical deposition process a chemical solution usually referred as "fluid precursor" undergoes a chemical change at a solid surface leaving a solid layer on the substrate at specific process parameters setting. Thin films from chemical deposition methods tend to be conformal, rather than directional. This process is further categorized based on precursor phase as
    a. Plating
    b. Chemical solution deposition (CSD) or Chemical bath deposition (CBD) or sol-gel method
    c. Spin coating
    d. Chemical vapour deposition (CVD)
        i. Plasma enhanced CVD (PECVD)
    e. Atomic layer deposition (ALD)

2. The physical deposition process applies electromechanical or thermodynamic, mechanical mode to produce a solid thin film on the substrate. Films deposited by this method is commonly directional, rather than conformal. This method includes the following processes:

    a. Physical vapour deposition (PVD)

        i. Sputtering

        ii. Evaporative deposition

        iii. Electron beam physical vapor deposition

        iv. Pulsed laser deposition

        v. Cathodic arc deposition (arc-PVD)

    b. Electrohydrodynamic deposition (electrospray deposition)

1.3 Basis of material selection for coating

It is an all time challenge to provide economical and efficient coating of engine component(s) with improved engine performance. As per selected application of coating in the present investigation, the appropriate basis of material selection are found to be compatible with substrate material, lubrication properties, cost (in bulk, nano). Graphite is selected from among solid lubricant materials namely, graphite, molybdenum disulfide, boron nitride, and poly-tetrafluorethylene as the coating material because of following reasons:

a) **Compatibility with substrate material**: The substrate material is gray cast iron, which has graphite in the form of flakes embedded in iron matrix. As graphite is already present in substrate without causing any functional degradation during heat treatment, so graphite can be applied on the surface without having any compatibility issues. Whereas, for other materials additional tests will be required to establish the compatibility parameters.

b) **Lubrication properties**: As coating is to be applied primarily for reducing frictional power of the engine, compatible materials with lubrication effects have advantage over other materials. So graphite appears to be one of the best options for the present application.

c) **Initial cost**: The market value of commercial graphite material (bulk) is reasonable, and can be easily procured world-wide.

d) **Nanoparticle making cost**: Market value of graphite fine powder (nano) is quite expensive, so its preparation in laboratory is a way out as an alternative to direct procurement from market. Laboratory synthesized graphite nanopowder is in-expensive.

Carbon based nanoparticle, specially, graphite nanoparticles have potential applications for weight reduction, reinforcements, corrosion resistance, conductive additives in composites or

coating materials, electrode material substituting platinum in dye-sensitized solar cell, and the raw materials for preparing diamond [206,204,191,92,133].

1.3.1 Graphite

Graphite is an allotropic form of carbon having hexagonal crystal system. It is thermodynamically the most stable form of carbon. Equilibrium P-T phase diagram of carbon (Fig 1-4) shows the state and phase of carbon for various temperatures and pressures [32,203], which confirms that at lower temperature and pressure graphite is most stable, and verified experimentally (Fig 1-5) [33]. Graphite finds several usage which also include applications in refractories, batteries, foundry, lubricants, steel making etc. The discovery of graphite as lubricant additive was made by Joseph Dixon in the early of 19th century.
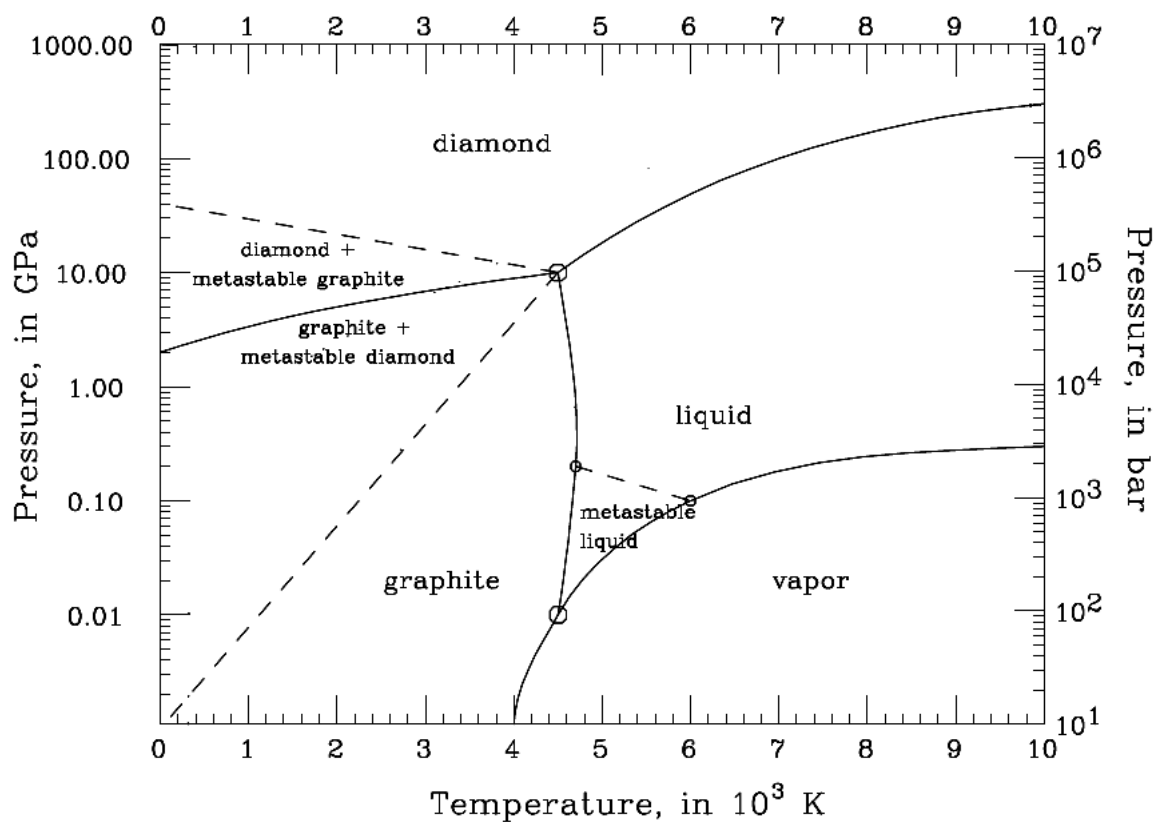
Fig 1-4 Theoretical Pressure – Temperature (P-T) phase diagram of carbon

1.3.2 Graphite nanomaterials consumption

The graphite is used for various applications whose consumption is reported by various firms working in graphite based product development from last few decades. The entry of graphite nanomaterials in market through various processes and product development is highlighted in Fig 1-6, which provide stable platform for graphite nanomaterials in future market and most probably going to cover major portion of the graphite applications soon.
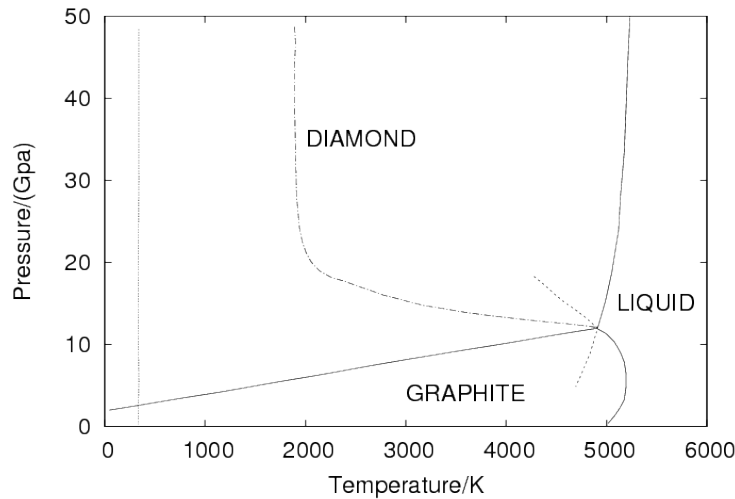
Fig 1-5 Equilibrium P-T phase diagram of carbon showing the domains where each of the allotropes are stable
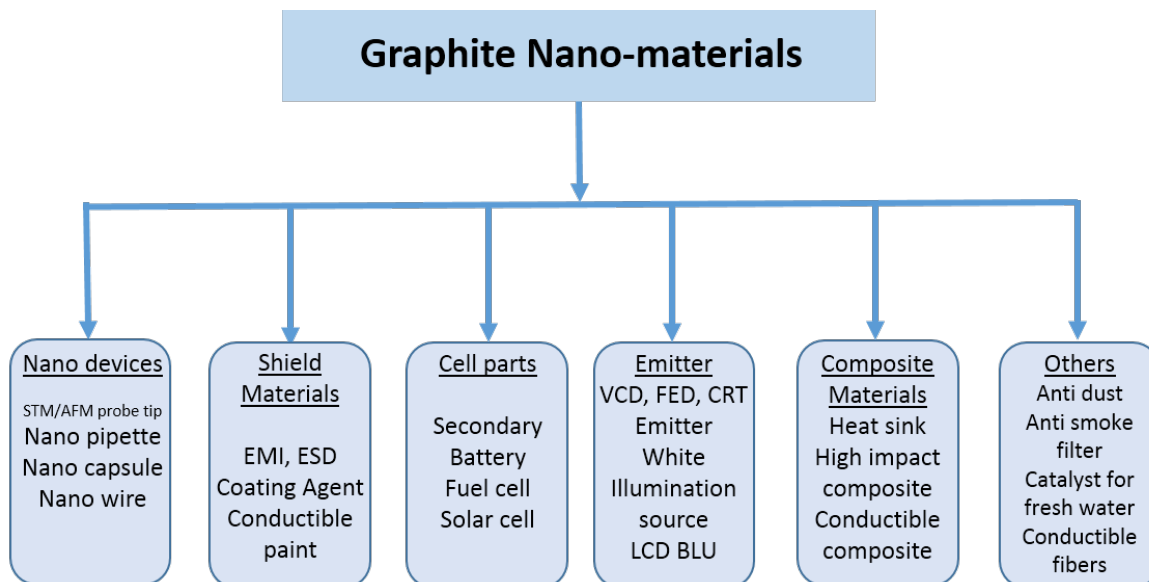
Fig 1-6 Graphite nanomaterials use in various applications

1.4 Thesis outline

Following the introduction chapter, the literature review is presented in Chapter 2 which includes the graphite at nanoscale, nanomaterials coating on IC engine, diesel engine performance studies and problem formulation. In Chapter 3, the materials, equipments and methodologies adapted in present study are presented with details of experimental set-up of the major experiments. The results and discussion are presented in Chapter 4 and Chapter 5. Chapter 4 includes synthesis of graphite nanoparticles (GNPs) and optimization of thin film coating of GNPs on the engine cylinder. Chapter 5 describes the testing of coated engine cylinder/block in a small DI compression-ignition engine test rig. Lastly, the conclusions drawn from the present work are given in Chapter 6.

Several synthesis and coating methods have been developed recently to synthesize and coat nanomaterials. In this context, testing of nanomaterials coating is still a challenge. In this chapter recently developed processes for nanomaterials synthesis and its coating are reviewed with special emphasis on nanoparticle synthesis with less contamination and homogeneous coating of nanomaterials. Apart from that a brief review on the coating of internal combustion diesel engine component(s) and the effect of coating on engine component performance are presented. There is very little published literature available on diesel engine cylinder coating using nanomaterials, with special reference to their effect on engine friction. In the later part of this chapter, the survey of recent studies on the performance analysis of internal combustion diesel engine with special emphasis on friction are also presented. Finally, the aims of the present investigation are briefed.

Literature relevant to the present investigation has been included under following headings namely coating material, nanomaterial synthesis, nanomaterial coating, coating of engine component and engine performance analysis as shown in Fig 2-1.

2.1 Coating material: Structure and properties

The structure of graphite is shown in Fig 2-2, as well as its atomic model presented in Fig 2-3. It provides insight of graphite structure make-up. However, crystalline graphite has a layered structure with strong in-plane covalent bonds and weak Van der Waal bonds across layers.
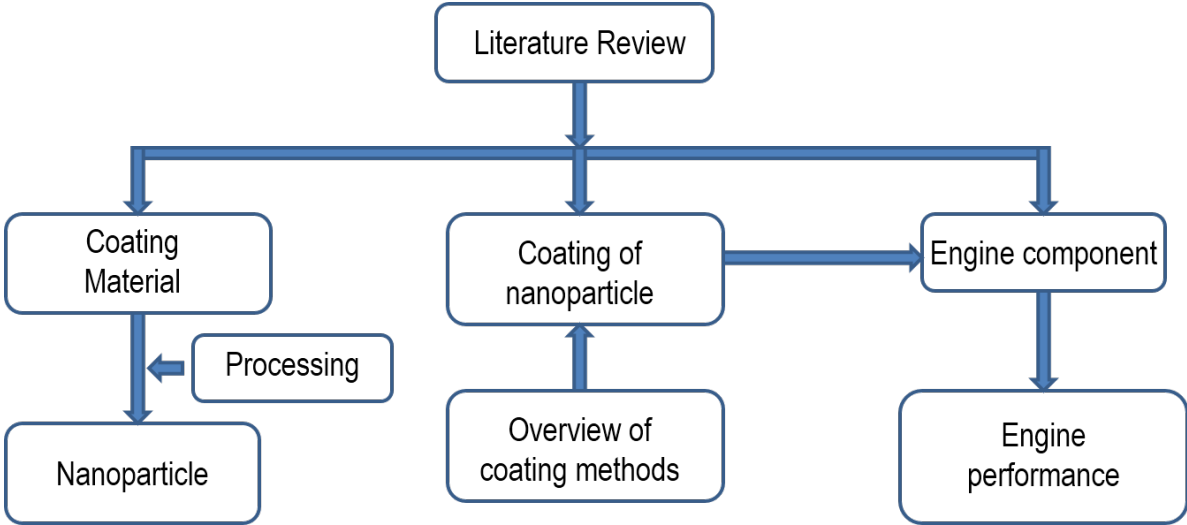
Fig 2-1 Overview of literature survey
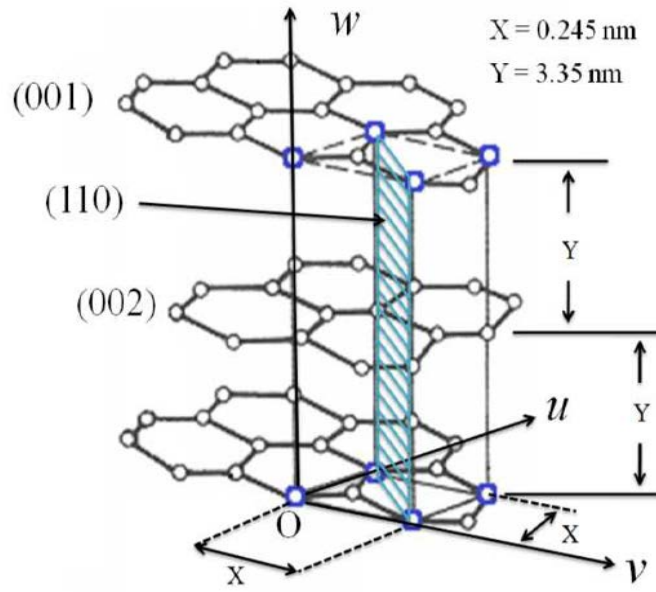
Fig 2-2 Sketch of graphite structure
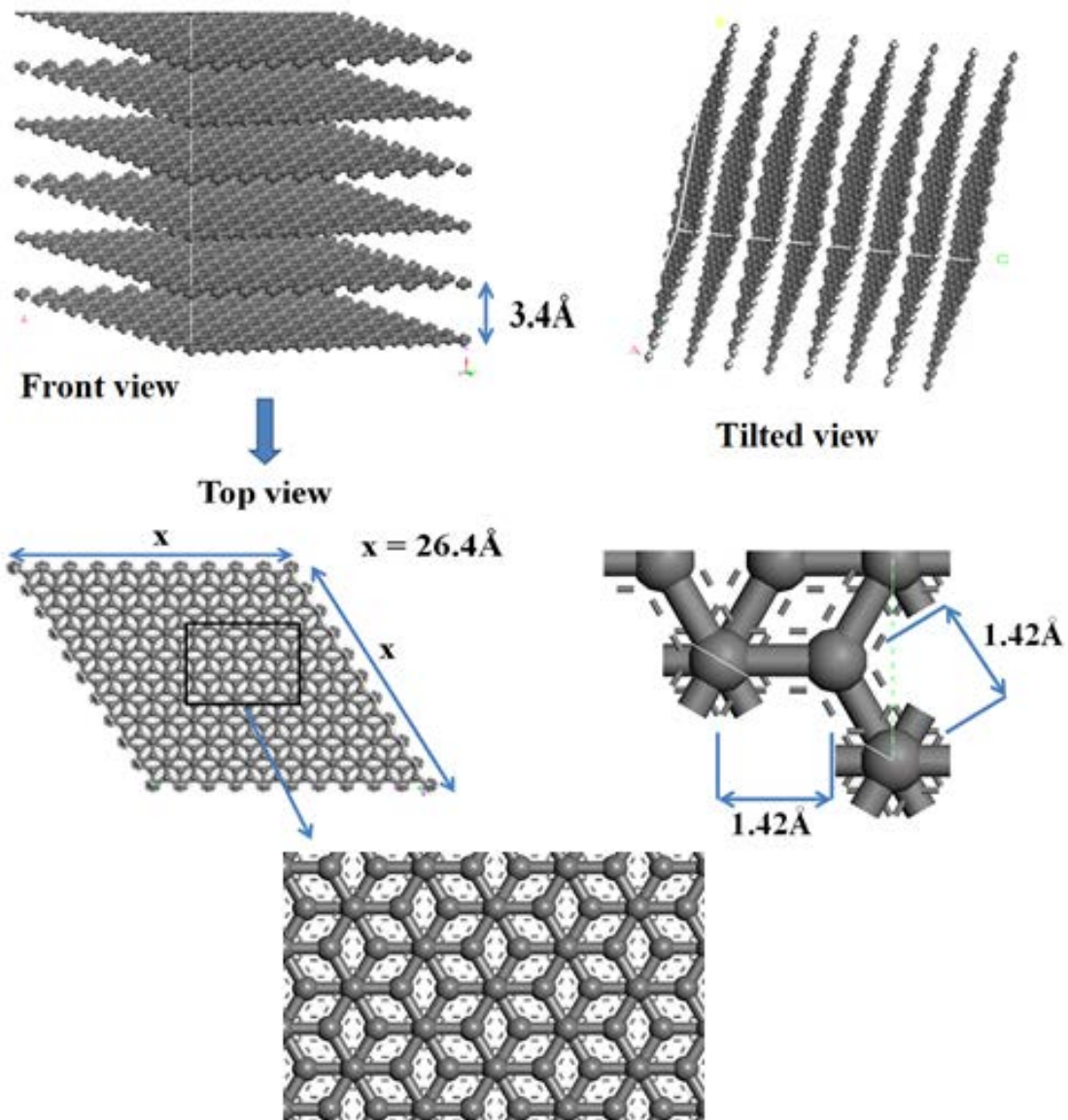
Fig 2-3 Atomic arrangements of carbon in graphite model

This crystal structure is the cause of unusual combination of properties for graphite. Two types of bonding in graphite structure acting in different crystallographic directions results in high degree of anisotropy. These two contrasting chemical bonds provide ability to graphite to form a solid film lubricant. The weak Van der Waals forces govern the bonding between adjacent layers, which allows individual layer to slide over one another making it an ideal lubricant. Graphite has many low temperature applications. It is also used as an excellent refractory material with a high melting point (3650°C). Selected properties of graphite are listed in Table 2-1.

Table 2-1 Properties of graphite ([a][130],[b][53],[c][80],[d][103],[e][162])

Sl.	Properties	Specification
1	Crystalline form[a]	Hexagonal
2	Modulus of Elasticity (GPa)[a,e]	8-1000 (vary with respect to C – axis)
3	Boiling point (K) [a]	4560
4	Bulk Density (g/cm^3)[a,e]	2.1-2.3
5	Coefficient of Thermal Expansion (X 10^{-6}/°K)[c,d]	5 – 36 (increases with temperature)
6	Heat of fusion (KJ/mol)[a]	46.84
7	Electrical resistivity (Ohm.m)[a]	3000 X 10^{-6} (c – direction)
		2.5 – 5.0 X 10^{-6} (a,b – direction)
8	Chemical behavior[a]	Inert and non toxic
9	Colour[a]	black
10	Thermal conductivity (W/m.K)[b,e]	50-3000 (high value for perfect crystals of large sizes)
11	Atomic volume (cm^3/mol)[a]	5.315

2.2 Nanomaterial synthesis

The approach adopted to synthesize nanomaterial invariably depends on type of application. At present, various successful applications of nanomaterials, and several technologies have been patented with quite a few of them available as commercial products. There are enormous supporting literature reporting the enhancement in materials properties when nanomaterials are used as additives, reinforcement etc. [12,14,15,41,63,81,83,87,152,164,170,179,185]. Few of nanomaterials applications are mentioned hereunder [35,157,142].

Nanomaterials in energy and environmental applications: Fuel cells, solar energy, hydrogen storage, lithium ion batteries, capacitors, air pollution control, water and waste water treatment, sensors.

There are many techniques available to synthesize nanoparticles, which are broadly classified under two types of processing, namely, physical method and chemical method. The differences in their approach are pictorially represented in Fig 2-4.
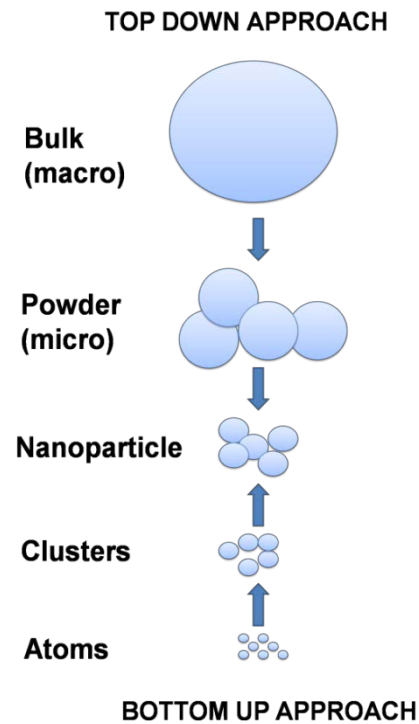
TOP DOWN APPROACH

Fig 2-4 Nanomaterials synthesis methods

Physical method is also called as top-down approach for nanomaterials production where nanoscale particles are formed from bulk state of the material through dissociation by various mechanical means, while chemical method usually called as bottom-up approach for synthesis of nanomaterials where atoms are basic building blocks which group together and spread its dimensions up to nanoscale length under specific conditions. The major categorical issues between above two methods are highlighted in Table 2-2 [142,183,62,56,25,57,35,180].

Table 2-2 Types of nanomaterials synthesis method

Sl.	Specification	Physical method	Chemical method
1	Principle	Breaking down of bulk material up to nanoscale length	Unification of atoms up to nanoscale length
2	Types	Such as Laser (pulse) ablation, mechanical attrition, high energy ball milling, pulsed wire discharge.	Such as Sol-gel technique, spray pyrolysis, solvo thermal reaction, vapour deposition.
3	Quality	Comparatively poor quality	Better quality
4	Production	Economical for large scale production	Not economical for large scale production
5	Approach	Top down	Bottom up, sometime also called as biological technique

Agglomeration is a common phenomena found in both methods due to higher surface energy of particles at nanoscale length. But, one of the main differences between the methods is the particle size control. Nanoparticles obtained via physical methods have a wide particle size distribution, while the chemical method yields a narrow distribution [183]. Literature overview

on synthesizing nanoparticles from their bulk state (graphite in present investigation) is presented here. During synthesis of nanoparticles, contamination is one of the major issue. Much of the emphasis is on the synthesis of graphite nanoparticles with negligible contamination, which is also discussed in literature several times [6,193,189,190]. The most popular approach is mechanical grinding in a ball milling device [135,52,39,40,188,152]. However, crystalline graphite has a layered structure with good lubrication property, so grinding is extremely difficult, especially to obtain submicron-size particles [82]. Using the same approach Chen et al. [39] reported that particle size of graphite powder reaches nanoscale with continuous porous structure, while most work reported on ball milling of graphite leads to mixture of amorphous and crystalline phases [175,189]. Based on source availability and feasibility of synthesis, for the present investigation mechanical milling was found to be very less expensive. A brief literature insight about mechanical milling for producing carbon nanomaterials is discussed here.

Chen et al. [39] reported that ball milling of graphite at ambient temperature resulted in a nanoporous structure with higher specific internal surface area of the micropores as compared to external surface area. The transformation of phase from hexagonal to turbostratic and amorphous structure is reported. And the confirmation of nanoporous structure formation mainly associated with disordered carbon is revealed. Antisari et al. [6] used mechanical milling method to prepare graphite nano-sheets. Bulk graphite was milled with water as a lubricant and finally graphite nano-sheets of 10 nm thickness was prepared. Another study reported that, nanocrystalline graphite can be prepared by ball milling and the milled nanocrystalline graphite was found to be thermally stable with large structural disorder [165]. Investigation by Chen et al. [40] reported that the new growth mechanisms involved in the process of one dimensional nanomaterials formation through high energy ball milling (HEBM). Graphite sample was milled for 150 hrs at ambient temperature and then heated in a tube furnace at 1400 °C for 6 hrs in inert atmosphere and finally CNTs were formed in the sample. It was concluded that the mass production of nanomaterial is possible by ball milling-annealing process [39].

Some of the studies reported the mechanical milling of graphite under vacuum [82,188]. In Kim et al. [82] study it is reported that milling method is effective method for graphite size reduction and pressure reduction in grinding jar promotes removal of chemical species. While study of Welham et al. [188] reported the formation of carbon ribbons with delamination, defects and translation is possible on extensive ball milling of graphite. Milling leads to the increase in surface area of milled powder particles.

2.3 Nanomaterial coating

It may be a protective or functional or decorative coating containing nanomaterials. The nanomaterial is suspended in a liquid/paste or powder form when applied to form a coating layer

on the substrate. Based on desired function, the fraction of a nanomaterial in a coating system is decided [163]. This section addresses the commonly used coating techniques of micro/nano materials. Sometimes these type of coatings are also referred as thin film coating or nano-structured coating [85,86,120,121,122,59]. Coating methodology has to be selected on the basis of new findings from basic and applied research in multidisciplinary fields. Nowadays, there are numerous coating systems ranging from simple coating with one or two steps to sophisticated coating methods with multilayer characteristic. The interest in research and development of nanomaterial coatings science and surface technology increased because of [94]:

a. High performance coatings at lower manufacturing cost is the key requirement of industry that can be achieved using nanomaterial(s)

b. There are enormous hazardous wastes produced (like volatile organic compound and hexavalent chromate) by conventional coating processes that results in water and air pollution. Significant reduction in the hazardous waste during the production of nanomaterial coating processes is observed.

Numerous techniques can be employed for nanomaterials coating onto a substrate. To name some of the major coating methods for nanomaterials coating, they are electrochemical coating, electroless chemical coating, conversion coatings, chemical vapor deposition (CVD), physical vapor deposition (PVD), spray coating, sol-gel method, spin coating, nanocomposite coating, and powder coating [94,107,112]. Nanomaterials coatings have emerged as a highly promising method in various fields such as solar cell application, bio-implant industry, adhesive industry, electronics and plasma industries.

It is not possible to discuss all the work done till date on nanomaterials coating. It is decided to showcase the use of nanomaterials based coating for various applications including studies similar to the present investigation which focuses on nanomaterials coating application in IC engine. Andrievski's investigation shows that thin films with nanograined structures are readily obtained using nanomaterials while difficult to obtain with bulk samples. It is also reported that the microhardness of multilayer nitride films increases as the number of layers increases [5]. In the study of Singh et al. [168], multi-layered mesoporous TiO_2 films were synthesized for dye-sensitized solar cells at different temperatures using sol-gel method followed with spin coating. The photo-conversion efficiency of dye-sensitized solar cells increases with the crystallinity of TiO_2 films. Investigation by Gao et al. [59] showed that using PVD technique nano-structured alloy coatings (Fe-Cr-Ni-Al-Y_2O_3 oxide dispersive strengthening alloy coating as well as Ti and Ti alloys coating) can be developed with enhanced high temperature properties such as corrosion and oxidation resistance. The composition of coating is controlled accurately

by adjusting the currents on the constitution of the composite target and the deposited coating average grain size found approximately 100 nm. Lin et al. [89] study shows that silver plating with nano-graphite filler can act as a conductive adhesive. The nano-graphite filled silver plating developed using electroless plating method. Patil et al. [126] studied the effect of nano and micro size ceria based coating on stainless steel and found that nanocrystalline ceria coating improved the high-temperature-oxidation resistance. Investigation performed by Paulmier et al. [128] showed that the nano-crystalline films of graphite can be deposited on Ti substrate by cathodic plasma electrolysis. The different composition coating as well as different structure coating can be developed with the help of varying applied load. A study on thermoelectric nanomaterial (boron- doped nanographite ensembles) for high temperature applications conducted by Xie et al. [197] and found that rapid annealing and quenching of the material leads to improvement in their thermoelectric power factors.

Recently electrophoretic deposition method has been adopted by many experts from the fields of chemistry, medical applications [187,8,44,124] and photoelectronics such as solar cells or electronics devices [201]. Electrophoretic deposition method is a type of electro-chemical method where coating over one electrode takes place under high potential of the system and few work showcase its use and their application are furnished in literature [37,75]. Workie et al. [194] also reported that electrophoretic deposition method of AlN is a better way to deposit coating as compared to ion beam nitridation, chemical or vapor deposition, or reactive sputtering. Another study by Farnoush et al. [49] on electrophoretic deposition method pointed out that apart from deposition potential and time, particle size also plays a major role. In a study by Jain et al. [75], nanomaterials coating performed with electrophoretic deposition method where nanocrystalline hydroxyapatite (HA) deposited on Ti6Al4V substrate with thermally grown TiO_2 layer of 0.74 µm thickness. Successful deposition of HA on substrate found over the deposition voltage of 100-250 V. Dual phase microstructure was obtained having HA phase islands and phase boundary of TiO_2 with faceted morphology. It was found that there is a strong dependency of deposition voltage on island size and porosity in HA as well as distribution of dense faceted TiO_2 structures. As the deposition voltage increases HA% increases and TiO_2% decreases in top surface of the deposition.

Wear study of nanomaterials based coating has also been reported in the literature showing positive effect of nanomaterials coating as wear resistant at macro and nano scale [15,14]. Balani et al. [15] studied the wear characteristics of Al_2O_3–CNT nanocomposite coating and it was found that the wear resistance behaviour is significantly affected by the amount of CNT in nanocomposite. The enhancement of macro wear resistance by approximately 49 times while the nano wear resistance hiked by 18 times was observed in comparison with Al_2O_3 parent

matrix alone. Balani et al. [14] studied the tribological behaviour of CNT-reinforced HA coating in physiological fluid environment. It was found that the presence of CNT in HA coating provides superior wear resistance as compared to HA coating apart from fracture toughness enhancement and biocompatibility. Nayak et al. [108] reported that nano indentation indicates the heterogeneity in mechanical properties of nanomaterials coatings present at nanoscale. Novel properties of nanostructure materials such as electrical, optical, and magnetic are factual due to quantum confinement of electrons in one or all dimensions. Presently, carbonaceous family of nanomaterials such as graphene, graphene oxides, carbon nanotubes (CNTs), carbon nanodots, graphite sheets hold the most promising variety among nanoscale materials [196].

2.4 Coating on IC engine components

The term engine performance enhancement always have general goal of reducing emissions with increase engine efficiency. Many studies showing coating of engine component(s) with various objectives can be found in the literature. Although there are published literature on coating of engine component(s), there is still a lack of research towards implementing these coating commercially. Some of the challenges are cost of coating and real-time engine performance with coating. The present investigation demonstrates the feasibility of producing cost effective coating with better real-time engine performance after coating. Louda [90] gave an overview of coatings of engine components and their functional impact over engine efficiency. He also discussed the use of thin coatings in automotive industry, even this study show cases the near future aspects of thin coatings with nanotechnology. The use of ceramics as coating material in the internal combustion engine is well known from last few decades [181,202,9] and so many times it was indicated as (TBC) thermal barrier coating [184,141,65,68].

Based on experimental investigations of Taymaz et al. and Hejwowski et al. [178,68] on diesel engine and by Nesbitt [109] on rocket engine it was found that if thin layer coating of an insulating oxide applied externally on engine cylinder wall, then heat loss reduction is obvious. And if cylinder bore inner surface is coated with insulating material then the heat loss is further reduced due to lower thermal gradient for conduction mode heat transfer.

Computer simulation of combustion chamber insulation and its effect on the performance of turbocharged turbocompound diesel engine was studied by Assanis [9]. It was concluded that thin (3 mm) spray coating of zirconia significantly reduces the heat loss (43%). The situation leads to significant drop in volumetric efficiency. Even for all levels of insulation it was reported that inter cooled turbocompound engine perform better than non-inter cooled engine. Buyukkaya et al. [34] studied the effect of ceramic coating on change in thermal behaviour of pistons. Their work showed that the coating of $MgO–ZrO_2$ on piston increases the maximum surface temperature of the piston, 48% for AlSi alloy and 35% for steel. Due to ceramic coating, strength

of piston materials are improved. Even effects of thermal barrier coating on engine performance in diesel engine evaluated by Gurbuz et al. [65]. It was found that thermal barrier coating increases the engine power, and at the same time increase in exhaust gas temperature observed which decreases the HC and CO emission and increases the (oxides of nitrogen) NO_x emission. Hejwowski et al. [68] studied the effect of thin TBC's on the diesel engine performance and wear. TBC's with NiCrAl bond coat and PSZ was used for producing efficient TBC on diesel engine. The optimum value of coating thickness was found to be slightly less than 0.5 mm. It was reported that thermal barrier coated engine has a specific fuel consumption, 15-20 % lower as compared to uncoated engine. Also, no significant wear was observed in engine components. Oner et al. [113] studied the effect of CrN coating using PVD method on engine cylinder. It was concluded that coating reduces wear and deformation by achieving hydrodynamic lubrication throughout engine running conditions. Reduction in pitting and ripping was also observed, which occurs due to thermal shocks and strains in combustion chamber. Prabhu et al. [132] studied the effect of CrN coating using PVD method on piston ring for reducing friction and wear apart from improving engine performance. The thin film coating on the piston ring reduced the surface roughness of piston ring by 60% and improved the engine output power.

Kamo [78] used the thermal barrier coating for making diesel-engine adiabatic, which raised the thermal efficiency and multi-fuel capability of the engine. Similar study of Taymaz [177] reported that thermal barrier coatings made of $CaZrO_3$ and $MgZrO_3$ onto the bond coat base of NiCrAl. The coated engine effective efficiency improved with reduced fuel consumption. Comparison made by Ciniviz et al. [43] shows that the ceramic coated engine is more effective compared to conventional engine (uncoated) for useful energy production. If coating wear and scuffing resistance is as good as cylinder/liner made of cast iron, then only coating can be used as a substitute [45,144]. Dahotre et al. [45] found that the limitations of conventional way of coating raises the need of new methods such as nanomaterials coating.

Based on literature survey it is clear that use of nanomaterials in the arena of engine performance improvement is still in the nascent stage. Several researchers have attempted to address various automotive industry related challenges using nanomaterials, but very little has been done till date to address critical aspects such as engine performance. In the present work we have tried to improve the engine performance by incorporating a graphite coating in the DI engine cylinder.

2.5 Engine performance

The two aspects which affect the engine performance, namely (a) engine friction and (b) engine performance parameters are addressed in this section. Engine friction section include literature which provide insight into friction under various types of situation. While engine performance

parameters section describes the literature of past efforts made towards improvement in engine efficacy.

2.5.1 Engine friction

In general, friction is the force resisting the relative motion of material elements sliding against each other. Generally it is represented by coefficient of friction, whose lower value is mostly favourable for many processes [60,61,88,143,45]. In case of engine, friction is represented as engine friction power, whose lowest possible value is always desirable. The literature which provides insight into the matter of friction under various types of situation is furnished here for developing awareness about such issues with their consequences.

Friction is an important concern in automotive industry (specifically for better engine performance) and the issues were raised and discussed by many experts time and again [88,143,45]. It is essential to have reciprocating and/or mating engine components with least frictional forces. As high frictional forces leads to higher wear rate of engine components which in turn affect the engine life. But friction is an inevitable phenomenon which takes place inside the engine cylinder during its continuous operation. The internal combustion diesel engine works in a cyclic manner, with a sequence of continuous processes namely intake, compression, combustion (including expansion) and exhaust, which take place at high temperature as shown in Fig 2-5 [58]. At that temperature, combustion chamber experiences thermal shock, pressure and negative effects of exhaust gases. As a result of combustion reaction, the chances of chemical corrosion and deformation of the surface of combustion chamber elements such as cylinder/liner, valve, piston, piston head increases. These phenomenon lead to gradual decrease in the performance of the engine.
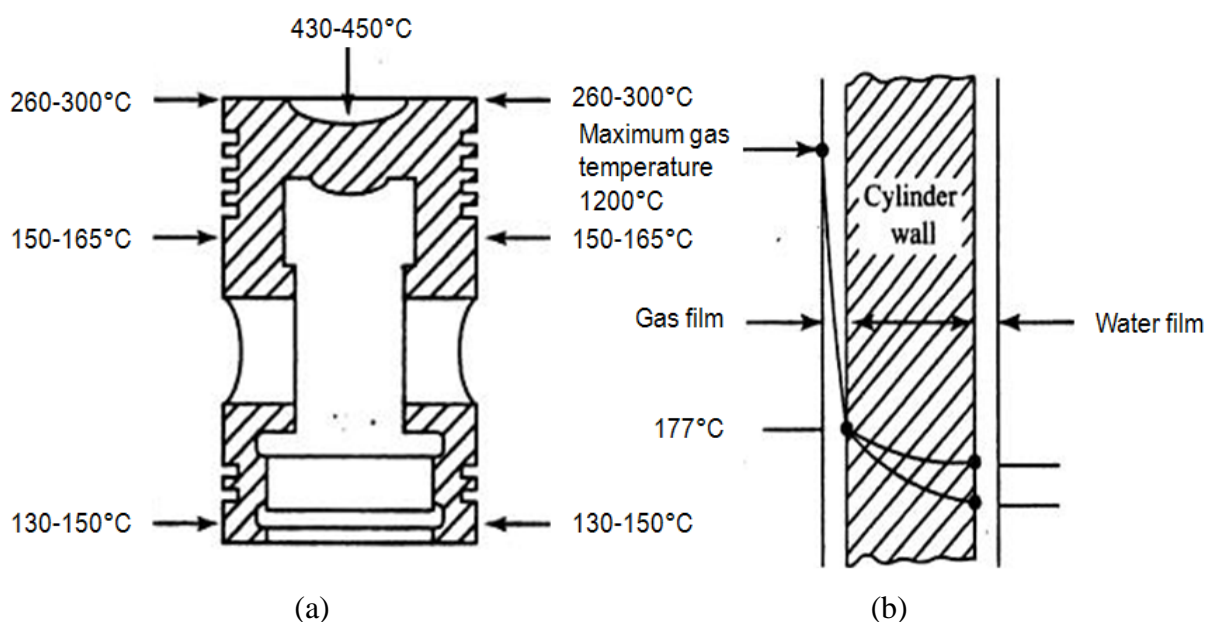
Fig 2-5 (a) Piston temperature distribution and (b) Cylinder wall temperature distribution of a properly cooled cylinder

Total frictional loss of the engine is the accumulation of all the accounted frictional losses in the engine. It was found that, of the total frictional loss cylinder-piston system alone accounted for 50-65% while other parts namely valve train system (tappet/cam journal) contributes 10–20% and crank - bearing system contributing the rest [143,88]. Lin et al. [88] mainly focused on mechanical friction in engine, which is mainly contributed by multiple engine parts combinations namely cylinder bore/piston and piston rings also termed as piston system's friction losses. Johansson et al. [77] experimentally studied friction in cylinder liner/piston ring contact using reciprocating tribometer. They concluded that 50% total frictional losses are caused by cylinder-piston system alone.

Michalski et al. [97] investigated piston-cylinder assembly wear in combustion engine based on cylinder liner roughness parameters and increased air dustiness. From experimental observation it was found that piston rings wear appeared more intensive as compared to cylinder liner and piston. Laboratory test conducted by Truhan et al. [182] to assess the friction and wear behaviour of piston ring and cylinder liner materials of heavy duty engines using wide variety of realistic lubricants. Geometric models for ring and liner wear volume calculation were developed and found to agree with actual engine wear rates.

2.5.2 Engine performance parameters

In the present investigation a small DI diesel engine is considered for testing of engine performance. Furthermore, diesel engine has gained interest because of its reduced fuel consumption compared to the gasoline engine. There are several engine performance parameters, which are broadly categorized under the following headings, namely, Power and Mechanical Efficiency, Fuel Air Ratio, Volumetric Efficiency, Specific Output, Specific Fuel Consumption, Thermal Efficiency and Heat Balance, Exhaust Smoke and Emissions, Effective Pressure and Torque.

But in the present investigation, the considered performance parameters are Brake specific fuel consumption (BSFC), Friction power , Mechanical efficiency, Specific emission carbon monoxide (sCO), Specific emission unburned hydrocarbon (sHC), Specific emission nitric oxide (sNO), and Smoke opacity. The study of engine performance (mainly with respect to coating) in terms of efficacy and emissions carried out by various researchers is given below.

Hazar et al. [67] conducted a comparative study between diesel and biodiesel fuel operated diesel engine with and without coating of engine parts. The study reveals that there is decrease in engine power, specific fuel consumption, as well as exhaust gas emissions (except NO_x) for all test fuels used in the coated engine when compared with that of the uncoated engine. Another investigation [72] also confirms that the engine coating considerably improve the performance of the test engine for all the test fuel/blends. All polluting emissions were reduced

except for oxides of nitrogen. Based on the study it was confirmed that coating process is a reasonable method for engine performance enhancement. Few studies on engine combustion and emission characteristics of a diesel engine using thermal barrier coating are reported in the literature [140,141]. Ramu et al. [140] concluded that the thermal barrier coating can increase engine performance with a slight increase in smoke density. Another study of Ramu et al. [141] reported that the thermal barrier coating of ZrO_2/Al_2O_3 is responsible for improved engine performance with decreased NO_x emission.

Based on studies conducted during last few decades, an underlying connection between engine emission and environmental instability is clearly established. As the emission percentage increases pollution level in environment increases, which has a negative impact on human health [1]. Due to health and environment issues, engine emission check becomes an essential step as the emissions from engine during its operating state is harmful [127,192,131,48,123,146]. Research and development about engine emissions measurement and control is a major concern for all engine manufacturer as worldwide emission legislation are becoming more stringent day by day. While a lot of effort is directed to improve the efficiency of the diesel engine, research on alternative fuels such as biodiesel which can be used in the same engine are gaining credence [199,186,148,137,138,139,10,11,2,4,7,13,70,73,79,98].

2.6 Problem formulation

On the basis of literature survey following are the objectives of the present study:

a. Synthesis of graphite nanoparticles
b. Thin film coating of graphite nanoparticles on small sample of engine cylinder
c. Thin film coating of graphite nanoparticles on engine cylinder
d. Testing of coated engine cylinder in small DI diesel engine test rig

The work flow chart adopted in the present study is shown in Fig 2-6.
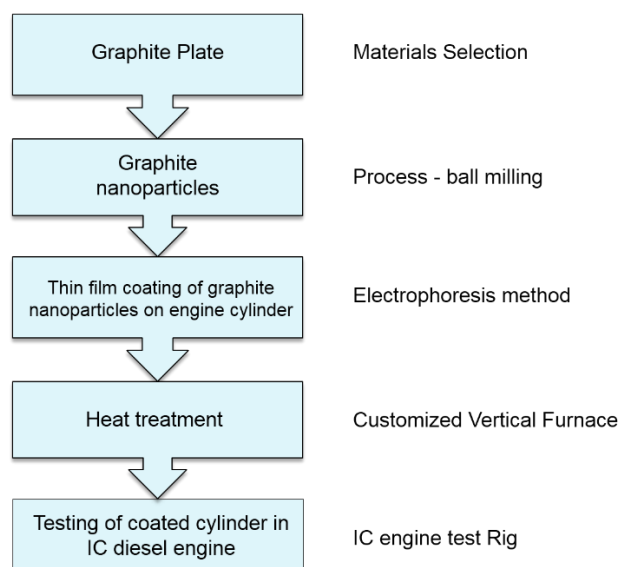
Fig 2-6 Work flow path of present study

CHAPTER 3
Experimental Details

In this chapter, methodologies adopted for the synthesis, coating and characterization of graphite nanoparticles and the real-time testing of graphite nanoparticle coated engine cylinder are described in detail.

A preliminary study of nanomaterial synthesis and its coating was undertaken before selecting the method for graphite nanoparticle synthesis and its coating. In the present investigation, the study also examined the effect of engine component coating on the engine performance. The chosen method for graphite nanoparticle synthesis was mechanical milling. Which was clubbed with a modelling approach involving artificial neural network to optimise the process. The ensuing nanoparticles were characterized at various intervals for the particle size and residual strain determination using electron/optical microscopy techniques and X-ray diffraction. The selection of method for graphite nanoparticles coating was based on literature with a hit and trial approach. Electrophoresis was selected based on its coating efficiency as compared to other methods. Upon successful coating of graphite nanoparticles, the coated sample underwent heat treatment for strengthening of the coating. Further, the graphite nanoparticle coating are characterized for their micro constituents and mechanical properties as per selected application in the present investigation. Microstructural characterization to identify the various phases, their distribution and surface morphology was carried out using X-ray diffraction, energy dispersive X-ray spectroscopy and electron microscopy technique. Mechanical property measurement was carried out on the coating for surface roughness, hardness and coefficient of friction analysis. Finally graphite nanoparticles coated engine cylinder underwent testing in a small DI diesel engine test rig to uncover the effect of coating on engine performance. And the best trade off between engine performance parameters are established through optimization methods, namely, Taguchi method and response surface methodology-genetic algorithm (RSM-GA) method. Engine testing were carried out at similar ambient conditions with regular flow of coolant as per designed setting.

The investigation details are given under four headings, namely (a) Materials, (b) Equipments, (c) Methods, and (d) Engine experimental setup.

3.1 Materials

Present investigation deals with the coating of cylinder block/sleeve made of cast iron. This is considered to be the most versatile material to be used as engine cylinder/liner for diesel engine. Cast iron act as a substrate during coating process, as the nanoparticle will be coated on it.

Selection of material for specific application requires background knowledge of all materials, as well as advance knowledge of the processes and in service conditions. Materials are to be chosen in such a manner so that they can fulfil all the required parameters of the specific application. Based on the literature survey and experimental outlook, the material considered for coating in the present investigation is graphite. As graphite nanoparticles are expensive, it was decided to synthesize nanoparticles of graphite in the laboratory using mechanical milling. For this purpose bulk graphite was procured from the market in the form of plates as shown in Fig 3-1.

Fig 3-1 Bulk graphite plate used for graphite nanoparticle synthesis

3.1.1 Cast iron engine cylinder/block

Greaves Cotton (model: G600 W-II) engine was considered as coating base which is generally used in small vehicle segment of automotive sector as three-wheelers and goods transport vehicle. Fig 3-2 shows the actual engine cylinder/block used in the present investigation, specifications of which are tabulated in Table 3-1.

Fig 3-2 Cast iron engine cylinder used in commercial vehicles

Table 3-1 Standards and mechanical properties of considered engine cylinder [24,153]

Material	ASTM Standard	SAE Standard	Poisson's ratio	Modulus of elasticity (GPa)	Hardness (BHN)
Engine Cylinder	ASTM A48	SAE J431	0.26	95-105	130-180

The microstructure and composition of the same engine cylinder is shown in Fig 3-3 and Table 3-2. Microstructure was obtained using optical microscope and the chemical composition is based on manufacturer specification.
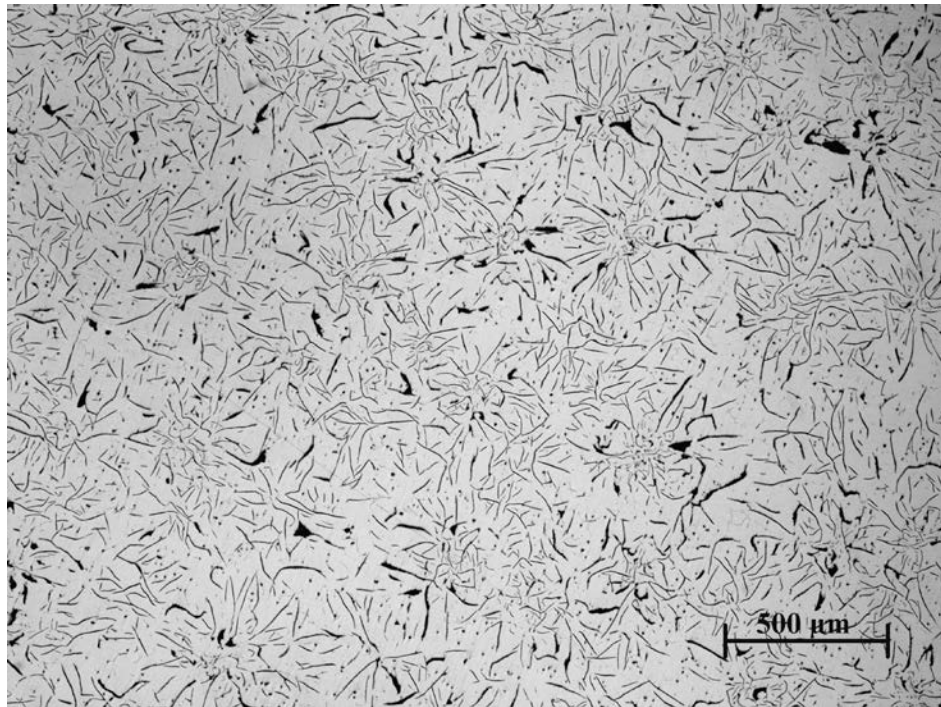
Fig 3-3 Microstructure of engine cylinder showing graphite flakes distribution in iron matrix

Table 3-2 Chemical composition of engine cylinder

Composition[%]	C	Si	Mn	P	Cr	S	Mo	Ni	Fe
Engine Cylinder	3.0	1.8	0.25	0.08	0.3	0.12	0.2	0.4	rest

3.1.2 Copper plate

Chemical route was selected for coating, which requires an active counter electrode. Copper was chosen as the counter electrode in the present work. Fig 3-4 shows the actual electrode used for coating the engine block.

3.1.3 Chemicals

The properties of chemicals used for chemical coatings are given in Table 3-3 (with the properties of graphite nanoparticle). The source and purity level of chemicals are additionally provided as per manufacturer specification.
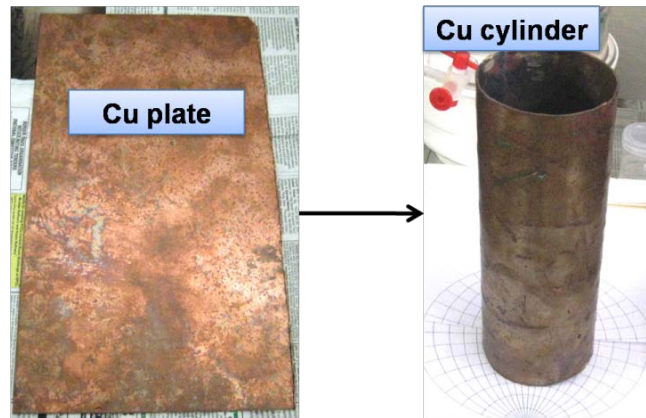
Fig 3-4 Copper plate and its cylindrical form used as an electrode during electrophoretic coating of engine cylinder

Table 3-3 Properties of chemicals/compounds considered in the present investigation

Sl.	Components	pH --	% Assay (%)	Molecular Weight (g/mol)	Density (g/ml)	Melting point (°C)	Boiling point (°C)	Source
1	Oxolane (or) Tetrahydrofuran (THF)	7-8	99.7	72.11	0.887	- 108.4	66	Merck Millipore
2	Tetra-Octyl Ammonium Bromide (TOAB)	7	98	546.74	--	95-98	--	Sigma Aldrich
3	Graphite Nanoparticle (GNP)	5-6	99.9	12.01	2.2 @ 20°C	--	--	In-house
4	Tetra-butyl ammonium bromide (TBAB)	--	99	322.38	--	100-104	--	Himedia

3.2 Equipments

Several equipments were used in the course of the present investigation. A few are described in characterization techniques as those equipment's are materials characterization instruments and others are described in engine testing setup section as those equipment's are used in conjunction with engine test rig or related with engine testing only.

3.2.1 Ball milling machine PM100

Planetary ball mill model PM 100 by 'RETSCH' was used for mechanical milling in the present investigation as it is most suitable for attaining highest degree of fineness by mechanical communition. Planetary ball mills are appropriate for both dry and wet grinding, where they pulverize and mix brittle, fibrous, soft, and medium-hard to extremely hard materials. PM 100 is a convenient bench-top model as shown in Fig 3-5 with one grinding station for grinding jars with a nominal volume of 12 to 500 ml. It has a counterweight for balancing purpose and this counterweight can be adjusted on an inclined guide rail. In this way the different heights of the

centres of gravity of differently-sized grinding jars can be compensated in order to avoid disturbing vibrations of the machine during grinding. The extremely high centrifugal forces developed during grinding result in very high pulverization energy and therefore short grinding times. The difference in speeds between the balls and grinding jars produces an interaction between frictional and impact forces, which releases high dynamic energies. The interplay between the grinding media and the jar walls causes very effective degree of size reduction in the planetary ball mill.

Fig 3-5 Planetary ball milling machine (Retch, Model PM100) used for graphite nanoparticle synthesis

3.2.2 Chemical Chamber

A customized chemical chamber shown in Fig 3-6, was made with 2 cm thick glass plate, as other material chamber were not fount suitable for containing the electrolyte solution during the coating process due to reactivity with chemicals used for coating.
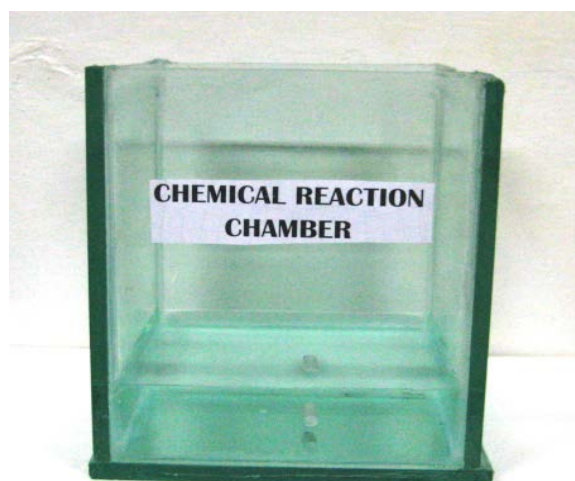
Fig 3-6 Chemical reaction chamber used for electrophoretic coating of engine cylinder

3.2.3 Furnace and furnace Attachment

A customized external furnace chamber was made with 3.5 mm thick stainless steel (SS-302). External furnace chamber was necessary to obtain good properties of coated samples after heat treatment. The external furnace chamber was designed and made to fit with the existing furnace set-up. The actual external furnace chamber with heat treatment set-up used in the present investigation is shown in Fig 3-7.
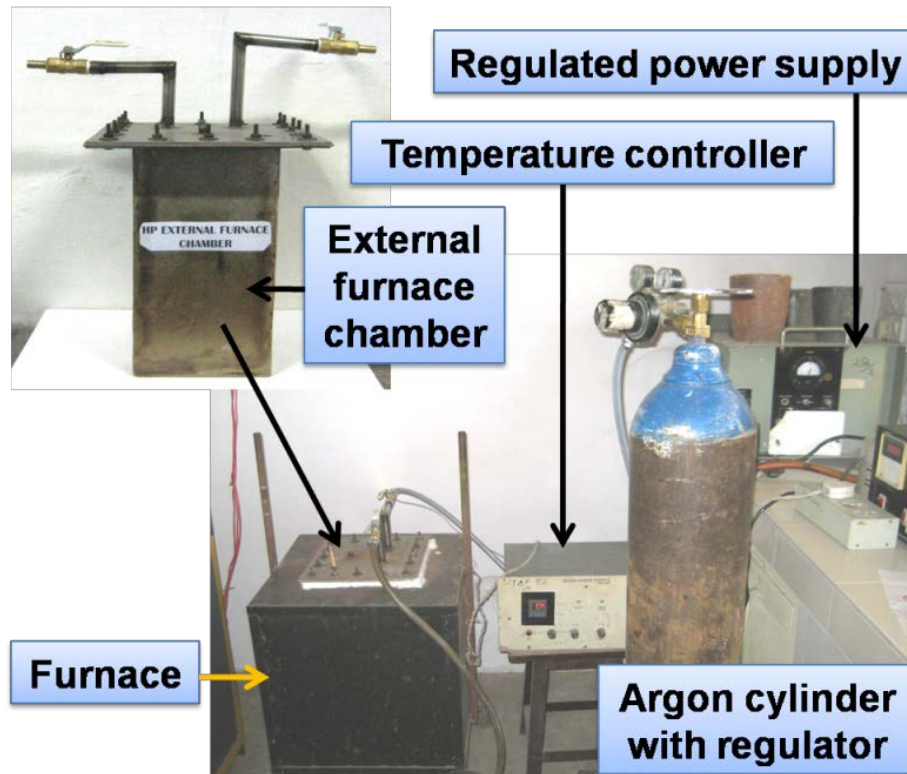
Fig 3-7 Heat treatment set-up, showing major items including customized external furnace chamber which was specially designed to accommodate the engine cylinder

The external furnace chamber has the option of independent selection of chamber inlet/outlet and all type of heat treatment options such as vacuum heating, inert atmosphere heating, ambient condition heating, and air tight heating.

3.2.4 Regulated DC Power Supply

A customized DC power supply was designed and made for performing chemical coating. To fulfil the power supply demand of selected coating process, a constant DC power supply was required with the range of 10-60 V. So power supply customization was done as per the requirement and ordered in market. The final regulated DC power supply unit is shown in Fig 3-8, which is used in the present investigation. The multimeter used in present case have calibration certificate, and used for regular cross verification of the regulated voltage supply.

Fig 3-8 Regulated DC power supply used as a potential source during coating process

Other supplementary devices partially used in the present investigation are digital weighting balance, ultrasonic cleaner and magnetic stirrer as shown in Fig 3-9.

Fig 3-9 Auxiliary devices used in present study; digital weighting balance,
ultrasonic cleaner and magnetic stirrer

3.3 Methods

In this section, methods or techniques adopted in the present investigation are discussed in detail. This section further divided into three sub- sections, namely statistical/modelling techniques, processing/synthesis techniques, and characterization techniques. In the present investigation modelling of milling process was performed using artificial neural network (ANN) to optimise the particle size reduction process such that the cumbersome intermediate particle size sampling and over milling can be avoided. And to establish the best trade off between engine performances

parameters two methods are explored, namely Taguchi method and response surface methodology clubbed with genetic algorithm (RSM-GA) method. ANN, Taguchi, and RSM-GA are well-established methods in the field of statistical, modelling and optimisation. An overview of these methods are briefly given in the following sub-sections. The present investigation also deals with nanomaterials, so its safe handling practice and precautions are also discussed.

3.3.1 Statistical/Modeling techniques

Artificial Neural Network

Artificial Neural Networks (ANN) are massive parallel computing system consisting of an extremely large number of simple processors with many interconnections. ANN model attempts to use some "organizational" principles believed to exist in the human brain [99]. ANN is believed to be made based on various functions that a human brain does, apart from intelligence; ANN represents the concept of human brain function (i.e. biological neural networks) and has many desirable characteristics such as:

   a. Massive parallelism
   b. Learning ability
   c. Generalization ability
   d. Inherent contextual information processing
   e. Low energy consumption

Computational model of neurons

McCulloh and Pitts [96] firstly proposed a binary threshold (activation function) unit as a computational model for an artificial neuron. McCulloh and Pitts model however contains a number of simplifying assumptions that do not reflect the true behaviour of biological neurons because of the use of threshold activation function. There are various activation functions shown in Fig 3-10 that can be used to model an artificial neuron which will reflect approximately the true behaviour of biological neuron [96,74]. The sigmoid function is by far the most frequently used in ANN. It is strictly an increasing function that exhibits smoothness and has the desired asymptotic properties. ANN can be viewed as weighted directed graphs in which artificial neurons are nodes and directed edges (with weights) are connected between neuron outputs and neuron inputs. Positive weights correspond to excitatory synapses, while negative weights model inhibitory ones.

   (a) Threshold   (b) Piecewise linear   (c) Sigmoid   (d) Gaussian
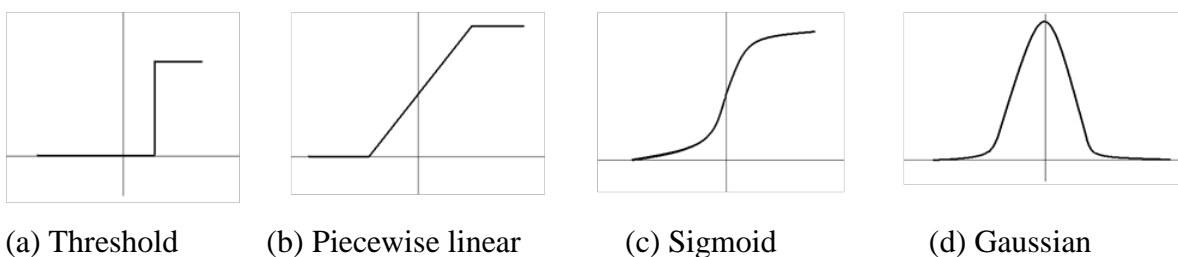
Fig 3-10 Different types of activation functions used to model an artificial neuron

Based on the connection pattern, ANN is grouped into two categories:

   a) Feed-forward networks, in which graphs have no loops, and

   b) Recurrent (or feedback) networks, in which loops occur because of feedback connections.

   In the most common family of feed-forward networks, called multilayer perceptron, neurons are organized into layers that have unidirectional connections between them as shown in Fig 3-11. Different connectivity yield different network behaviours. Generally feed forward networks are static, that is they produce only one set of output values rather than a sequence of values from a given input. Feed-forward networks are memory-less in the sense that their response to an input is independent of the previous network state.
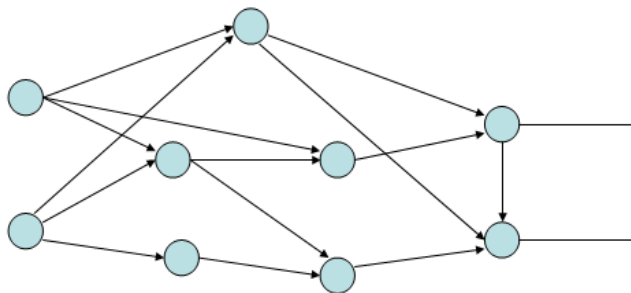
Fig 3-11 Feed forward network

   Recurrent or feedback networks are dynamic systems, when a new input pattern is presented, the neuron outputs are computed. Because of the feedback paths, the inputs to each neuron are then modified, which leads the network to enter a new state Fig 3-12.
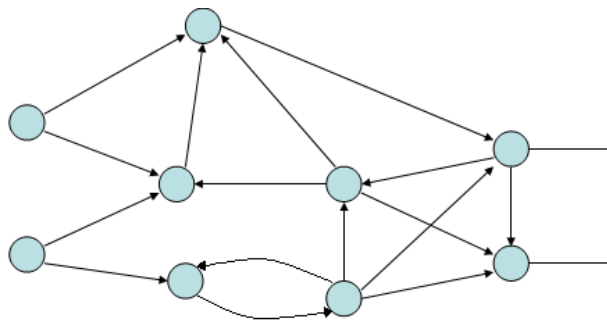
Fig 3-12 Recurrent or feedback network

   Different network architectures require appropriate learning algorithms. The ability to learn is a fundamental trait of intelligence. Although a precise definition of learning is difficult to formulate, a learning process in the ANN context can be viewed as the problem of updating network architecture and connection weights so that a network can efficiently perform a specific task. The network usually must learn the connection weights from available training patterns. Performance is improved over time by iteratively updating the weights in the network [99]. ANN ability to automatically learn from examples makes them attractive and exciting. Instead of following a set of rules specified by human experts, ANN appears to learn underlying rules (like

input-output relationships) from the given collection of representative examples. This is one of the major advantages of neural networks over traditional expert systems.

To understand or design a learning process, first we must have a model of the environment in which a neural network operates, that is, we must know what information is available to the network. This model is referred to as the learning paradigm. Second, we must understand how network weights are updated, that is which learning rules govern the updating process. A learning algorithm refers to a procedure in which learning rules are used for adjusting the weights. There are three main learning paradigms, namely supervised, unsupervised and hybrid. In supervised learning or learning with a teacher, the network is provided with a correct output for every input pattern. Weights are determined to allow the network to produce outputs as close as possible to the known correct outputs. In unsupervised learning or learning without a teacher, does not require a correct output associated with each input pattern in the training data set. It explores the underlying structure in the data, or correlations between patterns in the data, and organizes patterns into categories from these correlations. Hybrid learning combines supervised and unsupervised learning, part of the weights are usually determined through supervised learning, while the remaining are obtained through unsupervised learning.

Learning theory must address three fundamental and practical issues associated with learning from samples: capacity, sample complexity, and computational complexity. Capacity concerns how many patterns can be stored, and what functions and decision boundaries a network can form. Sample complexity determines the number of training patterns needed to train the network to guarantee a valid generalization. Too few patterns may cause 'over-fitting'. Computational complexity refers to the time required for a learning algorithm to estimate a solution from training patterns. There are four basic types of learning rules (a) Error-correction, (b) Boltzmann, (c) Hebbian, and (d) Competitive learning [74]. Out of above learning rules error-correction rule was used in the present work, therefore the explanation about this rule is presented in a brief manner.

Error-correction rule: In the supervised learning paradigm, the network is given a desired output for each input pattern. During the learning process, the actual output say *y* generated by the network may not equal the desired output *d*. The basic principle of error-correction learning rule is to use the error signal *(d-y)* to modify the connection weights for gradually reducing this error. The perceptron learning rule is based only on this error correction principle. A perceptron consists of a single neuron with adjustable weights, w_j, j=1, 2, 3...., n and threshold (u), as shown in Fig 3-13 [96].
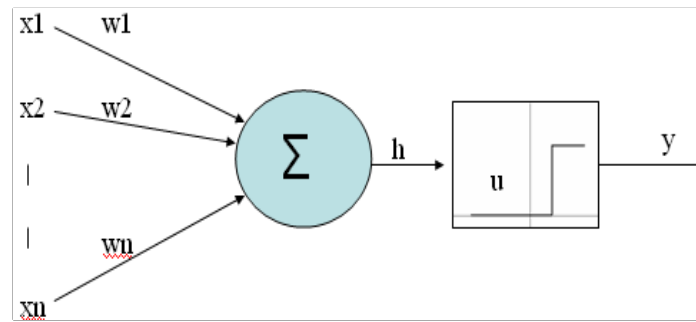
Fig 3-13 McCulloch-Pitts model of a neuron

ANN as technique

ANN is well established technique in research arena used by scientists around the world [169,23,104,17]. Artificial Neural networks are parameterized non linear models used for empirical regression and classification modeling. Their flexibility enables them to discover more complex relationships in data than traditional linear statistical model. Neurons in one layer are connected to neurons in the adjacent layer only, and the strength of connection between two neurons in adjacent layers is represented by coefficient known as weight. An ANN usually consists of three layers, an input layer, hidden layer(s) and an output layer. The neuronal model also includes an externally applied coefficient called as bias, which has the effect of increasing or decreasing the net input of the activation function, depending on whether it is positive or negative, respectively. A neural network is trained on a set of examples of input and output data. The outcome of this training is a set of coefficients (called weights w_{kj}) and a specification of the functions which in combination with the weights relate the input to the output as shown in Fig 3-14.
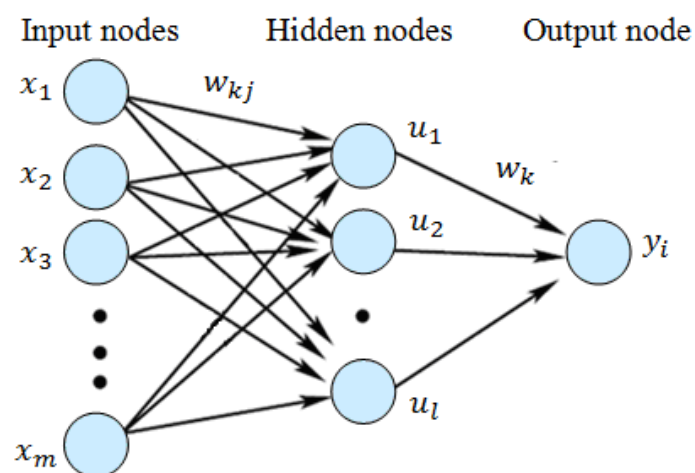
Fig 3-14 Schematic illustration of feed forward ANN with single hidden layer

The training process involves a search for the optimum non linear relationship between the inputs and the outputs. In artificial neural network similar to linear regression, linear functions of the inputs x_j are operated on by an activation/transfer function (Equation 3-1) so that each input

contributes to every hidden unit. Mathematically we can describe neural network by writing the following pair of equations:

$$u_k = \varphi\left(\sum_{j=1}^{m} w_{kj} x_j + b_{kj}\right) \qquad\qquad (3-1)$$

$$y_i = \varphi\left(\sum_{k=1}^{l} w_k u_k + b_k\right) \qquad\qquad (3-2)$$

where φ is hyperbolic tangent transfer function; $x_1, x_2,...x_m$ are the input signals; $w_{k1}, w_{k2},...w_{km}$ are the synaptic weights of neuron k; u_k is the linear combiner output due to the input signals; b_{kj} *and* b_k are the biases, analogous to the constant that appears in linear regression; and y_i is the output signal of the neuron. The strength of transfer function is in each case determined by the weight w_{kj}. The final output is defined as a linear function of hidden nodes and the constant (Equation 3-2). The combination of Equation 3-1 with a set of weights, biases, value of k and the minimum and maximum values of the input variables defines the network completely.

ANN model development procedure

First make the database of the actual process and store in a particular format having both the input and output variables. After completion of final database, they were normalized within the range ±0.5 as follows [104,169]:

$$p_n = \left(\frac{p_0 - p_{min}}{p_{max} - p_{min}}\right) - 0.5 \qquad\qquad (3-3)$$

Where p_0 is the point observed data, p_n is scaled data and p_{max}, p_{min} are the maximum and minimum observed data points. The above equation was used to scale average of inputs and output in order to provide consistency for the analysis. Before training, the database is randomized in order to divide the information into training and validation datasets in a fair manner. One of the datasets is used for training while the other for testing how the trained models behave with unseen data. An important step in developing an ANN model is the determination of its weight matrix through training. Gradient Descent (GD) algorithm had been used to train the network, which applies a function minimization routine and back propagate error into the network layers as a means of improving the calculated output. For a trained model the overall error E_D is the sum of squared error between the desired output t and calculated output y as given here in Equation 3-4 [19].

$$E_D \propto \sum_{j} (t_j - y_j)^2 \qquad\qquad (3-4)$$

To minimize the error during the training, gradient descent method is used where the idea is to find a minimum of $f(x)$ by repeatedly computing minima of a function $g(t)$ of a single variable t, as follows. Suppose that f has a minimum at X_0 and we start at a point x. Then we look

for a minimum of f closest to x along the straight line in the direction of negative direction of divergence of $f(x)$, which is the direction of steepest descent (= direction of maximum decrease) of f at x. That is, we determine the value of t and the corresponding point;

$$z(t) = x - t\nabla f(x) \qquad\qquad\qquad (3-5)$$

at which the function; $g(t) = f(z(t))$, has a minimum. We take this $z(t)$ as our next approximation to X_0 [84].

Another class of ANN models that employ an unsupervised training method on validation data is called as self organising neural network. It explores the underlying structure in the data, or correlations between patterns in the data, and organizes patterns into categories from these correlations. A committee is formed which consists of models that have contributed to the minimization of the overall test error. The committee prediction is the average value of individual model predictions.

Design of experiments

The experiments are planned and conducted to obtain relevant and sufficient data from a small number of experiments to infer the science behind the observed phenomenon. A well planned set of experiments, in which all parameters of interest are varied over a specified range, is a much better approach to obtain systematic data. Mathematically, such a complete set of experiments ought to give desired results. The selection of such experimental set is so called design of experiments (DOE).

DOE is an organized technique to establish the relationship between factors influencing a process and the output of that process. There are several DOE methods adapted to find the correlation between input factors and the output of the process, such as Taguchi orthogonal array, central composite design (CCD), D-optimal, full factorial design, box-behnken design etc. Out of which Taguchi method, full factorial design and box-behnken design have been used for designing of the test matrix in present study, details of which are furnished here under except for full factorial design as in this design all possible combinations of experiment are executed.

Taguchi Method

Genichi Taguchi developed a method based on "orthogonal array" experiments which gives a much reduced "variance" for the experiment with "optimum settings" of control parameters. Thus the combination of design of experiments with optimization of control parameters to obtain best results is achieved in the Taguchi method. Orthogonal Arrays (OA) provides a set of well balanced (minimum) experiments and Taguchi's Signal-to-Noise ratios (S/N), which are log functions of desired output, serve as objective functions for optimization, help in data analysis and prediction of optimum results. Taguchi method reported in several literatures as well as its use is reported by several researchers [149,150,173,174,147,38]. Taguchi method uses a standard

statistical technique called analysis of variance (ANOVA) to measure the confidence of results. Analysis provides the variance of controllable and noise factors. In addition S/N ratio in Taguchi method is very useful particularly if strong noise factors are present, it is calculated for each trial run separately (with repetitions). Repetition permits determination of a variance index also called the signal to noise (S/N) ratio. Greater this value, smaller the product variance around the target value. In S/N ratio mean squared deviation (MSD) is used as a measure that depends on both average and standard deviation of the data. But MSD requires separate definition for different quality characteristics which is discussed here. Signal-to-Noise ratio, S/N, is defined as:

$$^S/_N = -10\ log_{10}(MSD) \hspace{3cm} (3-6)$$

where, MSD – mean squared deviation from the target value of the quality characteristic, which is given as follows:

a) For smaller is better:

$$MSD = (y_1{}^2 + y_2{}^2 + y_3{}^2 + ..)/n$$

b) For nominal is best:

$$MSD = ((y_1\text{-}m)^2 + (y_2\text{-}m)^2 + (y_3\text{-}m)^2 + ..)/n$$

c) For bigger is better:

$$MSD = (1/y_1{}^2 + 1/y_2{}^2 + 1/y_3{}^2 + ..)/n$$

Where,

y_1, y_2,.. are results of repeated trial runs of experiment.

m – target value of results

n – number of repetitions (Y_i)

Box-Behnken design

Box and Behnken proposed some three-level designs for fitting response surfaces [28]. These designs are formed by combining 2^k factorials with incomplete block designs. The resulting designs are usually very efficient in terms of the number of required runs. The design is shown geometrically for three factors in Fig 3-15. Notice that the Box-Behnken design is a spherical design, with all points lying on a sphere of radius under root 2, which does not contain any points at the vertices of the cubic region created by upper and lower limits for each variable [101]. Box-Behnken design found to be appropriate for present study as in this method designing of experiments confine the input factor levels under range of study for all experimental runs as compared to central composite design method, where factor levels are considered beyond range of study. Compared to full factorial design, Box-Behnken method require less number of experimentations to know the process behaviour.
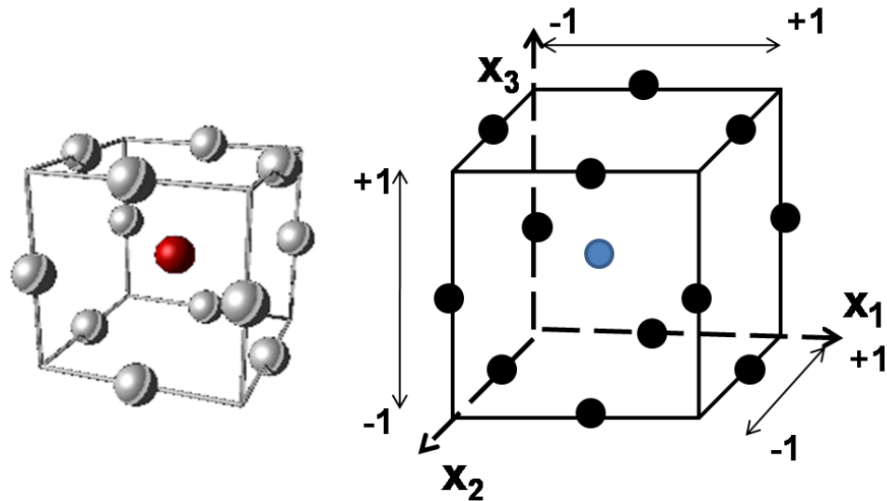
Fig 3-15 **3D** *model and geometry of Box-Behnken design*

Response Surface Methodology

Response Surface Methodology (RSM) is a statistical tool which searches the relationship between one or more response variable(s) and the several stimulant variables. This method was introduced by Box and Wilson in 1951 with main theme of using sequence of design experiments to obtain an optimal response [30].

As RSM uses statistical models, and therefore professionals need to affirm that even the best model is an approximation to actual consideration. In practice, both the parameter values and the models are unknown, and subjected to uncertainty. And an estimated optimum target need not be optimum in reality due to inadequacies of the model and the errors of the estimates. Nevertheless, RSM has an efficacious track-record of aiding researchers improve their services and products [101]. An elaborated view of the design of experiments theory is presented by Box and Draper [29], Myers and Montgomery [105] and Montgomery [100] work among numerous. Searle [161] has reexamined the application of experimental design for unbalanced data while Montgomery and Runger [102] study presented a complete survey of the use of statistics in design. Wu and Hamada [195] discussed the use of various designs for RSM and multidisciplinary design optimization.

In maximum RSM problems, the accurate response function f is unknown. In order to formulate a right approximation for f, the investigator usually starts with a low-order polynomial in more or less small region. If the output can be defined by a linear function of input variables, then the estimating function is a first-order model. A first-order model with two independent variables can be expressed as:

$$y = \beta_0 + \beta_1 x_1 + \beta_2 x_2 + \varepsilon \qquad\qquad (3-7)$$

where x_1 and x_2 are independent variables, $\beta_0, \beta_1, \beta_2$ are coefficients and e is the constant. If response surface is having a curvature, then a higher degree polynomial should be used. The approximating function with two independent variables is called a second-order model:

$$y = \beta_0 + \beta_1 x_1 + \beta_2 x_2 + \beta_{11} x_{11}^2 + \beta_{22} x_{22}^2 + \beta_{12} x_1 x_2 + \varepsilon \quad (3-8)$$

All RSM problems generally use either one or mixture of both of these models. Proper experimental design must be used to gather data in order to acquire the most efficient result in the approximation of polynomials. Once the data are gathered, the Method of least square is applied to estimate the parameters in the polynomials. The response surface analysis is executed by employing the fitted surface. The response surface designs are used for fitting response surface. Hence, the objective of studying RSM can be accomplished by following:

1. Interpreting the topography of the response surface (local minimum, local maximum, ridge lines), and

2. Determining the region where the optimal response occurs. The aim is to move quickly and efficiently along a path to get to a minimum or a maximum response so that the response is optimized.

For example, in the case of the optimization of the output say (z), which depends on two independent variables (x) and (y), and therefore practitioners wants to find the levels of (x) and (y) that minimize the (z). (z) is a function of the levels of (x) and (y), and expressed as:

$$z = f(x, y) + \varepsilon \qquad\qquad\qquad\qquad (3-9)$$

where ε represents the noise or error observed in the response z as well as other type of variations not counted in $f(x,y)$. The surface represented by $f(x,y)$ is called a response surface. The response can be presented graphically, either in the form of contour plots or in 3D space which helps in envision the shape of the response surface. Contours are the curves of constant responses drawn in the x, y plane by keeping all other variables fixed. Each contour corresponds to a particular altitude of the response surface, as shown in Fig 3-16 [101].
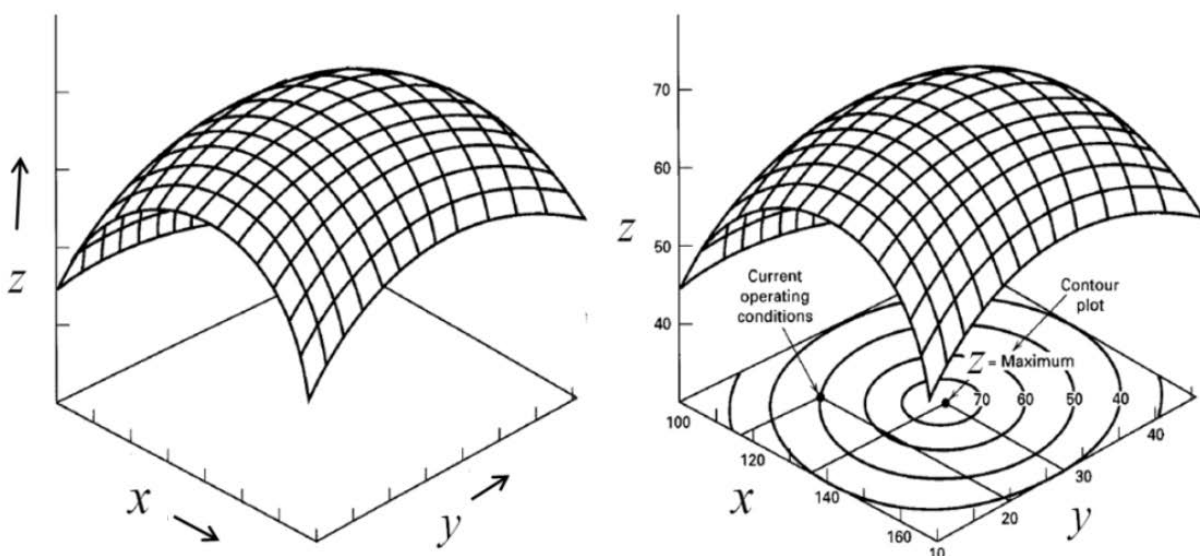
Fig 3-16 A three dimensional response surface showing the expected yield (z) as a function of (x) and (y) (left), Contour plot of a response surface (right)

RSM is a good tool for single objective optimization but when optimization of multiple responses which depends on more than three independent variables, then it is very difficult to deal with RSM, as multiple response variables create difficulty because what is optimal for one response may not be optimal for other responses. So use of multiple objective optimization tools is necessary to address the issue.

Multi-objective Optimization

Most of the time we need to formulate problems with more than single objective, as of a single objective with various constraints may not adequately represent the problem being computed. If so, there is a vector of objectives (Equation 3-10), that must be dealt in some way.

$$f(x) = [f_1(x), f_2(x), \ldots \ldots, f_z(x)] \qquad\qquad (3-10)$$

The relative importance of these objectives is generally not recognized until the system's best potentials are determined and tradeoffs between the objectives sufficiently understood. As the number of objectives increase, tradeoffs become complex and less easily quantified. In multi-objective optimization study (also known as multi-objective mathematical programming), the set of feasible solutions is not explicitly known in advance but it is restricted by constraint functions [31].

A multi-objective optimization problem involves a number of objective functions which are to be either minimized or maximized. As in a single-objective optimization problem, the multi-objective optimization problem may contain a number of constraints which any feasible solution (including all optimal solutions) must satisfy. Since objectives can be either minimized or maximized, we state the multi-objective optimization problem in its general form [46]:

$$
\begin{aligned}
\text{Minimize/Maximize} \quad & f_z(x), & & z=1,2,3........,Z; \\
\text{Subjected to} \quad & g_i(x)>=0, & & i=1,2,3..........,I; \\
& h_j(x)=0, & & j=1,2,3..........,J; \\
& x_k^{(1)}<=x_k<=x_k^{(1)}, & & k=1,2,3........,n.
\end{aligned}
\qquad (3-11)
$$

From above equation, it is clear that multi objective optimization is concerned with maximization or minimization of a vector objectives $f_z(x)$ that may be subjected to a number of constraints. And the final solution 'x' is a vector of 'n' decision variables.

Multi-objective optimization has now become a popular and useful field of research and application. As time changed its evolutionary development is shown in Fig 3-17. Conventional multi-objective optimization approach yield single solution while modern genetic algorithm (GA) based multi-objective optimization returns multiple solutions, which provides wide spectrum to user to choose the appropriate solution. In the present investigation GA based multi-objective optimization considered for optimization.
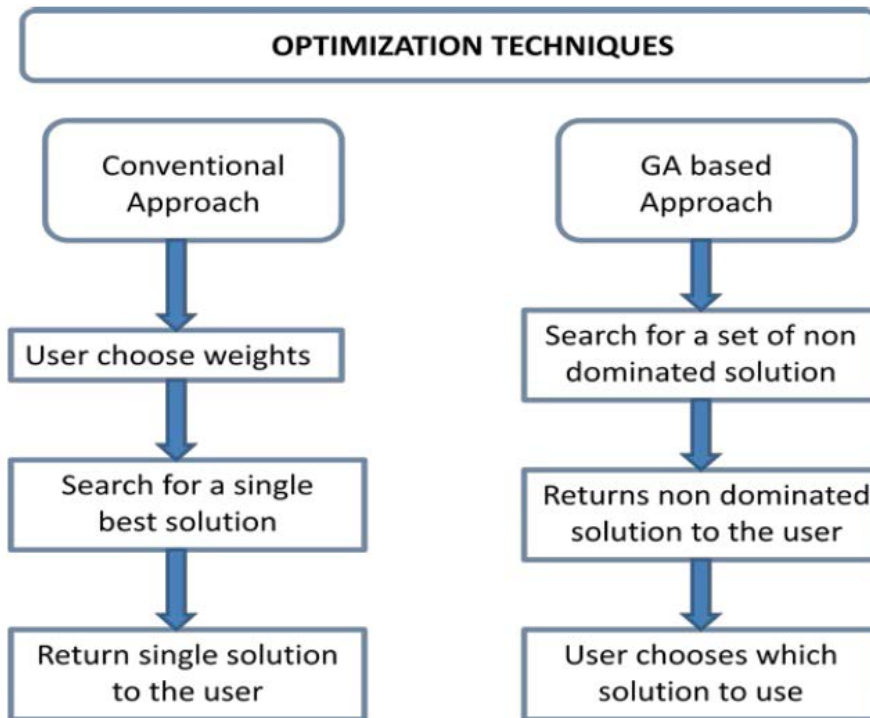
Fig 3-17 Multi-objective optimization approaches

GA based multi-objective optimization uses a population based approach in which more than one solution participates in iteration and evolves a new population of solutions. Multi objective optimization is not to search for optimal solution but for efficient solution that can provide the best solution. In multi objective optimization problem we cannot get a single solution that can simultaneously optimize both or all the objective functions. In fact there are many possible solution points called pareto. The advance level of optimization is multi objective optimization which is also addressed by Genetic Algorithms very efficiently and explained in next sub-section.

Most of the real world problems have several objectives which have to be satisfied simultaneously. For example if we look for buying an automobile then our objective will include less cost and more comfort. So it directly caters the real world problems which involve the optimization of various objectives to reach final decision.

Genetic algorithms

Genetic Algorithms developed by Prof. John Holland with colleagues and students at the University of Michigan around 1975. GA is basically a search algorithm or heuristic that mimics the process of natural evolution, it begins with a population of randomly generated structures where each structure encodes a solution to the task append. It proceeds to evolve generations, during each generation the genetic algorithm improves the structures in its current population by performing selection followed by crossover followed by mutation as shown in Fig 3-18. There are five phases involved in GA solution process which are (a) Initial population, (b) Fitness function, (c) Selection, (d) Crossover, and (e) Mutation
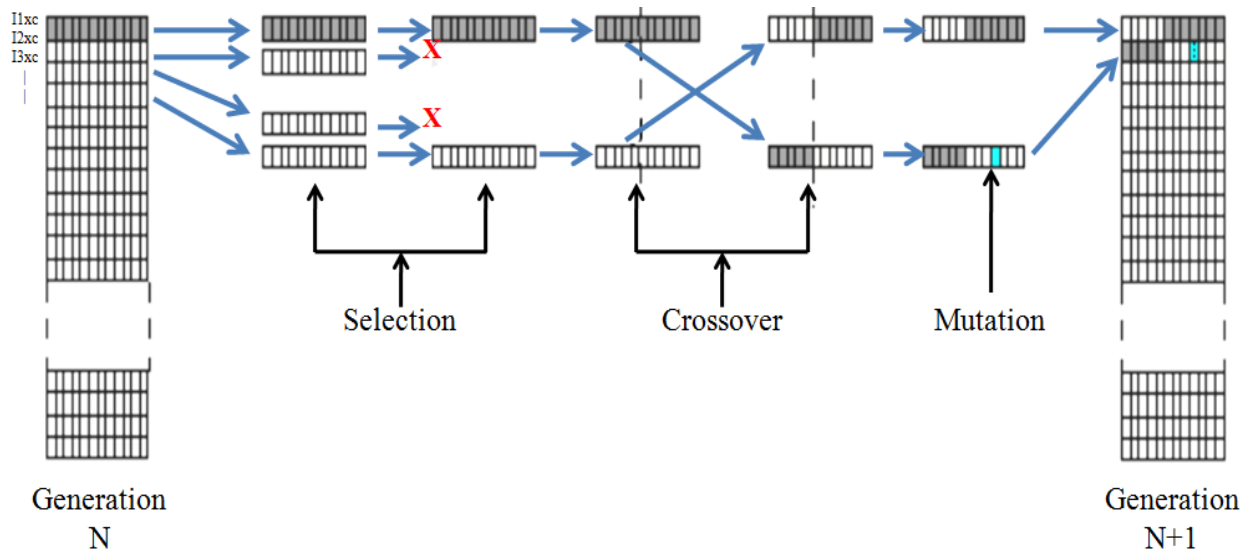
Fig 3-18 Schematic of the principles of GA

Genetic algorithms differ from traditional search and optimization methods in three significant points, first they search parallel from a population of points therefore it has the ability to avoid being trapped in local optimal solution like traditional methods, second genetic algorithms work on the chromosome which is an encoded version of potential solutions parameters rather than optimizing the parameter themselves and third genetic algorithm use fitness score which is obtained from objective functions without other artificial over engineered black box mathematics. The best structure of the last population is the final solution. The central theme of genetic algorithm is robustness which mainly includes balance between efficiency and efficacy necessary for survival in different environments. Example depicts the theme of GA compared to traditional optimization in proper fashion is shown in Fig 3-19.
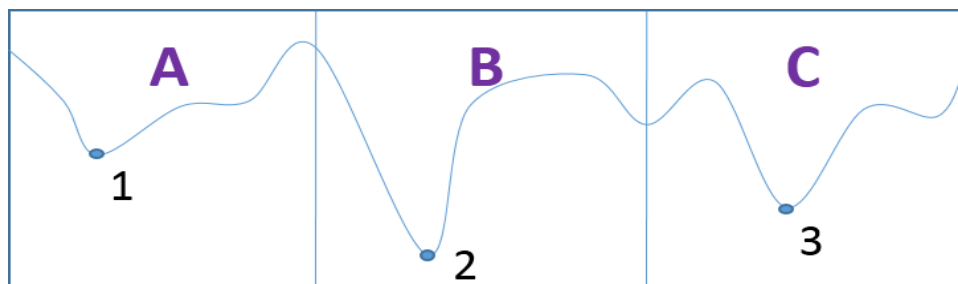
Initial guess	Traditional optimization	GA
A region	Converges to 1	Converges to 2
B region	Converges to 2	Converges to 2
C region	Converges to 3	Converges to 2

Fig 3-19 Comparison of traditional optimization with GA
(1, 3 - Local optimum and 2 - Global optimum)

There are many software packages which address optimization problem using GA, in present study Matlab 2011b was used to perform multi-objective optimization. GA used for multi objective optimization in Matlab actually performs the search to find a local pareto front for multiple objective functions and mainly concerned with the generation and selection of noninferior solution points. These noninferior solutions are also called pareto optima, so the main goal in GA based multi-objective optimization is constructing the Pareto optima. The algorithm used in Matlab GA command 'gamultiobj' is well described in literature [46].

Material Studio

Materials studio is a simulation and modeling software (developed by Accelrys, Version 5.0) for various materials at atomic, molecular and compound level. This software is used for atomic or molecular modeling, computational chemistry, molecular simulation, quantum mechanics etc. In the present investigation it is used for creating models and finding their properties.

3.3.2 Processing/Synthesis techniques

Mechanical milling

Mechanical milling is a top down method for the synthesis of nanomaterials. In comparison of all top down approach, mechanical milling has been widely exploited for synthesis of nanomaterials [200]. This method is mostly used to produce amorphous and nanocrystalline materials, while other main function of the method is to produce alloy of multiple elements by mixing them together followed by compaction and sintering. Fig 3-20 shows the basic phenomena that occurs during mechanical milling, in which due to jar rotation balls inside jar collides with each other and with material under process.
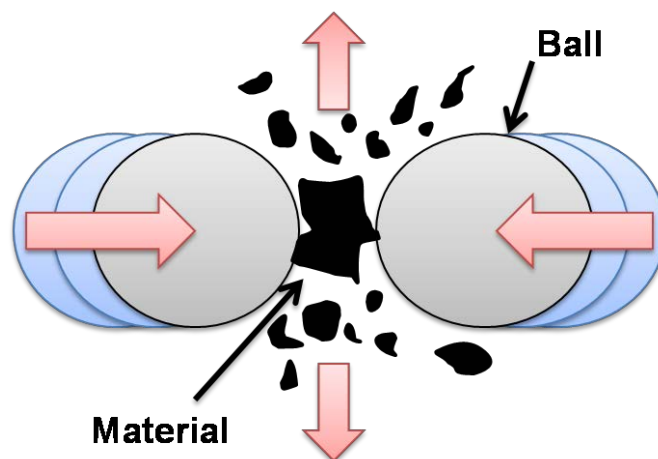
Fig 3-20 Schematic of ball powder ball collision during mechanical milling

A basic criterion of selecting balls and jar is that the material selected for milling should have lower hardness value than milling jar and balls, and then only milling will be effective. During collision less hard material undergoes deformation and fracture leads to decrease in particle size resulting in the development of finely dispersed particles.

Electrophoresis

Electrophoresis is a method in which dispersed particles movement is observed relative to the fluid (or "background electrolyte") under the application/influence of constant electric field. The main cause behind this motion is the presence of charge interface between dispersed particles surface and surrounded electrolyte solution. Based on this principle, analytical techniques developed to separate molecules based on their charge, size or binding affinity. Fig 3-21 depicts the electrophoresis phenomena occurrence in electrolytic solution. Electrophoresis of positively charged particles (cations) is called cataphoresis, while electrophoresis of negatively charged particles (anions) is called anaphoresis. When an electric field applied to the system, the ions in the running buffer will flow from one electrode to the other and provide the current needed to maintain the applied voltage. At the same time, positively charged ions in the sample will move toward the negative electrode (the cathode), while negatively charged ions will move toward the positive electrode (the anode). The result is a separation of these ions based on their charge and size [66].
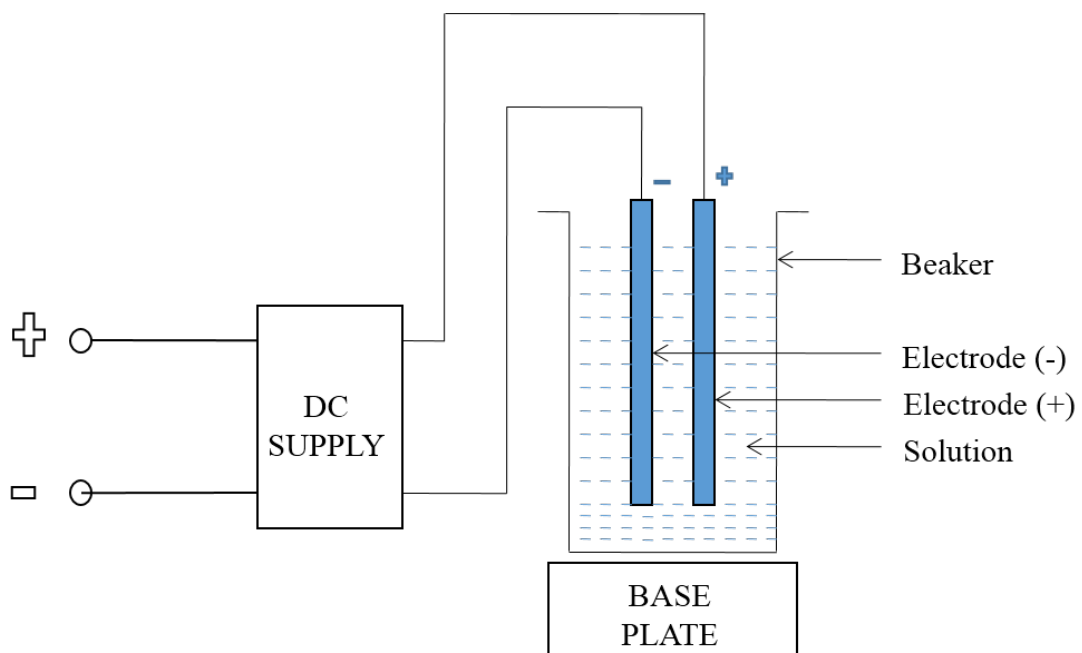
Fig 3-21 Schematic of electrophoresis experiment used in present investigation where 'Cu' used as negative electrode and 'engine cylinder' was positive electrode

Heat treatment

Heat treatment is a controlled process of heating and cooling of material, so that desired microstructure/properties of material can be achieved at the end of the heat treatment. Alteration of the microstructure/properties of materials performed using heat treatment to improve properties which will benefit the operational life of the material, for example increased ductility, surface hardness, strength and temperature resistance. Heat treatment processes generally include case hardening, annealing, tempering, solution and ageing treatment and normalizing.

3.3.3 Characterization techniques

This section describes characterization techniques employed in the present investigation, the details of each instrumental technique is explained briefly with their principle of working. Before detailing each technique it is good to know about electron beam interaction with the specimen under study. Primary electrons incident on to the sample and trigger other phenomena such as emission of various types of electrons, characteristic X-rays as shown in Fig 3-22. All emitted electrons and rays are used for various characterizations which are discussed from next section.

X-ray Diffraction

X-ray diffraction (XRD) is universally used technique for crystalline substances characterization. Powder XRD is one of the most versatile, powerful and non-destructive characterization techniques for unknown solids to identify the phases present.
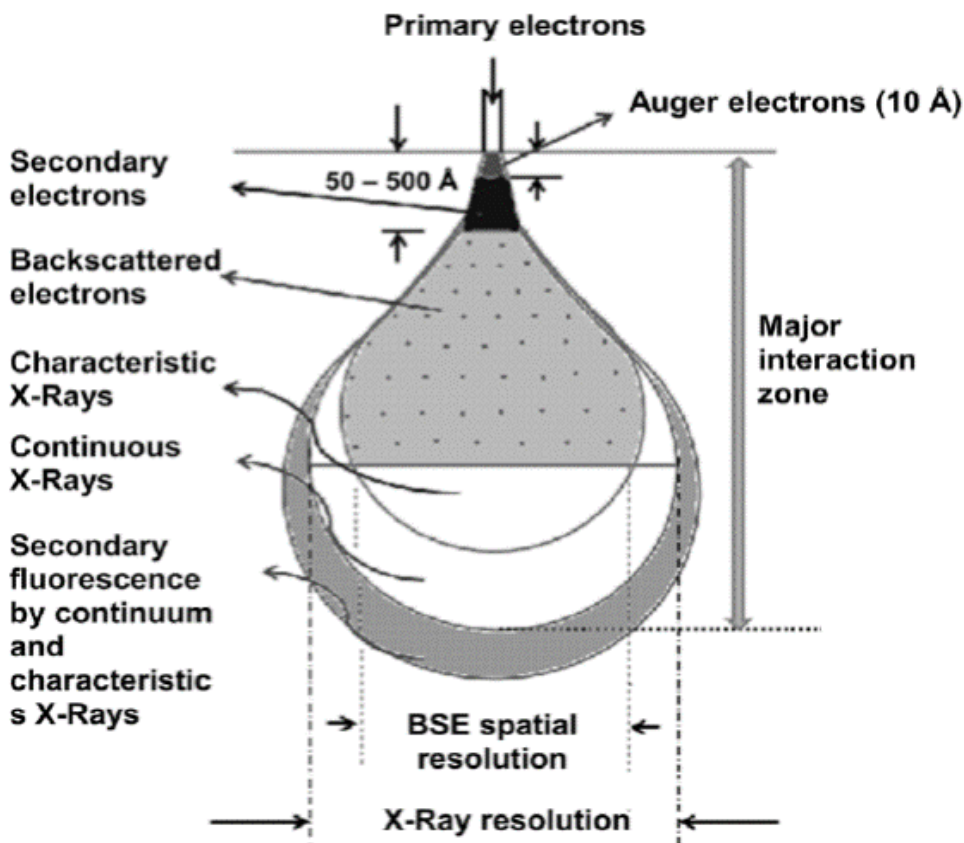
Fig 3-22 Water droplet model of electron beam interaction with specimen

X-ray diffraction occurs due to constructive interference of monochromatic X-rays, when incident X-rays falls on crystalline sample as shown in Fig 3-23. Normally copper is used as a target material for producing X-rays, with CuK_α radiation 1.54Å. And same X-rays are directed onto the sample in a collimated manner.
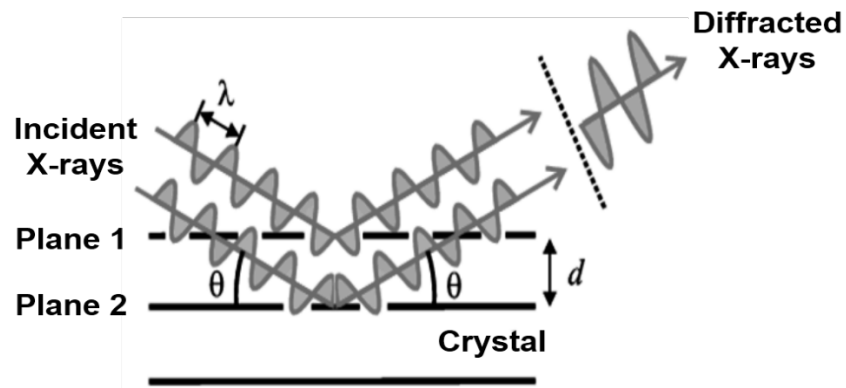
Fig 3-23 Diffraction of X-ray by crystalline material

When incident X-rays falls onto the planes of crystalline material at a certain angle of incidence, θ, the atoms scatter the X-rays in all directions. Only at certain angles constructive interference occurs, where the path difference among diffracted X-rays is equal to an integer multiple of wavelength, i.e. nλ. A detector records and processes this diffracted X-rays signal and converts it into a count rate. The constructive interference of diffracted X-rays is expressed by Bragg's Law, which states:

$$n\lambda = 2dSin\theta \qquad\qquad\qquad (3-12)$$

Where d is interplanar spacing, λ is the wavelength of the X-rays, θ is the incident angle, and n is the order of diffraction. The resulting XRD pattern consist of two entities namely positions (in terms of angle) and intensities of the diffraction effects. Further analysis of the XRD pattern leads to the knowledge of the materials grain size, unit cell dimensions, purity and residual strain. Fig 3-24 shows the picture of Bruker AXS D8 Advance powder diffractometer, which is used in present study.
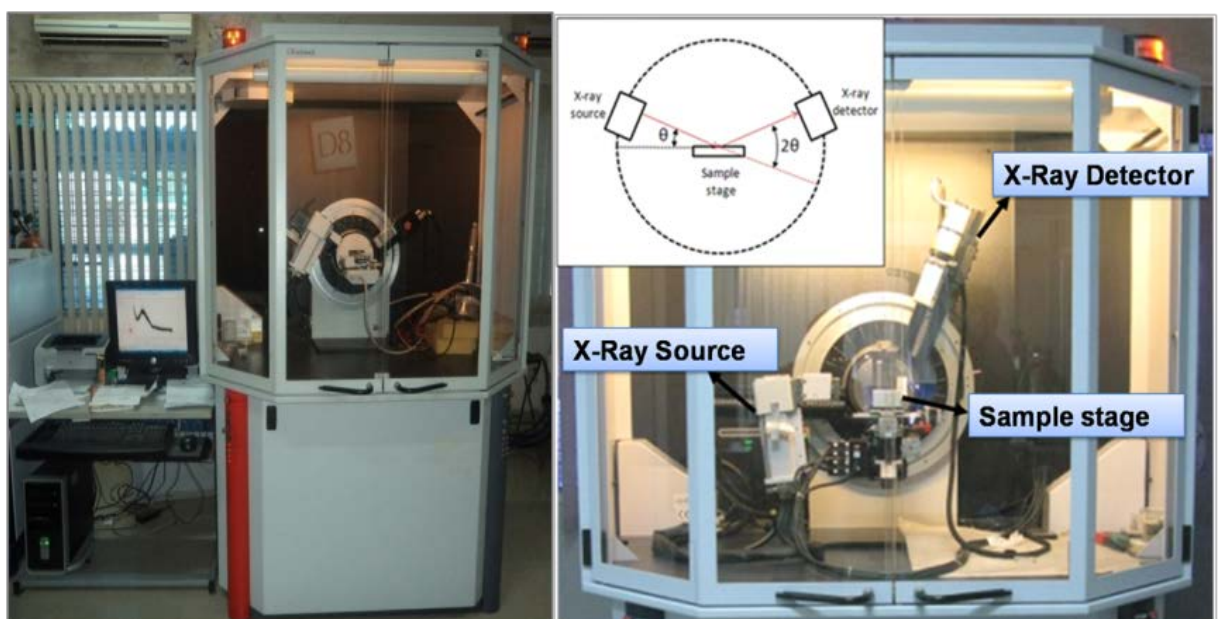
Fig 3-24 X-ray Diffractometer with schematic diagram of diffraction phenomena

Grain size determination using XRD pattern

XRD pattern can be used to determine average crystallite/grain size of the material under investigation with the help of Debye-Scherrer formula (Equation 3-13).

$$D = \frac{k\lambda}{\beta \cos\theta} \qquad (3-13)$$

Where, D is the crystallite size in microns, k is a constant (approximately, 0.9), λ is the wavelength of the incident X-ray (1.54 Å for Cu K$_\alpha$), β is the full width at half maximum (FWHM as shown in Fig 3-25) of the diffraction peak in radian on the 2θ scale, θ is the angle of the incident beam with the crystal plane.
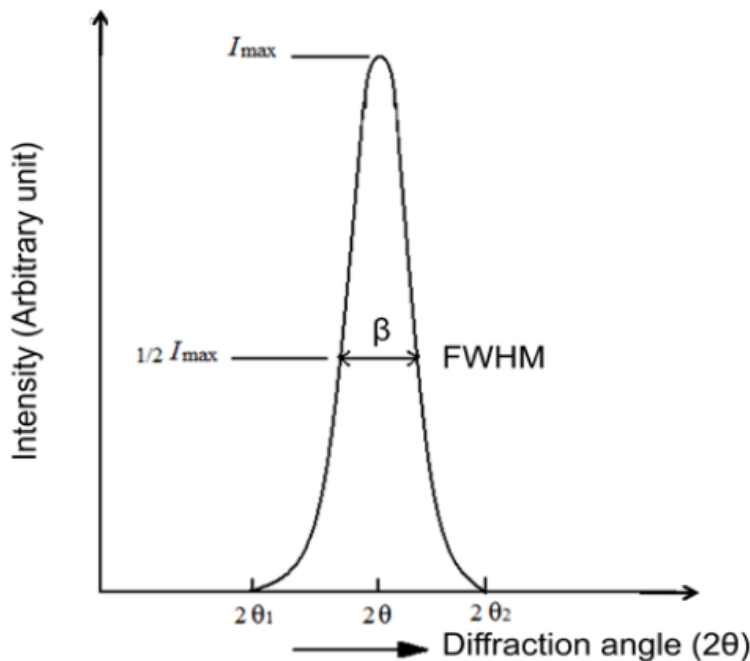
Fig 3-25 XRD peak showing FWHM

Strain determination using XRD pattern

As the materials undergo various processing steps, there are some residual stresses introduced into the grain which causes broadening as well as the shifting of XRD peaks. In order to calculate the strain through peak broadening Williamson-Hall method is used by eliminating the effects of instrumental and crystallite size broadening. The relation between internal strain and crystallite size can be obtained by fitting the Williamson-Hall equation, which is as follows:

$$\beta \cos\theta = \frac{k\lambda}{D} + 2\varepsilon \sin\theta \qquad (3-14)$$

where D is the crystallite size, ε is the inhomogeneous internal strain (%).

The analysis can be performed by measuring β of every peak in XRD pattern. Instrumental broadening (β_i) determined from polycrystalline silicon standard sample and found

to be 0.01. The measured β is the observed peak width and can be denoted as β_o, while peak width due to sample β_s (size and strain) can be determined according to Gaussian profile as follows:

$$\beta_s = \sqrt{\beta_o^2 - \beta_i^2} \qquad\qquad (3-15)$$

Using $\sin\theta$ and $\beta_s\cos\theta$, plot the graph with $\sin\theta$ values in X – coordinate and $\beta_s \cos\theta$ values in Y – coordinate against each peak of XRD pattern. Further fitting the plotted points in a straight line equation (Equation 3-16) the crystallite size and internal strain can be resolved. In straight line equation, m is the slope and represents strain in the crystallite, while c is the constant. And the intercept of straight line can be resolved for crystallite size.

$$y = mx + c \qquad\qquad (3-16)$$

Scanning electron microscopy

In scanning electron microscopy (SEM) the secondary electrons are used to display the morphology and topography of the sample under study, the backscattered electrons are used for illustrating composition contrasts in multiphase systems and the diffracted backscattered electrons are used to verify crystals grain orientation. Basically SEM uses a fine electron beam to examine the specimen surface and a detector is used to collect the secondary electrons signal emitted from specimen. SEM is versatile due to its multiple signals generation, wide magnification range, simple image formation process, and tremendous depth of field. Fig 3-26 shows the schematic diagram of the SEM setup and photograph of the SEM used in the present investigation.
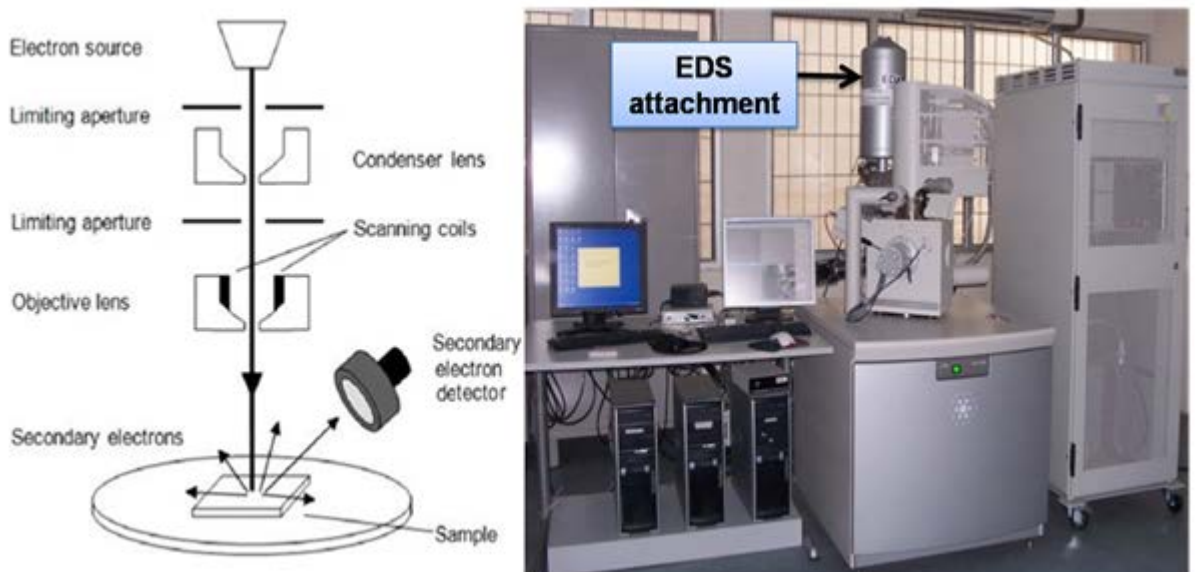
Fig 3-26 Schematic diagram of the SEM setup and photograph of FEI Quanta 200F SEM

Field emission gun source was used for higher resolution and electrons accelerating energy is frequently between 10 to 25 kV. SEM found suitable for accurate dimensioning of very small matter down to 50 nm in size. SEM is comparatively easy to operate as well as its sample preparation is nominal. But SEM is limited to studying conducting specimen only. In case of non- conducting specimen, it is required to make them conducting by coating the specimen with a thin film of conductive material like platinum or gold in order to make specimen surface conductive. Otherwise localized electrostatic charge concentration takes place on the specimen surface during analysis.

Optical Microscopy

An optical microscope Lieca (Model – 5000M) with magnification range of 100X to 1000X used for examination of sample microstructure (Fig 3-27). Sample for microstructural examination was prepared as per ASTM standard (ASTM E3-11) using slow speed isomet saw followed by polishing on belt polisher and emery sheet series from coarse to fine grade. Final polishing was performed on a velvet cloth dispersed with 0.05 micron alumina powder mounted on a rotating disc. Initial and final polishing of the optical microscope sample performed with the help of belt and disc polisher.

Fig 3-27 Optical microscope (Lieca) used for examination of sample microstructure

Energy Dispersive X-ray Spectrometry

Energy Dispersive X-ray Spectrometry (EDS) is used to obtain localized chemical composition from the X-ray spectrum emitted by a solid specimen under analysis when bombarded with a

monochromatic beam of electrons. EDS is capable of detecting all elements from Beryllium (atomic number 4) to Uranium (atomic number 92) except light elements (atomic number < 4). EDS frequently equipped with SEM unit which is capable of detecting emitted X-rays from the specimen under analysis during the electron beam and specimen interaction. EDS consists of three basic components the X-ray detector or spectrometer, the pulse processor, and the analyzer. The spectrometer actually detects and converts individual X-rays energy into a voltage signal of proportional size. EDS (Model EDXA) attached to SEM as shown in Fig 3-26 used for chemical composition analysis in the present investigation. The characteristics EDS spectrum is plotted between X-ray counts and energy (keV).

Transmission electron microscopy

Transmission electron microscopy (TEM) is a universal tool for analysis of the atomic arrangements in the material as well as it can be used to study internal microstructure of material at nanometer scale. TEM analysis is accepted worldwide for high magnification measurement, in which the images are formed due to the transmission of a beam of electrons through a specimen. TEM specimen preparation is a hectic job for a solid sample while fine powder samples can also be used as a sample for TEM analysis. The thickness of TEM specimen actually decides the amplitude and phase variations in the transmitted beam, as the amount of material is restricted to such a level to allow electron beam passage.
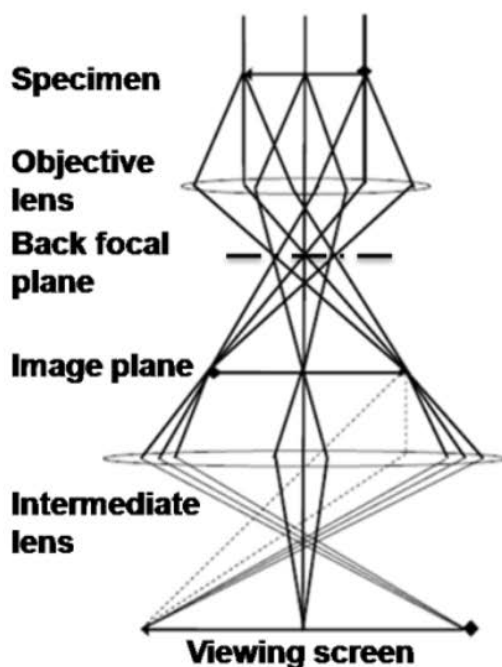
Fig 3-28 A ray diagram of TEM in image mode and photograph of FEI Tecnai-20 TEM

In TEM electrons are focused on specimen using electromagnetic lenses, which provides this method edge over other methods and this phenomena also allows one to obtain real-space image of material under analysis with resolutions as low as 10^{-2} nm to a few nanometres. TEM

operates on the same basic principle as of optical microscope but uses high accelerating energy electrons instead of visible light [145,54]. The shorter wavelength of electrons about 0.025 Å (for 200 keV electrons accelerating energy) can be attained using TEM which makes it possible to get a very high-resolution of 0.2 nm as well as high magnification compared to light microscope. Fig 3-28 shows the TEM image mode ray diagram [54] and the picture of the TEM used in the present investigation.

Brinell Hardness Testing

In the present investigation, hardness variation due to coating has big impact on the wear resistance property of the engine block to be used in diesel engine. So hardness measurement of the material before and after coating is a matter of great significance. VEP-WPM Leipzig Brinell hardness testing machine with hardened steel ball indenter (of diameter 1.5875 mm) was used in the present investigation which is shown in Fig 3-29 with the schematic of hardness testing procedure.
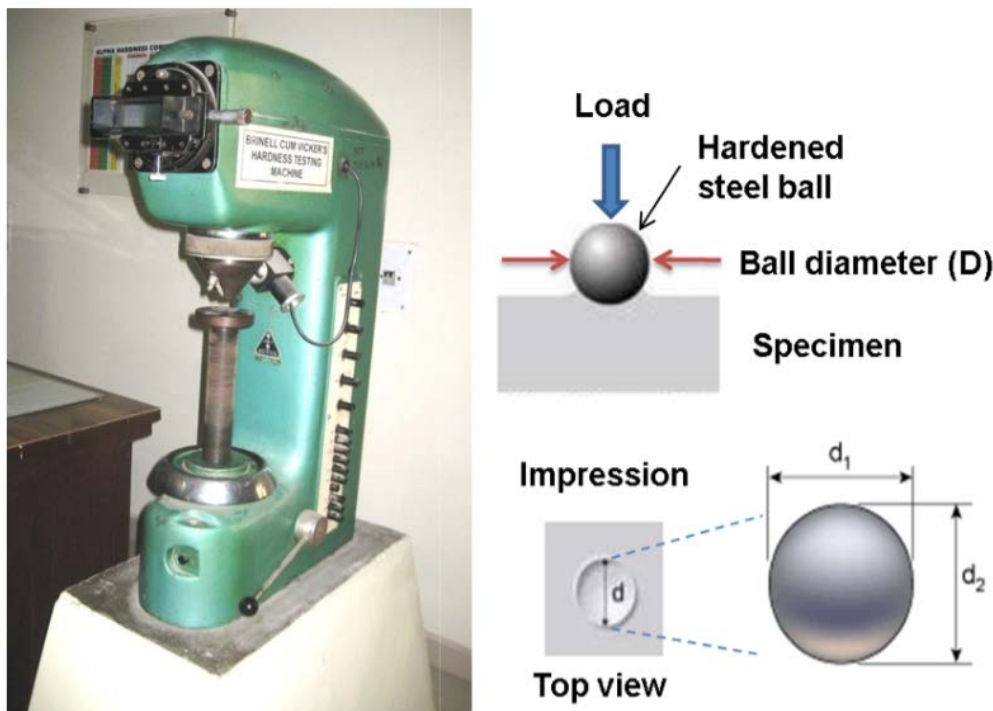
*Fig 3-29 Brinell hardness testing machine used to measure sample hardness
and schematic of testing procedure*

Material to be analyzed for its hardness are placed kept on the specimen round table and a known load (15.625 kg in the present investigation) is applied on it using a lever arm for a fixed duration, usually 30 s. Afterwards the indenter is retracted, the specimen is left with an impression of indenter whose dimensions are measured using a calibrated microscope. After estimating the average impression diameter ($d=(d_1+d_2)/2$), the hardness can be calculated by the following equation:

$$BHN = \frac{2P}{\pi D\left(D-\left(\sqrt{D^2-d^2}\right)\right)} \qquad\qquad (3-17)$$

where, BHN – Brinell hardness number, D – diameter of ball indenter in mm, d - diameter of impression in mm and P- load in kg.

Surface profiler

It is required to know the surface profile of the engine block in the present investigation, as the effect of profile plays a major role in engine wear due to directly proportional relation between surface roughness and coefficient of friction of the material. So measurement of surface profile becomes a necessary condition here for better analysis of friction study. Fig 3-30 shows the photograph of surface roughness tester used in the present investigation. Surface profile analysis and report creation capabilities are achieved using the surface roughness analysis program FORMTRACEPAK V5 installed with computer interface.
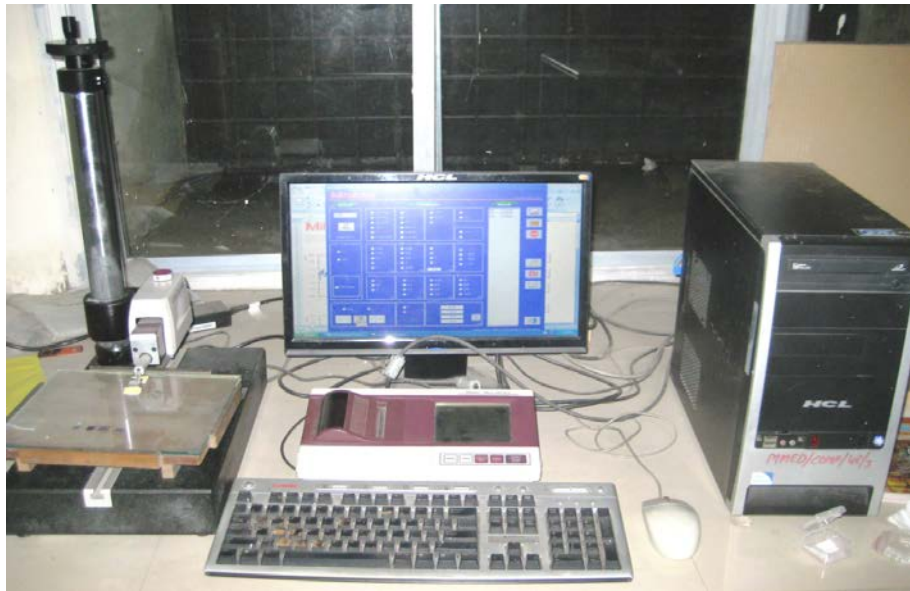
Fig 3-30 Surface tester (Mutitoyo surftest SJ-400) used to measure sample surface profile

Thermogravimetric Analysis

Thermogravimetric analysis (TGA) considered as an analytical technique, generally deals with the thermal stability of the materials under various conditions of temperature and environment. By examining the weight change of material that occurs during heating of the specimen, the fraction of volatile component, as well as thermal behavior of material can be found. TGA measurement are generally carried out in ambient air or in an inert atmosphere (nitrogen or argon) and the weight of specimen recorded as a function of increasing temperature. A TGA instrument mainly consists of a furnace and a sample pan which is supported by a precision balance, driven coil and a detector as shown in Fig 3-31. The furnace is heated or cooled during the analysis and the weight of the sample is regularly monitored during the experiment. TGA is capable of

recording temperature differences between the samples with one or more reference pans. Which is known as differential thermal analysis (DTA) and the samples heat changes can be monitored.
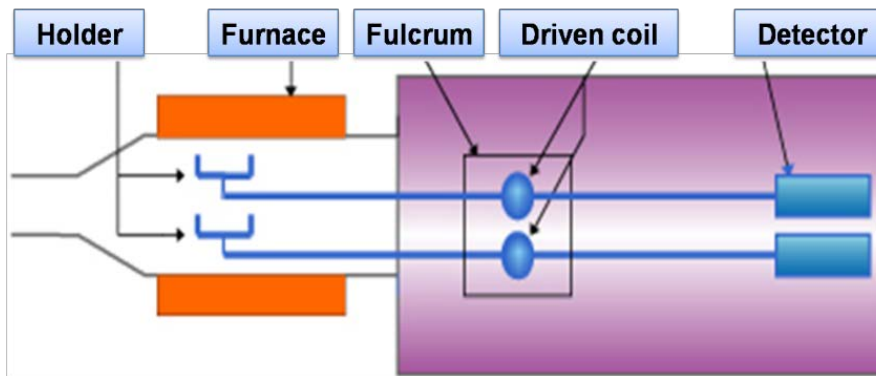
Fig 3-31 A block diagram of thermo gravimetric analysis instrument

The sample pan is normally made of ceramic materials and it can hold powder, liquid, films and solid crystals. The sample with small pieces is better than a bulk because it has larger surface area achieves thermal equilibrium faster. A linear temperature ramp is used in TGA analysis for heating the specimen and the maximum temperature is fixed such that the specimen weight should be stable at the end of the testing. A heat source used in TGA to force the reactions and physical changes in specimen which provides quantitative measurement of weight variations in specimen associated with and thermal degradation and phase transformation [55]. Weight variations occur due to dehydration, decomposition and oxidation of specimen as a function of temperature/time. Thermal stability measurement of specimen actually indicated by the oxidation temperature in air, higher oxidation temperature is the indicator of pure sample with fewer defects. TGA can be used to analyse a variety of materials for the following information:

a. Thermal stability of a material

b. Rate of degradation

c. Moisture content

d. Organic content

e. Oxidative stability

f. Decomposition temperature of a material

g. Level of inorganic component in materials

h. Effect of reactive atmosphere on the material

In the present investigation, measurements for TGA were carried out using a Perkin-Elmer (Pyris Diamond) instrument (Fig 3-32) from room temperature to the maximum set temperature. TGA results of the graphite at various dimensional scales are depicted in the next chapter.

Fig 3-32 A photograph of TGA system used to measure thermal stability of the samples under various conditions of temperature and environment

Micro hardness testing

Nanovea mechanical tester model-M1 (Fig 3-33) is used for micro hardness and micro scratch studies of uncoated and coated engine block samples. A pyramidal diamond Berkovich indenter with 200 µm tip radius used for hardness and Vickers 200 spherical diamond indenter with tip radius of 20 µm for scratch studies. Hardness value can be obtained using constant loading condition while the scratches can be made with both constant and ramp normal loads. The instrument is provided with maximum capability of 40 N, 25 mm maximum scratch length and having facility of providing both hardness and Young's modulus from indentation data. This instrument uses ASTM E384 standard method for hardness measurement and ASTM G171 standard method for scratch hardness of the material.
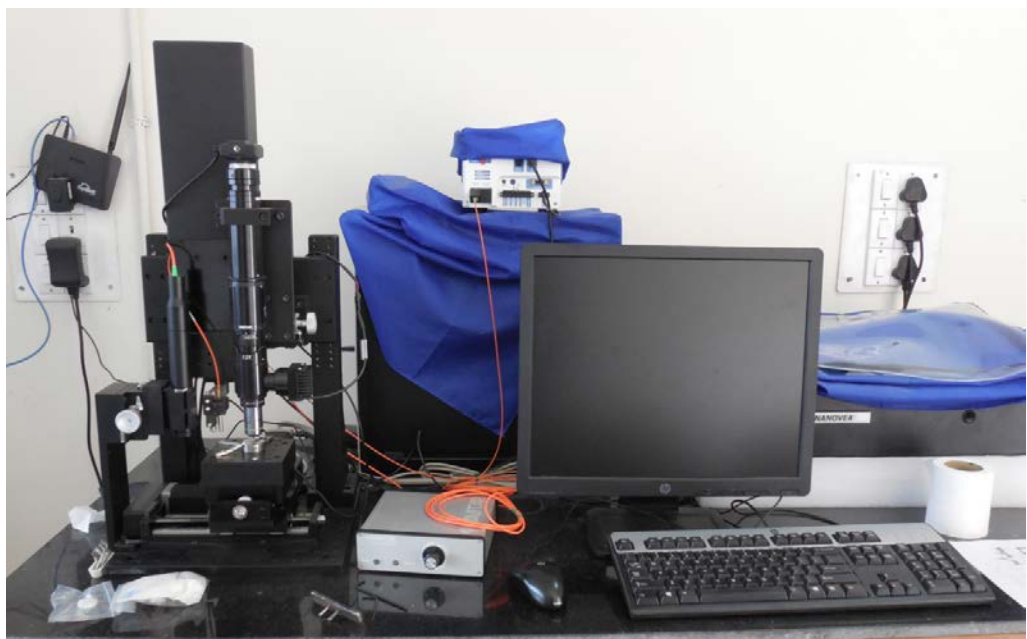
Fig 3-33 Photograph of Nanovea mechanical tester model-M1 used for micro hardness and micro scratch studies

3.3.4 Safe research practice with nanomaterials

The present investigation deals with nanoparticles, so it is necessary to maintain the code of conduct for working with nanoparticles which is described briefly here. Nanoparticles are present in earth's atmosphere, sometimes occurring naturally (such as in volcanic ash), sometimes produced as unintentional by-products (such as emissions from vehicles) and other times specifically engineered or created for specific purpose. These small particles possess significantly different properties than larger particles, making them potential material of interest to researchers. But its short term and long term impact on human health and environment is yet to be explored completely, so there is the standard code of conduct (ISO 10808:2010) which focuses on safe lab practices to protect working persons from the potential hazards of engineered nanoparticles. All the items requisite for maintaining safe practice/handling of nanomaterials in workplace without contamination are listed below. Some of them are shown in Fig 3-34:

a. Gloves (preferably nitrile gloves)
b. Safety glasses
c. Appropriate protective clothing (apron/lab uniform)
d. Clean room
e. Tissue paper/butter paper/aluminium foil for nanomaterials transfer/cleaning
f. Mask

The major problems human experience with exposure to nanoparticles are skin diseases, internal organ failure and damage of respiratory system. Based on past observations it is found that most probable routes of workplace exposure to nanoparticles are inhalation, skin absorption, ingestion, and injection. So it is necessary to adhere to the safe practice in workplace where exposure to nanoparticles is likely.

Fig 3-34 Items to be used strictly when working with nanomaterials (Mask, Glass & gloves)

3.4 Engine experimental setup

The main objective of the present investigation is to study the effect of engine cylinder coating on the considered engine performance parameters, namely, brake specific fuel consumption, friction power, mechanical efficiency, smoke opacity and specific emissions of CO, HC and NO. To perform the study a small direct injection diesel engine test rig is used. The engine test rig interfaced with several equipments such as dynamometer for regulating speed and load of the engine, AVL DiTEST MDS 450 for complete engine test results display. AVL control panel used to control the dynamometer. MDS 450 (AVL) is a modular diagnostic system interfaced with emission measuring equipment, smoke measuring equipment, cylinder pressure – crank angle measuring equipment and temperature sensors for providing all the engine testing result data in a common platform. The details of all the instruments used in present engine experimental setup is discussed here. Finally the characteristics of fuel used for engine testing discussed.

Initially the engine was warmed up before experimental data acquisition, which was also cross verified by stable readings of engine speed and load with minimum variation with respect to time. This section has been organized in three sub sections (a) Test engine, (b) Measuring equipment and methods, (c) Test fuel and their characteristics, and (d) Engine testing.

3.4.1 Test engine

The present investigation was performed with the help of small single cylinder naturally aspirated 4-stroke water cooled direct injection diesel engine. The specifications of the engine are given in Table 3-4, and the complete details is given in Appendix-I. This engine is recently being used in small automotive vehicle applications. For conducting the experiments and to gather necessary data from the engine, it is essential to have experimental setup with all required instruments mounted at the appropriate location.

Table 3-4 Test engine technical details

Parameters	Specifications
Engine	Small DI compression ignition
Number of cylinder	One
Cooling type	Water cooled
Stroke (mm)	92
Bore (mm)	92
Maximum power at rated rpm (kW)	11
Compression ratio	18:1
Displacement (cm^3)	611
Rated rpm	3000
Maximum torque	32 Nm @ 1600-1800rpm
Capacity of oil sump (Litre)	1.75
Dry weight (kg)	75 (Approx.)

A schematic layout of test rig set-up (actual picture shown in Fig 3-35) including all the auxiliaries used in the present investigation is given in Fig 3-36. AVL control panel interfaced with dynamometer and DYCON 201A module in AVL control panel is used to control the load and speed of the engine through dynamometer. AVL DiTEST MDS 450 is a modular diagnostic system used to provide a common platform for complete engine test result display.
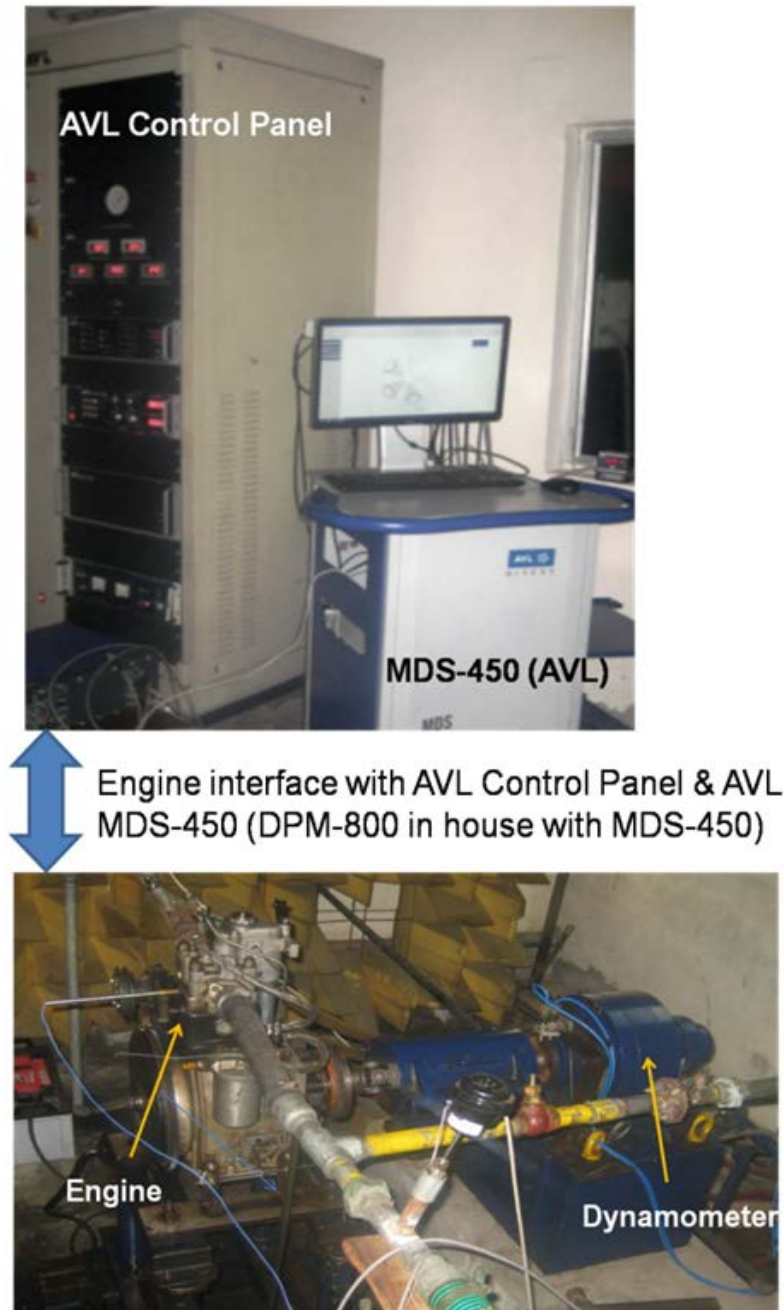
Fig 3-35 Photograph of test engine set-up showing engine with control and measurement display interfaces

The engine coupled with AVL Zollner type Alpha - 20 eddy current dynamometer for engine loading/unloading purpose. The technical specification of the dynamometer is listed in Table 3-5. An orifice meter coupled to a manometer used to measure mass flow rate of intake air.

Table 3-5 Technical features of AVL Zollner alpha-20 dynamometer

Feature	Value
Maximum Speed	17000 rpm
Permissible torque	25 Nm
Permissible power	20 kW
Mass moment of inertia	0.0225 kg m^2
Max. proportionate load on cantilever	3 kg/17000 rpm
Air gap between stator and rotor	0.2 - 0.25 mm
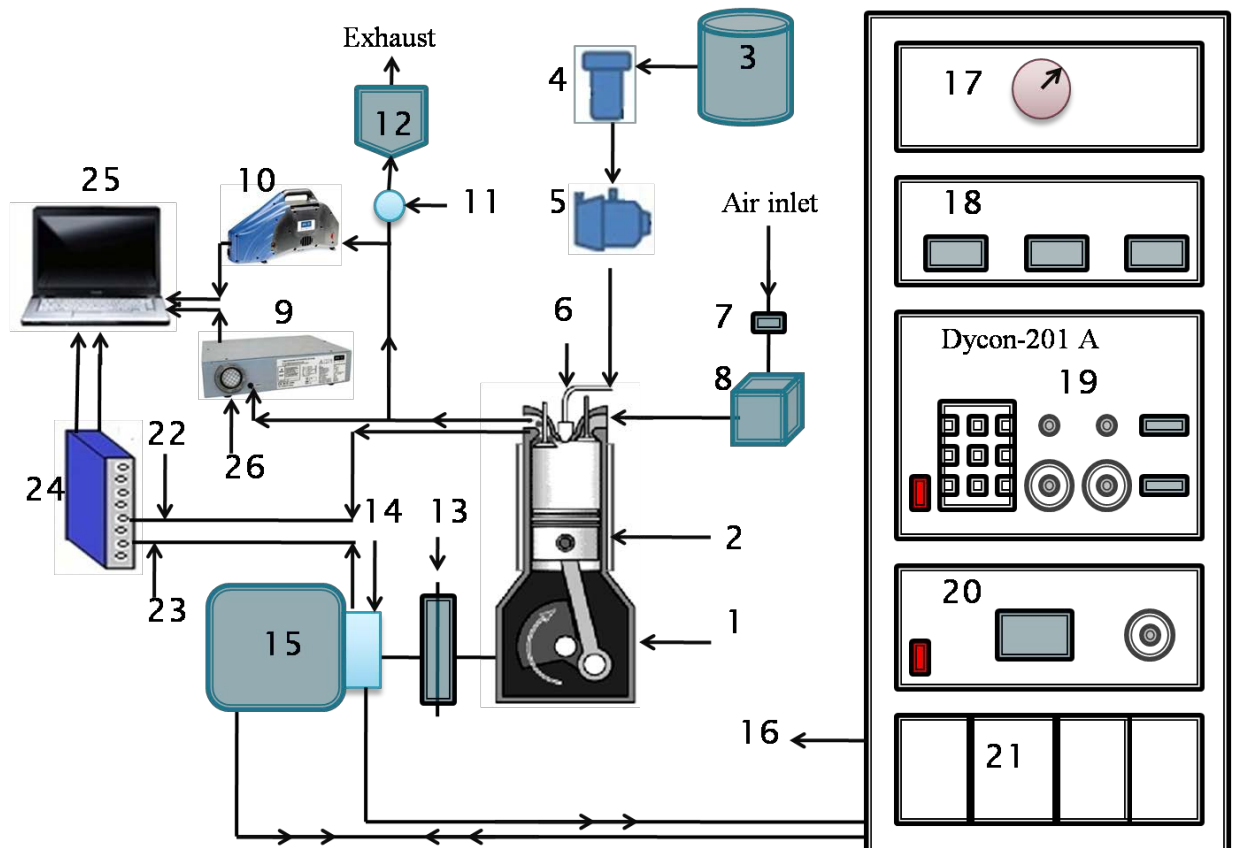
(1) Test engine (2) Water cooling Jacket (3) Diesel tank (4) Fuel filter (5) Fuel pump (6) Fuel injector (7) Intake air manometer (8) Intake air surge tank (9) AVL DiTEST Gas 1000 gas analyser (10) AVL DiSmoke 480 BT smoke meter (11) Valve (12) Exhaust gas surge tank (13) Coupling (14) AVL Crank angle pickup (15) AVL Eddy current dynamometer (16) AVL Control panel (17) Lubricating oil pressure gauge (18) Lubricating oil, cooling water, and exhaust gas temperature indicators (19) Dynamometer controller – 201 A (20) Additional speed controller (21) Signal condition rack (22) Engine cylinder pressure cable connection (23) Crank angle cable connection (24) AVL DiScope 802 data acquisition system (25) Personal computer (PC) (26) Lubricating oil temperature signal from Auxiliary module

Fig 3-36 Schematic layout of experimental set-up

For steady flow of air through the intake manifold a surge tank was used to damp out the pulsations produced by the engine. The fuel consumption rate was determined using conventional method. Miniature pressure transducer GM12D (AVL made) was used to measure the in-cylinder pressure during engine testing. AVL 333 inductive pulse pick-ups were used for TDC

and crank angle signals monitoring and collection. The engine speed was measured using AVL FGL3/1 inductive speed pick-up. AVL DITEST Gas 1000 exhaust gas analyzer was used to measure the exhaust gas components such as CO_2, CO, unburned HC, and NO, while smoke opacity was measured using AVL DiSmoke 480 BT smoke meter.

Data Acquisition

Data from engine test was collected using various measuring instrument module with the help of compatible softwares which are described in this section. AVL DiX 2.0 software is used for computer interface operation between engine and the AVL DiTEST DPM 800 module. It also displays the engine cylinder pressure vs crank angle data. AVL DiTEST CDS 1000 software is used to operate and display the smoke opacity. AVL DiX AU software is used to operate the AVL DiTEST Gas 1000 for displaying the engine exhaust emissions.

3.4.2 Measuring equipment and methods

Exhaust gas and smoke measurement

AVL DiTEST Gas 1000 exhaust gas analyzer was employed for exhaust gas analysis of the engine exhaust components CO, NO, HC, O_2 and CO_2. During measurements the exhaust gas probe adjustable with Viton hose was connected to the exhaust gas analyzer. For ensuring accurate readings of exhaust gas components, first leak test performed by firmly closing the probe tip, and for measurement the probe is inserted into the exhaust tail pipe and the sample is collected. Fig 3-42 shows the connection layout of AVL DiTEST Gas 1000 exhaust gas analyzer. AVL DiTEST Gas 1000 also coupled with auxiliary module AVL DiTEST AUX 2000, for measurement of engine lubricating oil temperature. Table 3-6 shows the technical specification of AVL DiTEST Gas 1000.

Table 3-6 AVL DiTEST Gas 1000 technical specification

Measurand	Measuring Range	Resolution	Accuracy
CO	0 - 15 % vol	0.01 % vol.	< 10.0 % vol.: ± 0,02 % vol. ± 3 % v.M.
			≥ 10.0 % vol: ± 5 % v.M.
CO_2	0 - 20 % vol.	0.1 % vol.	< 16.0 % vol.: ± 0, 3 % vol. ± 3 % v.M.
			≥ 16.0 % vol: ± 5 % v.M.
HC	0 - 30.000 ppm vol.	≤ 2.000: 1 ppm vol. > 2.000: 10 ppm vol.	< 2000 ppm vol.: ±4 ppm vol. ±3 % v. M.
			≥ 5000 ppm vol.: ±5 % v. M.
			≥10000 ppm vol.: ±10 % v. M.
O_2	0 - 25 % vol.	0,01 % vol.	± 0,02 % vol: ± 1 % v. M.
NO	0 - 5.000 ppm vol.	1 ppm vol.	± 5 ppm vol: ± 1 % v. M.

The AVL DiSmoke 480 BT smoke meter employed for the measurement of the smoke content in the engine exhaust. Technical data of AVL DiSmoke 480 BT is given in Table 3-7.

Connection layout of AVL DiSmoke 480 BT smoke meter in engine test rig is shown in Fig 3-37. For smoke measurements the exhaust probe was connected to the smoke meter. For ensuring accurate readings of smoke in engine exhaust, warm up test of device is performed first, upon successful warm up device is ready for actual measurement.
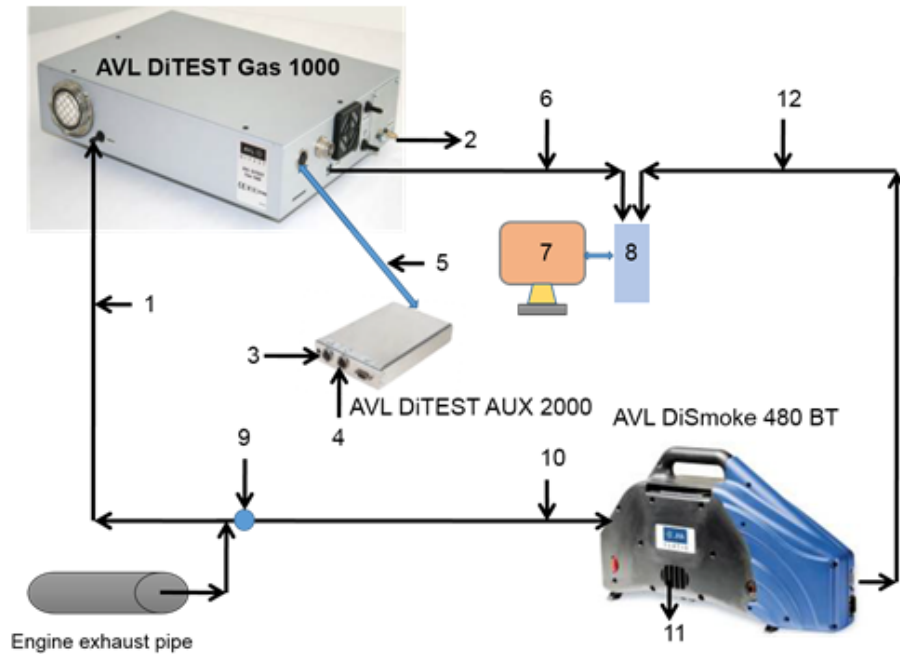
1. Gas Input to AVL Gas 1000; 2. Gas Output from AVL Gas 1000; 3. Temperature sensor signal from lubricating oil sump; 4. Speed sensor signal from AVL Dispeed 492; 5. Connection cable between AVL gas 1000 and AUX module; 6. USB cable connection to PC; 7. Monitor; 8. Central Processing Unit; 9. Valve; 10. Gas Input to AVL DiSmoke 480 BT; 11. Gas Output from AVL DiSmoke 480 BT; 12. RS 232 cable connection to PC

Fig 3-37 Connection layout of exhaust gas and smoke measurement

Table 3-7 Technical data of AVL DiSmoke 480 BT

Parameter	Specification
Measuring Principle	Extinction Measurement
Operating Temperature	+5 ... +40°C
Storage Temperature	-20 ... +60°C
Maximum exhaust temperature	200°C
Humidity	max. < 90 %, non condensing
Nominal Voltage	230 VAC
Voltage Range	85 - 264 VAC
Frequency	47 ... 63 Hz
Power Consumption	approx. 78 VA (incl. heating)
Dimensions	490 x 285 x 136 (W x H x D)
Weight	4.6 kg
Connection	RS232; Bluetooth Class1

Cylinder pressure and crank angle measurement

The cylinder pressure vs crank angle (P-θ) record was obtained by miniature pressure transducer AVL-GM12D mounted flush with inside surface of combustion chamber. Important technical specifications of the sensor are given in Table 3-8. The GM12D cylinder pressure sensor was integrated with an AVL DiTEST DPM 800 amplifier (properties tabulated in Table 3-9) and AVL DiScope 802 in series for precise pressure data flow. Calibration of the cylinder pressure sensor was performed by balancing the pressure, prior to its installation into the engine's head. Crank Angle signals are needed for analyzing cylinder pressure signals. For obtaining the crank angle signals, AVL 3069A02 angle pick-up was used in series with AVL DiScope 802. The pressure crank angle measurement connection layout is shown in Fig 3-38.

Table 3-8 Technical Specifications of Pressure Transducer (GM12D)

Sl.	Parameter	Range
1	Sensitivity	15 pC/bar
2	Measurement Range	0-200 bar
3	Life Time	$> 10^8$ load changes
4	Sensitivity shift (thermal)	20-400ºC $\leq \pm 2\%$, 200-300 ºC $\leq \pm 0.5\%$
5	Acceleration Sensitivity	< 0.001 bar/g
6	Operating temperature (Max)	400ºC
7	Overload	250 bar
8	Linearity	$\leq \pm 0.3\%$ FSO
9	Natural Frequency	130 kHz
10	Insulation Resistance (at 20ºC)	$>10^7$ M Ohm
11	Capacitance	7pF
12	Mounting Torque	1.5 Nm
13	Weight (without Cable)	2.3 g
14	Shock Resistance	>2000g
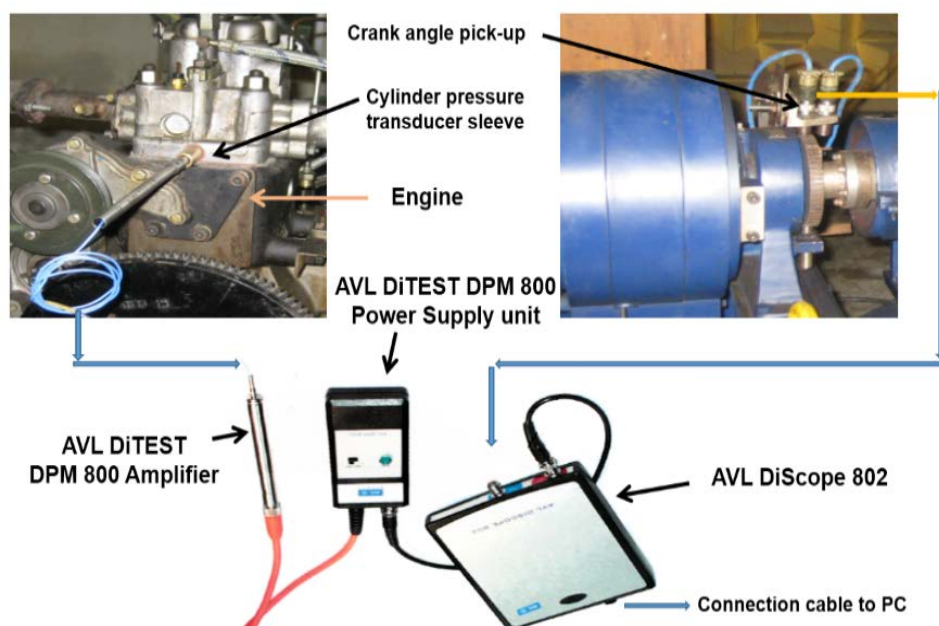
Fig 3-38 Layout of cylinder pressure and crank angle measurement connection

Temperature measurement

K-type (Chromel-Alumel) thermocouples are used to measure temperatures of intake air, exhaust gas, coolant inlet, coolant outlet and lubricating oil temperature.

Table 3-9 Properties of AVL DiTEST DPM 800 amplifier

Sl.	Parameter	Range
1	Input range	6000 pC
2	Signal output	1 mV / pC
3	Zero offset	0.5 V
4	Signal amplitude	0.5 V – 4.5 V
5	Temperature range	-10°C – 120°C
6	Power supply	8 V – 32 V
7	Dimensions	length = 131 mm, diameter=13.8 mm

Gas chromatograph

In the present investigation, gas chromatograph is used to measure the amount of hydrogen in engine exhaust. Gas chromatograph is an instrument used for chemical analysis of a complex sample by separating different chemical constituents of the sample. Schematic of gas chromatograph set-up is shown in Fig 3-39. During analysis regular flow of carrier gas is maintained at specific flow rate.
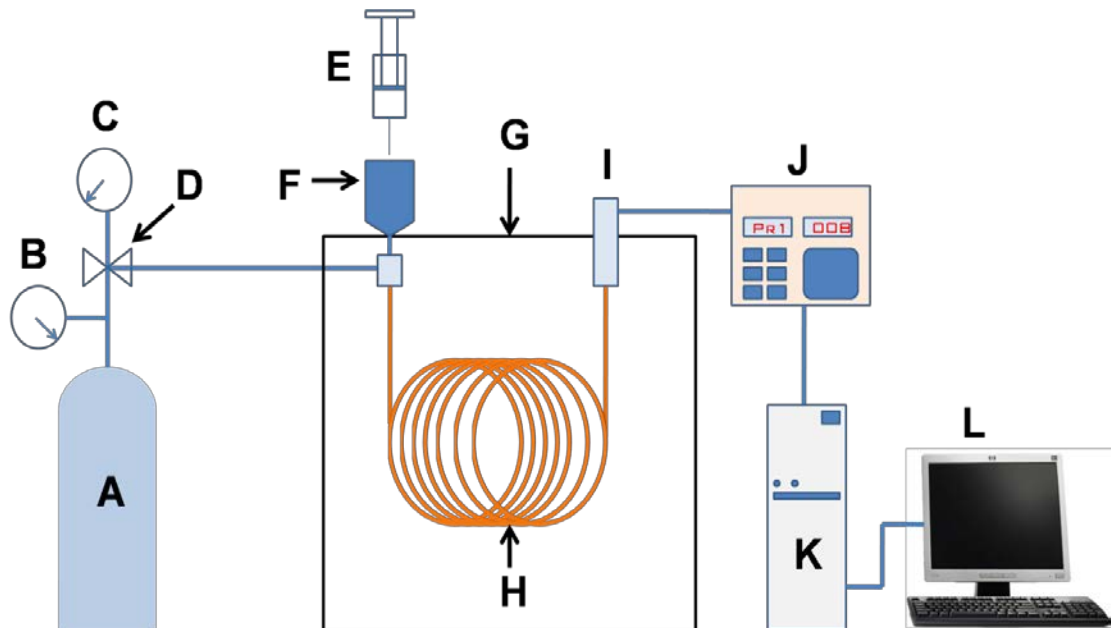
Fig 3-39 Schematic of gas chromatography set-up. (A) Carrier gas cylinder (B) Cylinder pressure gauge (C) Flow pressure gauge (D) Flow control valve (E) Syringe-Hamilton made (F) Injector (G) Oven (H) Column (I) Detector (J) Program controller (K) Central Processing Unit (L) Desktop

In gas chromatograph a known volume of gaseous or liquid sample is injected using a syringe (or a gas source input through pipe) into the entrance of the column. When sample comprises of different chemical constituents injected in to column head, the carrier gas sweeps the sample molecules through the column, during which the flow of sample molecules is obstructed either by column wall or column filling due to adsorption. Different molecules in

sample adsorbed at different rate along the column, which differentiate the motion of individual gas molecule of sample. As rate of progression is different for each type of sample molecules in column, the various molecules of sample mixture are separated and will reach the column end at different times for detection. The time signal and corresponding peak corresponds to the amount of each component of the sample can be displayed in the monitor simultaneously with the help of proper interface and supporting software. Real set-up of gas chromatograph used for experiments is shown in Fig 3-40. In the present investigation, stainless steel column with molecular sieve 5Å packing was used. Thermal conductivity detector (TCD) employed to detect the amount of hydrogen in engine exhaust.

Fig 3-40 Gas chromatograph experimental set-up

Nitrogen was used as a carrier gas with constant flow pressure of 4 bar and gas tight syringe (Hamilton) is used for sample injection in gas chromatograph. The oven temperature was maintained at 100 °C for all experiments. During experiment, the engine exhaust sample of 0.5 ml taken from tail pipe of the engine outlet using gas tight syringe and injected into the head of the column. The response peaks of engine exhaust gases appeared on desktop monitor interfaced with gas chromatograph. The peak area calculation was performed to estimate the amount of hydrogen in engine exhaust.

3.4.3 Test fuel characteristics

Density of fuel

A precision balance used to measure weight of a fixed volume of fuel to compute the density of fuel. The measurements were made as per the standard ASTM-D4052 at 15°C temperature. Multiple readings of the fuel density measurement considered and averaged for calculation purpose.

Kinematic viscosity of fuel

Viscosity of the fuel is a measure of its resistance to flow. The viscosity of the fuel actually affects the atomization of fuel and its delivery rates. The fuel kinematic viscosity is measured using Redwood viscometer (Fig 3-41). The Redwood Viscometer provides indirect measurement of viscosity in absolute units. It compares the fuel samples by measuring the time of efflux of 50 cc oil through a standard orifice under standard conditions of 40°C (as per standard ASTM D445-15).

Flash point of fuel

Flash point of fuel is the minimum temperature at which fuel produces enough of vapour and when mixed with air forms an ignitable mixture. And the mixture gives a momentary flash on application of a small pilot flame. The flash point of the fuel measured as per the standard of ASTM D93-15. A Pensky Martens apparatus shown in Fig 3-41 used to determine the flash point of the fuel.

Fig 3-41 Photographs of fuel characteristic measuring instruments

Cloud and pour points

Cloud and pour points are significant fuel properties for checking the feasibility of using the fuel in engine at lower ambient temperatures. Fuels of high cloud and pour point have flow problem at lower temperature and hence it cannot be recommended for engine operating at low

temperatures. The measurement of cloud and pour points of the test fuels performed using cloud and pour point apparatus as shown in Fig 3-41 as per standard ASTM D2500-11 and ASTM D97-12 respectively. For cold atmosphere, low pour point of fuel is a desired property.

Calorific value of fuel

The calorific value of fuel was determined using Bomb calorimeter (Fig 3-41) as per the standard ASTM D240-14. Calorific value of fuel is defined as the number of heat units liberated when unit mass of fuel is completely burnt in a calorimeter under specified conditions. The combustion of fuel takes place in the presence of oxygen at constant volume in an enclosed vessel where the fuel sample was ignited electrically.

All the measured properties of fuel used for engine testing is given in Table 3-10.

Table 3-10 Basic measured fuel properties of test fuel

Property	Test method	Diesel
Calorific value (MJ/kg)	ASTM-D240-14	43.25
Flash point (°C)	ASTM-D93-15	52
Cloud point (°C)	ASTM-D2500-11	-2
Pour point (°C)	ASTM-D97-12	-15
Kinematic viscosity at 40°C (cSt)	ASTM-D445-15	4.23
Density at 15°C (kg/m^3)	ASTM-D4052	840

3.4.4 Engine testing

In the present investigation, study of the effect of variation of operating parameters on the performance of the diesel engine in specific experimental design space has been carried out. In the present investigation, the selected parameters which were varied to see their effect on the performance of the diesel engine are engine design parameter (engine cylinder) and engine operating parameters speed, load, and coolant flow rate. The engine performance parameters (BSFC, friction power, mechanical efficiency, specific emissions with respect to indicated power and smoke opacity) considered are defined below.

A) Brake specific fuel consumption (BSFC)

BSFC is the term used to indicate the instant rate of fuel consumption with respect to brake power of the engine. BSFC can be calculated using following equation:

$$BSFC = \frac{3600 * V * \rho}{BP * t} \qquad (3-18)$$

where *V* is volume of fuel consumed in time duration of *t* seconds (cm^3), ρ is density of fuel (g/cm^3), *BP* is the brake power (kW), *t* is the time duration for *V* consumption of fuel (s) and *BSFC* is brake specific fuel consumption (g/kWh)

B) Friction power (FP)

It is the difference between indicated power (IP) and brake power (BP), which indicates the power loss in the mechanical components of engine (due to friction). And this can be computed using following equation:

$$FP = IP - BP \qquad\qquad (3-19)$$

To compute friction power, it is necessary to compute IP and BP earlier. The IP is calculated with the help of pressure-crank angle diagram as mentioned in literature [69]. Using data from pressure-crank angle diagram, the pressure-volume (PV) plot can be generated. A sample data from the experiment displaying pressure variation against crank angle is shown in Fig 3-42 and its corresponding PV diagram is shown in Fig 3-43.
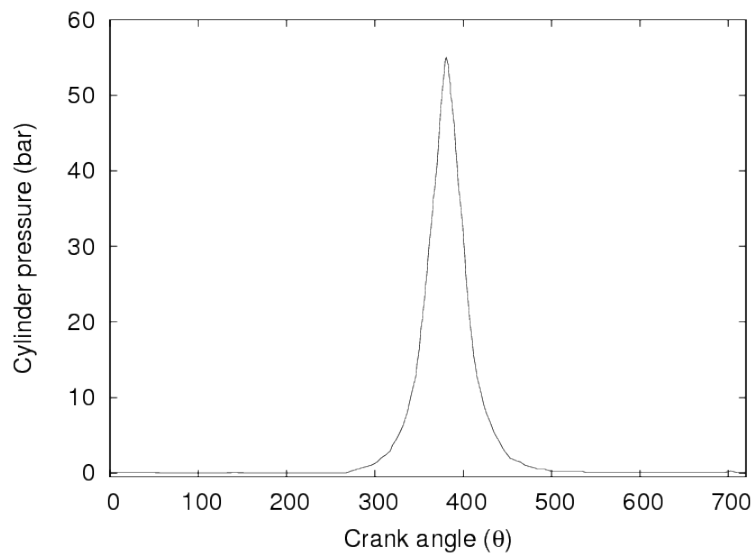
Fig 3-42 Pressure crank angle diagram
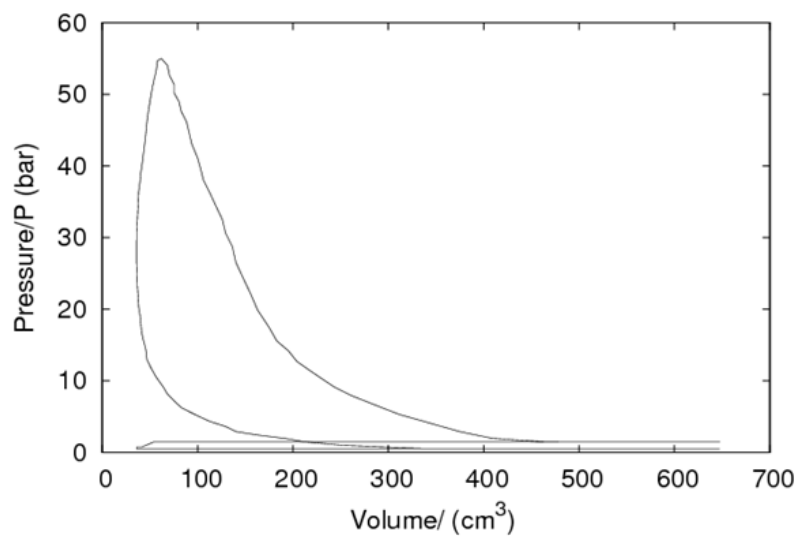
Fig 3-43 P-V diagram

The area enclosed in a Pressure-Volume diagram is the actual indicated work per cycle (W_i) produced by the engine. The indicated work per cycle is related to the indicated power by Equation 3-20 [69].

$$IP = \frac{W_i * N}{n_i} \qquad\qquad (3-20)$$

where N is the crankshaft rotational speed (rev/s), W_i is the indicated work per cycle (Nm), n_i is the number of crank revolutions for each power stroke per cycle per cylinder, and IP is indicated power (W) and it is the rate of work transfer from the combustion gas within the cylinder to the piston. For two stroke cycles, n_i equals 1; for four stroke cycles, n_i equals 2. IP can also be computed using indicated mean effective pressure (*imep*), which is also available with the help of DPM800 in the present investigation. Both the methods are cross checked and found equally reliable for computing IP.

The power delivered by the engine at the shaft and absorbed by the dynamometer is the product of torque and angular speed, also called as 'BP'. For computing BP, following equation can be used

$$BP = \frac{2 * \pi * N * T}{60} \qquad\qquad (3-21)$$

where N is the crankshaft rotational speed (rpm), T is the torque (Nm), and BP is brake power (W).

C) Mechanical efficiency

The mechanical efficiency is the term used to indicate the percentage of useful work available against total generated or produced work (or) mechanical efficiency indicates the efficacy of an engine in transforming the energy and power that is available to the machine into an output force and movement. The following equation can be used to compute mechanical efficiency (%)

$$Mechanical\ efficiency = \frac{BP}{IP} * 100 \qquad (3-22)$$

D) Specific emissions

The specific emissions are carbon monoxide (CO), unburned hydrocarbons (HC) and oxides of nitrogen (NO + NO_2 together designated as NO_x). Generally the levels of emissions of HC, CO, NO, and particulates are significant engine operating characteristics. In the present investigation, emissions of HC, CO and NO are considered for study, while the measurement of particulates in engine exhaust though not done extensively, its presence was confirmed by transmission electron microscope (TEM) analysis. The presence of particulates and its appearance in one of the experimental runs is shown in Fig 3-44. It was observed that with increase in load keeping speed constant, particulate in engine exhaust increases, and that may be due to increase in the amount of injected fuel on loading, for the same amount of inducted arc. In the engine exhaust the concentrations of gaseous emissions are usually measured in

percent by volume or parts per million (corresponds to the mole fraction multiplied by 10^2 or by 10^6, respectively).
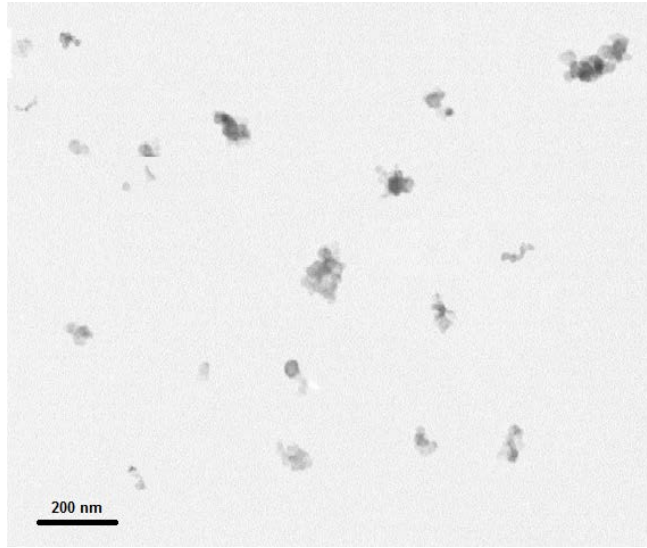
Fig 3-44 TEM image of diesel engine exhaust particulates

Specific emission of the engine is a more useful term as it gives a normalized indicator of emissions level. Complete exhaust/combustion gas measurement is required for determining specific emissions of the engine under study. The total engine exhaust is divided into 8 terms, whose mole fraction addition should be unity as shown in Equation 3-23, where $\hat{w}$ represents the mole fraction [69].

$$\hat{w}_{HC} + \hat{w}_{CO} + \hat{w}_{H_2} + \hat{w}_{H_2O} + \hat{w}_{N_2} + \hat{w}_{NO} + \hat{w}_{CO_2} + \hat{w}_{O_2} = 1 \qquad (3-23)$$

For water-gas reaction, constant K can be obtained from following equation:

$$\frac{\hat{w}_{H_2O}\,\hat{w}_{CO}}{\hat{w}_{H_2}\,\hat{w}_{CO_2}} = K \qquad (3-24)$$

where, K is the equilibrium constant whose value can be taken as 3.5 for engine exhaust [171,50]. In specific emission calculation of present study, particulate in exhaust gas is not considered.

Specific emission is defined as the mass flow rate of specific gaseous pollutant per unit power output [69], and equation for the same is as follows for specific emission CO (sCO):

$$sCO = \frac{\dot{m}_{CO}}{P} \qquad (3-25)$$

where sCO is specific emission CO (g/kWh), $\dot{m}_{CO}$ is mass flow rate of CO (g/h), and P is the power in kW (for defining indicated and brake specific emissions). In the present investigation, specific emissions were computed with respect to indicated power. Similarly

specific emission calculations can be done for other gaseous pollutants (HC and NO). For specific emissions, following terms are necessary

i) Volume flow rate of fuel (v_f) in cm^3/s

$$v_f = \frac{v}{t} \qquad\qquad (3-26)$$

ii) Volume flow rate of air (v_a) in cm^3/s

$$v_a = c_d * A * \sqrt{2 * g * h} \qquad\qquad (3-27)$$

where c_d is coefficient of discharge (constant equals 0.62), A is cross section area of orifice (cm^2) having orifice diameter of 30 mm, g is the acceleration due to gravity (cm/s^2), and h is manometer head (cm).

iii) Exhaust gas mass flow rate ($\dot{m}_e$) in g/s

$$\dot{m}_e = \dot{m}_f + \dot{m}_a \qquad\qquad (3-28)$$

iv) Mass flow rate of emission species ($\dot{m}_s$) in g/s

$$\dot{m}_s = \dot{m}_e * f_s \qquad\qquad (3-29)$$

where $\dot{m}_e$ is the exhaust mass flow rate (g/s), and f_s is the mass fraction of emission species. Using above Equations, specific emissions for all the emission species such as CO, HC and NO are determined.

In the present investigation, the specific emission values are computed using exhaust gas components (CO, CO_2, HC, O_2, H_2, NO) measurement and with the help of above relations given in equations (Equation 3-23 to 3-29).

E) Smoke opacity

Smoke opacity is the term used to indicate the percentage of smoke cloudiness in the exhaust gas of the engine under testing. Smoke principally consists of combustion generated carbonaceous materials (soot) on which some organic compounds are absorbed. Most carbonaceous material results from incomplete combustion of fuel hydrocarbons and the lubricating oil contributes some [69,115,160]. Smoke opacity is measured using AVL Dismoke 480 BT.

Uncertainty analysis is performed for the basic derived engine parameters (BP, IP, v_f, v_a), and it was found that their uncertainties would not effect the uncertainties of other results significantly. The detailed description of uncertainty analysis can be referred in Appendix-II. The variability associated with the phenomena can be uncovered through repetitions of an experimental condition as stated in ASTM standard E1847. In the present investigation each experimental run of engine testing set was repeated three times to ensure repeatability.

CHAPTER 4

Synthesis of Graphite Nanoparticles and its Coating

This chapter deals with the detailed process description of synthesizing graphite nanoparticles as carried out in the present work. Modelling and characterization study was performed in parallel with the experimentation for better understanding of the process to synthesize uncontaminated nanoparticles. In later part of this chapter, coating of graphite nanoparticles on the engine cylinder (based on selected application of coating in IC diesel engine in present study) discussed with experimental evidences. Further, several characterizations (SEM, EDS, XRD, Surface roughness, Hardness test, Scratch test) was carried out on coated samples to understand the influence of GNPs on coating.

Pure graphite nanoparticles synthesis using top down approach is still a significant challenge. Due to the difficulties of synthesizing pure graphite nanoparticles several researchers have modified their approach to synthesize graphite nanoparticles with reduced contamination, which is well discussed in the literature [6,193,189,172]. Graphite in its various forms is of research and industrial interest due to its unique properties. Some of the popular applications include solid lubricant, arc lamp electrode, refractories, batteries, brake linings and foundry facings. In the last decade several applications involving graphite nanoparticles, such as flexible and conductive support of anode materials for lithium ion batteries, highly conductive enzyme biosensor for electrochemical glucose detection, reinforcement of electrospun polyacrylonitrile nano-fibers, conductive additives in composite or coating materials, and the raw materials for preparing industrial diamond have seen the light of day [27,91,129,206,191,92]. The most popular approach for synthesizing graphite nanoparticles in large quantities is by mechanical grinding in a ball mill [135,52,39]. However, crystalline graphite has a layered structure with strong in-plane covalent bonds and weak Van der Waal bonds across layers. Such a structure is not amenable to fracture and makes grinding extremely difficult, especially to obtain submicron particle sizes [82].

4.1 Modelling graphite nanoparticle synthesis with ANN

In the present investigation a modelling effort using ANN is undertaken to understand the graphite bulk particle reduction until nanoparticle formation during mechanical milling. Such an exercise is useful to optimize the particle size reduction process such that cumbersome intermediate particle size sampling and over-milling is avoided. Though graphite is categorized as a brittle material, it still undergoes deformation with a small amount of strain before fracture, which is also discussed in this investigation.

4.1.1 Material and methods

Graphite powder with average size ~ 28 µm (purity 99.85%) was the starting material. The milling was carried out in the Planetary Ball Mill (Retsch PM100). A Stainless steel grinding jar of 50ml capacity and 20 stainless steel balls of 8mm diameter were used as the milling media. In all runs, the ball-to-powder weight ratio (BPR) was maintained at 10:1 and the jar rotation speed was either 200 rpm or 250 rpm. A fresh sample was used for each ball milling run to maintain BPR and to prevent sample mixing. X-ray diffraction studies were carried out on samples taken at regular intervals using Cu Kα (λ=0.15406 nm) radiation to follow the progress of mechanical milling on the graphite powder. Scanning Electron Microscope operating at 30 kV equipped with Energy Dispersive X-Ray Spectroscopy was used to get information on the particle size distribution, fragmentation mode and impurity analysis. The Soft imaging System of Dewinter Material Plus (version 4.1) for professional and industrial microscopic imaging solution was utilized for measuring the mean particle size of graphite powders based on SEM images. ANN was used to determine the average particle size dependence on milling time and to forecast the milling time for nanoparticle formation [119]. The milled powder was analysed under the Transmission Electron Microscope operating at 200 kV for imaging and diffraction pattern analysis.

4.1.2 Experimentation and Modelling

The milling experiment was conducted at two different speeds 200 rpm and 250 rpm for various hours of run (1 hr, 2 hrs, 3hrs, 5 hrs, 8 hrs, 10 hrs, 12 hrs, 15 hrs, 20 hrs, and 25 hrs) with same initial particle size of graphite. Each run was distinct with no repetition. Based on observations of graphite particle size under SEM for all the experimental runs, database built with 280 observations whose range is specified in Table 4-1. These data are used to develop an ANN model to predict average particle size as a function of milling time.

Table 4-1 Data base spread used for ANN modelling

Input/output	Parameters	Minimum	Maximum	Average	Standard Deviation
Input	Milling speed (*rpm*)	200	250	211.9	21.3
	Time (*hrs*)	1	25	13	7
	Initial particle size (*µm*)	16.71	47.30	28.25	7.71
Output	Particle size (*µm*)	0.39	1.63	0.88	0.28

ANN frequently used to show the specific output variation due to influence of multiple input parameters [23,74,104,36] and it consists of at least three layers as shown in Fig 4-1a. In ANN, linear functions of the inputs are operated by an activation/transfer function (Equation 3-1) so

that each input contributes to every hidden unit. Mathematically we can express neural network using a pair of equations (Equation 3-1 and Equation 3-2).

The data base spread used for modelling is shown in Table 4-1. In present investigation, the data were normalized according to Equation 3-3. The ANN model developed in a MATLAB environment (version 8). In developing the model, 70% of the randomly chosen data was used for training, 15% for validation and 15% for testing. Gradient Descent algorithm has been used to train the network, which apply a function minimization routine and back propagate error into the network layers as a means of improving the calculated output. The best performance of training was found with a single hidden layer comprising of 12 nodes and overall behaviour of the model is illustrated in Fig 4-1b.
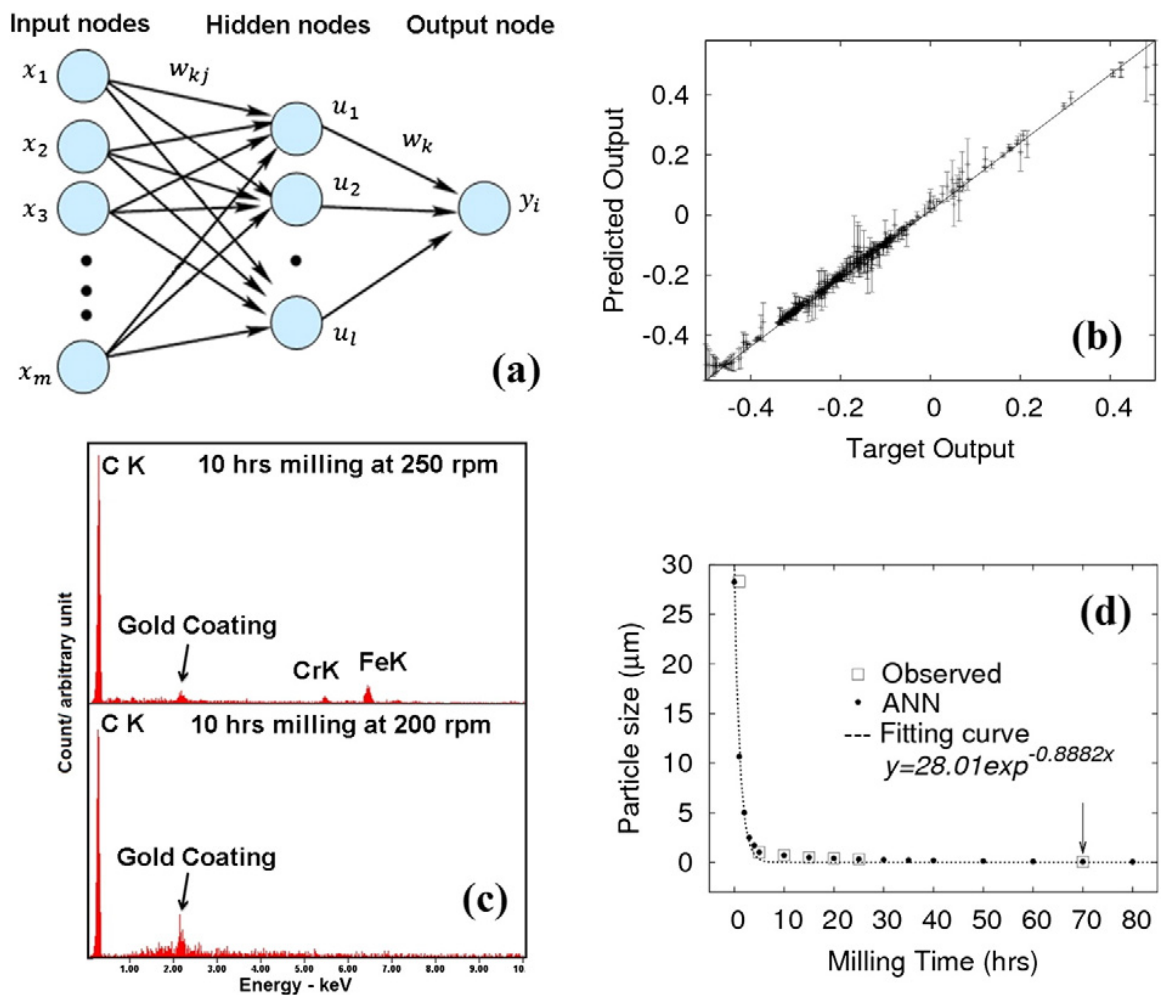
Fig 4-1 (a) Schematic of feed forward ANN with single hidden layer, (b) shows overall behaviour of ANN model, (c) EDS results of graphite powder milled at 200 and 250 rpm, and (d) mean graphite powder particle size decreases with progression of milling. The arrow indicates ANN prediction which was verified experimentally

EDS analysis done for the milled powder after 10 hrs of milling at different jar rotation speed of 200 rpm and 250 rpm, which shows that the contamination is inevitable at higher rotational speed (Fig 4-1c). Based on EDS results we opted for a lower jar rotation speed of 200

rpm for graphite nanoparticle synthesis with consideration of relatively lower amount of contamination will incur during milling. So ANN was used for particle size prediction after various hours of milling at constant milling speed of 200 rpm. The model output for the mentioned input data is shown in Fig 4-1d, where dots represent the mean particle size after milling for specified time intervals. The statistical fitting curve is generated for the particle size evolution predicted from ANN model. Based on prediction made by ANN, trial runs were carried out for 70 hrs of milling at jar rotation speed of 200 rpm for synthesis of graphite nanoparticle with less contamination. It had been noticed that on continuous running of jar at higher rotation speed affirm higher amount of contamination while the contamination level is lower in case of lower rotational speed of jar during milling. Contamination level can be further reduced by interrupting the milling at frequent intervals.

The initial graphite powder and the final milled graphite powder are shown in Fig 4-2. It is very difficult to differentiate graphite before and after milling, as both appeared as black.

Fig 4-2 Graphite powder in container; before and after milling

4.1.3 Characterization

XRD Analysis

X-ray diffraction patterns of milled graphite powder samples taken at several time intervals are shown in Fig 4-3a. The diffraction pattern was used to follow the structural evolution during milling. Williamson-Hall method was used to determine the grain size and lattice strain using Equation 4-1 [135] which is based on peak broadening of the diffraction pattern due to the internal strain 'β_{strain}' and grain size 'β_{size}'.

$$b \cos \theta = 0.9\, \lambda/d + 2\varepsilon \sin \theta \qquad (4-1)$$

where 'b' is FWHM (full-width at half maximum) of diffraction peak (rad), 'θ' is the angle of incidence of the X-ray beam with lattice plane, 'd' is the average crystallite size, 'ε' is the residual strain in the lattice. A standard defect-free silicon sample was used to correct for instrumental broadening 'β_i'. A Gaussian peak profile analysis approach applied to estimate the broadening effect due to size reduction and induced strain according to Equation 4-2 where 'β_o' is the FWHM of observed peak.

$$\beta = \beta_{size} + \beta_{strain} = \sqrt{\beta_o^2 - \beta_i^2} \qquad (4-2)$$

Using Williamson-Hall method, the XRD pattern of graphite powder milled for different time interval was analyzed (Fig 4-3b) and fitted to a linear equation where the slope represents the lattice strain and the y-intercept is a constant.
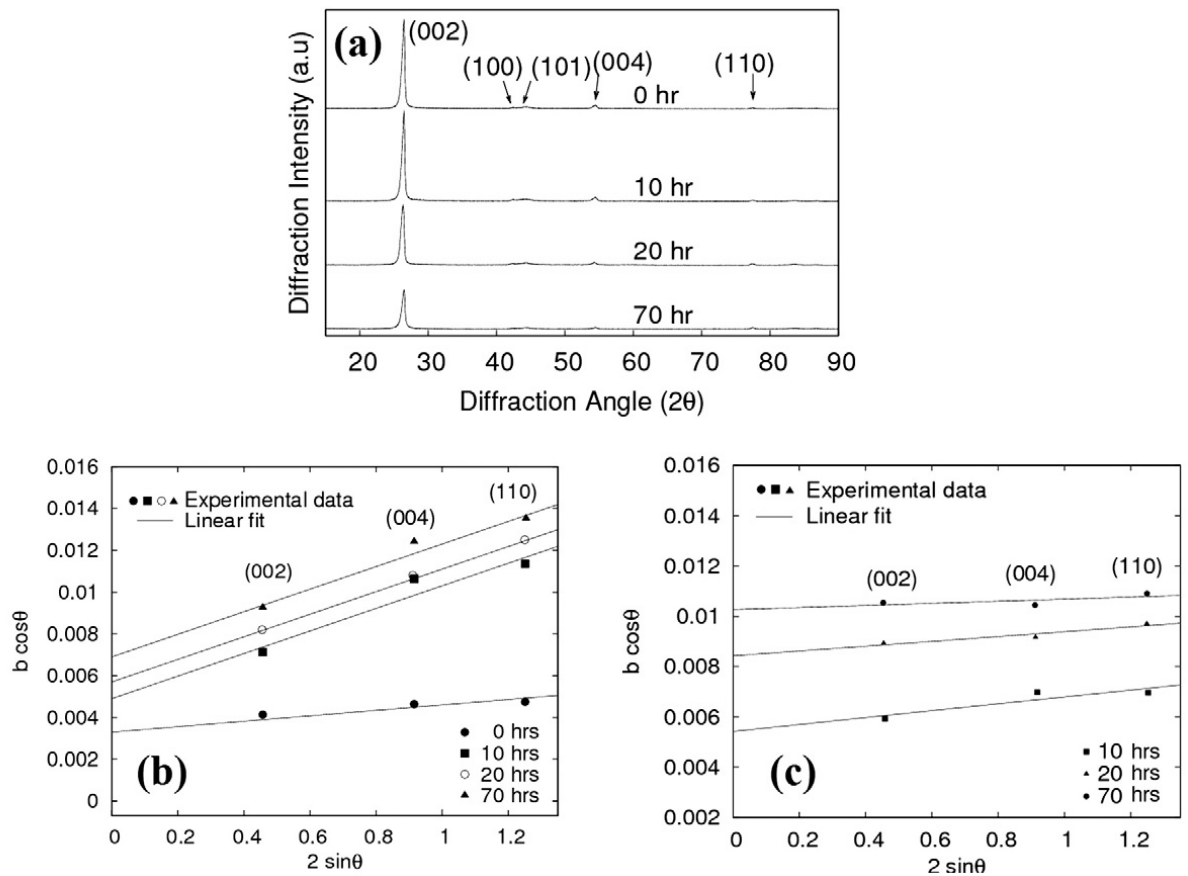
Fig 4-3 (a) XRD pattern of graphite powder after various milling times (b) shows Williamson–Hall plot for milled graphite powder with a linear fit for each sample, (c) shows Williamson–Hall plot for heat treated milled graphite powder at 600 °C for 1 hr

From the XRD analysis it is evident that the graphite particles have not lost its crystallinity even after prolonged milling [118]. Graphite has a layered structure with strong covalent bonds in plane in a hexagonal structure and weak Van der Waals bonding between layers. The weak bond between layers is the reason for the excellent lubricating property of

graphite. The strong bonds in-plane does not allow it to fragment in a finer scale, whereas, it does fracture in a brittle manner in the macro-scale with negligible strain inducement. The result obtained from XRD shows that the reduction in average particle size reaches saturation and subsequent size reduction is rather low with longer milling duration. Significantly, the lattice strain is nearly constant for all the milled samples [119]. The milled graphite powder was heated at 600°C for one hour to relieve stresses (Fig 4-3c).

Induced strain evaluation in graphite during milling

The mechanical milling of graphite induces strain in the lattice. Deviation in interplanar spacing is an indirect indication of dimensional variation in the lattice structure. Based on observations inferred from XRD pattern (refer Table 4-2) it is clear that basal planes undergo less deviation in their internal dimensions due to strong covalent bond between atoms whereas, the dimensional difference is comparatively higher in the direction normal to the basal plane. This is because the layers of sp^2 hybridized covalently bonded layers are bound together by weak Van der Waals bond. Three planes, namely, (002), (004) and (110) are considered for study and the strain behaviour in graphite using Williamson Hall plot. The plane (002) is half of the basal plane contributing main peak in XRD pattern of graphite while plane (004) plane is the second order reflection plane of the same plane which is the second major peak in the XRD pattern.

The structure of graphite is detailed elsewhere in the literature [42]. From XRD results and Bragg's law the calculations made for interplanar spacing of above considered planes is furnished in Table 4-2.

Table 4-2 XRD results showing deviation in structure due to strain

Condition	2θ (°)	Relative Intensity	Plane index	Interplanar spacing d_{hkl} (nm)
Graphite (0 hrs milling)	26.42	100	(002)	0.3369
	54.42	5.2	(004)	0.1683
	77.44	2.4	(110)	0.12308
Graphite (10 hrs milling)	26.47	100	(002)	0.3363
	54.45	4.67	(004)	0.1683
	77.47	1.83	(110)	0. 12305
Graphite (20 hrs milling)	26.34	100	(002)	0.3379
	54.28	4.89	(004)	0.1687
	77.40	2.71	(110)	0. 1231
Graphite (70 hrs milling)	26.51	100	(002)	0.3357
	54.43	5.18	(004)	0.1683
	77.46	4.66	(110)	0. 12307

The strain computation for milled powder and heat treated powder after milling done using Williamson-Hall method and the error in strain values for a set of data points is calculated using the following equation:

$$Error = \frac{1}{n}\sum_{i=1}^{n}|y - x_i| \qquad\qquad (4-3)$$

where, y is the estimated strain, x_i is the strain value estimated by considering pairs of strain data. There are n such pairs. Table 4-3 contains the summary of the strain data and the estimated error in strain measurement. It is clear that the error in strain measurement is small compared to the strain stored in the lattice due to mechanical milling. Therefore, the measured strain is not due to any instrumental error. After milling for 10 hrs the strain reaches saturation and further milling does not change the lattice distortion. Nevertheless, the error associated with the strain measurement is significantly lower than the measured value. On heat-treating the milled graphite powder for one hour at 600°C the lattice is free from strain. The measurement confirms this as the difference in the strain measured after annealing is within the measured error of the strain data.

Table 4-3 Lattice strain measurements

Conditions	Milling time (hrs)	Annealing time (hrs)	Strain	Error
Initial graphite	0	0	0.0013	0.0006
Milled graphite	10	0	0.0054	0.0018
Milled graphite	20	0	0.0054	0.0002
Milled graphite	70	0	0.0054	0.0012
Milled graphite	10	1	0.0013	0.0007
Milled graphite	20	1	0.0009	0.0003
Milled graphite	70	1	0.0004	0.0005

SEM and TEM analysis

SEM images provide information of surface morphologies and the agglomerated condition of the graphite particles. Dewinter Material Plus is utilized for measuring the mean particle size of graphite particles from the SEM images. Fig 4-4a shows the unit cell of graphite structure while Fig 4-4b shows the SEM image of initial graphite powder where the average particle size is about 28 µm. Particle size reduction and its distribution after 10 hrs of milling is shown in Fig 4-4c which indicates that milling is an effective fragmentation process for graphite. Fig 4-4 (d and e) show the TEM image and selected area electron diffraction pattern of the final milled graphite powder.

TEM image appears translucent showing polycrystalline graphite structure which indicates that mechanically milled graphite powder particles have retained its crystallinity at the nanoscale with an average particle size of 67 nm which is fairly close to the ANN model predicted value of 86 nm. Using the same method Chen et al. [39] earlier reported that particle size of graphite powder reaches nanoscale with continuous porous structure, while most work reported on ball milling of graphite leads to mixture of amorphous and crystalline phases [39,175,165]. TEM image of graphite nanoparticles confirmed the formation of nanoparticles. Most of the

particles are semi transparent which indicates there are very few grain boundaries in a particle and their thickness is of the order of a few nanometres. Fig 4-4f shows a monotonic distribution of particle size with a very narrow size range. At this size, graphite particles are endowed with the large surface area.
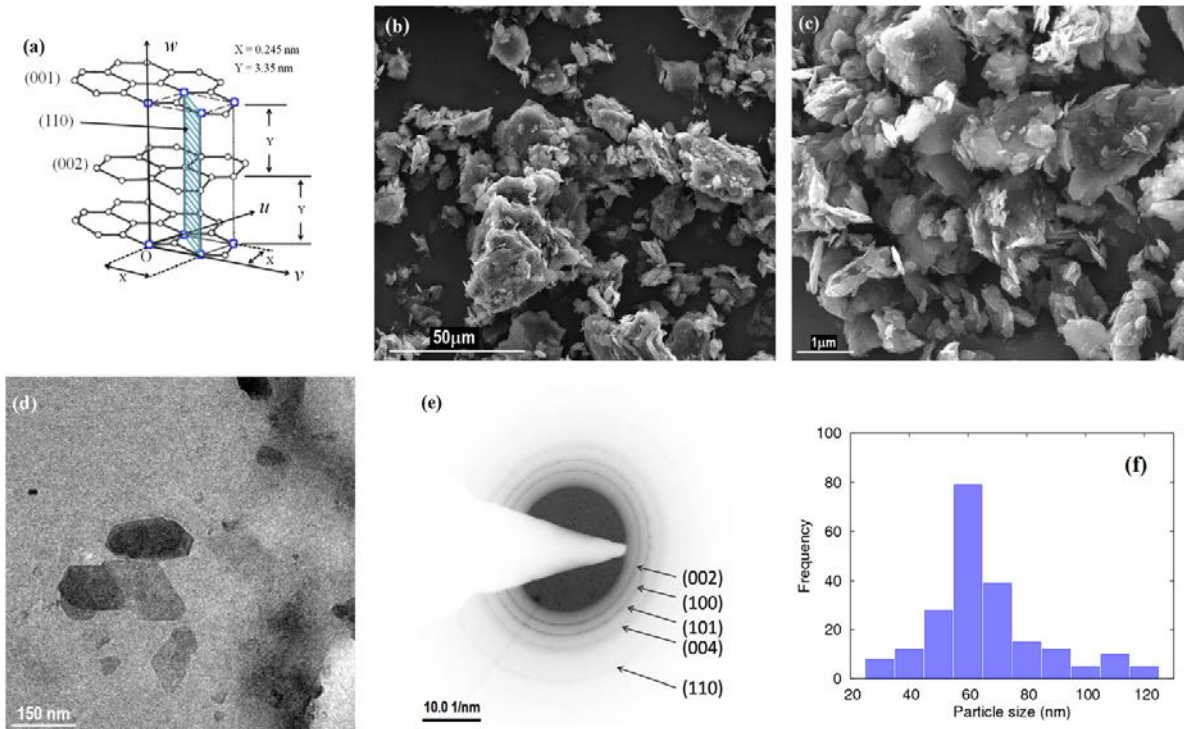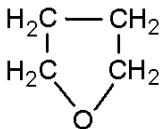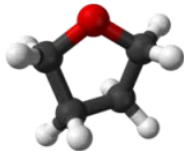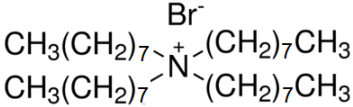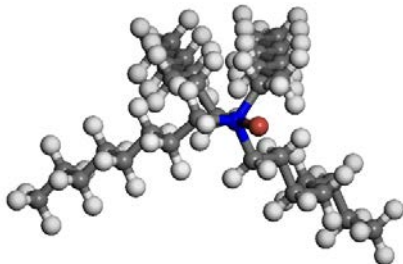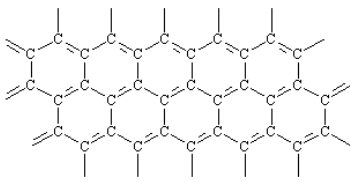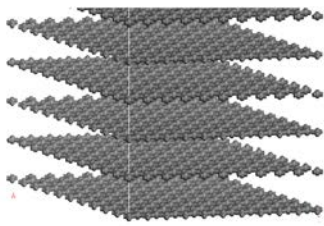
Fig 4-4 (a) Unit cell of graphite structure, (b) SEM image of initial graphite powder, (c) SEM image of 10 h milled graphite powder, (d and e) show the TEM image and selected area electron diffraction pattern of the 70 hrs milled graphite powder, (f) distribution of particle size for 70 hrs milled graphite powder

4.2 Coating of graphite nanoparticles

To conduct the testing trials at small scale is a cost-effective and energy efficient method as compared to large scale testing trails. So initially, the coatings were performed on small coupon of engine block. After standardization of all the coating parameters, coatings performed on the engine cylinder.

Pure GNP's synthesized by mechanical milling method were found to disperse homogeneously in an organic solvent (such as acetone, acetic acid, 2-butanone, benzene, 2-butanol, oxolane) through mechanical agitation. The carrier or capping agent required to transfer GNP's to electrode surface was chosen as quaternary ammonium salt (TOAB, source: Sigma Aldrich) as it was found to be good capping agent for negatively charged nanoparticles [37]. The organic solvent 'oxolane' is used in present investigation for preparation of resultant solution to be used for electrophoretic deposition process. The chemical formula and structural details of the components used in coating process is given in Table 4-4.

Table 4-4 Structural details of components used for coating

Sl.	Component	Chemical formula	Structure	Atomic model
1	Oxolane (or) THF	C_4H_8O	H_2C — CH_2 H_2C CH_2 O	
2	Tetra-Octyl Ammonium Bromide (TOAB)	$[CH_3(CH_2)_7]_4$ N (Br)	Br^- $CH_3(CH_2)_7$ N^+ $(CH_2)_7CH_3$ $CH_3(CH_2)_7$ $(CH_2)_7CH_3$	
3	Graphite Nano-particle (GNP)	C	Infinite sheet; in layers	

With all above considered component, electrolyte solution prepared by mixing them in molar ratio 0.43052:0.00033:0.0016 of Oxolane: TOAB: GNP respectively. The mixture was sonicated for 30 minutes followed by magnetic stirring for 5 minutes resulted in stable dark colour suspension as shown in Fig 4-5. Magnetic stirring is used for maintaining homogeneity of the solution before starting of the experiments, and duration of magnetic stirring is used to complete the experimental set-up. The suspension found to be stable for 20-25 minutes only, while it was observed that after 5 hrs from removal of external stimuli for mixing to the solution particles eventually settled at the bottom of the solution as shown in Fig 4-5 (The particles can be resuspended by shaking the settled suspension solution).

Freshly prepared suspension consisting of TOAB capped GNP in organic solvents 'oxolane' found completely stable for 20 minutes. In present study based on zeta potential analysis, it is confirmed that TOAB bind to the GNP through hydrophobic interaction of its alkyl chains as shown in the Fig 4-6.
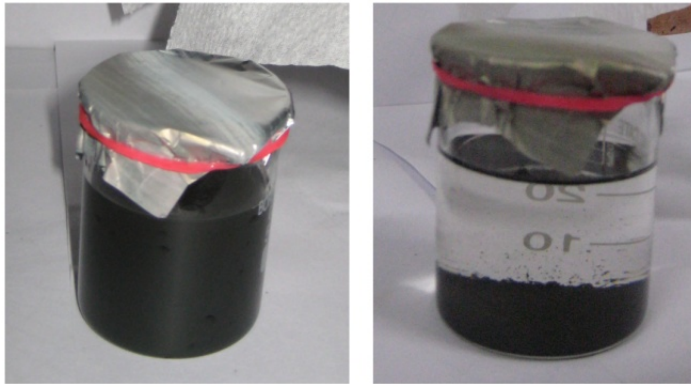
Fig 4-5 Stable dark colour suspension of electrolyte (left) and GNP settled at bottom of the solution after 5 hrs (right)

The stability of the nanoparticles could be ascribed to the considerably higher zeta potential. Negatively charged particles contribute to the high stability of the solution. Moreover, the electrostatic repulsive forces among the negatively charged surface of the nanoparticles prevent them from agglomerating in the suspension state thus maintaining the stability of the system. The zeta potential value of the graphite nanoparticle in oxolane solvent diluted with distilled water was found to be – 5.39 mV. The value lies within the stable range, signifying that the nanoparticles in solution lead to the formation of a stable system. The zeta potential of graphite nanoparticle capped with TOAB in oxolane solvent diluted with distilled water was found to be – 3.34 mV. Which is enumerating the entrapment of the graphite nanoparticle by TOAB. The zeta potential of the samples were measured using a Zetasizer (Malvern, Nano ZS 90).
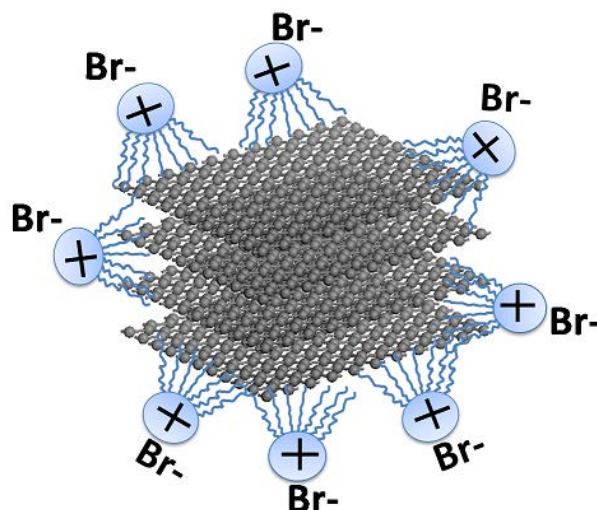
Fig 4-6 Sketch of TOAB bind GNP

Observations made for appearance of the electrolyte solution is tabulated in Table 4-5. The reason of Trial 3 (Table 4-5) result in suspension type of mixture is due to its appearance alone, while the amount of solute decides the actual type of mixture. In the present study, both TOAB and GNP are kept in such amount so that most of the TOAB molecules in electrolyte

solution are utilized as GNP capping agent. If amount of TOAB component increased in electrolyte solution then the solution will have mixed solution state with Oxolane-TOAB solution and Oxolane-TOAB-GNP suspension, but the appearance is analogous to suspension only.

Table 4-5 Variation in solution mixture type due to solute content

Trial	Solvent	Solutes		Result	Observation
		TOAB	GNP	Type of mixture	Appearance
1	Oxolane	yes	--	Solution	Transparent
2	Oxolane	--	yes	Suspension	Cloudy (black)
3	Oxolane	yes	yes	Suspension (dominating)	Cloudy (black)

Coating process selection was done on the basis of practical considerations of the present investigation which are as follows:

- o Original component size consideration
- o Nanoparticles compatibility with component
- o Feasibility for large scale coating

4.2.1 Electrophoretic deposition of GNP's layer on engine block coupon

The experimental set up for conducting coating of GNP on small coupon of engine block (2.5 cm × 2.5 cm with approximate thickness of 3 mm) is shown in Fig 4-7. Two electrodes were placed in parallel at a distance of 5-7 mm to each other in the electrophoretic cell. The external potential applied in the electrophoretic cell is within the range of 1 – 100 V.
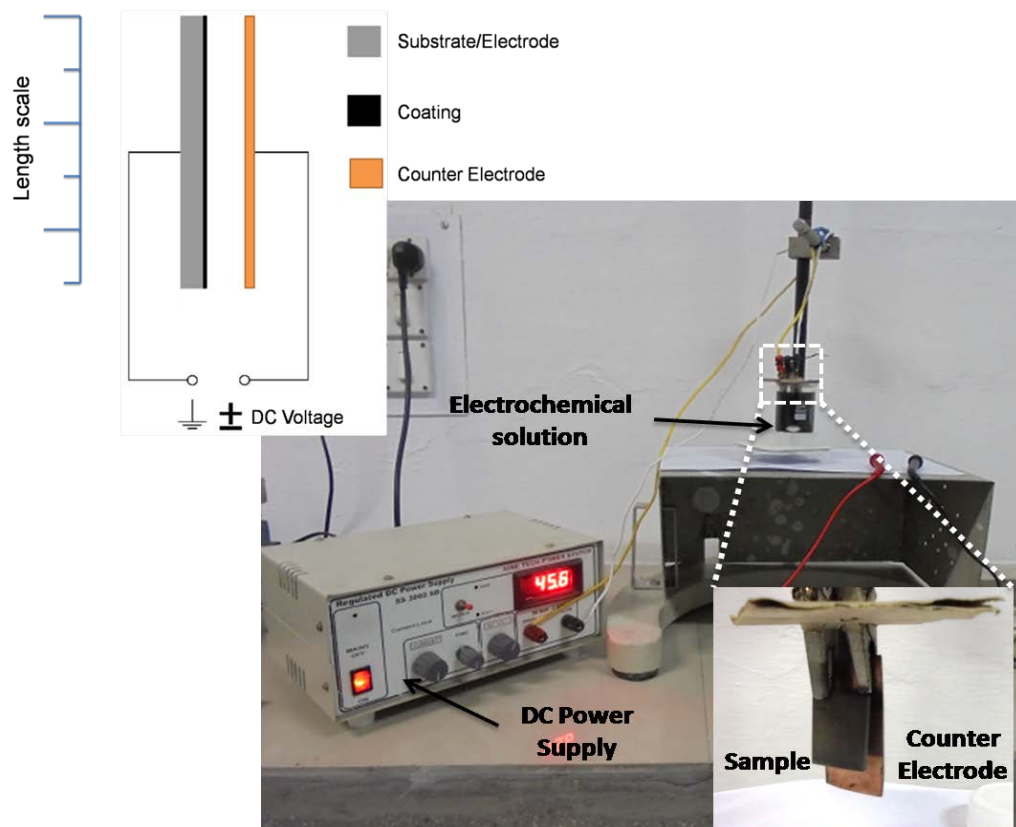
Fig 4-7 Figure (top) showing sketch of experiment on small sample with indication of length scale and figure (bottom) showing real set for experiment on small sample

Initially, the applied external potential has no effect, but as the applied external potential is increased to 40 V, deposition of GNP over anode surface observed. As the potential is raised further, the GNP deposition was found to be proportional to the applied external potential till 80 V. If the applied external potential is raised above 80 V, GNP forms agglomerates at various local sites on the sample surface. Coating trials were conducted on small coupon of engine block using different ratio of composition several times for acquiring the feasible process parameters of coating. A few of the trial runs and there details are given in Table 4-6 which give some details for successful coating. The microstructure of coated samples under different trial conditions with 45 V DC power supply for 10 min (Trial – 1, 2 and 3 mentioned in Table 4-6) are shown in Fig 4-8. From microstructure it is evident that Trial 1 and 2 are very poor compared to Trial 3.

Table 4-6 Coating trial runs detail

Trial	Composition	Sonication time (min)	Method details	Experiments	Reaction time (min)
1	Oxolane + TBAB + GNPs	30	DC 20-100V	10	6, 10
2	Oxolane + TBAB + TOAB + GNPs	30	DC 20-100V	10	6, 10
3	Oxolane + TOAB + GNPs	30	DC 20-100V	10	6, 10
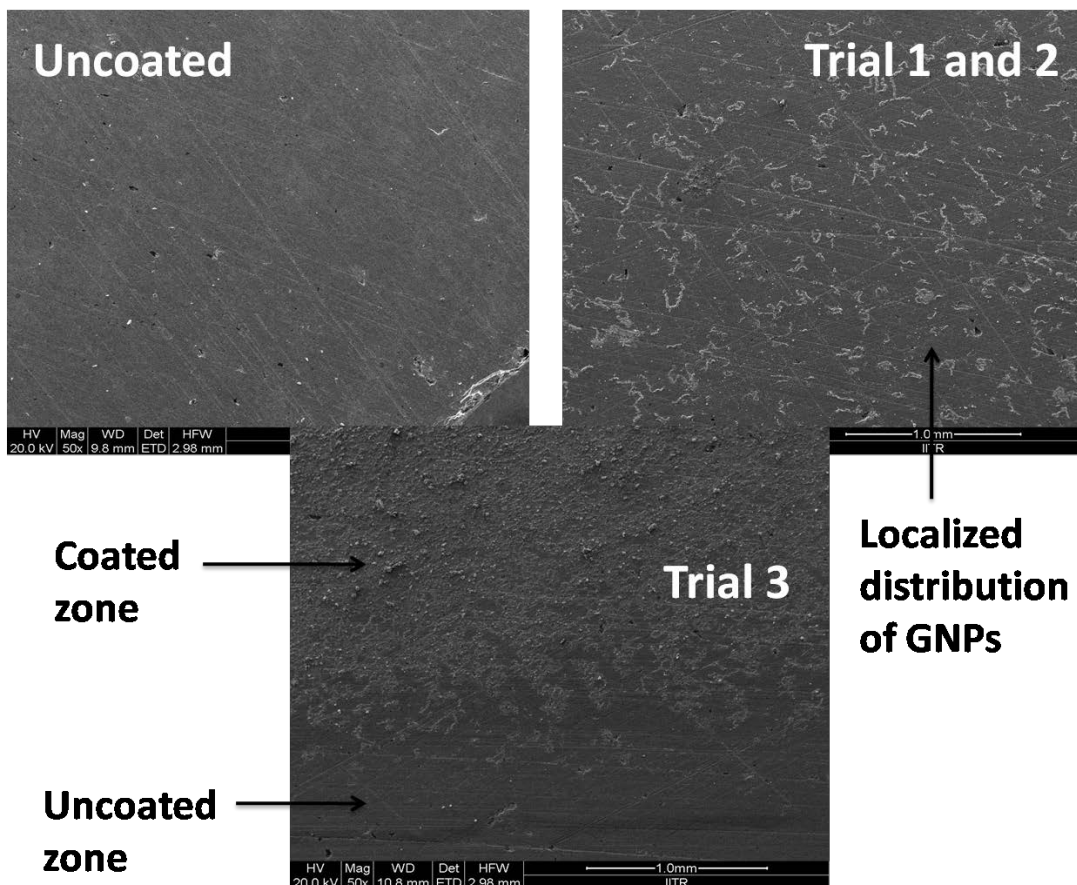
Fig 4-8 Microstructure of coated samples under different trial conditions

Based on Trial 3 outcome it is confirmed that it is feasible to coat GNPs on small coupon of engine block. Moreover, this method can be extended to the engine cylinder/block. In current coating method electrophoretic electro-chemical cell supplied with a dc voltage of 45-50 V resulted in better GNP thin film deposition. So experiments were carried out with same external dc voltage supply. Constant supply of dc voltage for 6-10 min in electrophoretic electro-chemical cell resulted in the formation of GNP thin film on the sample electrode surface. The thickness of GNP layer formed by electrophoretic deposition is directly proportional to time at constant dc voltage.

Fig 4-9 depicts the atomic model of coating process with the internal structural details of the coating particles as well as the substrate used for coating. The GNPs are transferred from solution to the substrate surface with the help of TOAB. During coating of GNPs the basal plane of GNPs are most probable site for bonding in comparison to sites on thickness side (Fig 4-10), as the GNPs possess high surface to thickness ratio which causes the surface of GNPs (basal plane) to form bonding with exposed surface of substrate as shown in Fig 4-9.
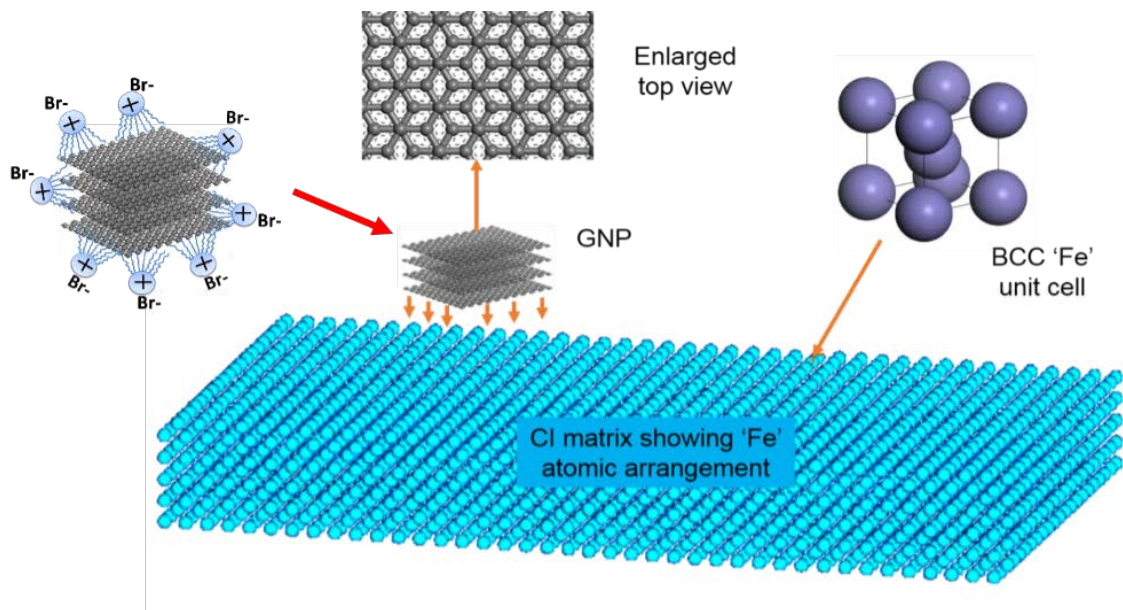
Fig 4-9 Atomic model of the electrophoretic coating of GNP on cast iron matrix
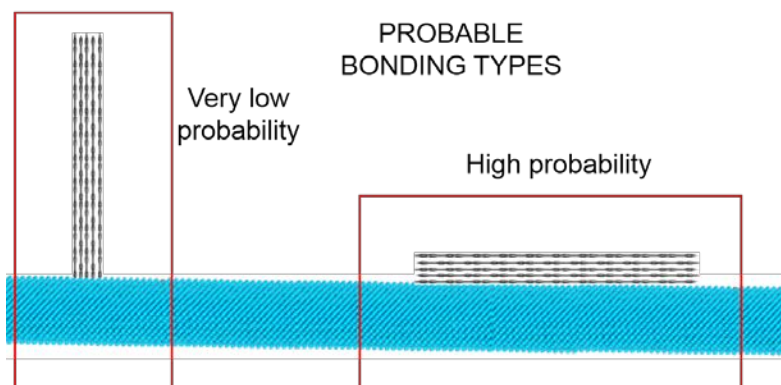
Fig 4-10 Atomic arrangement of nanoparticle and substrate showing probable bonding type

The basal plane of GNP has more number of atoms compared to thickness side of GNP to interact with other surface, as well as the regular arrangement of atoms in basal plane of GNP compared to thickness side provides uniform bonding sites throughout the surface area of GNP. The maximum benefit of coating can be obtained when the coated GNPs arranged systematically and close to each other without leaving any gap in between. But it is not practical as the shape and size of nanoparticles are not fully controllable during fabrication/synthesis process. So it is obvious that the coating will have mix type of coated particles arrangement as shown in the Fig 4-11. Fig 4-12 shows the successful coating of the flat engine block coupon with similar surface roughness value as in the engine block.
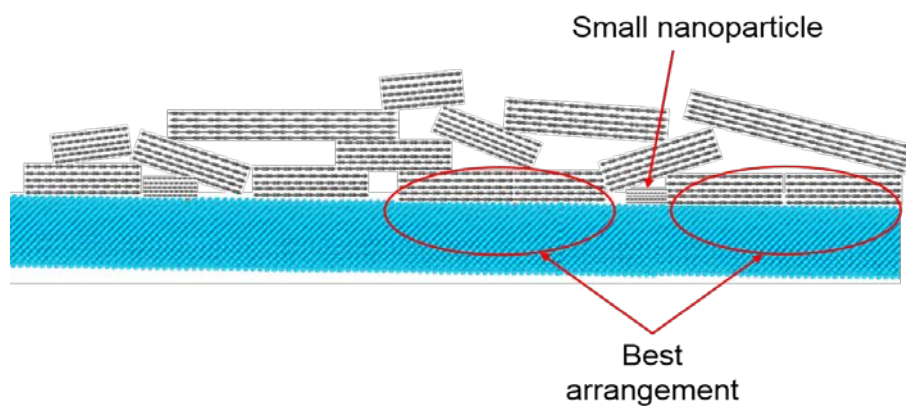
Fig 4-11 Atomic model showing all possibilities of coated nanoparticles arrangement
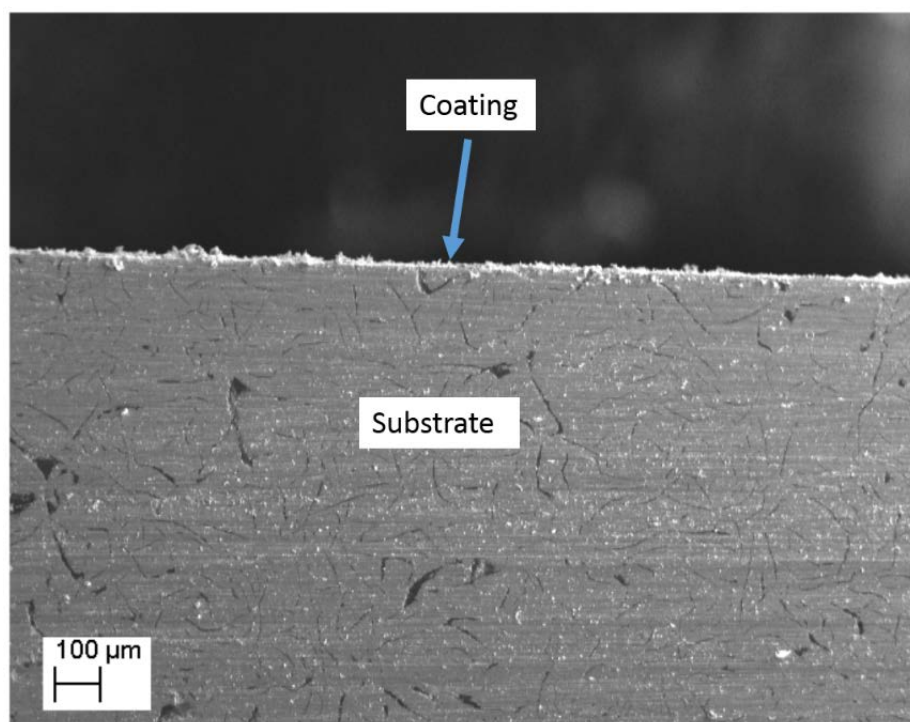
Fig 4-12 Coated engine cylinder coupon (flat sample) showing thin layer
of coating on the cast iron substrate

Coating interface study during trial runs

This study was performed to check the coating efficiency when the sample is partially submerged or submerged till top surface of the solution in electrochemical solution during coating process. It was found that the intermediate zone have less deposition of graphite nanoparticles, and from top of the coating deposition to approximately 0.8 mm depth the lack of GNPs is significant, below which the deposition is found to be uniform throughout as shown in Fig 4-13. The probable cause for this differential coating near the surface is presence of low density polymer TOAB floating on the top of the solution. At the top of the solution the polymers are not untangled during sonication and do not take part in the coating process. With this study it is confirmed that the sample to be coated has to be submerged in electrochemical solution to a minimum depth of 1 mm from top surface of the solution, which was adhere to in later experiments.
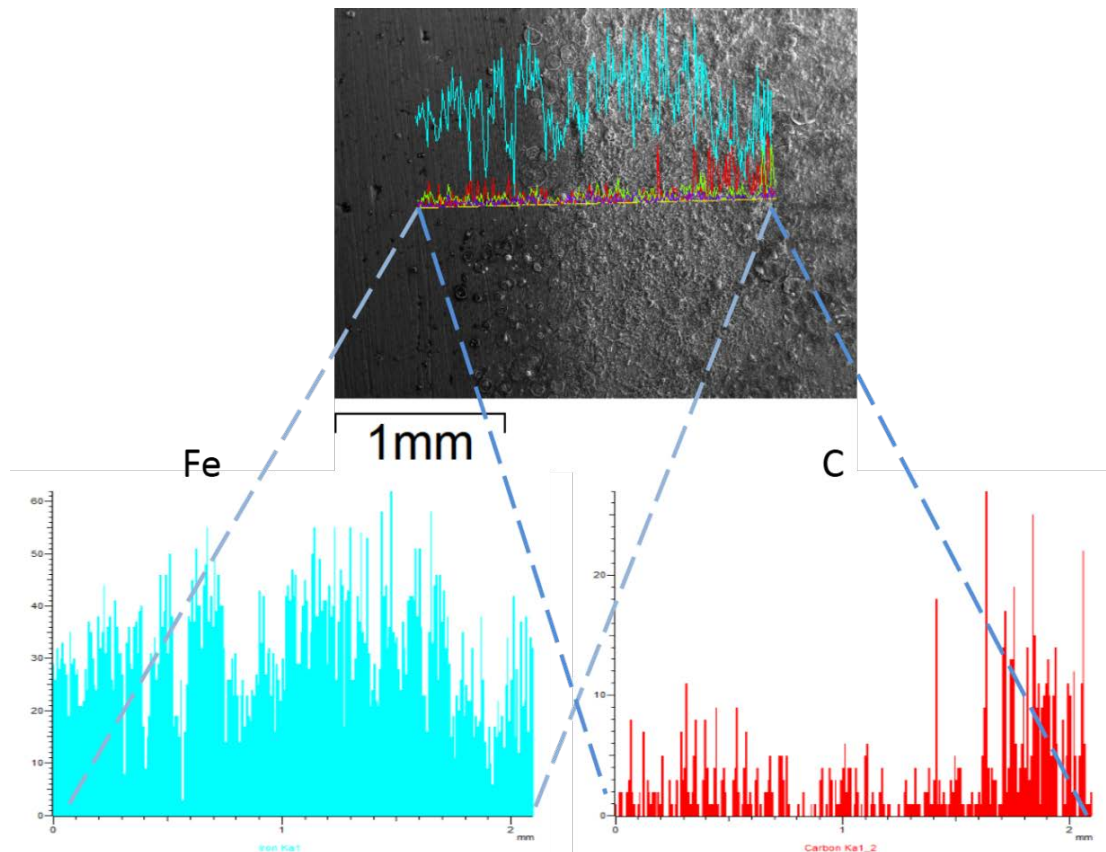
Fig 4-13 Chemical composition analysis of the interface using EDS line scanning of the surface from uncoated zone to coated zone

4.3 Heat treatment of sample

Coated samples did not having enough adhesive strength between substrate and coated particles (GNPs). Heat treatment of coated samples was performed to improve coating adhesion. The heat treatment process adapted based on engine cylinder working environment, as well as nanoparticles behaviour at high temperature (near to engine cylinder working environment) as shown in Fig 4-14.
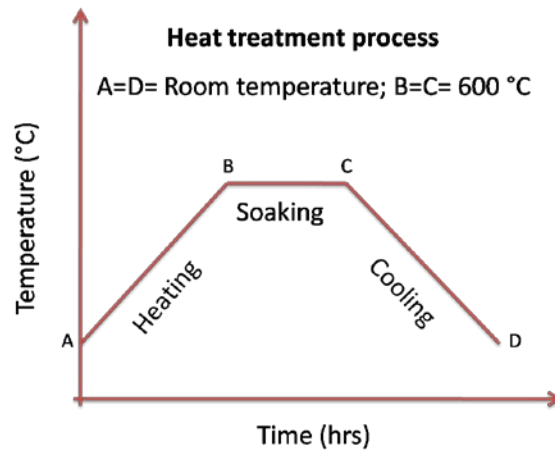
Fig 4-14 Heat treatment process opted for the coated sample

The environment of engine cylinder and the piston during IC engine combustion process is properly depicted in Fig 2-5, while the thermal behaviour of the graphite bulk and nanoparticles analysed using TGA is shown in Fig 4-15. In TGA analysis, initially sample weight of 10.5 mg approximately considered (in all cases) against reference powder (alumina, weight 10.5 mg) for TGA experiment in EXSTAR TG/DTA 6300. The temperature range selected for experiment was from 32° C to 1100° C with heating rate of 10° C/min and air as operating gas with a flow rate of 200 ml/min. From the plot it is clear that the bulk graphite is more stable as compared to graphite nanoparticles until 600° C temperature. In present investigation the considered material is graphite nanoparticles whose thermal behaviour is shown in the diagram Fig 4-15 and represented as 'Graphite-Nano'. Graphite nanoparticles decomposition started close to ambient temperature and continued till 636° C, as it decomposes to CO and CO_2. At 600° C, 50% decomposition of graphite nanoparticles is observed, so from TGA analysis it is clear that in presence of air maximum 50% decomposition of graphite nanoparticles is possible up to 600° C.
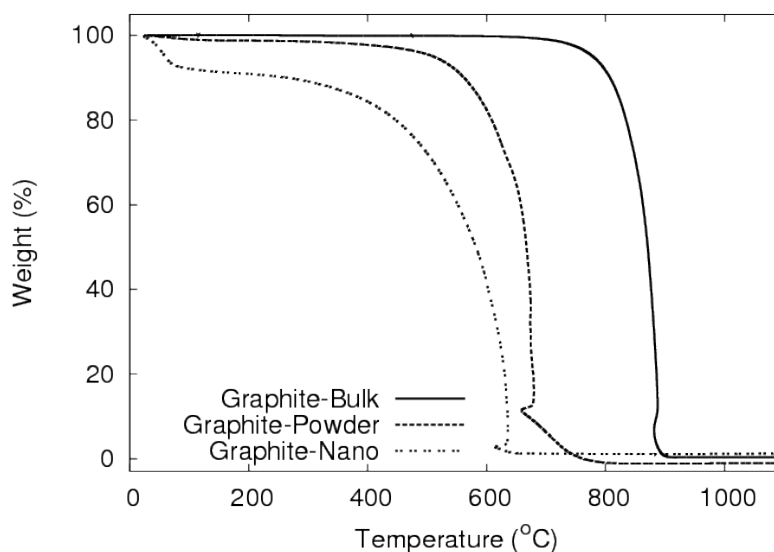
Fig 4-15 TGA curve for graphite bulk, powder and nanoparticles, showing their decomposition with the variation of temperature

The heat treatment process standardized and conducted in the customized heat treatment set-up with inert atmosphere provision (argon) as shown in Fig 3-7. The heat treatment of coated sample performed in inert (argon) atmosphere, where coated sample heated with 5 ℃/min rate from room temperature to 600 ℃, soaked for 1 hr at 600 ℃ and then cooled to room temperature in furnace. To improve the bonding between the substrate and the GNP coating it is desirable to have some form of bonding establishment between the two.

Saito et al. and Nagatsu et al. [151,106] reported that fine particles of iron can be wrapped in multi layered graphitic sheets using electric arc discharge method. The graphite layers are also bent to form complex shape for complete coverage of iron fine particles. With these considerations it is expected in present investigation that GNPs can cover all the surface of the substrate. Few more studies reported similar phenomenon of graphite encapsulated iron particles and even the bonding between iron and graphite particles highlighted using TEM analysis [154,155,156].

The coating of graphite layer on iron is done by many researchers, but the interaction between the atoms is rarely reported in the literature. In a recent study by Shin et al. [166] it is shown that the transition metals with unfilled d-orbitals may form ionic bonds with the carbon atoms of graphitic basal plane. At the same time it is also reported that the overall bonding strength between the basal plane of transition metal 'Ti' and a single plane of graphene is found to be five times higher than that between non-transition metal 'Al' and carbon of graphene.

In case of metal and carbon layer bonding, there is little reported work, which confirms that the interfacial interaction between metal particles and carbon layers are primarily due to Van der Waals interaction [21,20,166] and even the presence of ionic bond between transition metal and carbon layer is reported in literature [166]. Even in the literature it is reported that the carbon nanoparticles can reduce wear rate of test materials by 1.4 - 1.8 times when used in conjunction with lubricants [167]. Hence it can be concluded that graphite nanoscale materials acts like a reinforcement to the base material, especially transition metals with low volume fraction addition. In the present investigation it was found that the coating layer of graphite nanoparticles improves hardness of the base material and reduces friction coefficient.

Heat treatment process actually provides thermal energy to the system for various purpose like stress relieving, recrystallization, diffusion etc. In present investigation it is expected that heat treatment may improve the bonding between graphite nanoparticles and cast iron substrate. The improved bonding will minimise the gap between carbon atomic layer of graphite nanoparticles and iron atomic layer of the substrate. TOAB particles are used during coating process as a transfer agent of the GNPs for proper coating of the cast iron substrate. They are present in the coating between the GNPs and cast iron substrate. After coating the residual

polymer is removed during heat treatment as the boiling point of TOAB is very low (~200º C), while the heat treatment is carried out at ~600º C in inert atmosphere. As the TOAB evaporates away, the distance between the bottom graphite nanoparticle layer and the cast iron substrate is minimised which may help in two ways:

a) Interface bonding between carbon atoms of graphitic basal plane and iron atoms of BCC iron in cast iron substrate

b) The diffusion of carbon atoms from graphite nanoparticles to the substrate feasible zone that is iron matrix portion of the cast iron substrate.

The site for diffusion is shown in Fig 4-16 which is also favoured for interfacial bonding.
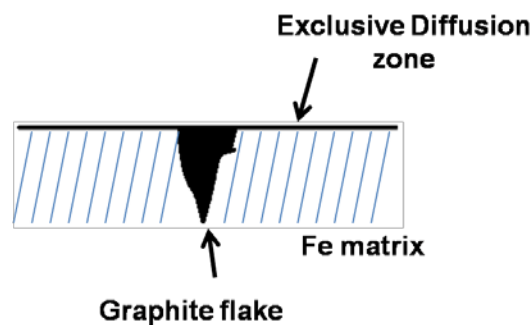
Fig 4-16 Sketch of engine cylinder base matrix suitable for diffusion

A point to be noted is that, the material considered is gray cast iron, which have ferrite and graphite in their microstructure. Ferrite has bcc structure with 0.022 wt% carbon solubility at 1000K [76]. So interface bonding and diffusion with the help of thermal energy are realistic possibilities and lends itself for better mechanical properties. Shin et al. [166] have studied interfacial bonding between iron and carbon.

The dissolution of carbon in bcc Fe is an endothermic process. The most likely and intuitive hopping mechanism for interstitial atom diffusion of carbon in the bcc lattice is the linear movement of the interstitial element from an octahedral site to another nearest neighbour octahedral site via the tetrahedral site [76]. Thus the octahedral site in between becomes a local minimum which has a small tensile stress along one direction, and causes its energy to be a little higher than the initial state. The diffusion barrier reported to be 0.86 eV, which also confirmed with the experimental value of 0.87 eV [76]. Above a certain threshold of the electron energy, the atoms of the object can be displaced from their positions so that structural transformations are unavoidable. The displacement threshold energy in graphite is highly anisotropic, knocking carbon atoms onto interstitial positions is easier normal to the plane than it is in any direction parallel to the plane [16].

4.4 Characterization of uncoated and coated surfaces

Various characterizations of uncoated and coated samples (cast iron cylinder coupons) are performed to verify the coating from different point of view and to establish the process.

4.4.1 Physical and microscopic observations

Fig 4-17 shows the engine block used in the present investigation. In which the closed view of engine block is shown with the cross hatch mark and its enlarged view using SEM is shown here to highlight its surface morphology. Further, the coupons of engine block had been made for various characterization purposes and the physical appearance of the engine block coupons sample can be seen in the Fig 4-18.
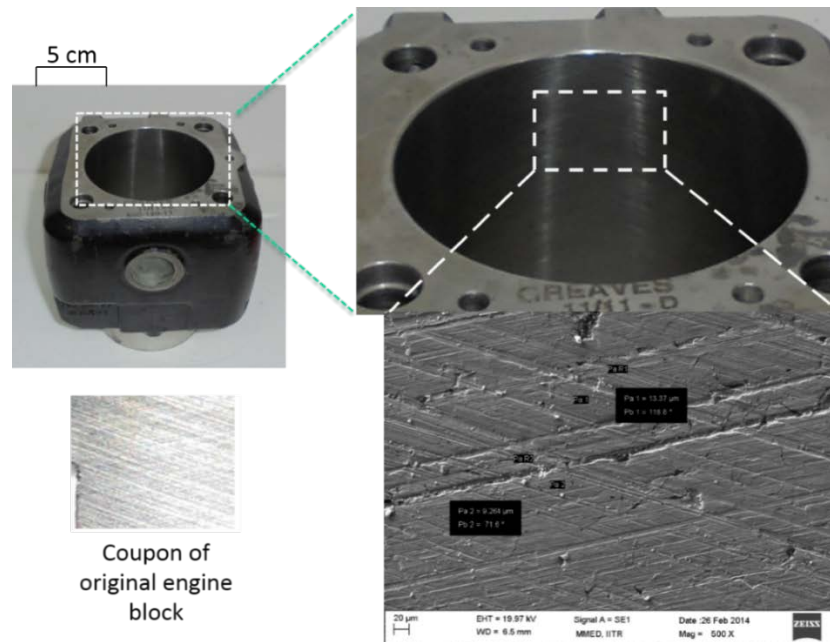
Fig 4-17 Physical appearance of engine cylinder and its coupon with a microstructure showing the surface morphology
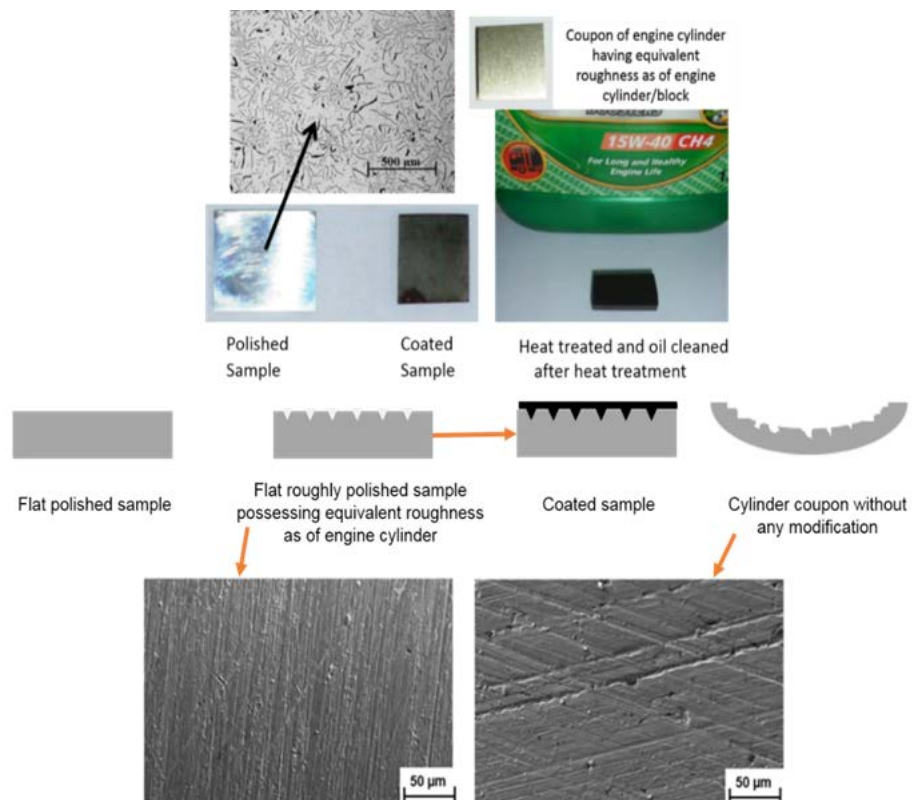
Fig 4-18 Physical appearance, sketch and microstructural view of engine block coupons; specially made for coating and characterization at laboratory scale

It is surmised that the characterization on laboratory scale sample is valid on the engine block sample. The surface morphology of the engine block is very rough or uneven. So to maintain the same sample surface condition, the polishing of all the laboratory scale samples (or coupons) had been done in the way so that it would result in similar surface roughness as of the engine block.

4.4.2 The chemical composition analysis

After successful coating of flat coupon of engine block, the surface chemical composition analysis performed to check the change in surface chemical composition due to coating. Fig 4-19 shows the EDS elemental analysis for uncoated sample surface composition using point scan, similarly Fig 4-20 shows for coated sample surface.

Sl	Element	Weight %
1	C	3.72
2	Si	2.66
3	Mn	0.84
4	Fe	92.79
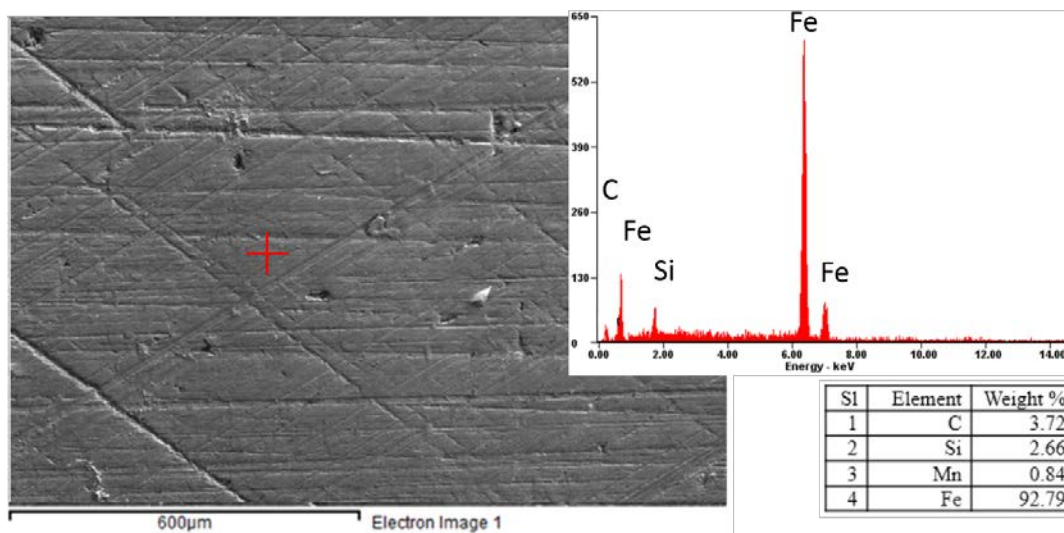
Fig 4-19 Chemical composition analysis of the uncoated surface using EDS point scan; showing 'Fe' as major constituent

Sl	Element	Weight %
1	C	45.49
2	Si	0.66
3	Mn	0.18
4	Fe	53.66
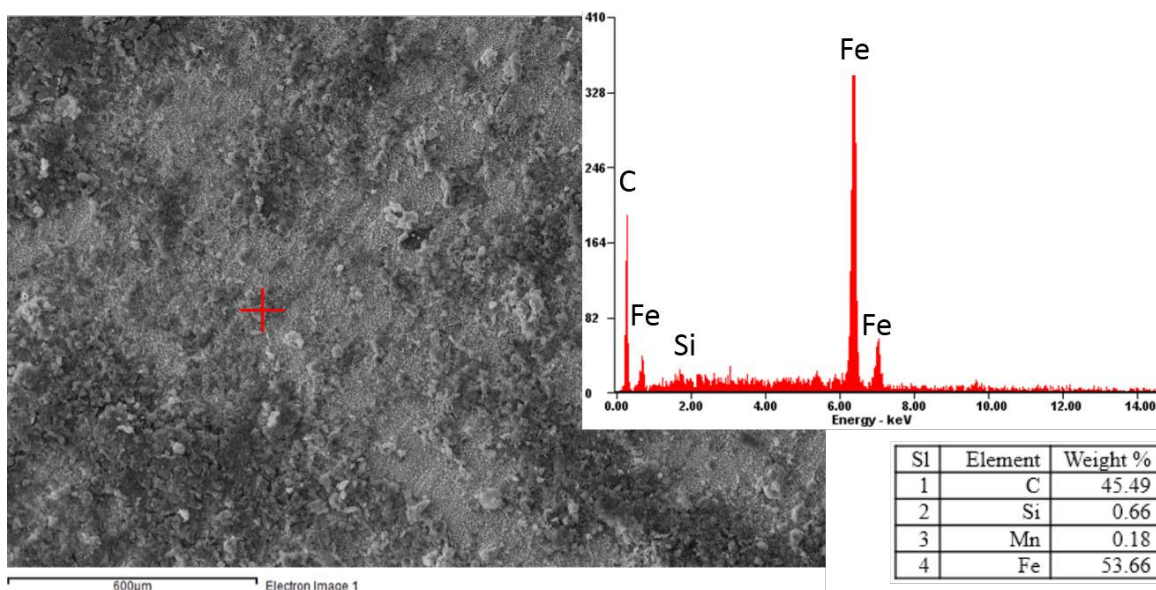
Fig 4-20 Chemical composition analysis of the coated surface using EDS point scan; showing 'Fe' and 'C' as major constituents

For better confirmation of coating, the EDS elemental analysis of coated sample performed using line scanning and area scanning as shown in Fig 4-21 and Fig 4-22 respectively. From the EDS analysis it is confirmed that the GNPs are present all over the coated surface, which is represented by element 'C' in the Fig 4-21 and Fig 4-22. Fig 4-19 represents the localized chemical composition analysis of uncoated engine block sample surface at a point, which is assumed to be similar throughout the sample. While coated sample chemical composition analysis performed in localized, linear and surface setting, which clearly showing the presence of graphite locally, linearly and regionally. The presence of graphite on the surface is uneven due to the irregularity of the substrate surface used during coating.
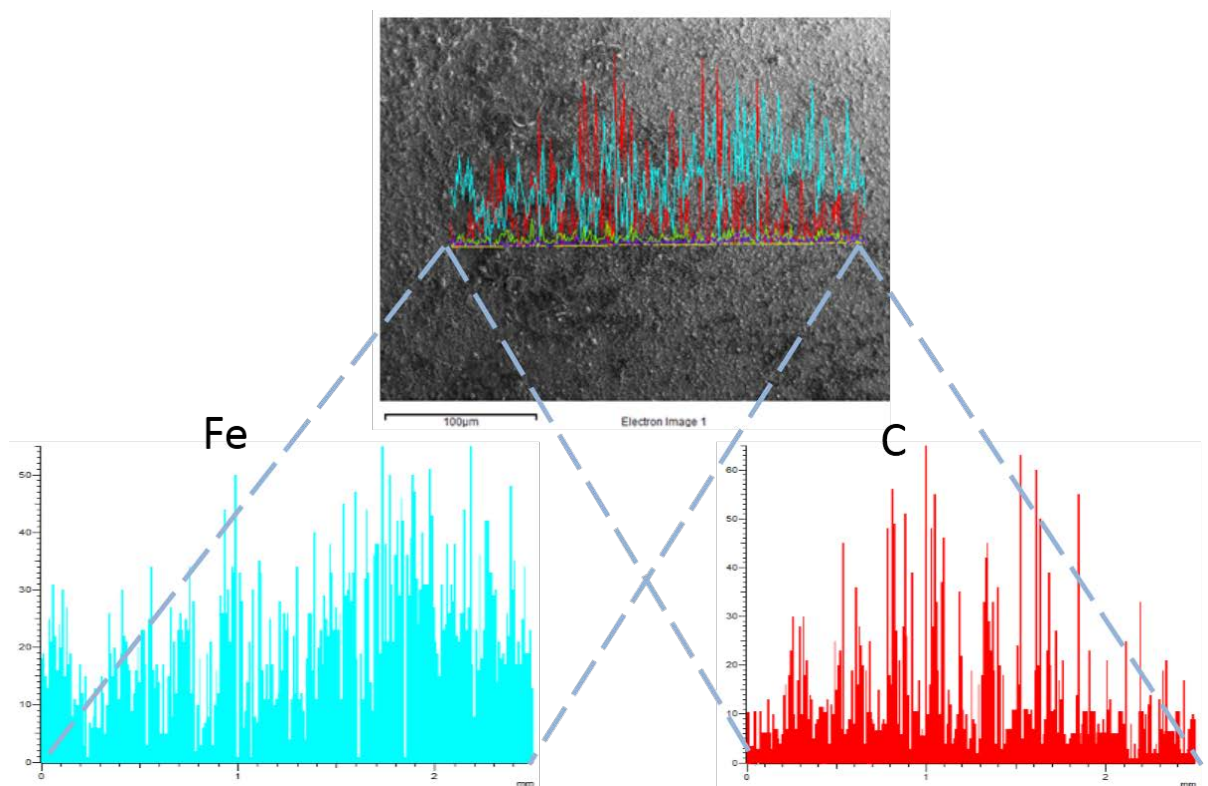
Fig 4-21 Chemical composition analysis of the coated surface using
EDS line scan; showing uniform distribution of carbon

4.4.3 XRD Analysis of coated sample

XRD analysis was carried out on the coated sample before and after heat treatment. Fig 4-23 shows the XRD pattern of components used in coating such as GNPs, polymer TOAB, uncoated sample i.e. flat cylinder block coupon and the coated sample after heat treatment. From Fig 4-23 it can be observed that the polymer TOAB peaks disappear in heat treated coated sample, which is due to high temperature thermal exposure, where the polymer escape out in the form of gas. These TOAB particles are acting as transfer agent for GNPs from electrochemical solution to the surface of substrate to be coated during electrochemical reaction.
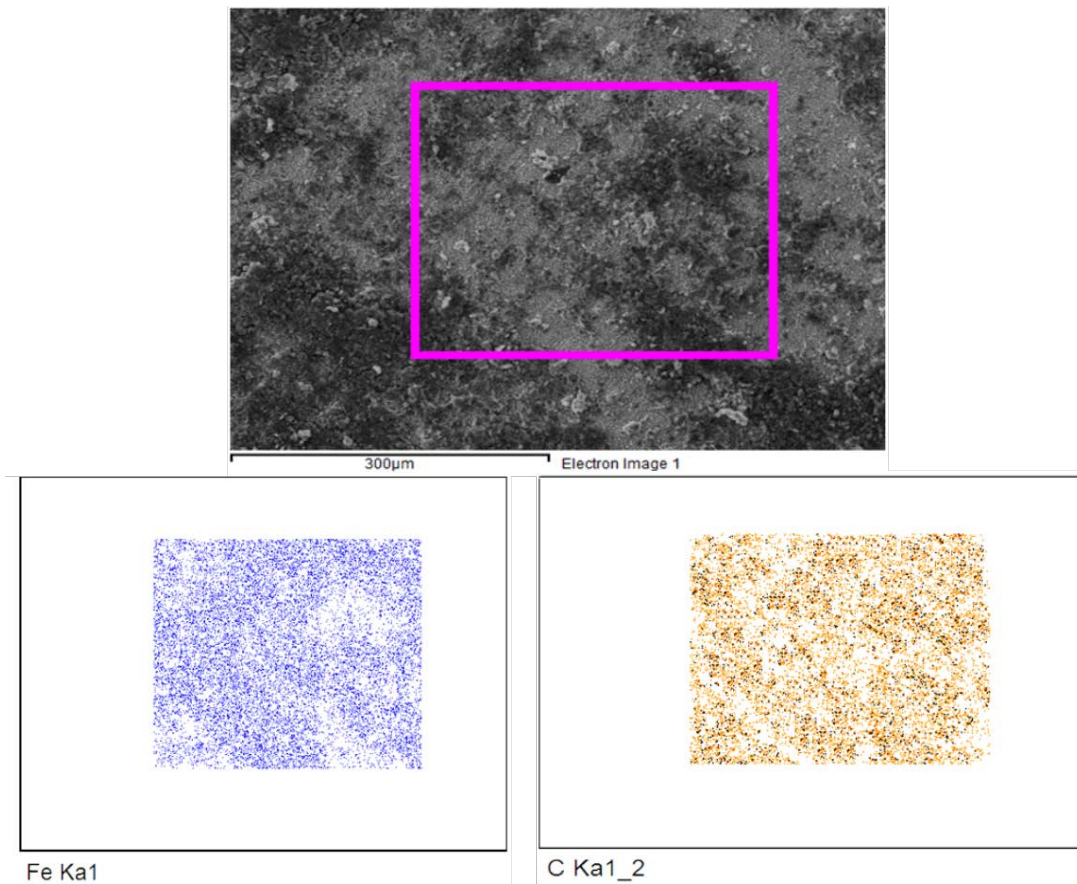
Fig 4-22 Chemical composition analysis of the coated surface using EDS area scan; showing uniform distribution of carbon
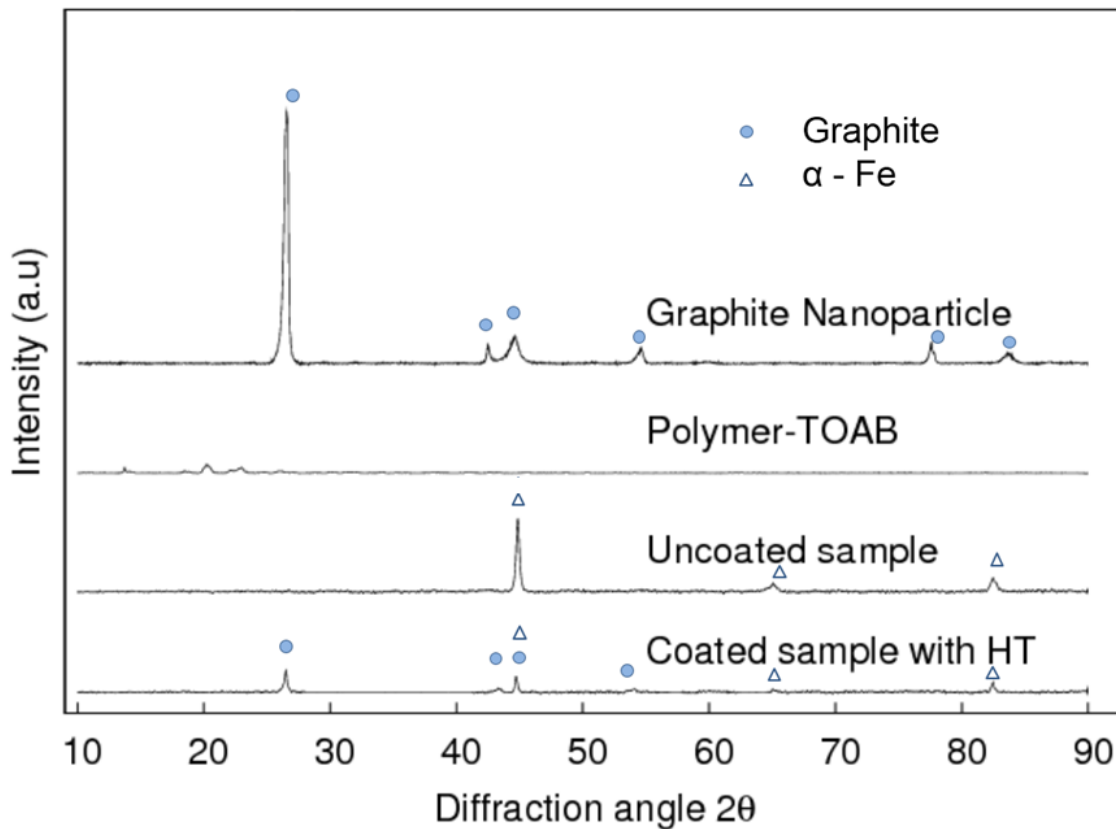
Fig 4-23 XRD pattern of GNP, polymer TOAB, cylinder block coupon and coated sample; the coated sample showing presence of GNPs on its surface even after heat treatment

From XRD peak pattern shown in Fig 4-23, it can be observed that for GNPs the peaks are very sharp and with high intensity confirming crystallinity. For uncoated sample there are three major XRD peaks which correspond to (110), (200) and (211) plane of iron. From Fig 4-23 it can be seen that the XRD peaks for coated samples are suppressed but significantly showing the presence of graphite and iron. So finally it can be concluded that the GNPs are present on the coated surface even after heat treatment.

4.4.4 Surface roughness of the samples

The surface roughness of all the samples was investigated before and after coating to check the variation in surface condition. The surface roughness was measured using Mutitoyo Surftest SJ-400. The surface roughness of various engine block coupon samples are tabulated in Table 4-7. And the surface profile of engine block coupon and coated engine block coupon and oil cleaned coated engine block coupon is shown in Fig 4-24, Fig 4-25 and Fig 4-26 respectively. The average roughness for engine block coupon was found to be 0.63 µm while the laboratory prepared sample with flat finished surface polished using various grades of emery sheet to attain the similar surface roughness of the sample was found to have 0.61 µm average surface roughness, which is in good agreement with the engine block average surface roughness value. This is done to counter the effect of surface morphology on coating process.

Table 4-7 Surface roughness of engine block samples

Sl.	Sample	Average Surface roughness (µm)	Standard deviation
1	Engine block coupon	0.63	0.01
2	Flat polished coupon analogous to engine block surface	0.61	0.01
3	Coated engine block coupon	0.97	0.01
4	Coated engine block coupon cleaned with engine oil	0.21	0.02
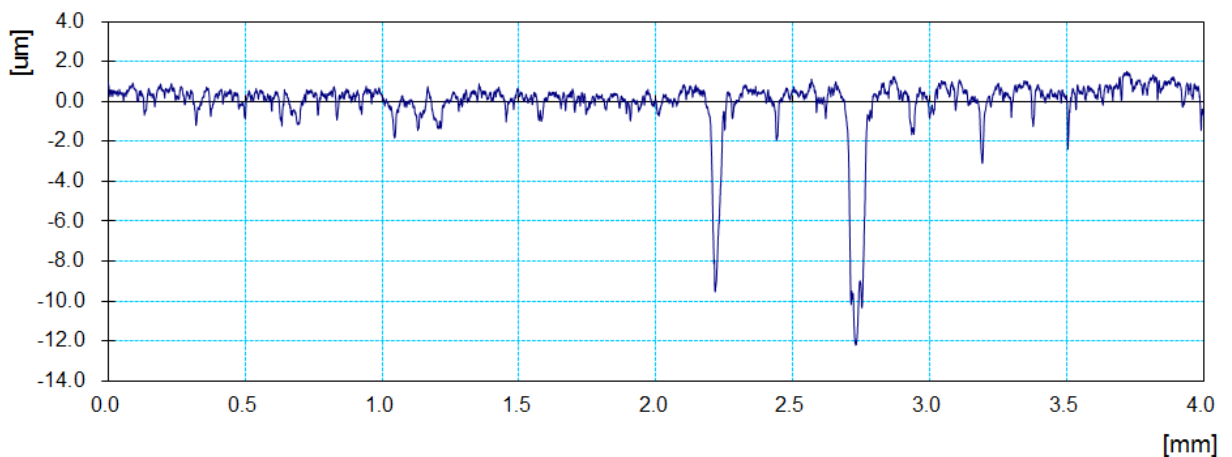
Fig 4-24 Measured profile of the engine block coupon surface (Average Ra = 0.63 µm)
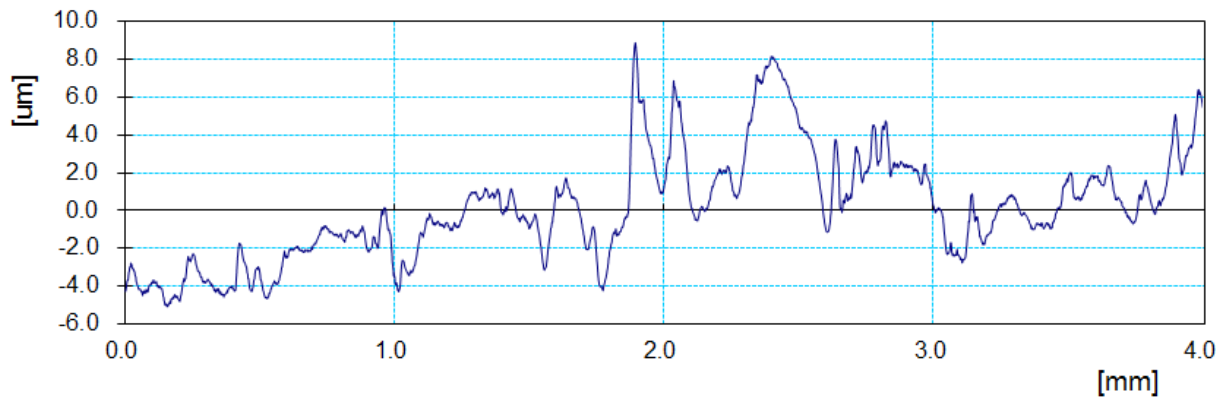
Fig 4-25 Measured profile of flat coated engine block coupon surface (Average Ra = 0.97 μm)
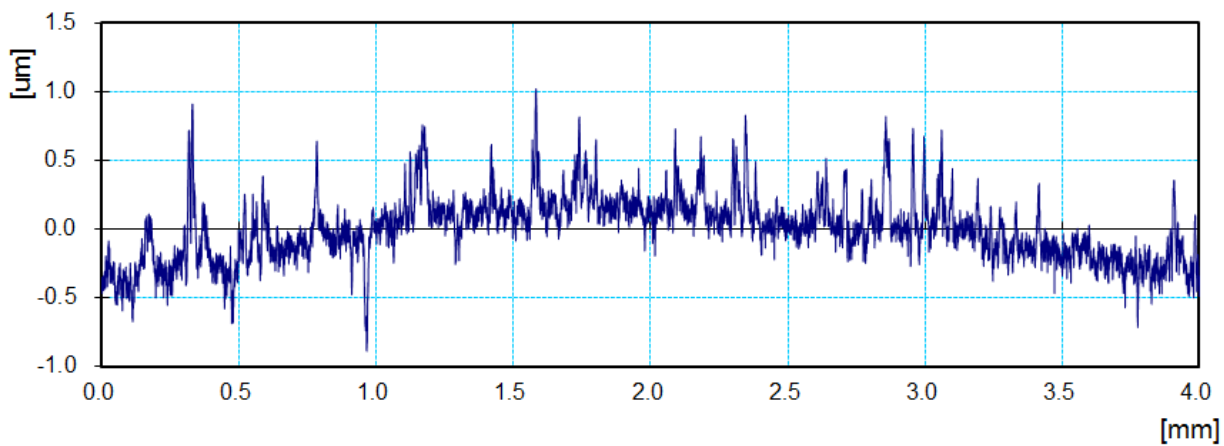
Fig 4-26 Measured profile of the engine oil cleaned surface
(flat coated engine block coupon have average Ra = 0.21 μm)

The flat polished coupon sample with roughness similar to the engine block surface was coated and later heat treated. The heat treated sample surface roughness was measured and found to be ~0.97 μm, which shows that the coating process increases the surface roughness of the sample. After cleaning using engine oil the average surface roughness was found to be 0.21 μm. This is because the extra GNPs layer and foreign material which was deposited on the surface during coating was wiped out due to loose bonding between layers or particles. This extra deposition of particles and foreign materials are the cause of increased surface roughness of the coated sample.

4.4.5 Hardness measurement

The hardness measurement performed with VEP-WPM Leipzig Brinell hardness testing machine. Brinell hardness testing is used for engine cylinder coupons hardness measurement. The hardness value of various engine block coupon samples are given in Table 4-8. From observation it can be observed that the hardness of coated engine block sample is ~13.5 % higher than that of uncoated engine block sample. The improvement in hardness may be contributed due to the diffusion of carbon atom into the cast iron substrate and reinforcement effect of bonded

graphite nanoparticles with the substrate. Another study was carried out with Nanovea mechanical tester model-M1, where a pyramidal diamond Berkovich probe with a 200 µm tip radius was used for indentation in both the cases of engine block.

Table 4-8 Surface hardness of engine block samples

Sl.	Sample	Average hardness (BHN)	Standard deviation
1	Engine block coupon	----	----
2	Flat polished sample	133	2
3	Coated engine block coupon (flat) heat treated and cleaned with engine oil	151	4

Fig 4-27 shows the depth load curve for uncoated engine block coupon and coated engine block coupon. And from that it can be observed that the depth of penetration for coated sample is less compared to uncoated sample with the same loading condition of 1 N. The rise in hardness of the coated sample could be due to two phenomena, namely, interfacial bonding between GNPs and iron matrix of cast iron substrate, and the diffusion of some carbon atoms into the iron matrix of cast iron substrate.
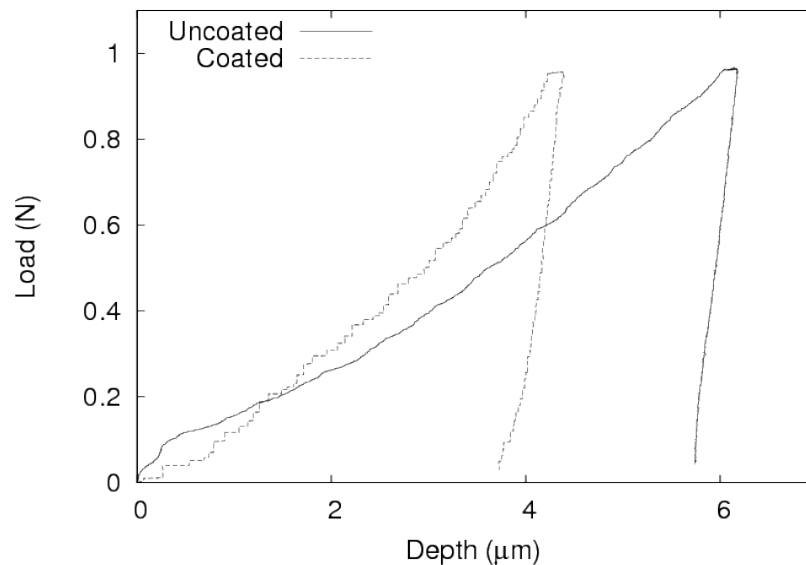
Fig 4-27 Depth load curve of uncoated and coated coupons of engine block; showing less depth of penetration for coated sample with same loading condition of 1 N

4.4.6 Coefficient of friction analysis

Surface friction coefficient is a significant parameter for deciding friction force. Its higher value raises the friction force. In present investigation, scratch test was performed with Nanovea mechanical tester model-M1 machine to find the coefficient of friction of the uncoated and coated samples. Vickers 200 spherical diamond indenter with tip radius of 20 µm used for scratch test. The scratch length of 2 mm chosen for conducting the scratch test with the travel speed of 0.5 mm/min for both the conditions, uncoated samples (properly polished without scratches) and

coated samples. The scratch test is repeated several times to estimate the value of coefficient of friction for each sample. Fig 4-28 shows the scratch test mark on the uncoated and coated samples under investigation, while Fig 4-29 shows the frictional coefficient variation along scratch length of both uncoated and coated sample.
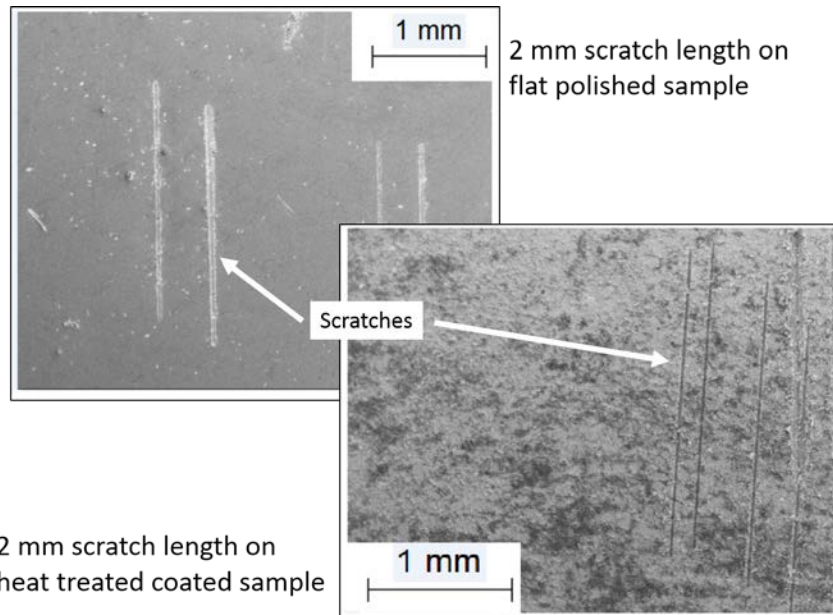
Fig 4-28 Showing scratch of 2 mm length made during scratch test on flat polished sample and coated sample
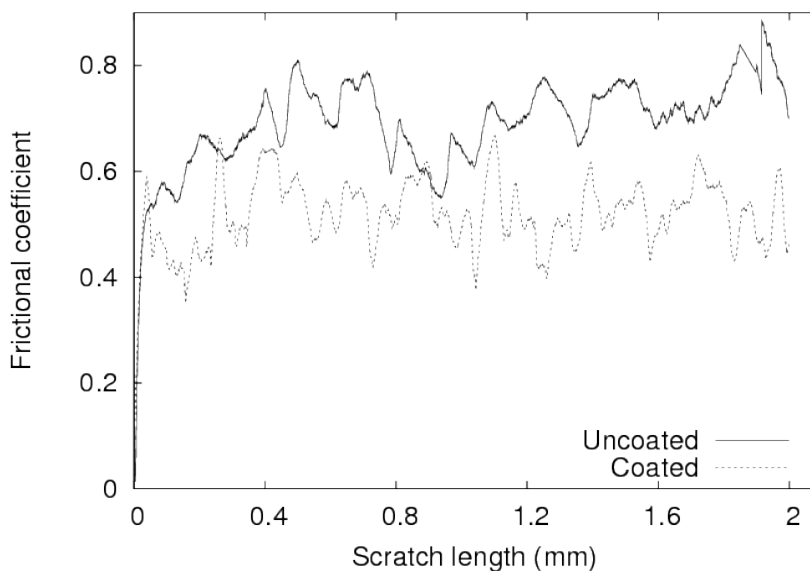
Fig 4-29 Figure showing variation of friction coefficient value with respect to scratch length of uncoated and coated coupons of engine block

From Fig 4-29 it can also be observed that the coefficient of friction in case of uncoated sample always found to be higher in comparison to coated sample. The average value of coefficient of friction is provided in Table 4-9. The scratch test performed on the uncoated sample (perfectly polished) and coated sample (initially sample had similar surface roughness value as of engine cylinder) to show the effect of coating.

Based on the scratch test analysis it is confirmed that the coated surface have ~38 % less coefficient of friction compared to the uncoated flat surface. But it is surmised that the engine cylinder surface having higher coefficient of friction as compared to uncoated flat sample due to higher surface roughness of the engine cylinder. Hence the difference in coefficient of friction between engine block samples (uncoated and coated) can be greater that ~38 %.

Table 4-9 Coefficient of friction (COF) value of different engine block samples

Sl.	Sample	Average COF	Standard deviation
1	Flat polished coupon of engine block	0.71	0.04
2	Coated engine block coupon (flat) heat treated and dry cleaned	0.44	0.03

4.4.7 Coating thickness

As the coating is of uneven thickness it is challenging to measure the thickness. And due to characterization limitation in examining the nanomaterials coating layer of bulk sample, in present investigation, EDS analysis was carried out to investigate the GNPs coating on the cast iron substrate. Multiple straight line elemental scanning performed through the substrate and coating. The EDS is a qualitative analysis and these scans only highlighting the variance in coating thickness. The sample EDS analysis is shown in Fig 4-30, while and inclined line scan across the substrate and coating also shown in Fig 4-31 which also confirms the coating.
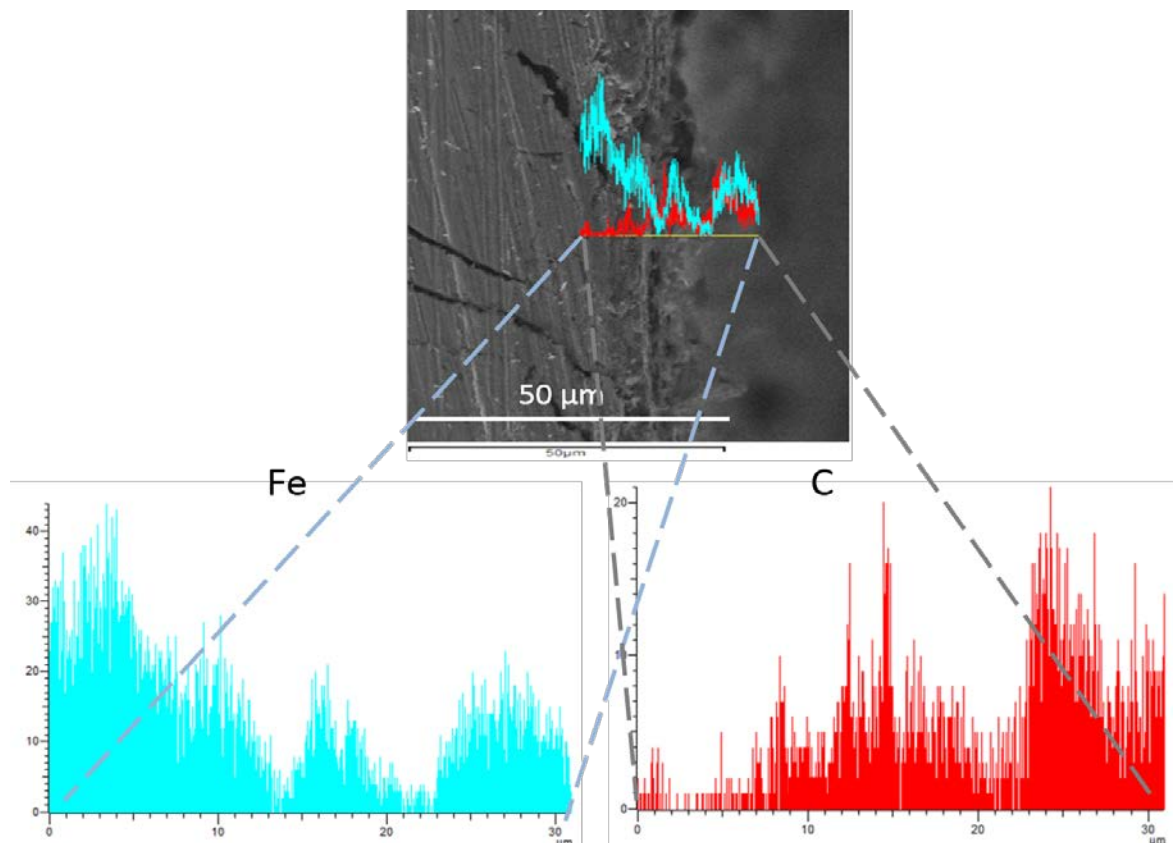
Fig 4-30 EDS line scan showing the coating chemical composition of the flat coated coupon
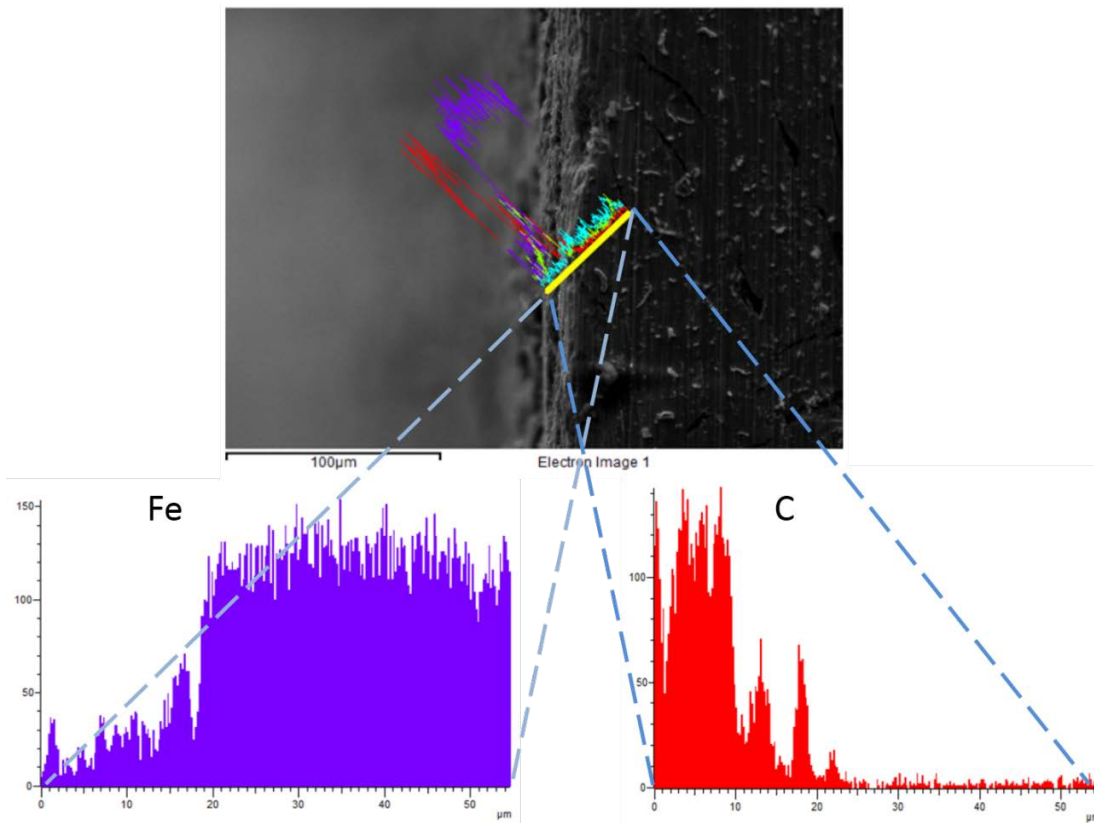
Fig 4-31 EDS angular line scan of the flat coated coupon
showing coating chemical composition
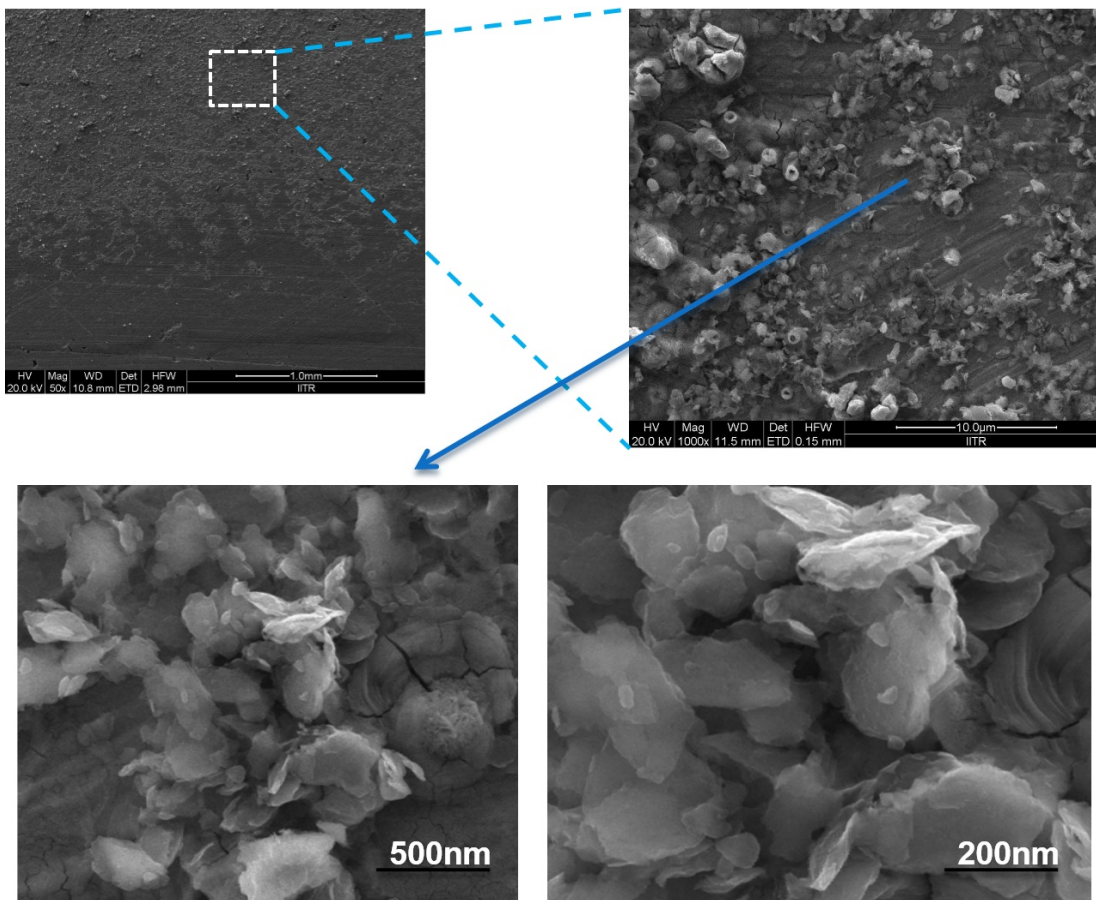
Microstructure expanded view

Fig 4-32 SEM image showing presence of GNPs on the coated surface

The elemental analysis plot of iron and carbon shown in Fig 4-30 and Fig 4-31 help in confirming the presence of GNPs coating as well as its thickness. From EDS analysis, it can be observed that, there are patches of uniform 'C' element distribution on the surface of the cast iron substrate, which confirms the presence of graphite nanoparticles. From the EDS analysis, the average coating thickness of the coated sample was found to be ~5.6 μm. Fig 4-32 shows the presence of coated graphite nanoparticles on the coated surface and the GNPs presence is significant on coated surface which can be seen in enlarged view of the coating.

4.5 Coating of graphite nanoparticles on engine block

Particle size distribution in electrolyte solution may influence the coating as the fine nanoparticle distribution is homogeneous throughout solution but the coarse nanoparticles (>> 50 nm) tend to settle at the bottom. The coating with fine nanoparticles will yield better results compared to coarse nanoparticles coating as the layer formation is better with fine nanoparticles.

After full scale confirmation of the laboratory scale coating and its characterization, the coating was performed on the engine cylinder/block. The size of electrode depends on sample size. The engine block size is very large compared to the test specimens, so to maintain the coating parameters, everything is scaled with respect to the original sample size. There are many options that exist for counter electrode from platinum to copper, but in terms of cost and availability, copper is the best option. Fig 4-33 shows the photograph of engine block used in present investigation (which is acting as working electrode) and original copper hollow cylinder (customised to act as counter electrode). Based on several hit and trial runs of engine block coating it was found that the coating is not proper throughout the engine cylinder surface, so the counter electrode i.e. copper hollow cylinder has been modified as shown as pair B in Fig 4-33 to allow transport through the electrode.
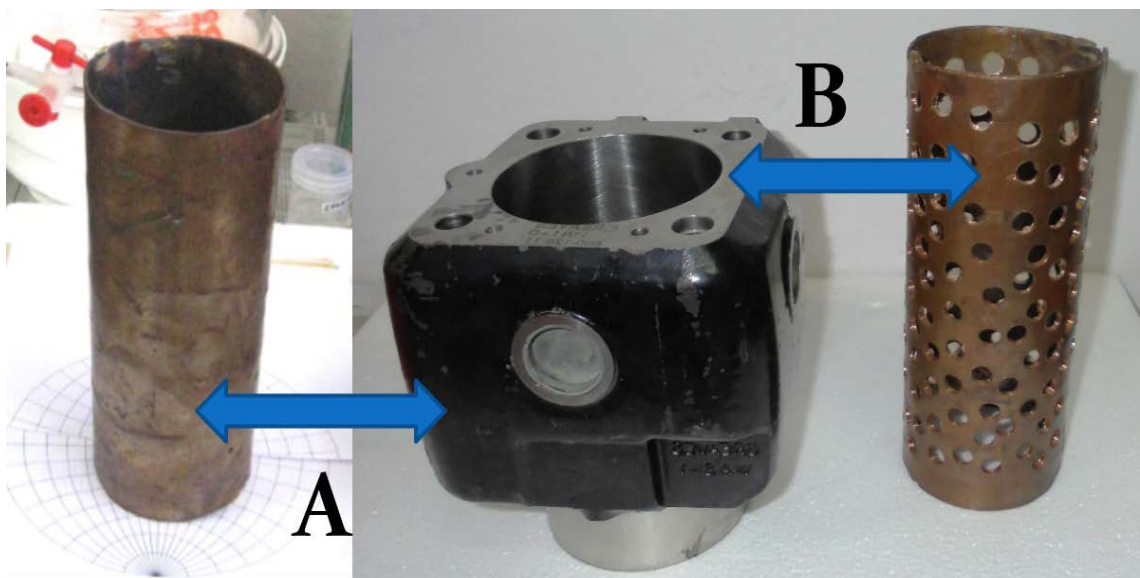
Fig 4-33 Figure showing experimental pairs of work and counter electrodes used in electrophoretic coating; pair 'B' found better for engine cylinder coating

Fig 4-34 shows the sketch and real scale arrangement of the experimental setup used for engine block coating. The chemical reaction chamber and the counter electrode were customised for best results. The distance between working electrode and counter electrode was maintained at 5 mm throughout. A wire was tied to the working electrode for potential supply terminal, as the working electrode completely submerged in the electrochemical solution at approximately 2 cm depth from top surface of the solution for better coating results as pointed out during laboratory scale coating study. The coating experiment on engine cylinder was done along the same lines of the coupon sample coating as shown in Fig 4-35. The experiment continued for 10 min before the DC supply was stopped. The variation of the display voltage was monitored and found to be 0.1 V maximum.
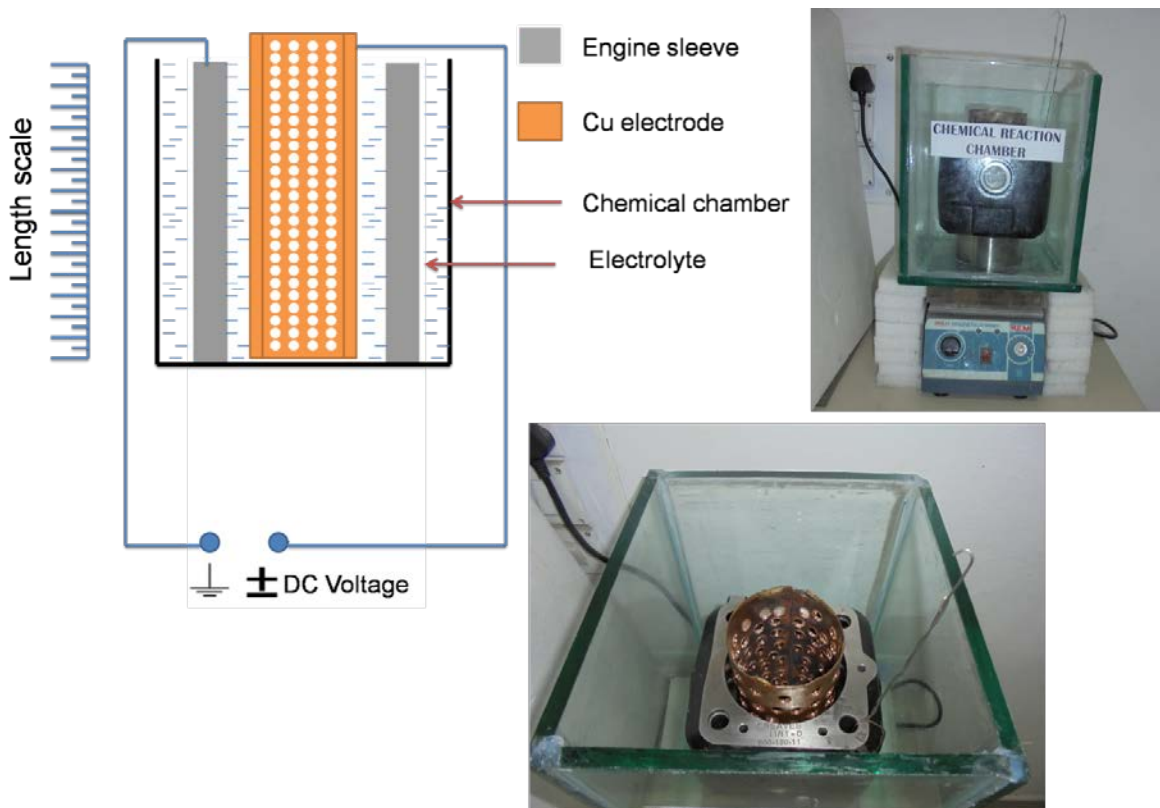
Fig 4-34 Experimental set-up used to coat engine block (sketch with photograph)

The coated engine block was shifted to the muffle furnace chamber with inert atmosphere for heat treatment. The details of heat treatment setup used here are given in section 3.2.3. The heat treatment cycle opted in the present investigation is furnished in section 4.3. After completion of heat treatment the coated engine block was cleaned with engine oil.

4.6 Comparative study of the uncoated and coated engine block

Before proper testing of the engine block, initially the running in operation was performed for 40 hours with five time repetition of 8 hrs continuous engine running period at low speed without load in the real engine test rig whose details are given in section 3.4.

Fig 4-35 Photograph of real time coating experiment of engine block; showing DC supply (~45 V) connection to work and counter electrode in electrochemical cell

Later the performance of engine was tested against selected experimental settings and discussed in the next chapter. Further in this chapter, coated engine block after 800 hrs usage is characterized to understand the effect of testing on the coating layer. Fig 4-36 shows the uncoated and coated engine blocks before and after undergoing testing. From Fig 4-36, it can be observed in both uncoated and coated engine cylinders that multiple circumferential belts/zones are present in inner surface of the engine cylinders from top surface. These circumferential zones corresponds to combustion deposit zone, maximum wear zone and normal engine cylinder inner surface when considered form top surface. Out of all zones, maximum wear zone is an important zone for study in present investigation. This is the zone where piston ring reverses from top dead centre to bottom dead centre during crank revolution. In case of uncoated engine, the cross hatch markings are missing in maximum wear zone as compared to the middle portion of the engine cylinder. But it case of coated engine cylinder there is minor difference in the maximum wear zone and middle portion of the engine cylinder.

Fig 4-36 Pictures of engine blocks before and after use; uncoated (top right and left) and coated (bottom right and left)

4.7 Coating status after use

After completion of experimentation on coated engine block it was sectioned for coating thickness analysis- to confirm the presence of graphite nanoparticles on the surface of cast iron engine cylinder after use. Fig 4-37 shows the image of sectioned piece of used coated engine block and Fig 4-38 shows the sample EDS elemental analysis of iron and carbon for analysing coating thickness of coated sample after use. From several observations it was found that the coating thickness after engine testing vary between 1-2 µm with average value of 1.7 µm.
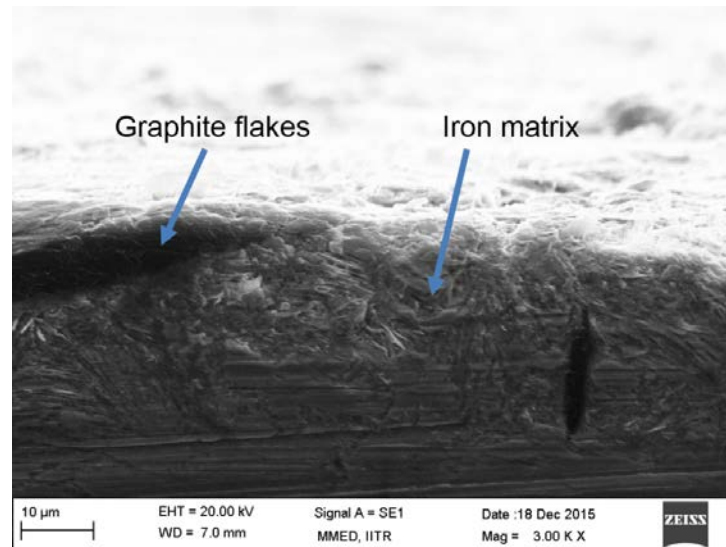
Fig 4-37 Showing SEM image of used coated engine block coupon
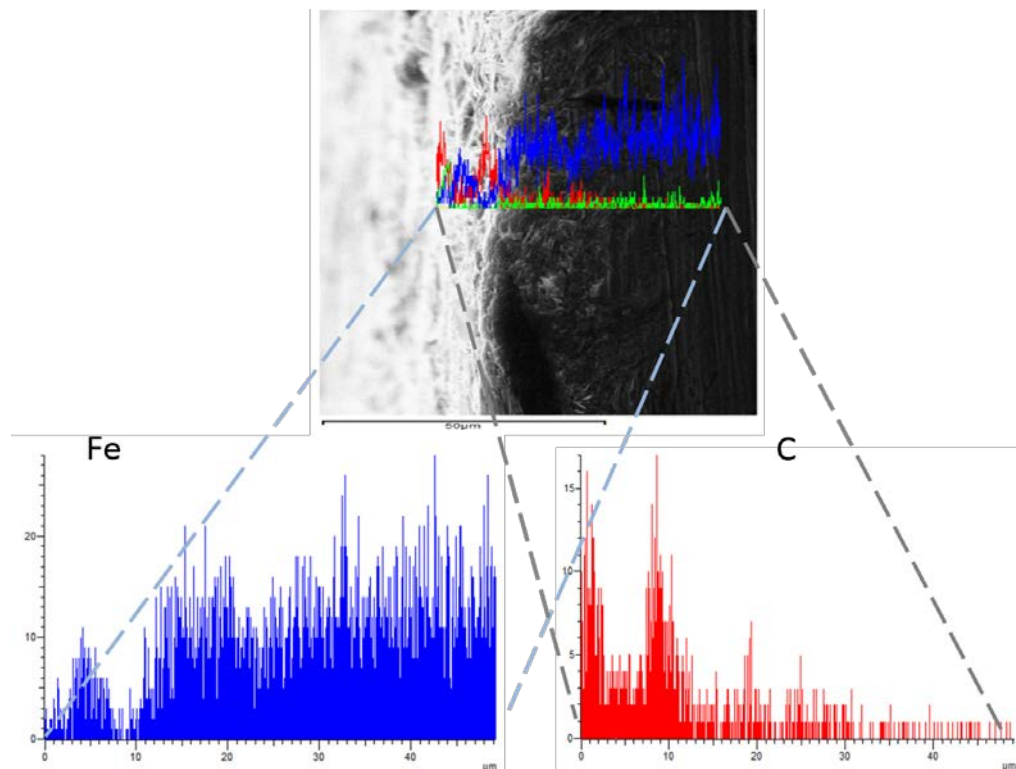
Fig 4-38 Showing coating chemical composition of the used coated engine block coupon

The difference in coating thickness of coated sample before use and the coated engine cylinder sample after use is listed in Table 4-10. With these facts, it can be concluded that the GNPs coating thickness reduces on use and it is stable at ~1.7 µm in present investigation. As the loosely or unbonded coating layers are wiped out during initial engine run itself. But the coated GNPs which are bonded firmly with substrate are retained till 800 hrs of rigorous engine testing.

Table 4-10 Coating thickness of different engine block samples

Sl.	Sample	Average thickness (µm)	Standard deviation
1	Coated engine block coupon (flat - heat treated)	5.6	0.4
2	Coated engine block coupon (after use)	1.7	0.2

SEM samples were prepared from top, middle and bottom portion of used coated engine block as shown in Fig 4-39, and same was used for the surface chemical composition analysis. The microscopic view of different portion of used coated engine cylinder is shown in Fig 4-39. From which it was observed that, the surface morphology of used coated engine cylinder is changed. The trenches are filled and the surface is appearing dull. And to resolve the differences in surface characteristic of used uncoated and coated engine cylinder, further EDS, XRD and surface profile analysis is carried out.

EDS analysis was performed to know the surface chemical composition of used uncoated and coated engine block. The EDS analysis primarily done for iron and carbon elements distribution on the surface of the considered portions of coated engine cylinder and uncoated engine cylinder. The results of analysis are shown in Fig 4-40, Fig 4-41, Fig 4-42 and Fig 4-43 respectively.
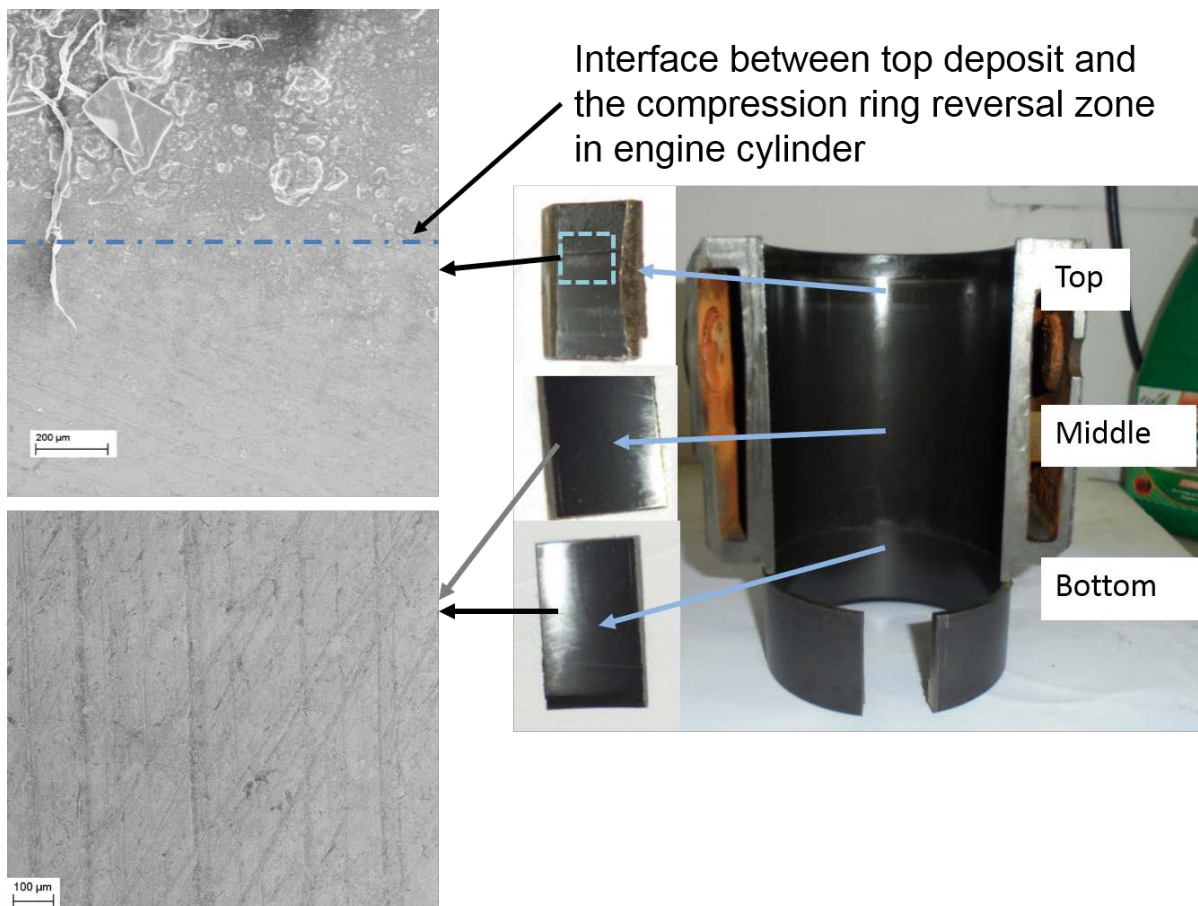
Fig 4-39 Coated engine block sampling zone after 800 hrs of use and their SEM images
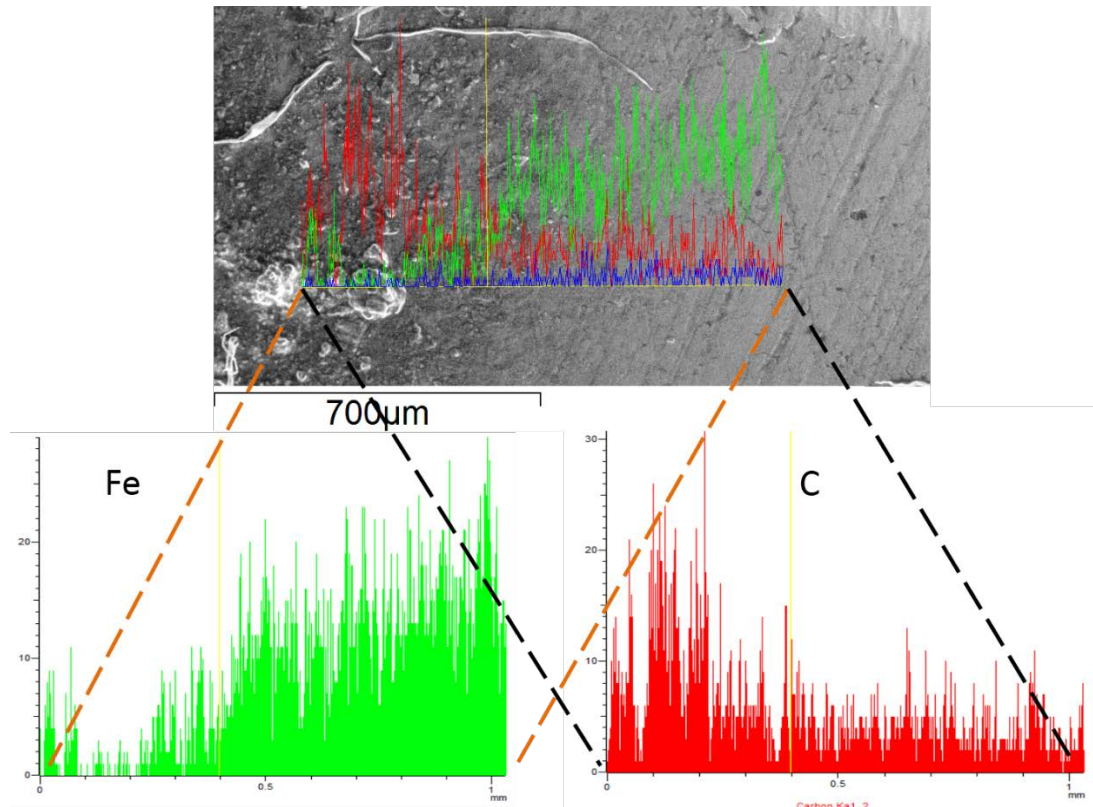
Fig 4-40 Chemical composition analysis of the coated engine block after 800 hrs of use (top portion) using EDS line scan; showing throughout distribution of carbon in maximum wear zone
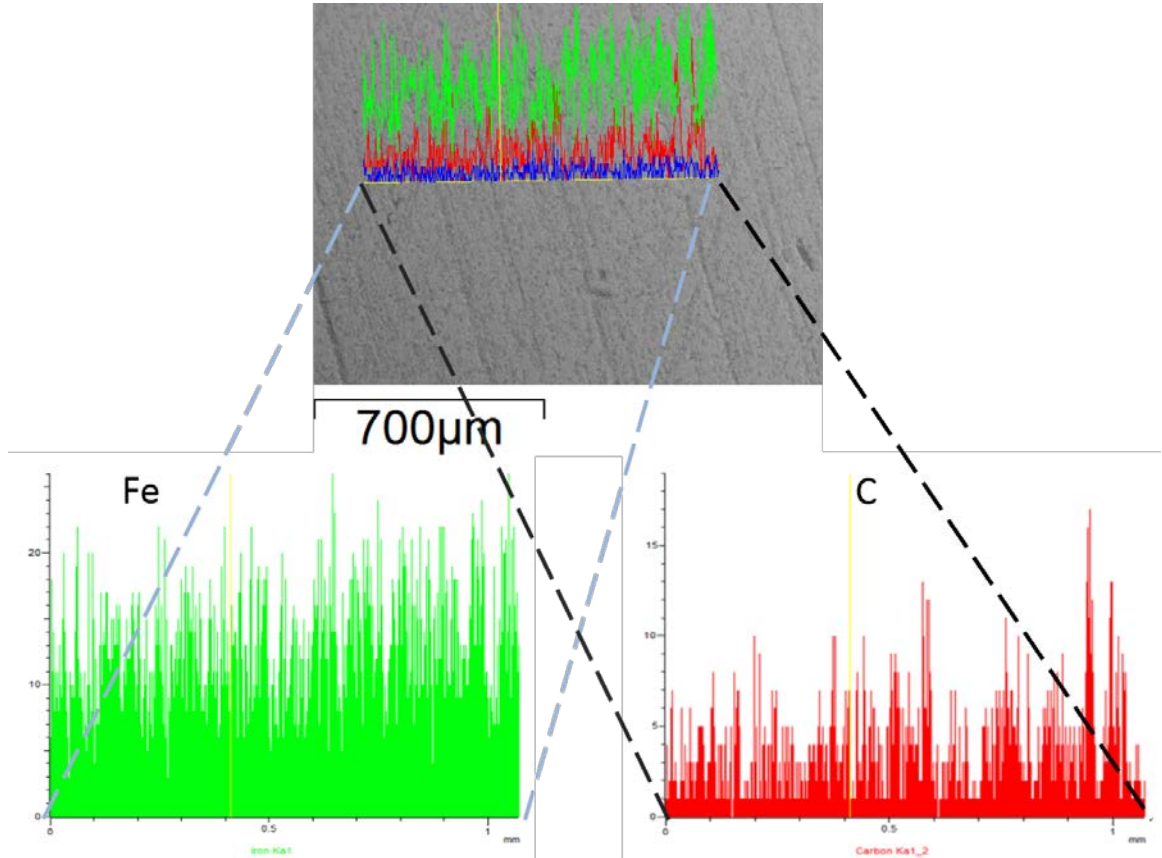
Fig 4-41 Chemical composition analysis of the coated engine block after 800 hrs of use (bottom portion) using EDS line scan; showing presence of carbon throughout
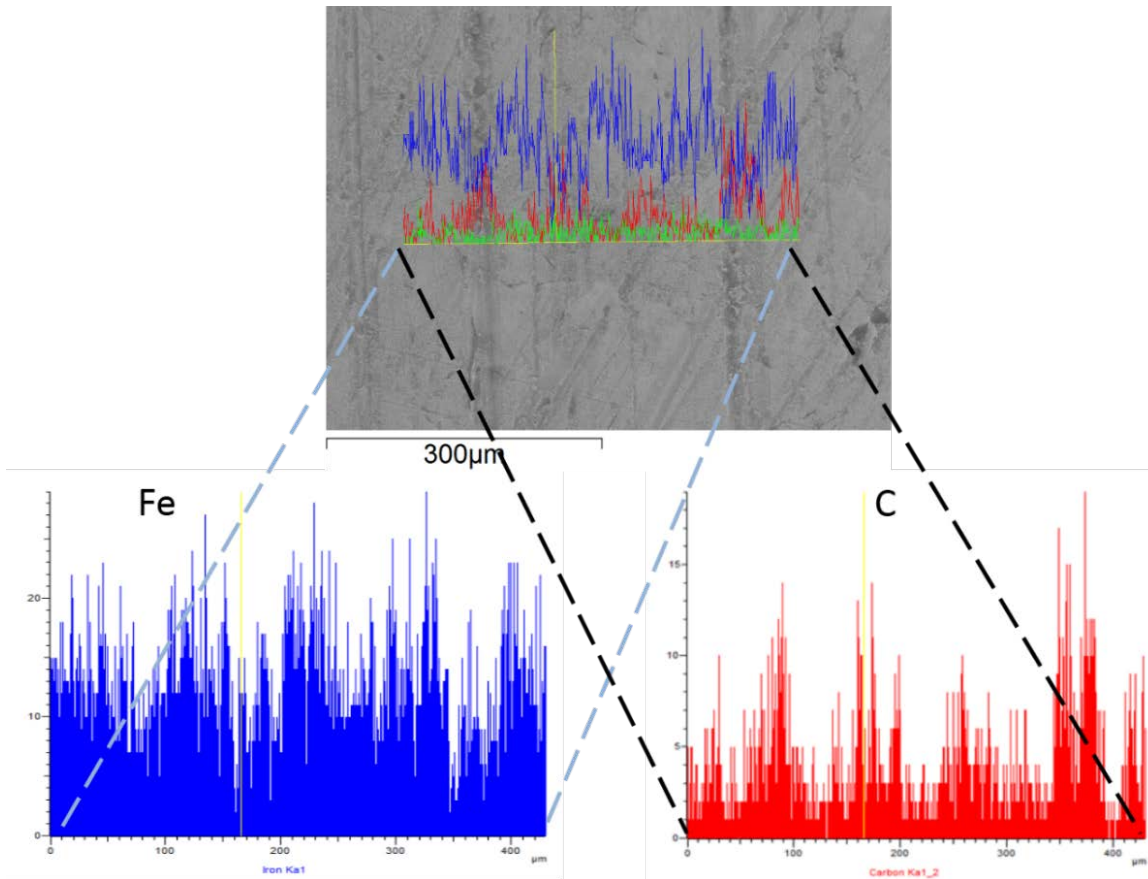
Fig 4-42 Chemical composition analysis of the coated engine block after 800 hrs of use (mid portion) using EDS line scan; showing presence of carbon throughout; with higher percentage in some places indicates the filling up of GNPs in trenches of engine cylinder surface
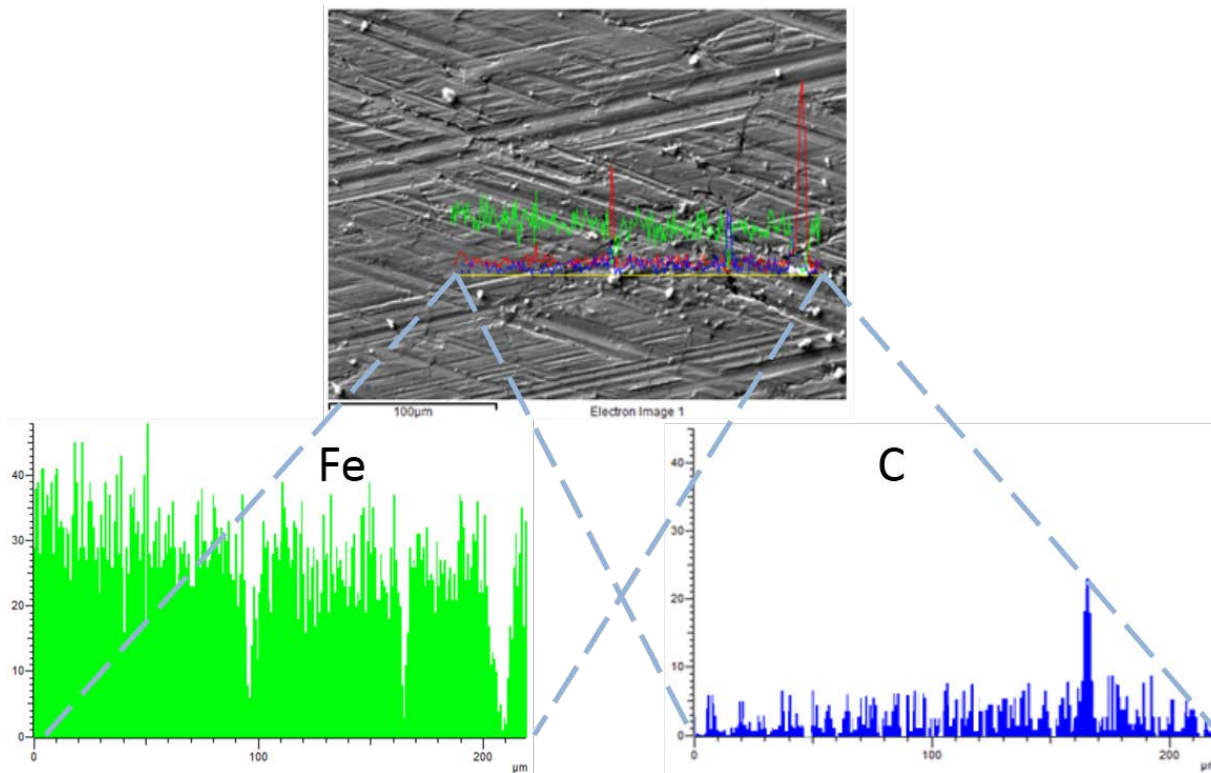
Fig 4-43 Chemical composition analysis of the uncoated engine block after 800 hrs of use (mid portion) using EDS line scan

From Fig 4-40, Fig 4-41 and Fig 4-42, it was observed that the presence of carbon is significant on the surface of used coated engine cylinder. It is the indication of the presence of coated graphite nanoparticles. The carbon element distribution in used uncoated engine cylinder is shown in Fig 4-43, and found to be less as compared to the used coated engine cylinder.

XRD analysis performed to differentiate the phases present on the surface of the used uncoated and coated engine cylinder. The results of analysis is shown Fig 4-44. From XRD plot it is confirmed that the graphite nanoparticles are retained on the surface of the engine block throughout. In case of used coated engine cylinder surface, the XRD peak for graphite is showing peak broadening, which may be contributed to the particle size reduction of the GNPs.
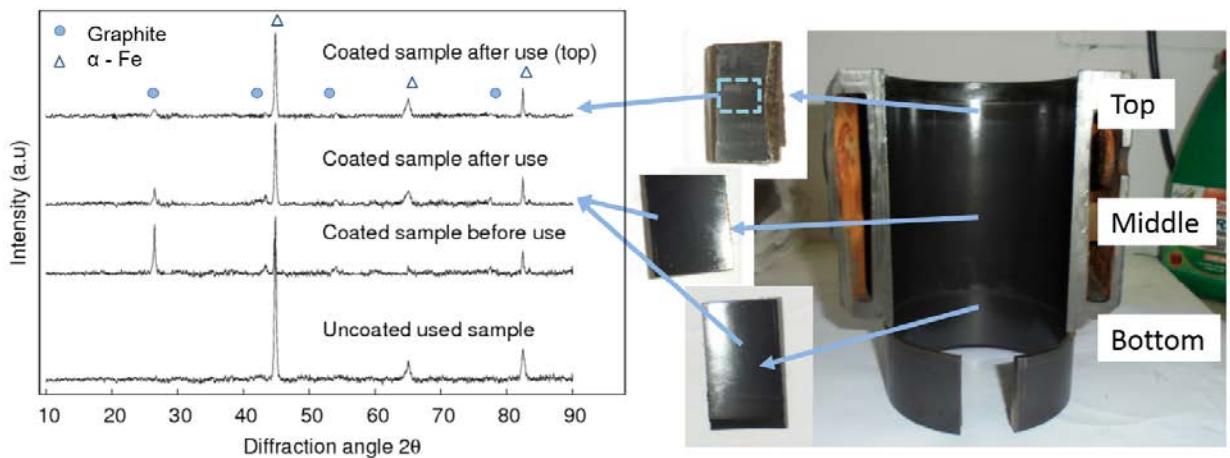
Fig 4-44 XRD pattern of the uncoated used sample and coated engine block samples before and after use; the presence of GNPs on the used coated engine block coupons is significant
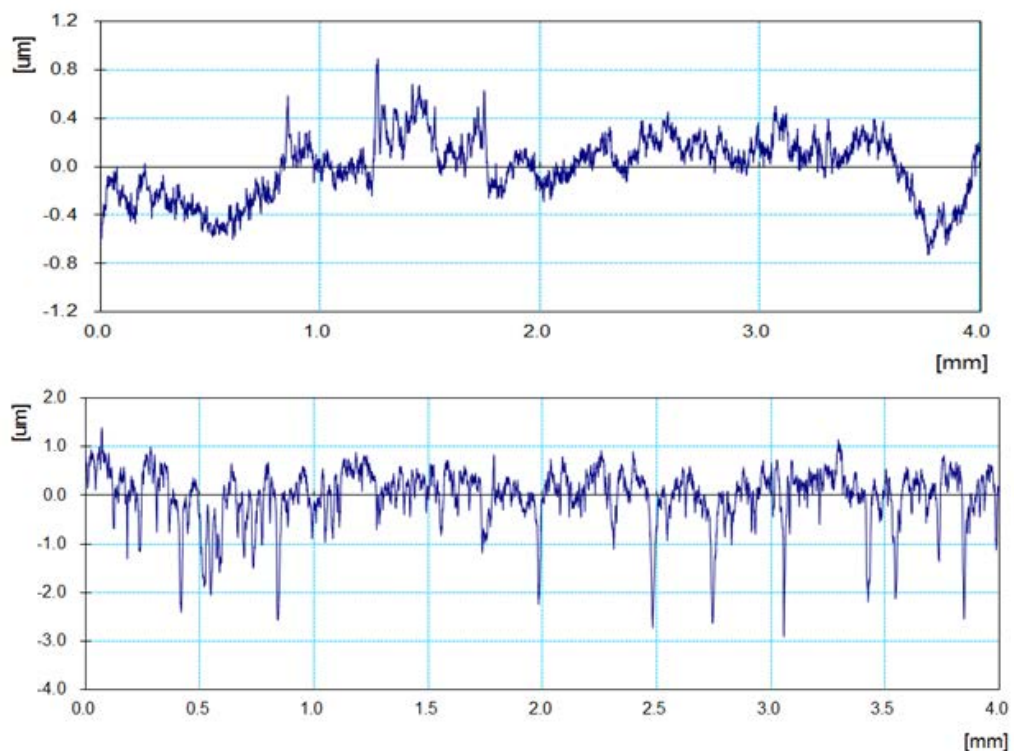
Fig 4-45 Surface profile of the coated (top) and uncoated (bottom) engine block after 800 hrs of use (Ra = 0.14 μm for coated; Ra = 0.42 μm for uncoated)

The measurement of surface roughness performed for middle portion of the used uncoated and coated engine block to check the variation in surface roughness value before and after engine testing. The general surface profile of uncoated and coated block sample after 800 hrs of use is shown in Fig 4-45. The surface roughness value of coated engine found to be ~0.14 µm and for uncoated engine is ~0.42 µm.

4.7.1 Graphite nanoparticles in coating after use

With respect to all the above results, it is concluded that the coated GNPs still exist on the engine cylinder surface after 800 hrs of engine testing. The effect of GNPs presence in coating is highlighted by several characterization techniques, such as EDS analysis for the presence of 'C' element, XRD analysis for examining GNPs phase on the coated surface after engine testing and surface profile measurement for examining the difference in surface roughness due to GNPs coating.

From Fig 4-42 it can be observed that the trenches in coated engine block act as a GNPs deposition zone, where carbon presence is significant. From XRD analysis shown in Fig 4-44 it is clear that the graphite nanoparticles remain in the engine cylinder wall even after 800 hrs of engine testing. The presence of graphite nano particles throughout engine cylinder was confirmed by EDS analysis as shown in Fig 4-40, Fig 4-41 and Fig 4-42. Nevertheless, the coating thickness after engine testing was reduced compare to the original coating thickness.

CHAPTER 5

Application of Nano-graphite Coating in IC Engine

In the previous chapter, coating of engine cylinder was discussed and it was observed that coating followed by heat treatment have significant effect on hardness, surface roughness and coefficient of friction. Earlier, Dahotre et al. [45] raised the issue of nanomaterials coating for engine application. But no detailed work on the effect of nanomaterials coated engine cylinder on the engine performance was reported. Hence in the present investigation, nano-graphite coated engine cylinder was tested under various conditions. The engine performance parameters of the coated engine cylinder were evaluated and compared with uncoated engine cylinder which was also tested under similar conditions. Further, optimisation of engine performance parameter was undertaken using Taguchi and RSM-GA (Response Surface Methodology – Genetic Algorithm) methods for both the conditions (coated and uncoated engine cylinder). These methods used to uncover the effect of each engine setting parameters on performance parameters and to establish the best trade-off between all considered engine performance parameters.

The real time application of nanomaterials coating in diesel engine is considered here for study. Experimentations performed to check the effect of coating on the performance of the considered diesel engine. The experimental results of the real time application is shown and discussed in this chapter. The engine considered in the present investigation is Greaves Cotton make model "G600 WII". From the market survey it was found that the selected or similar engine model was used in all the three wheelers and non-passenger automobiles like pickup vans and small transportation vehicles. In Fig 5-1 (left image), it can be seen that when the engine cylinder is having good surface finish then there is no gap present for combustion gas to escape.
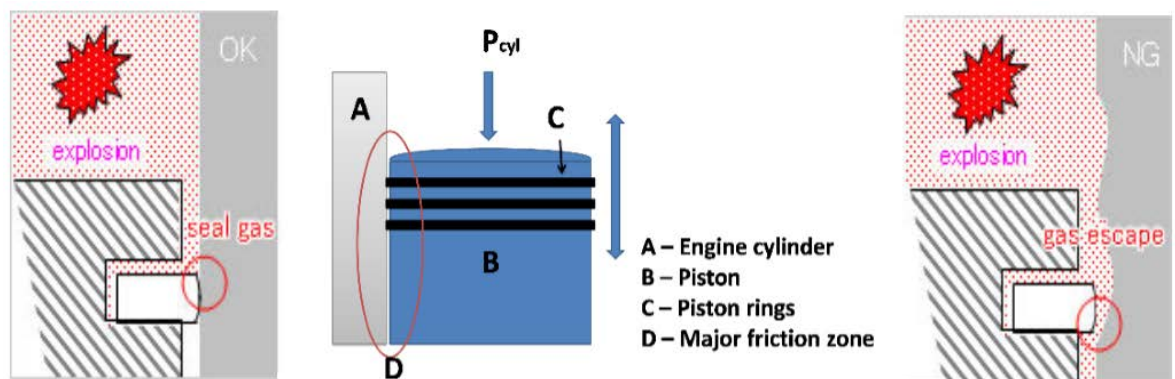
Fig 5-1 Figure depicting the piston assembly interactions with engine cylinder

If combustion gas escapes during operation, then there is high chance of reduction in the efficiency of the engine. If the surface of the cylinder liner is abrupt as shown in Fig 5-1 (right image), combustion gas can escape very easily. But it is not possible to make the engine cylinder

inner surface exactly flat, practically the engine cylinders are having machined finish, and then used in automobile industry. The inner surface of the engine cylinder is shown in Fig 5-2, in which we can see many scratch marks, which were produced during their machining process.
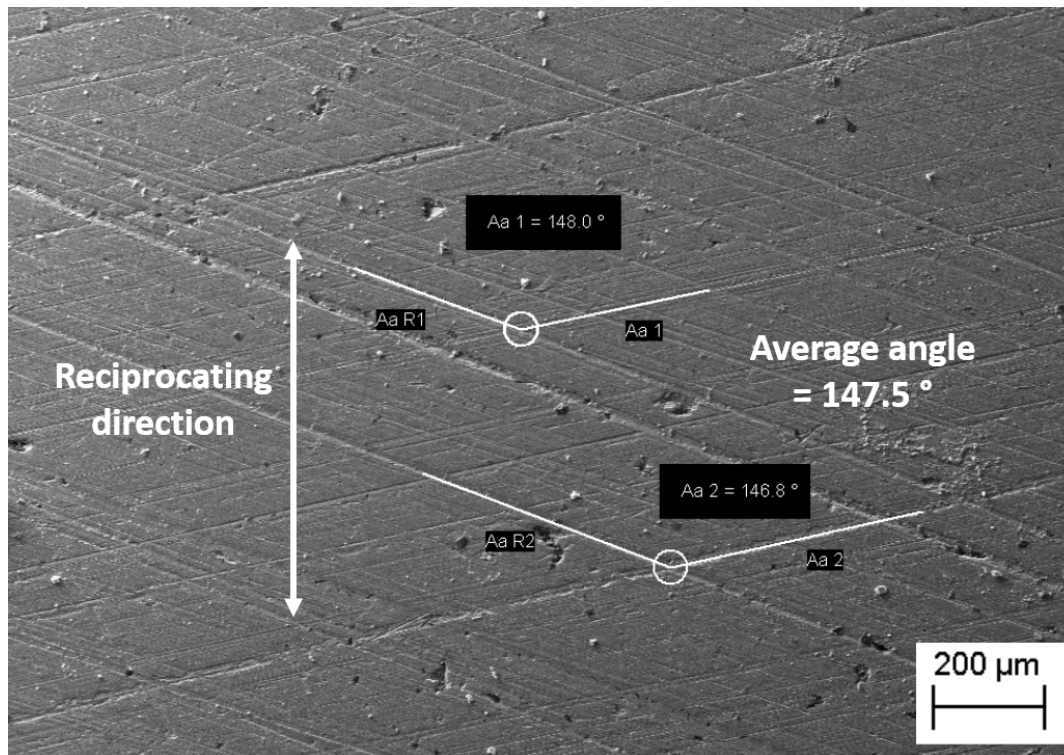
Fig 5-2 Inner surface profile of the newly purchased engine cylinder

The details of inner surface of the engine cylinder is shown in Fig 5-2. This shows the surface profile microstructure as well as the interaction direction between piston assembly and engine cylinder. The long scratches on the inner surface of engine block as shown in Fig 5-2 can act as filling site for nanoparticles and even it may act as accumulation drains for GNPs while coating. In case of engine cylinder failure, usually cylinder damages occurred during functioning of IC engine. The main reason behind failure is the lack of lubrication and high friction between the mating parts during the engine cyclic process.

5.1 Engine coating

Coating of engine cylinder using GNPs made the base material out of direct contact with another body (piston assembly) during the engine operation. Which may lead to less wear of main engine components such as engine cylinder, piston and piston rings. Fig 5-3 shows the sketch of coating, if coating is perfect then no part of the base material should be exposed to surrounding atmosphere, which actually provide the hindrance to wear of the base material. After successful coating of graphite nanoparticles on diesel engine cylinder, it has to be tested for its effect on engine performance.
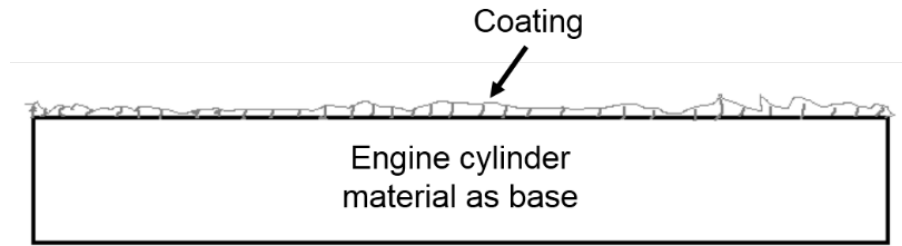
Fig 5-3 Sketch of coating showing uniform coverage of coating

5.2 Experimental design planning

The experiments were designed in two phases in such a manner that the layout of the engine behaviour can be understood mostly and effectively based on engine characteristics. The torque-speed characteristic curve of the engine considered in present investigation is shown in Fig 5-4. There are two test conditions selected for study, first testing of engine with uncoated engine block while in second case testing of engine with coated engine block.
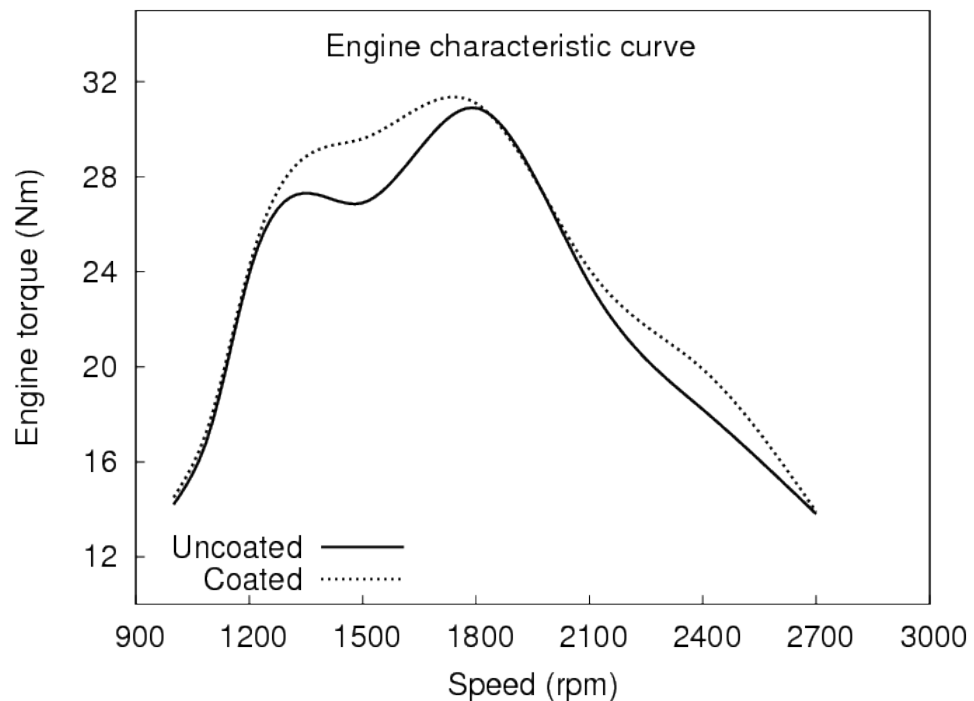
Fig 5-4 Engine characteristic curve of the considered small DI diesel engine in present study

The experiments were conducted in two phases, firstly (Phase-I) to check the engine performance at high speed limit and then at higher loading condition in Phase-II. As both the conditions can not be tested in a single experimental design, so the experiments are divided in two phases. The considered engine performance parameters in both the phases are friction power, brake specific fuel consumption (BSFC), mechanical efficiency, specific emissions (*sCO, sHC, sNO*) with respect to indicated power and smoke opacity.

5.2.1 Phase-I: Experimental design

Experimental design of Phase-I was planned to evaluate the engine performance at high speed limit of the engine. In the present investigation, preliminary running-in of the new engine piston-cylinder set as well as coated engine cylinder-piston set was conducted for 40 hrs in five non-stop cycles of 8 hrs each. The experimental test matrix selected for Phase-I was based on full factorial design approach to obtain comprehensive and significant results. The final test matrix parameters and their levels are shown in Table 5-1.

Table 5-1 Test matrix input details (Phase-I)

Parameters (factors)	Levels				
	1	2	3	4	5
Engine load (N)	4	10	16	22	28
Engine speed (rpm)	1400	1700	2000	2300	2600
Coolant flow rate (l/s)	0.18	0.22	0.26	-	-
Engine cylinder	Uncoated - 1	Coated - 2	-	-	-

From Table 5-1, it can be seen that there are five different levels for engine speed and engine load, while there are three different steps for coolant flow rate (CFR) and two levels (significantly possible levels) of engine cylinder. This selected step size of engine speed (300 rpm) was expected to have a significant effect on engine output variables. For the load, 6 N was selected as a level difference and this step was expected to have distinct effects on fuel economy and exhaust emissions, although the effects maybe less significant for friction power. While coolant water flow rate step size is taken based on the limit and range of CFR specified in the literature [95]. For engine cylinder type, there are only two possibilities and hence selected as two levels namely uncoated (as 1) and coated (as 2). Both the considered cylinders were new, one without coating and other with coating. As the engine testing experiments were based on full factorial design approach, so one parameter was varied according to its step size while keeping other parameters fixed during the experiments. The experimental matrix input and output parameters considered in Phase-I of present investigation is tabulated in Table 5-2.

Table 5-2 Experimental matrix input and output details

Parameters	
Input	Output
Engine load (N)	Friction power (kW)
Engine speed (rpm)	BSFC (g/kWh)
CFR (l/s)	Mechanical efficiency (%)
Engine cylinder	Specific emission CO (g/kWh)
	Specific emission HC (g/kWh)
	Specific emission NO (g/kWh)
	Smoke opacity (%)

Based on the structure of test matrix (Table 5-1), the complete set of experiments comprises of total 150 experimental runs (5 × 5 × 3 × 2). And further their multiple repetitions performed for estimating uncertainty in the responses. The experimental test matrix is presented in Table 5-3.

Table 5-3 Experimental matrix (Phase-I)

Sl.	Speed (rpm)	Load (N)	CFR (l/s)	Engine cylinder
1	1400	4	0.18	1
2	1400	10	0.18	1
3	1400	16	0.18	1
4	1400	22	0.18	1
5	1400	28	0.18	1
6	1700	4	0.18	1
7	1700	10	0.18	1
8	1700	16	0.18	1
9	1700	22	0.18	1
10	1700	28	0.18	1
11	2000	4	0.18	1
12	2000	10	0.18	1
13	2000	16	0.18	1
14	2000	22	0.18	1
15	2000	28	0.18	1
16	2300	4	0.18	1
17	2300	10	0.18	1
18	2300	16	0.18	1
19	2300	22	0.18	1
20	2300	28	0.18	1
21	2600	4	0.18	1
22	2600	10	0.18	1
23	2600	16	0.18	1
24	2600	22	0.18	1
25	2600	28	0.18	1
26	1400	4	0.22	1
27	1400	10	0.22	1
28	1400	16	0.22	1
29	1400	22	0.22	1
30	1400	28	0.22	1
31	1700	4	0.22	1
32	1700	10	0.22	1
33	1700	16	0.22	1
34	1700	22	0.22	1
35	1700	28	0.22	1
36	2000	4	0.22	1
37	2000	10	0.22	1
38	2000	16	0.22	1

39	2000	22	0.22	1
40	2000	28	0.22	1
41	2300	4	0.22	1
42	2300	10	0.22	1
43	2300	16	0.22	1
44	2300	22	0.22	1
45	2300	28	0.22	1
46	2600	4	0.22	1
47	2600	10	0.22	1
48	2600	16	0.22	1
49	2600	22	0.22	1
50	2600	28	0.22	1
51	1400	4	0.26	1
52	1400	10	0.26	1
53	1400	16	0.26	1
54	1400	22	0.26	1
55	1400	28	0.26	1
56	1700	4	0.26	1
57	1700	10	0.26	1
58	1700	16	0.26	1
59	1700	22	0.26	1
60	1700	28	0.26	1
61	2000	4	0.26	1
62	2000	10	0.26	1
63	2000	16	0.26	1
64	2000	22	0.26	1
65	2000	28	0.26	1
66	2300	4	0.26	1
67	2300	10	0.26	1
68	2300	16	0.26	1
69	2300	22	0.26	1
70	2300	28	0.26	1
71	2600	4	0.26	1
72	2600	10	0.26	1
73	2600	16	0.26	1
74	2600	22	0.26	1
75	2600	28	0.26	1
76	1400	4	0.18	2
77	1400	10	0.18	2
78	1400	16	0.18	2
79	1400	22	0.18	2
80	1400	28	0.18	2
81	1700	4	0.18	2
82	1700	10	0.18	2
83	1700	16	0.18	2
84	1700	22	0.18	2

85	1700	28	0.18	2
86	2000	4	0.18	2
87	2000	10	0.18	2
88	2000	16	0.18	2
89	2000	22	0.18	2
90	2000	28	0.18	2
91	2300	4	0.18	2
92	2300	10	0.18	2
93	2300	16	0.18	2
94	2300	22	0.18	2
95	2300	28	0.18	2
96	2600	4	0.18	2
97	2600	10	0.18	2
98	2600	16	0.18	2
99	2600	22	0.18	2
100	2600	28	0.18	2
101	1400	4	0.22	2
102	1400	10	0.22	2
103	1400	16	0.22	2
104	1400	22	0.22	2
105	1400	28	0.22	2
106	1700	4	0.22	2
107	1700	10	0.22	2
108	1700	16	0.22	2
109	1700	22	0.22	2
110	1700	28	0.22	2
111	2000	4	0.22	2
112	2000	10	0.22	2
113	2000	16	0.22	2
114	2000	22	0.22	2
115	2000	28	0.22	2
116	2300	4	0.22	2
117	2300	10	0.22	2
118	2300	16	0.22	2
119	2300	22	0.22	2
120	2300	28	0.22	2
121	2600	4	0.22	2
122	2600	10	0.22	2
123	2600	16	0.22	2
124	2600	22	0.22	2
125	2600	28	0.22	2
126	1400	4	0.26	2
127	1400	10	0.26	2
128	1400	16	0.26	2
129	1400	22	0.26	2
130	1400	28	0.26	2

131	1700	4	0.26	2
132	1700	10	0.26	2
133	1700	16	0.26	2
134	1700	22	0.26	2
135	1700	28	0.26	2
136	2000	4	0.26	2
137	2000	10	0.26	2
138	2000	16	0.26	2
139	2000	22	0.26	2
140	2000	28	0.26	2
141	2300	4	0.26	2
142	2300	10	0.26	2
143	2300	16	0.26	2
144	2300	22	0.26	2
145	2300	28	0.26	2
146	2600	4	0.26	2
147	2600	10	0.26	2
148	2600	16	0.26	2
149	2600	22	0.26	2
150	2600	28	0.26	2

The responses against each experimental settings are repeated three times to determine response variation corresponds to identical input experimental setting. The uncertainty analysis of the basic engine parameters in Phase-I are shown in Appendix-II (Table AII-2). Based on observations it was found that the variation in coolant flow rate does not have significant effect on engine performance parameters. Because of this mid value of coolant flow rate (0.22 *l/s*) was used for further investigation.

5.2.2 Phase-II: Experimental design

Experimental design of Phase-II was planned to evaluate the engine performance at higher loading condition of the engine. In the present investigation, the experimental test matrix opted for Phase-II was also based on full factorial design approach. The final test matrix parameters and their levels are shown in Table 5-4.

Table 5-4 Test matrix input details (Phase-II)

Parameters (factors)	Levels				
	1	2	3	4	5
Engine load (N)	12	24	36	48	60
Engine speed (rpm)	1200	1350	1500	1650	1800
Engine cylinder	Uncoated - 1	Coated - 2	-	-	-

The experimental matrix input and output parameters considered in Phase-II of present investigation is tabulated in Table 5-5, keeping the coolant flow rate constant (at 0.22 l/s) for all experiments.

Table 5-5 Experimental matrix input and output details

Parameters	
Input	Output
Engine load (N)	BSFC (g/kWh)
Engine speed (rpm)	Friction power (kW)
Engine cylinder	Mechanical efficiency (%)
	Specific emission CO (g/kWh)
	Specific emission HC (g/kWh)
	Specific emission NO (g/kWh)
	Smoke opacity (%)

Based on the structure of test matrix (Table 5-4), the complete set of experiments comprises of total 50 experimental runs ($5 \times 5 \times 2$). And further their multiple repetitions performed for estimating uncertainty in the responses. The uncertainty analysis of the basic engine parameters in Phase-II can be referred in Appendix-II (Table AII-3). The Phase-II experimental matrix is given in Table 5-6.

Table 5-6 Experimental matrix (Phase-II)

Sl.	Speed (rpm)	Rated load (%)	Engine cylinder
1	1200	20	1
2	1200	40	1
3	1200	60	1
4	1200	80	1
5	1200	100	1
6	1350	20	1
7	1350	40	1
8	1350	60	1
9	1350	80	1
10	1350	100	1
11	1500	20	1
12	1500	40	1
13	1500	60	1
14	1500	80	1
15	1500	100	1
16	1650	20	1
17	1650	40	1
18	1650	60	1
19	1650	80	1
20	1650	100	1
21	1800	20	1
22	1800	40	1
23	1800	60	1
24	1800	80	1
25	1800	100	1
26	1200	20	2

27	1200	40	2
28	1200	60	2
29	1200	80	2
30	1200	100	2
31	1350	20	2
32	1350	40	2
33	1350	60	2
34	1350	80	2
35	1350	100	2
36	1500	20	2
37	1500	40	2
38	1500	60	2
39	1500	80	2
40	1500	100	2
41	1650	20	2
42	1650	40	2
43	1650	60	2
44	1650	80	2
45	1650	100	2
46	1800	20	2
47	1800	40	2
48	1800	60	2
49	1800	80	2
50	1800	100	2

5.2.3 Experimental results and discussion

The effect of variation in engine operating parameters on engine performance of the small DI diesel engine is discussed here. The results were analysed and presented in two different sections by considering constant coolant flow rate of 0.22 *l/s* for both experimental phases. First section describes the engine behaviour with variation of engine operating parameters, namely, speed and load, and next section describes the effect of nano-graphite coating on engine performance parameters. The responses of Phase-I experiments are represented as dash-line while the responses of Phase-II experiments are shown in continuous line in all the response plot.

Effect of speed and load variation on engine performance parameters

The effect on engine performance parameters namely friction power, brake specific fuel consumption (BSFC), mechanical efficiency, sCO, sHC, sNO and smoke opacity due to variation of engine operating parameters (speed and load) is discussed here.

Engine performance parameter – Friction power

It can be observed from Fig 5-5 (for uncoated engine cylinder) and Fig 5-6 (for coated engine cylinder), the friction power increases as speed increase. Similar trend of friction with respect to increase in speed has also been reported in literature [69].
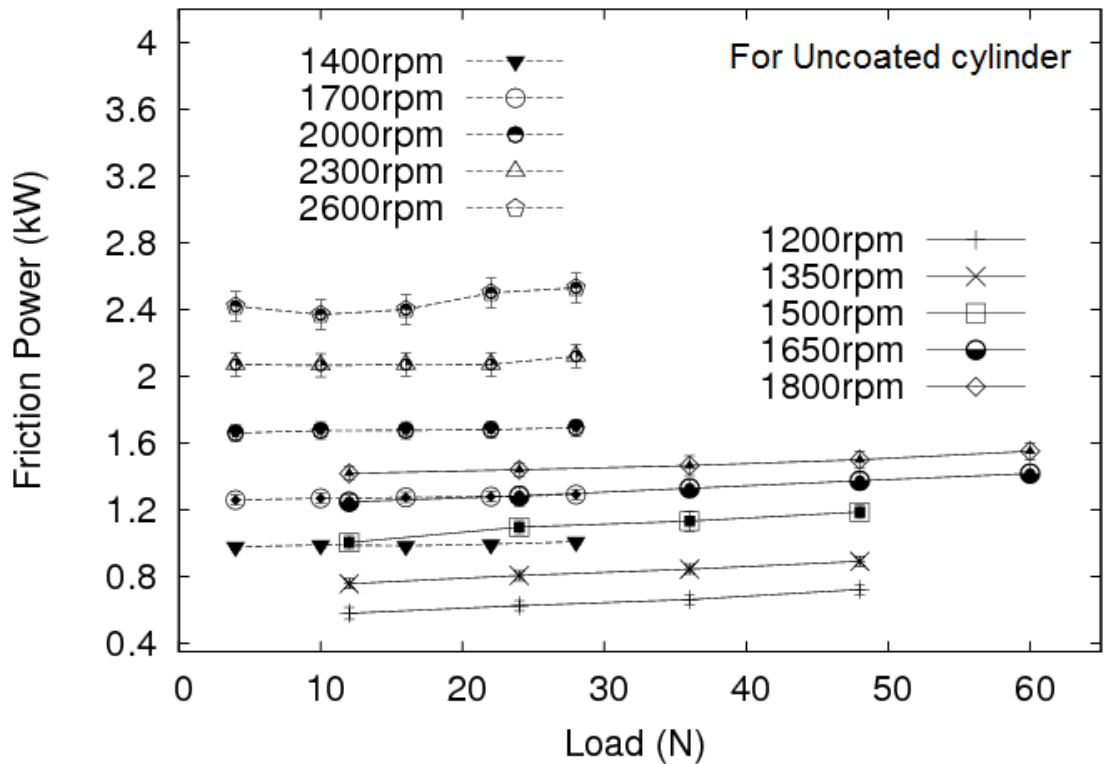
Fig 5-5 Engine performance parameter - Friction power (for uncoated engine cylinder); showing slight increment in friction power with increase in load (Phase-I in dash-line and Phase-II in continuous line)
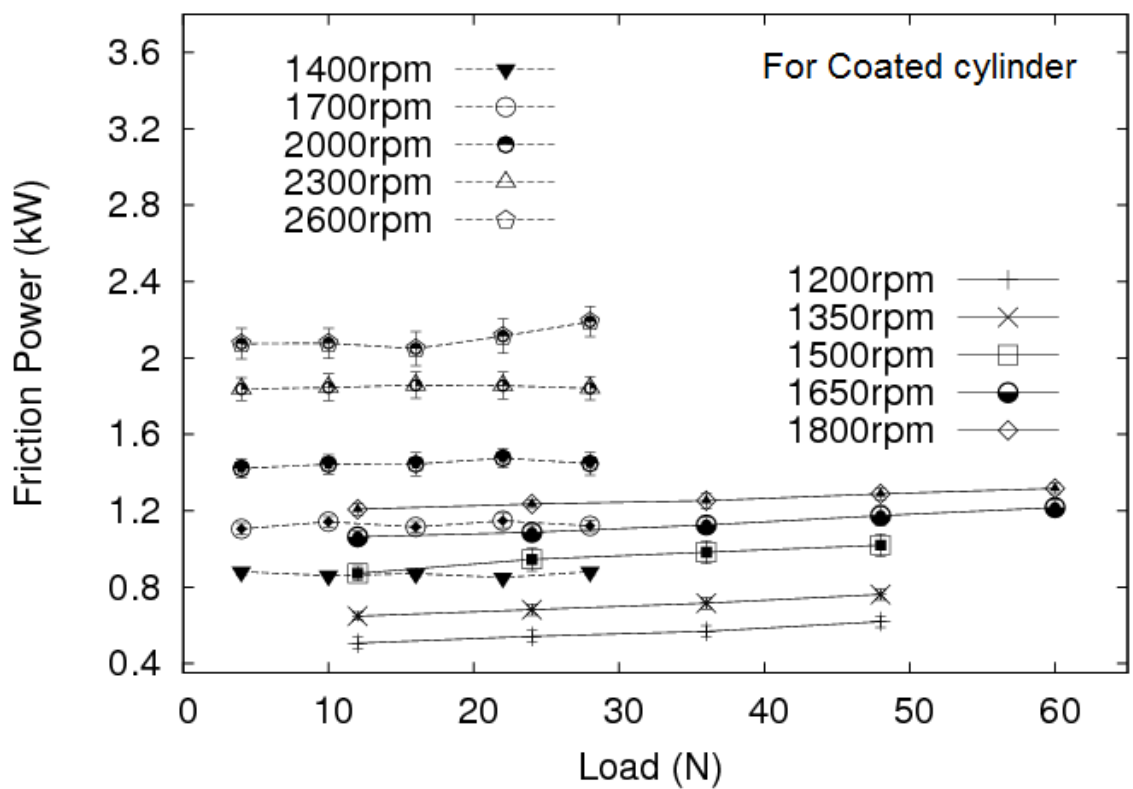
Fig 5-6 Engine performance parameter - Friction power (for coated engine cylinder); showing slight increment in friction power with increase in load (Phase-I in dash-line and Phase-II in continuous line)

From Fig 5-5 and Fig 5-6, it is clear that the friction power increases slightly on increasing load. The variation is around 5.37 % for both the conditions, i.e. coated and uncoated engine. This variation actually may be due to increased load which leads to higher thrust of piston set against engine cylinder wall.

Engine performance parameter – BSFC

In the present investigation, for both cases of uncoated and coated engine, BSFC is found to decrease with increase in engine load (Fig 5-7 and Fig 5-8). No significant variation has been observed in BSFC with respect to change in speed. This trend is similar to that reported in Heywood [69] and also in other literature [3,139,70,125,116,136]. The fuel consumption with increased loading conditions always tends to decrease because the amount of fuel used for producing per unit of power decreases with increase in load [3,22,47,116,70,125]. The rate of increase in brake power is much more than that of the increased fuel consumption owing to a rise in the combustion temperature with load [70].
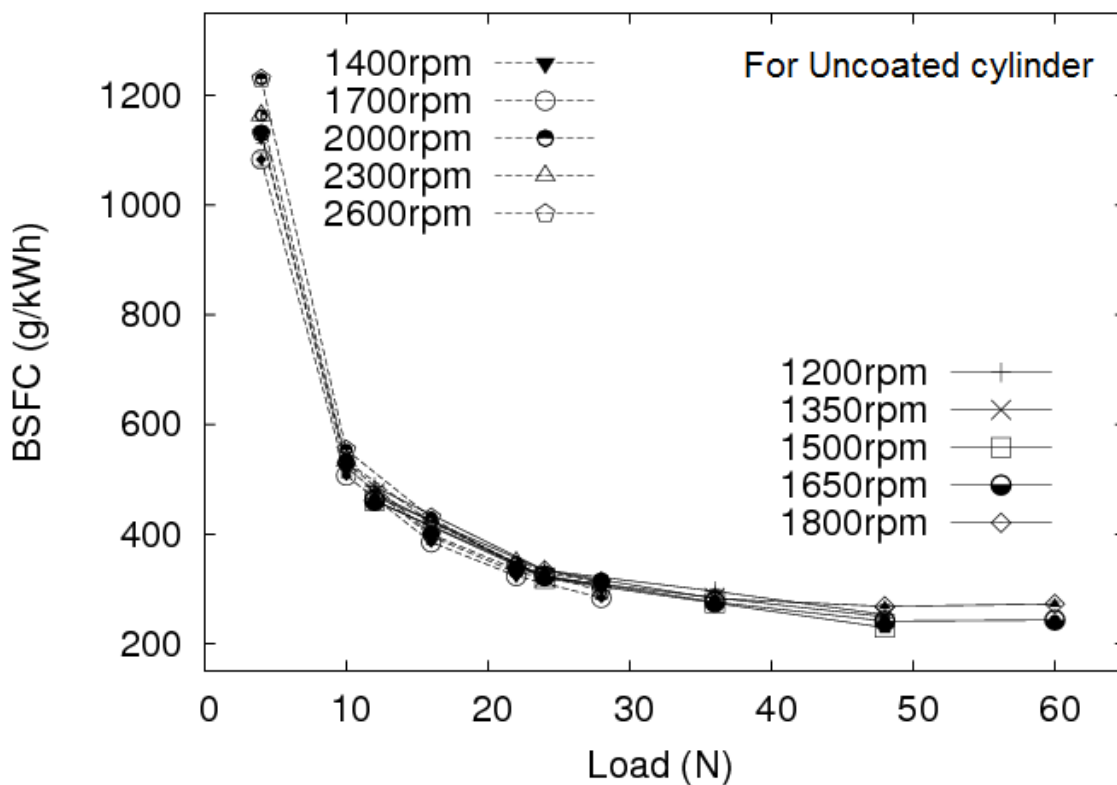
Fig 5-7 Engine performance parameter - BSFC (for uncoated engine cylinder); showing significant reduction in BSFC with increase in load (Phase-I in dash-line and Phase-II in continuous line)
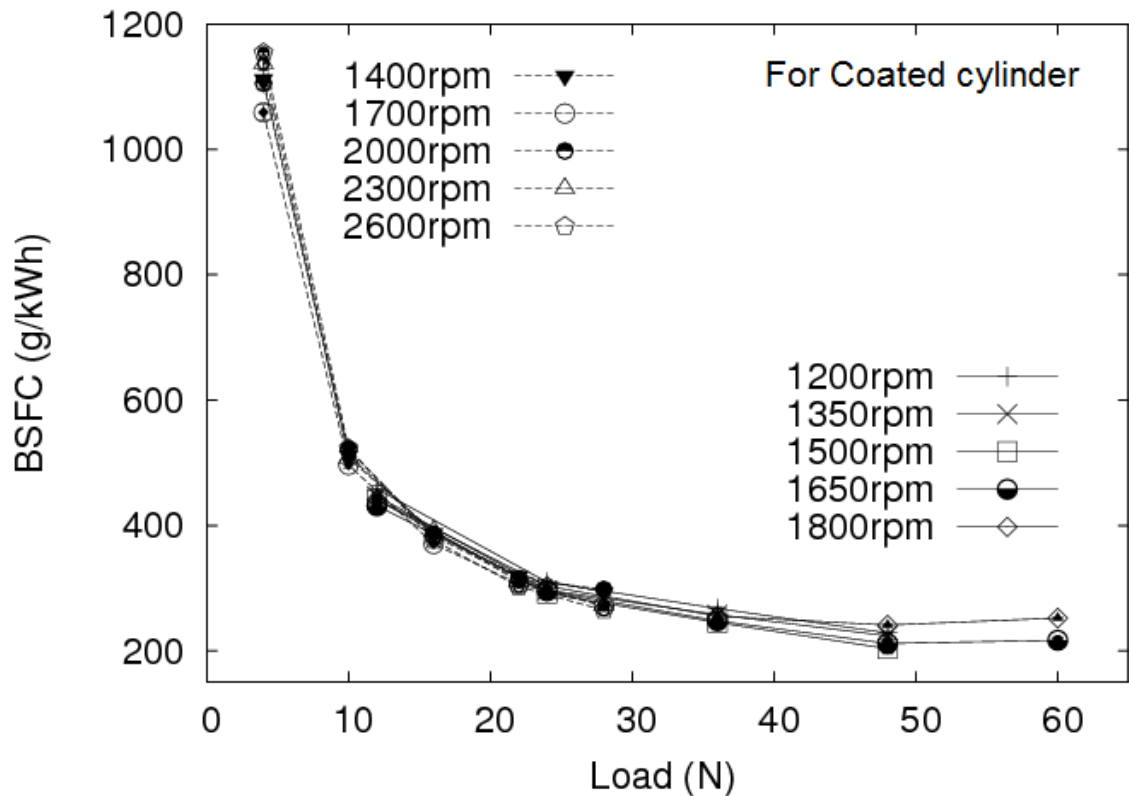
Fig 5-8 Engine performance parameter - BSFC (for coated engine cylinder); showing significant reduction in BSFC with increase in load (Phase-I in dash-line and Phase-II in continuous line)

Engine performance parameter – Mechanical efficiency

It can be observed clearly from Fig 5-9 and Fig 5-10, as the load increases the mechanical efficiency of the engine increases. The trend is the same for coated and uncoated engine. With increase in engine load, the rise in brake power is higher due to rise in the combustion temperature. Very less variation has been observed in mechanical efficiency with respect to change in speed. As speed increases, the mechanical efficiency decreases for both coated and uncoated engines. Similar trend of variation of mechanical efficiency with speed has been reported in the literature [69]. The decrease in mechanical efficiency with increase in speed at specific loading condition is contributed to increased friction power during engine operation.

Engine performance parameter – Specific emission CO (sCO)

Fig 5-11 and Fig 5-12 indicate that for both coated and uncoated engine blocks, sCO decreases as load increases. Similar trend of sCO has also been reported in the literature [3,70,71,125].

Engine performance parameter – Specific emission HC (sHC)

It is observed from Fig 5-13 and Fig 5-14 that, the sHC decreases as the load increases. The trend is similar for uncoated and coated engine block. The similar trend of sHC has also been reported in the literature [3,125,110].
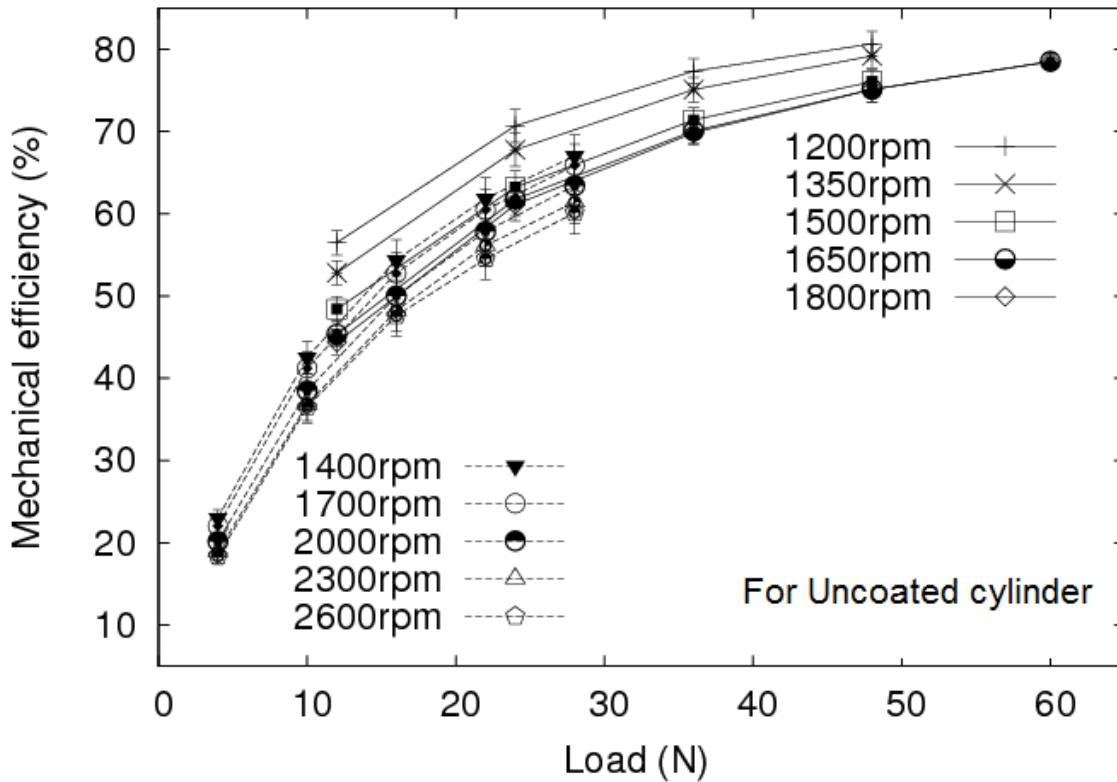
Fig 5-9 Engine performance parameter – Mechanical efficiency (for uncoated engine cylinder); showing significant increase in mechanical efficiency with increase in load (Phase-I in dash-line and Phase-II in continuous line)
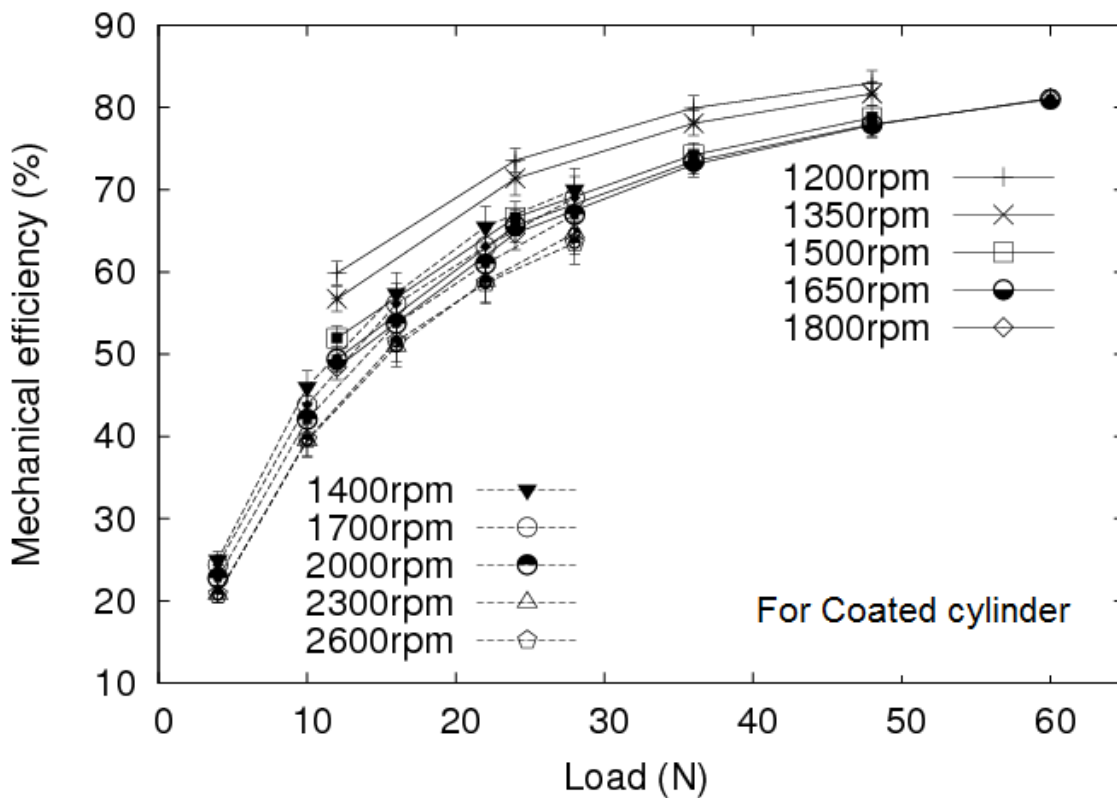
Fig 5-10 Engine performance parameter – Mechanical efficiency (for coated engine cylinder); showing significant increase in mechanical efficiency with increase in load (Phase-I in dash-line and Phase-II in continuous line)
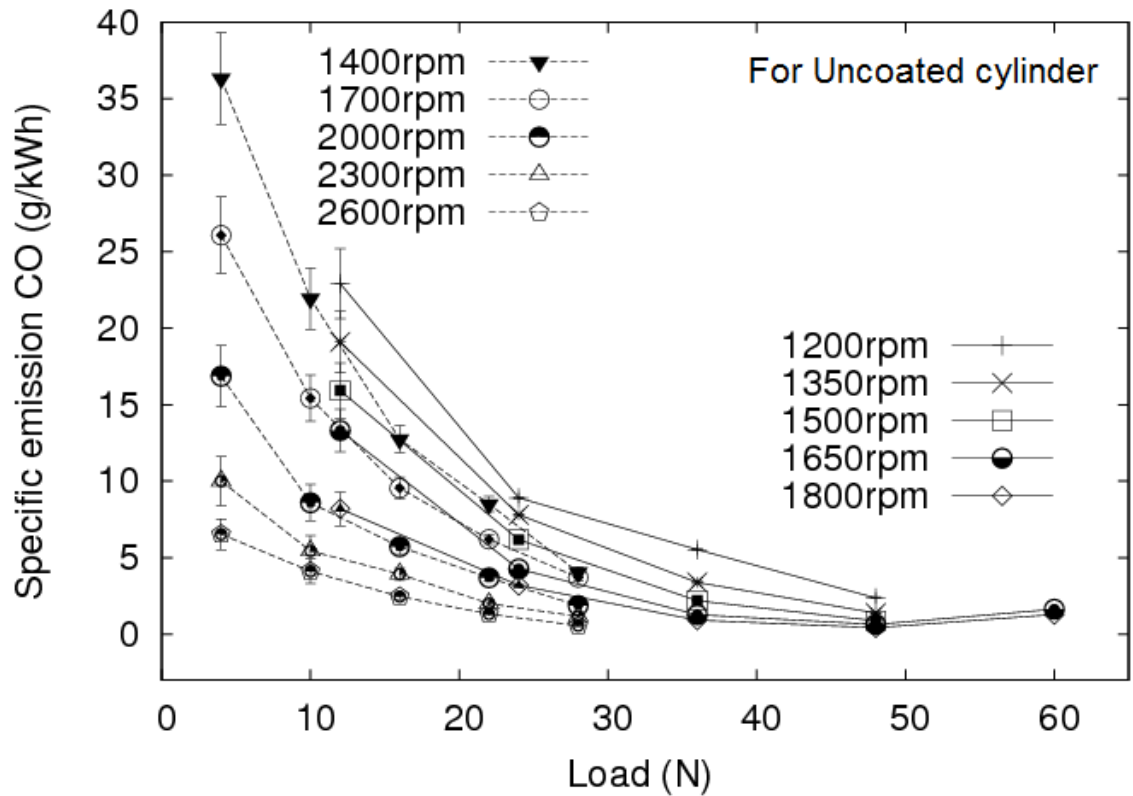
Fig 5-11 Engine performance parameter - sCO (for uncoated engine cylinder); showing significant decrease in sCO with increase in load (Phase-I in dash-line and Phase-II in continuous line)
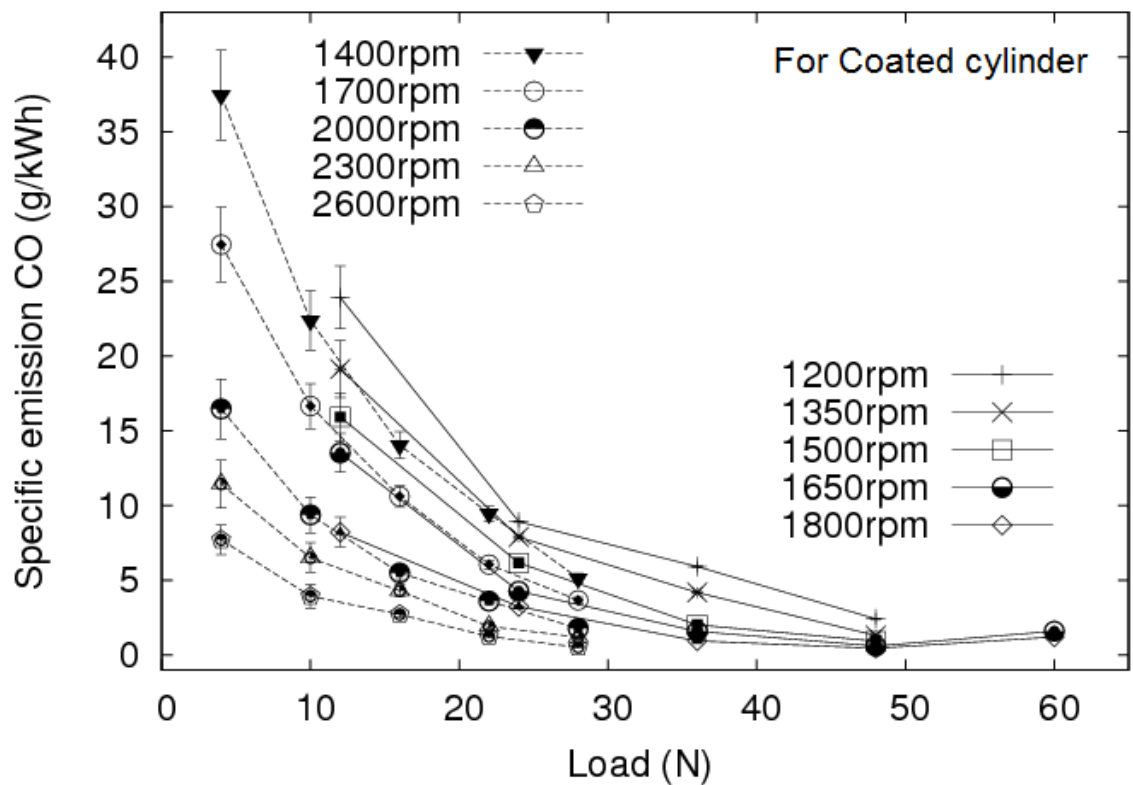
Fig 5-12 Engine performance parameter - sCO (for coated engine cylinder); showing significant decrease in sCO with increase in load (Phase-I in dash-line and Phase-II in continuous line)
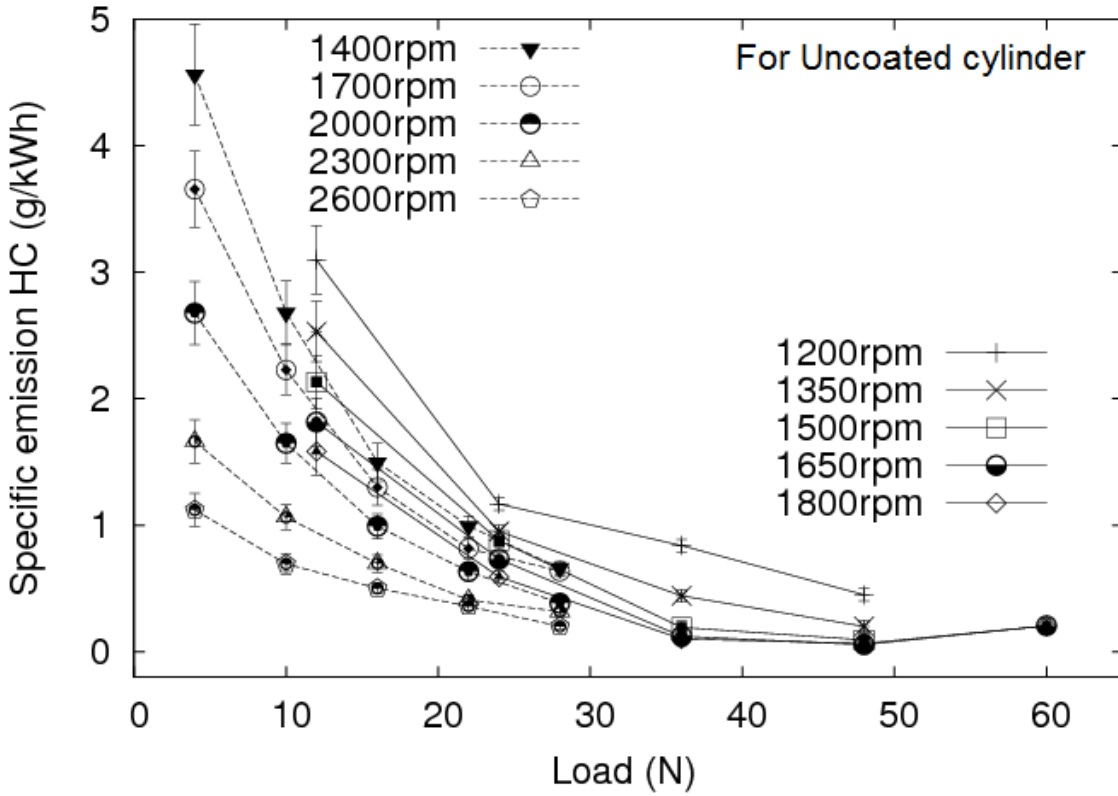
Fig 5-13 Engine performance parameter - sHC (for uncoated engine cylinder); showing significant decrease in sHC with increase in load (Phase-I in dash-line and Phase-II in continuous line)
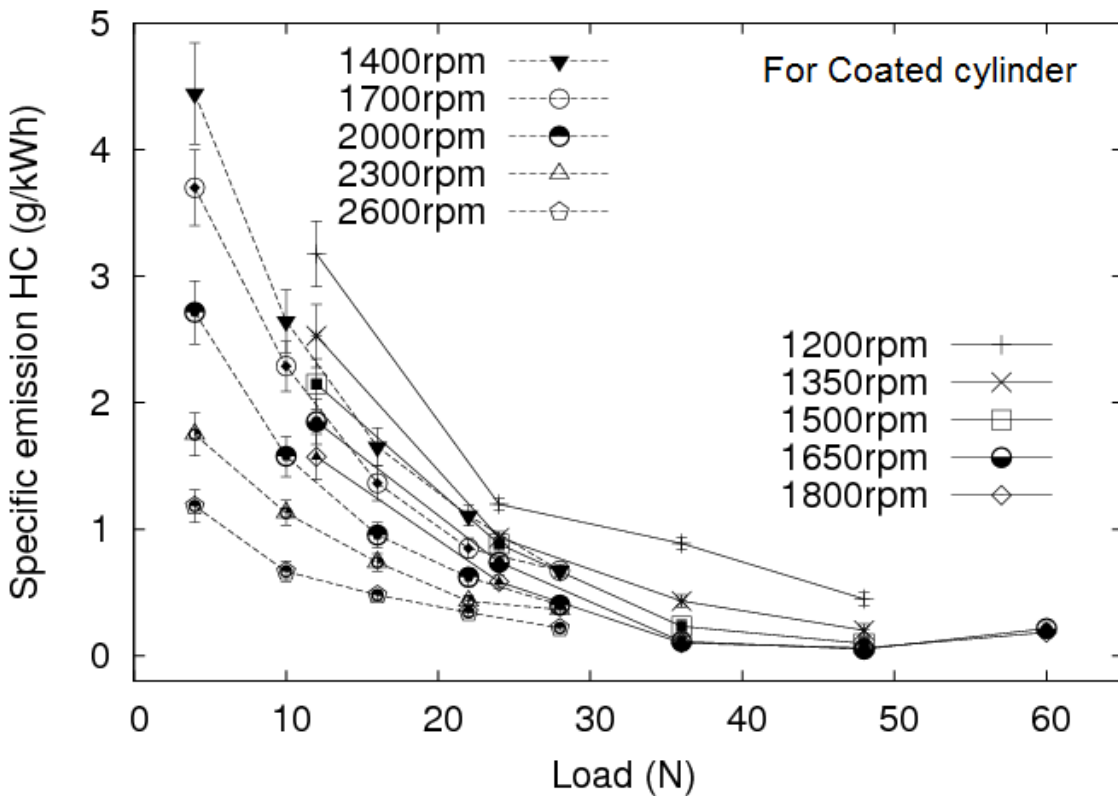
Fig 5-14 Engine performance parameter - sHC (for coated engine cylinder); showing significant decrease in sHC with increase in load (Phase-I in dash-line and Phase-II in continuous line)

Engine performance parameter – Specific emission NO (sNO)

Fig 5-15 and Fig 5-16 shows that sNO decreases when the load increases. This trend is similar for uncoated and coated engine block. The similar trend of sNO is also reported in the literature [70,125,110]. While at the same time it can be observed that the sNO decreases as speed increases. The decreased residence time for NO formation reaction with increase of speed resulted in decrease of sNO emission. Similar results are observed in the studies done by other researchers [198,64].

The specific emission NO (or NO emission) represents the engine emission of NO content. The specific emission NO, sNO, is the most troublesome emission from diesel engines. Generally it comes under NO_x, which refers to a class of compounds called oxides of nitrogen, which usually represents a mixture of nitric oxide (NO) and nitrogen dioxide (NO_2). In diesel engine exhaust, NO is usually the major component of total oxides of nitrogen and constitutes more than 70–90% of total NO_x [93,64]. In general the significant factors like combustion temperature, availability of oxygen and nitrogen in the combustion chamber, and the reaction time (also called as residence time) determine NO_x emissions during the combustion process [69,205,93,64,117,125,158,159,26,18,70]. The production of NO_x is proportional to combustion efficiency [125]. Better combustion efficiency gives higher value of the exhaust temperature, which increases the level of NO_x production [64,117]. Temperature is the main factor for the formation of NO compared to the availability of oxygen and other factors. NO formation in a diesel combustion peaks between the start of combustion and shortly after the occurrence of peak cylinder pressure which reduces the ignition delay. After the occurrence of peak pressure the burned gas temperature decreases as the cylinder gases expand which causes the combustion temperature to decrease resulting in freezing of NO without further reduction [69].

Engine performance parameter – Smoke opacity

It is observed from Fig 5-17 and Fig 5-18 that as the load increases the smoke opacity also increases. This trend is similar for uncoated and coated engine. The similar trend of smoke opacity is also been reported in the literature [3,70,125,22]. At higher load, more amount of fuel for combustion results in higher smoke opacity. While at the same time it can be observed that the smoke opacity decreases with increase in speed. Similar trend of smoke opacity has been observed by Oprescu et al. [114]. Smoke levels in the diesel engine exhaust always tend to decrease with increase of engine speed for constant loading conditions. It can be attributed to more complete combustion, as the speed increases the turbulence within the engine cylinder increases during the intake process. The enhanced charge motion in the combustion chamber result in more homogeneous air-fuel charge [114].
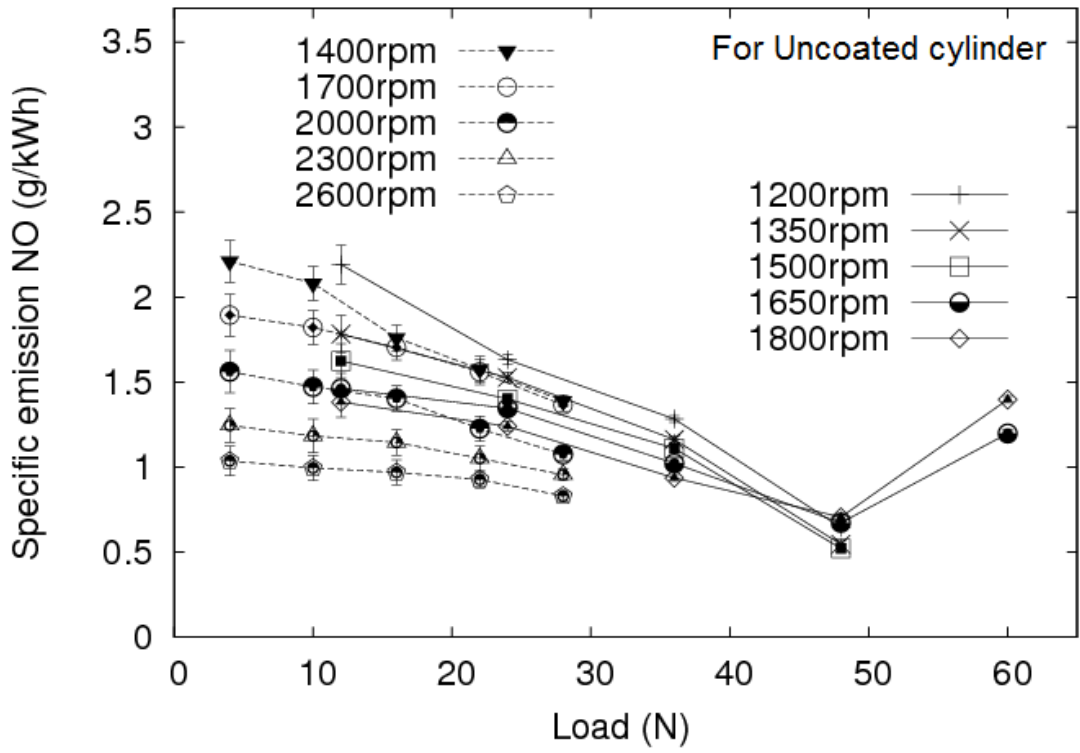
Fig 5-15 Engine performance parameter - sNO (for uncoated engine cylinder); showing significant decrease in sNO with increase in load (Phase-I in dash-line and Phase-II in continuous line); In Phase-II sNO increases at higher load due to very high combustion temperature
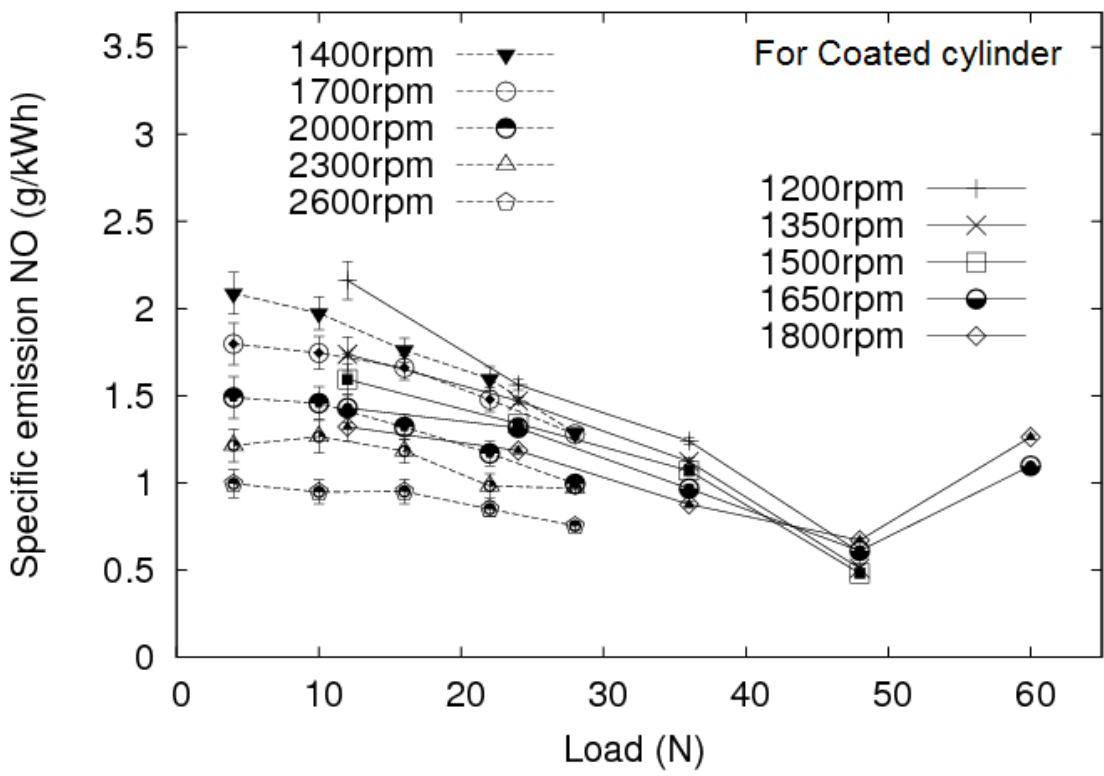
Fig 5-16 Engine performance parameter - sNO (for coated engine cylinder); showing significant decrease in sNO with increase in load (Phase-I in dash-line and Phase-II in continuous line); In Phase-II sNO increases at higher load due to very high combustion temperature
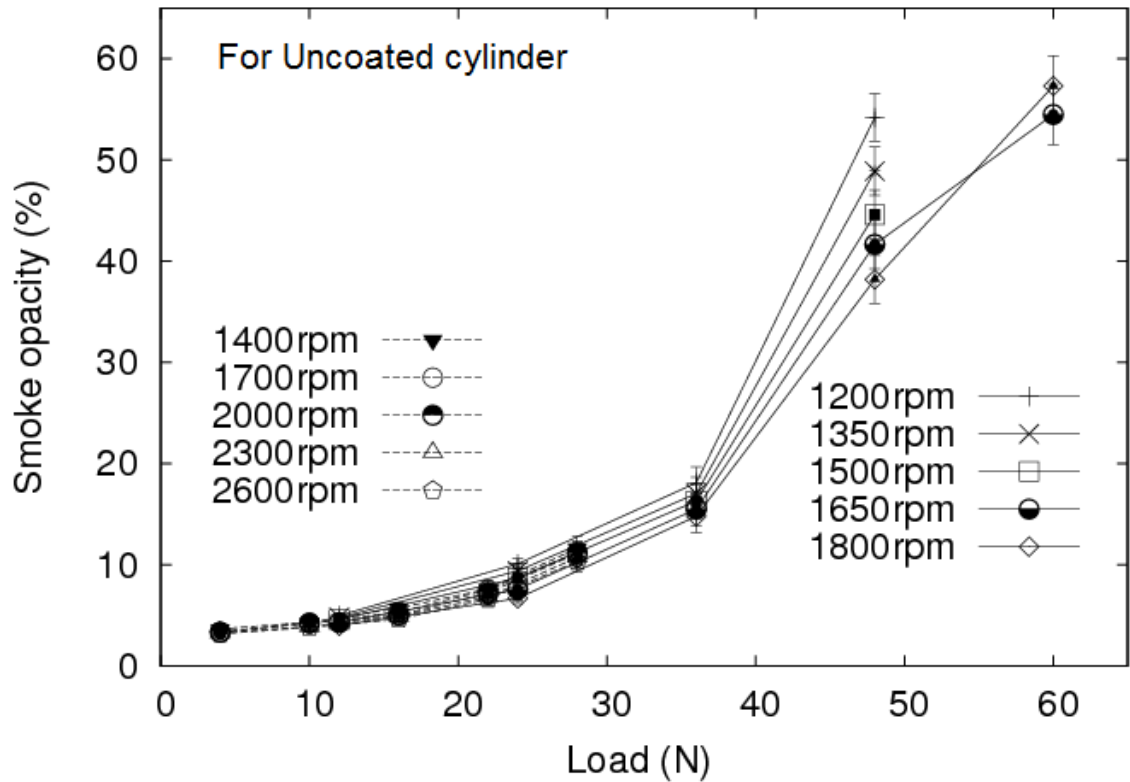
Fig 5-17 Engine performance parameter - Smoke opacity (for uncoated engine cylinder); showing significant increase in smoke opacity with increase in load (Phase-I in dash-line and Phase-II in continuous line)
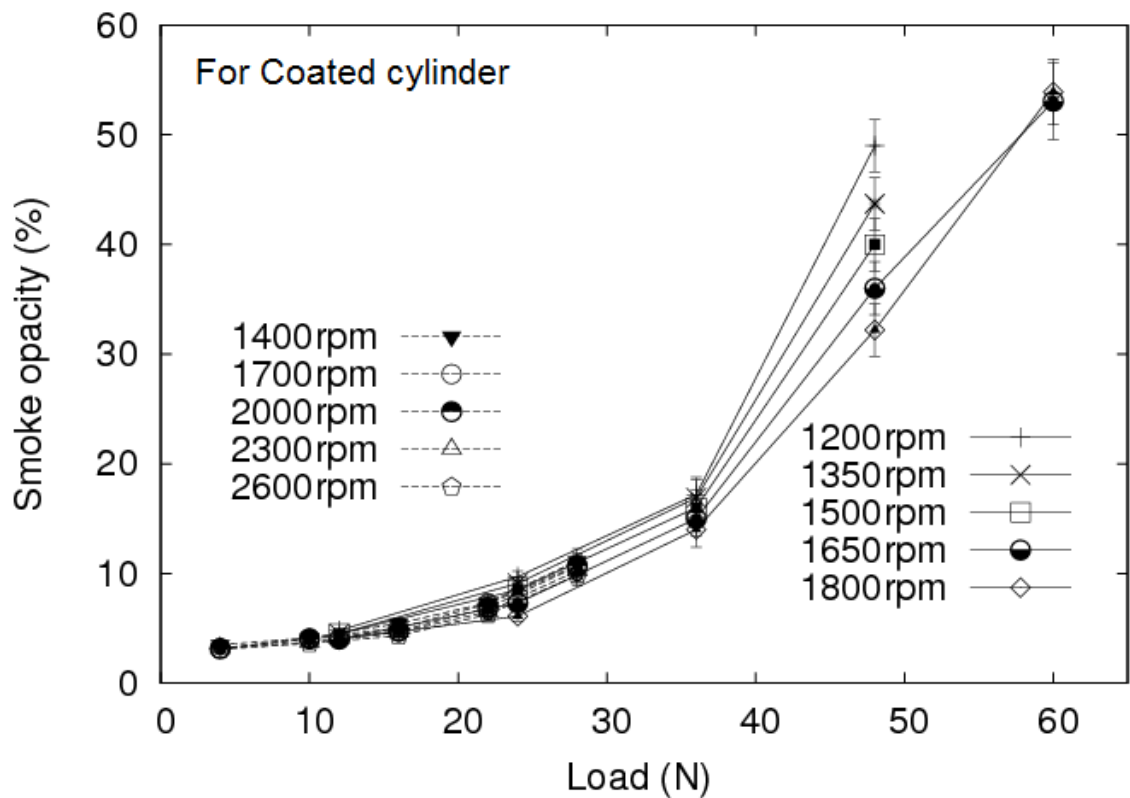
Fig 5-18 Engine performance parameter - Smoke opacity (for coated engine cylinder); showing significant increase in smoke opacity with increase in load (Phase-I in dash-line and Phase-II in continuous line)

Effect of nano-graphite coating on engine performance parameters

To study the effect of coating on engine performance at higher speed as well as at higher loading condition, the experimental observations of Phase-I (dash-line) and Phase-II (continuous line) are combined together and presented on the same diagram which shows the comprehensive behaviour of the engine when operated with two different engine cylinders.

It is observed from the Fig 5-19 that the friction power is higher for uncoated engine block compared to that for the coated engine block, indicating that the coating on the engine block affects the friction power. The reduction in friction power in coated engine is around ~14 % throughout the loading conditions. The main reason behind this reduction of friction power may be due to reduced coefficient of friction and low surface roughness of the coated engine cylinder, as was observed for small scale sample of engine cylinder material. As a consequence of the reduction in friction power for the coated engine, for the same brake power out-put, the indicated power out-put should be less leading to decreased fuel consumption.

It is observed from Fig 5-20 that the BSFC for coated engine is less compared to uncoated engine. There is a slight variation in the percentage of this reduction observed from low load to high load. At low load the reduction is around 5.6 % while at high load the difference is increased up to 12.5 %. Due to reduction in friction power of the coated engine, requirement of indicated power reduced for obtaining same brake power. And the indicated power is directly proportional to the source of energy which is diesel fuel here. The reduction in indicated power is directly affecting the fuel consumption, so when IP demand is reduces the fuel consumption also reduce which actually represented by BSFC.

From Fig 5-21, it is observed that the mechanical efficiency of engine with coated cylinder is higher than that of uncoated engine over the operating range of load. The difference in the mechanical efficiency is around 13.5 % at lower load while the difference at higher loading side is less around half of that at low loading condition and that is around 7.5 %. The reason behind this enhancement is the reduction in friction power (because of nano-graphite coating on the cylinder block) for obtaining same BP in case of coated engine.

Fig 5-22 shows the specific CO emissions variation with load. The variation of sCO with load is similar for uncoated and coated engine blocks. At low load and higher speed it is observed that sCO emissions for coated engine block is around 12 % higher while at higher loads there is not much difference in the sCO levels for the coated and uncoated engines. The reason behind the increased sCO for coated engine at lower load and higher speed is the lower fuel consumption by the coated engine as explained above, resulting in the lower combustion temperatures. It is already an established fact that the sCO emission will be higher at low combustion temperature due to incomplete combustion of fuel [69]. While at higher loading conditions the combustion

temperature reached to its optimum level and hence there is no significant variation found in sCO for both the conditions coated and uncoated engines.
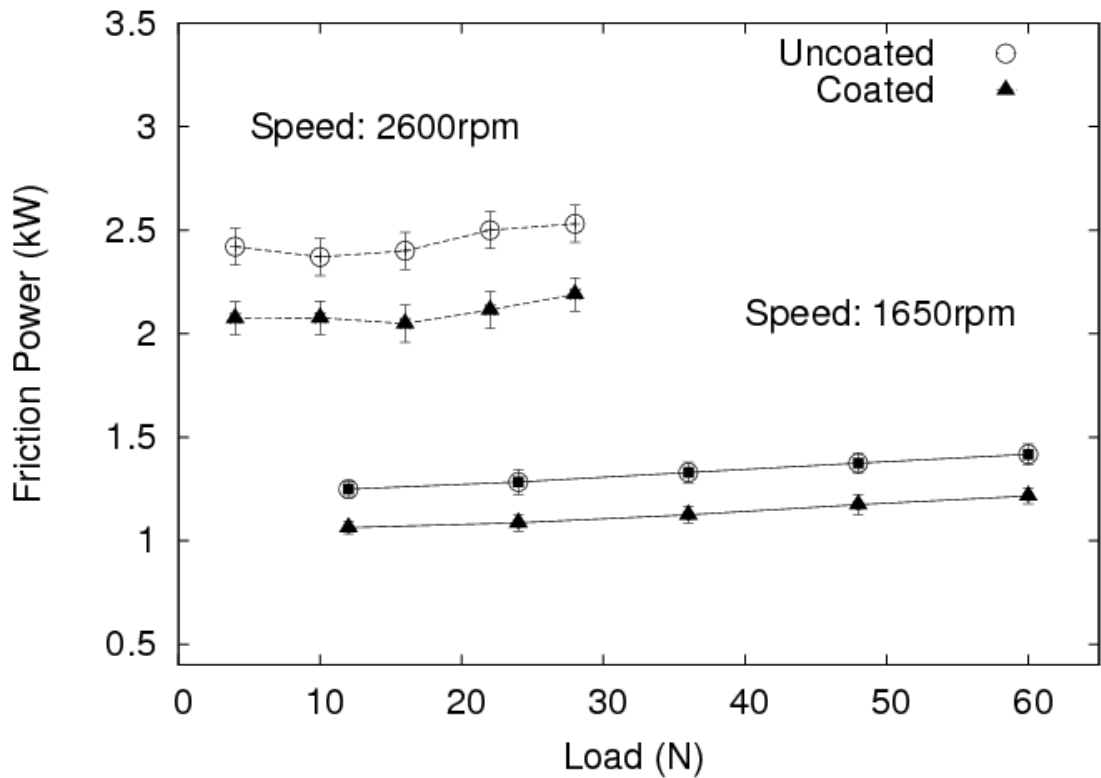
Fig 5-19 Engine performance parameter - Friction power; showing reduction in friction power in case of coated engine cylinder
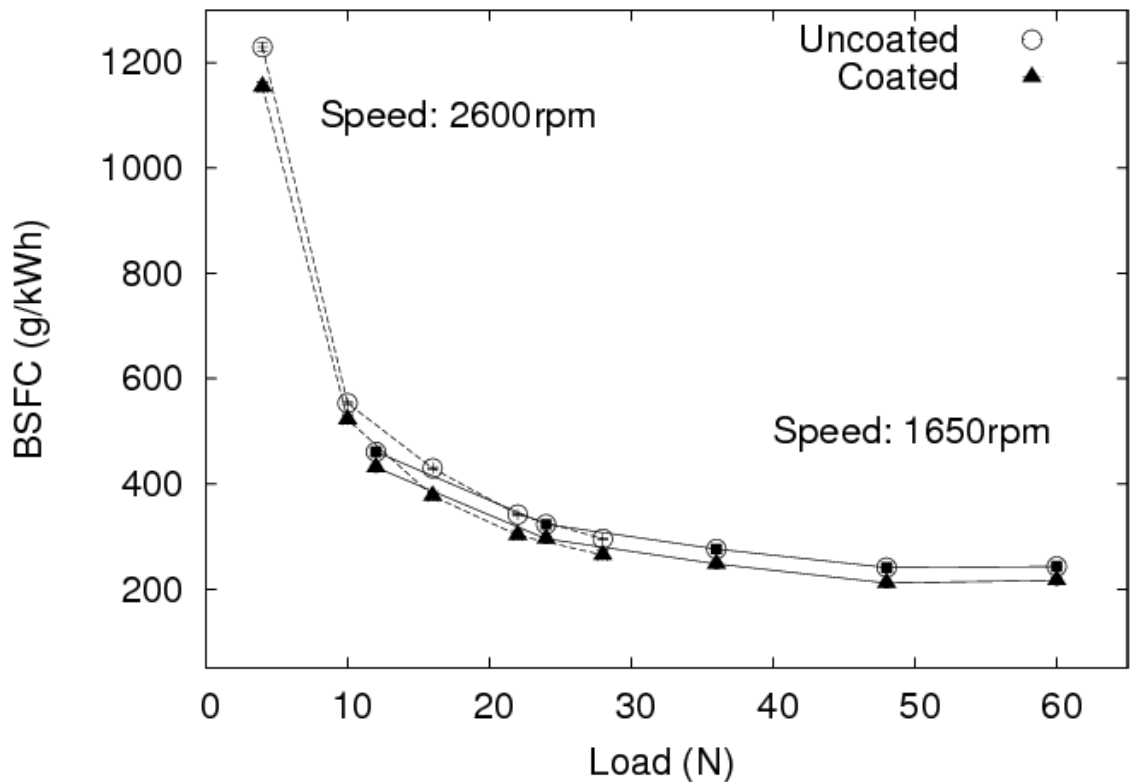
Fig 5-20 Engine performance parameter - BSFC; showing reduced BSFC for coated engine cylinder
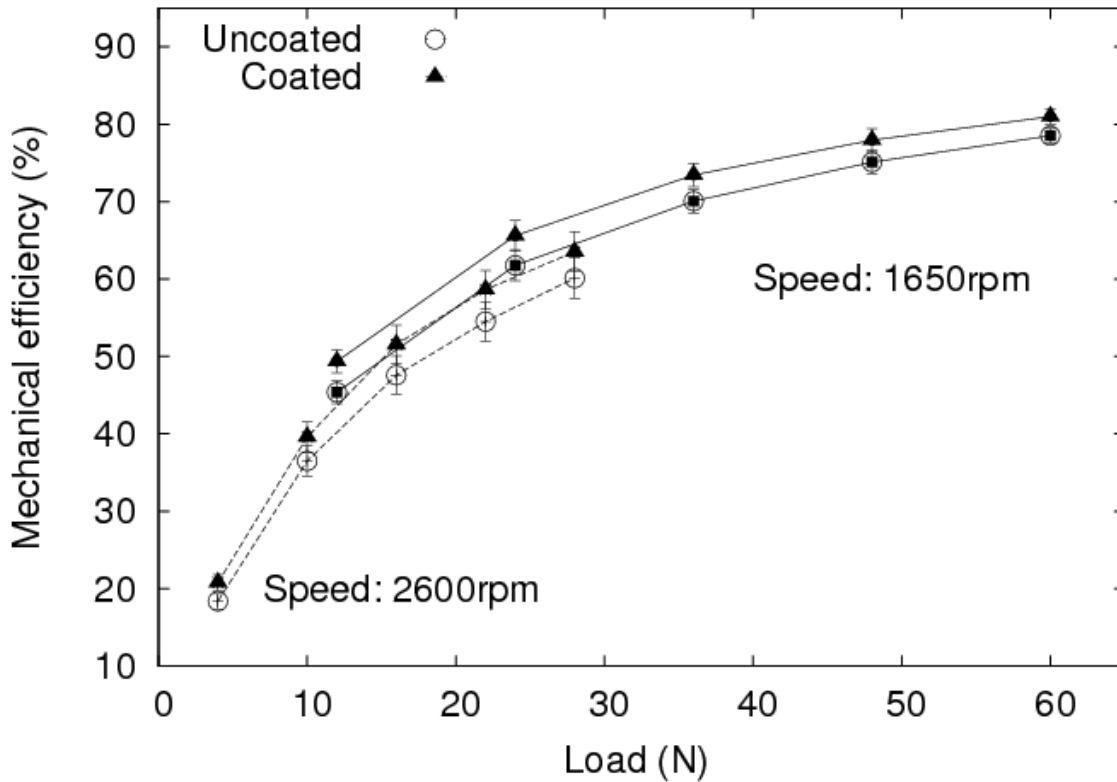
Fig 5-21 Engine performance parameter - Mechanical efficiency; showing enhancement of mechanical efficiency for coated engine cylinder
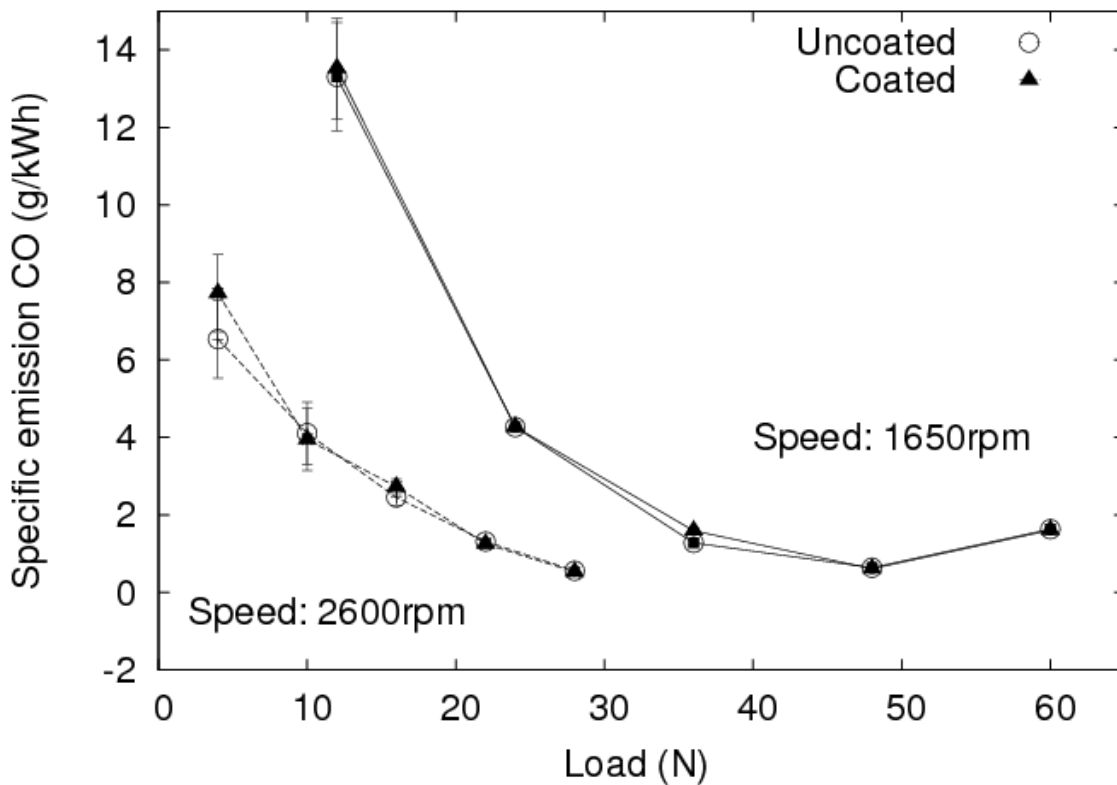
Fig 5-22 Engine performance parameter - sCO; showing negligible difference in sCO for uncoated and coated engine cylinder except at low load, where sCO for coated engine cylinder is higher

Fig 5-23 shows the specific HC emissions variation with load. The variation of sCO with load is similar for uncoated and coated engine blocks. At low load and higher engine speed it is observed that sHC emission for coated engine block is higher while at higher loads the difference in sHC emission for the coated and uncoated cases is not much. The percentage variation observed from the experiment is around 6.5 % at low load.
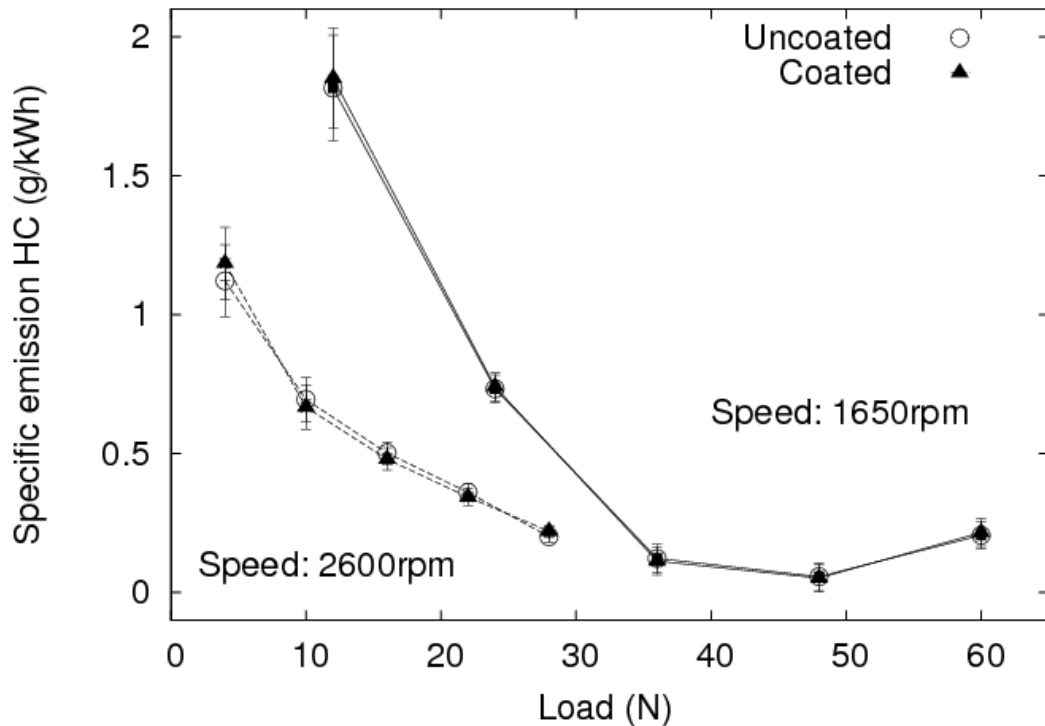
Fig 5-23 Engine performance parameter - sHC; showing negligible difference in sHC for uncoated and coated engine cylinder except at low load, where sHC for coated engine cylinder is slightly higher

Fig 5-24 shows the specific NO emissions variation with load. The variation of sNO with load is similar for uncoated and coated engine blocks. The *sNO* is lower for the coated block than that for the uncoated block throughout the range of loads. Initially sNO decreases to a minimum value and with further increase in load it increases. The difference in sNO emission observed between uncoated and coated engine block is around 10 %. Lower combustion temperatures for the coated engine block as explained earlier leads to lower emission of sNO for coated engine block.

Fig 5-25 shows the variation of smoke opacity with load. The variation of smoke opacity is similar for uncoated and coated engine block. It can be observed from the figure, at low loads the difference in smoke opacity is very less between that of coated and uncoated engine blocks, and however as load increases the difference also increases. It is also observed that the smoke opacity is less for coated engine block (~5.7 %) than that for uncoated engine block. The reason behind lower smoke opacity for coated engine block is lower fuel consumption.
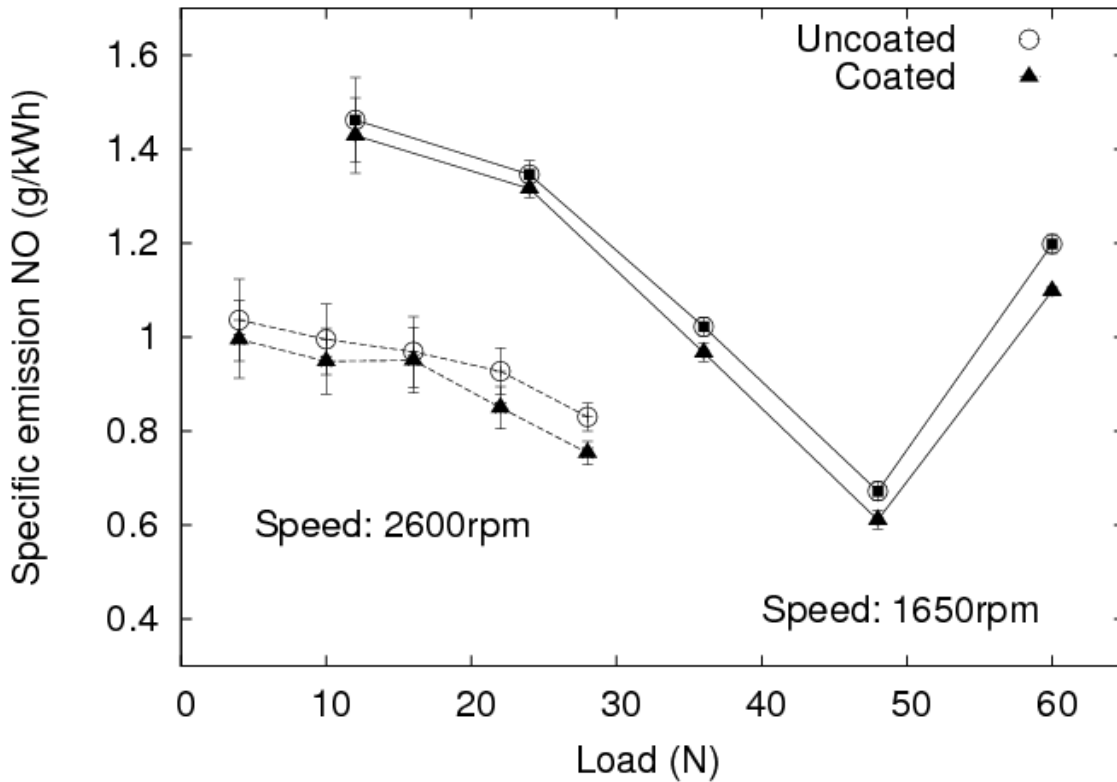
Fig 5-24 Engine performance parameter - sNO; showing reduced sNO in case of coated engine cylinder at all loading conditions
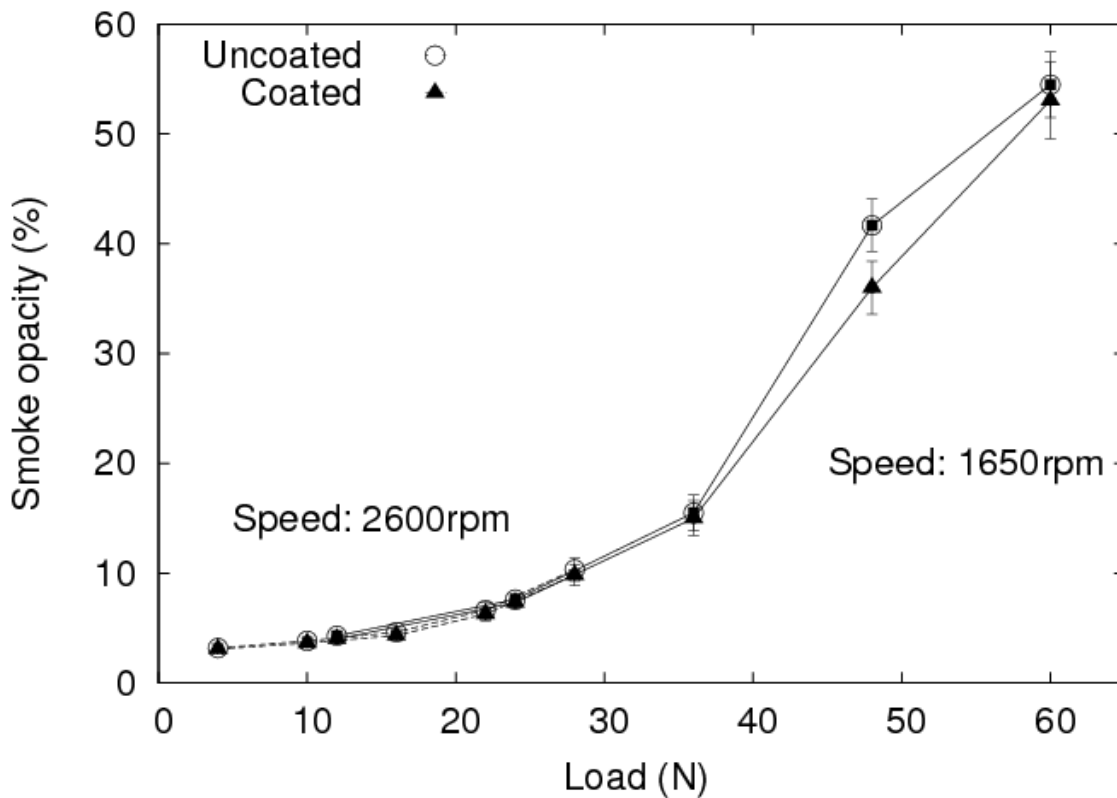
Fig 5-25 Engine performance parameter - Smoke opacity; showing negligible difference in smoke opacity for uncoated and coated engine cylinder except at higher loading conditions (>30 N), where smoke opacity for coated engine cylinder is less at all loading conditions

5.3 Inference of engine testing

When engine is coated with graphite nanoparticles they form a layer between the piston assembly and engine cylinder wall which actually prevents the solid contact between piston assembly and engine cylinder wall during engine operation. Consequently, the friction power is reduced leading to reduced specific fuel consumption and higher mechanical efficiency. Thus, graphite nano- particles coating on the cylinder surface leads to the improvement in the performance of the engine.

Consequent to the reduction in the fuel consumption in the coated engine, the combustion temperatures are lower leading to increase in the specific emissions of sCO and sHC (at low load ≤12 N only) and decrease in sNO emissions and smoke opacity.

5.4 Optimization of engine performance

Optimization is to find best trade-off between multiple responses of the system/process with respect to the input factors of the system. In the present investigation the engine performance parameters namely friction power, brake specific fuel consumption (BSFC), mechanical efficiency, sCO, sHC, sNO and smoke opacity are considered for optimization. Out of all considered parameters mechanical efficiency has to be maximized while others need to be minimized. So the optimization of engine performance parameters is carried out to uncover the best setting of the engine under present investigation for both the cases, i.e. coated engine cylinder and uncoated engine cylinder. To perform optimization two methods were opted, namely, Taguchi method and Response Surface Methodology-Genetic Algorithm (RSM-GA) method.

5.4.1 Optimization using Taguchi method

Based on the condition in present investigation, L_{32} ($2^1 \times 4^9$) orthogonal array was found to be best experimental design for analysis and optimization. As in present investigation, the experimentations are bound for one factor i.e. engine cylinder (only 2 levels, uncoated and coated) and the maximum level for this input factor can be 2 only. While other considered factors in present investigation (speed, load, CFR-Coolant flow rate) can be varied accordingly. So based on the given condition L_{32} orthogonal array was found to be suitable. In the present investigation the experimentations are conducted with one factor with two level and three other factors with four levels. The experimental design matrix of considered L_{32} orthogonal array is provided in Table 5-7. In present investigation, the considered input factors as well as responses are tabulated in Table 5-8.

Table 5-7 L₃₂ Orthogonal array

			Factors							
No.	A	B	C	D	E	F	G	H	I	J
1	1	1	1	1	1	1	1	1	1	1
2	1	1	2	2	2	2	2	2	2	2
3	1	1	3	3	3	3	3	3	3	3
4	1	1	4	4	4	4	4	4	4	4
5	1	2	1	1	2	2	3	3	4	4
6	1	2	2	2	1	1	4	4	3	3
7	1	2	3	3	4	4	1	1	2	2
8	1	2	4	4	3	3	2	2	1	1
9	1	3	1	2	3	4	1	2	3	4
10	1	3	2	1	4	3	2	1	4	3
11	1	3	3	4	1	2	3	4	1	2
12	1	3	4	3	2	1	4	3	2	1
13	1	4	1	2	4	3	3	4	2	1
14	1	4	2	1	3	4	4	3	1	2
15	1	4	3	4	2	1	1	2	4	3
16	1	4	4	3	1	2	2	1	3	4
17	2	1	1	4	1	4	2	3	2	3
18	2	1	2	3	2	3	1	4	1	4
19	2	1	3	2	3	2	4	1	4	1
20	2	1	4	1	4	1	3	2	3	2
21	2	2	1	4	2	3	4	1	3	2
22	2	2	2	3	1	4	3	2	4	1
23	2	2	3	2	4	1	2	3	1	4
24	2	2	4	1	3	2	1	4	2	3
25	2	3	1	3	3	1	2	4	4	2
26	2	3	2	4	4	2	1	3	3	1
27	2	3	3	1	1	3	4	2	2	4
28	2	3	4	2	2	4	3	1	1	3
29	2	4	1	3	4	2	4	2	1	3
30	2	4	2	4	3	1	3	1	2	4
31	2	4	3	1	2	4	2	4	3	1
32	2	4	4	2	1	3	1	3	4	2

Table 5-8 Input and output parameters details used in Taguchi method

Sl.	Parameters	Levels	Values	Symbolic representation	Factor/Response
1	Engine cylinder	Level 1	1- Uncoated	A1	Input factor (A)
		Level 2	2- Coated	A2	
2	Speed (rpm)	Level 1	1400	B1	Input factor (B)
		Level 2	1800	B2	
		Level 3	2200	B3	
		Level 4	2600	B4	
3	Load (N)	Level 1	4	C1	Input factor (C)
		Level 2	12	C2	
		Level 3	20	C3	
		Level 4	28	C4	
4	CFR (l/s)	Level 1	0.18	D1	Input factor (D)
		Level 2	0.20	D2	
		Level 3	0.23	D3	
		Level 4	0.26	D4	
5	BSFC (g/kWh)	---	---	R1	Response
6	Friction power (kW)	---	---	R2	Response
7	Mechanical efficiency (%)	---	---	R3	Response
8	sCO (g/kWh)	---	---	R4	Response
9	sHC (g/kWh)	---	---	R5	Response
10	sNO (g/kWh)	---	---	R6	Response
11	Smoke opacity (%)	---	---	R7	Response

After selecting all the input parameters and their levels based on selected orthogonal array, experimentations are conducted in random order (to avoid systematic error in taking readings) and the responses are tabulated in Table 5-9 with the mean and signal to noise ratio (S/N) for each response. The mean and S/N value was computed for three repetitive responses for each experiment.

Table 5-9 Response of testing

R1		R2		R3		R4		R5		R6		R7	
mean	S/N	mean	S/N	mean	S/N	mean	S/N	mean	S/N	mean	S/N	mean	S/N
1130.19	-61.06	0.98	0.18	23.03	27.25	36.31	-31.2	4.43	-12.93	2.23	-6.98	2.23	-6.98
478.26	-53.59	0.99	0.06	46.37	33.32	18.95	-25.55	2.26	-7.08	1.97	-5.89	1.97	-5.89
353.33	-50.96	1.01	-0.09	59.45	35.48	9.53	-19.58	1.14	-1.16	1.61	-4.14	1.61	-4.14
306.95	-49.74	1.07	-0.59	65.73	36.36	3.98	-12	0.69	3.22	1.36	-2.69	1.36	-2.69
1099.56	-60.82	1.37	-2.71	21.42	26.62	22.42	-27.01	3.34	-10.47	1.79	-5.06	1.79	-5.06
478.93	-53.61	1.39	-2.84	44.19	32.91	11.7	-21.36	1.78	-5.01	1.67	-4.47	1.67	-4.47
350.42	-50.89	1.42	-3.07	57.02	35.12	6.59	-16.38	0.88	1.08	1.5	-3.5	1.5	-3.5
292.55	-49.32	1.41	-3	64.72	36.22	3.31	-10.39	0.54	5.35	1.24	-1.89	1.24	-1.89
1150.96	-61.22	1.95	-5.82	19.44	25.77	12.12	-21.67	1.95	-5.79	1.36	-2.69	1.36	-2.69
495.15	-53.89	1.97	-5.9	41.99	32.46	5.91	-15.43	1.09	-0.75	1.31	-2.35	1.31	-2.35
356.7	-51.05	1.96	-5.83	53.94	34.64	3.2	-10.11	0.59	4.58	1.13	-1.09	1.13	-1.09
310.3	-49.84	2.02	-6.12	61.59	35.79	1.52	-3.62	0.36	8.87	0.99	0.09	0.99	0.09
1229.73	-61.8	2.42	-7.68	18.36	25.28	6.53	-16.3	1.12	-1.01	1.04	-0.31	1.04	-0.31
512.03	-54.19	2.32	-7.3	40.72	32.2	3.71	-11.38	0.63	3.97	1.01	-0.09	1.01	-0.09
370.22	-51.37	2.65	-8.45	50.49	34.06	1.69	-4.57	0.38	8.4	0.9	0.88	0.9	0.88
295.73	-49.42	2.53	-8.06	60.11	35.58	0.56	5.09	0.2	13.98	0.83	1.62	0.83	1.62
1114.62	-60.94	0.87	1.21	25.2	28.03	39.46	-31.92	4.57	-13.19	2.06	-6.3	2.06	-6.3
465.62	-53.36	0.86	1.31	50.17	34.01	19.51	-25.81	2.3	-7.23	1.9	-5.57	1.9	-5.57
339.72	-50.62	0.86	1.35	62.97	35.98	11	-20.82	1.28	-2.14	1.64	-4.3	1.64	-4.3
294.09	-49.37	0.83	1.62	71.2	37.05	4.57	-13.2	0.64	3.87	1.31	-2.35	1.31	-2.35
1071.24	-60.6	1.24	-1.84	23.44	27.4	23.02	-27.24	3.31	-10.4	1.66	-4.4	1.66	-4.4

462.24	-53.3	1.24	-1.84	47.63	33.56	12.5	-21.94	1.75	-4.84	1.63	-4.24	1.63	-4.24
329.58	-50.36	1.24	-1.9	60.54	35.64	6.46	-16.2	0.9	0.96	1.43	-3.08	1.43	-3.08
281.39	-48.99	1.2	-1.58	68.38	36.7	3.01	-9.58	0.52	5.61	1.21	-1.65	1.21	-1.65
1132.06	-61.08	1.7	-4.63	21.46	26.63	13.16	-22.38	2.01	-6.08	1.29	-2.24	1.29	-2.24
469	-53.42	1.74	-4.79	44.17	32.9	7.31	-17.28	1.15	-1.25	1.27	-2.07	1.27	-2.07
336.34	-50.54	1.71	-4.64	57.5	35.19	3.29	-10.33	0.58	4.74	1.15	-1.22	1.15	-1.22
271.25	-48.67	1.71	-4.64	65.59	36.34	1.67	-4.45	0.37	8.63	0.95	0.45	0.95	0.45
1154.33	-61.25	2.07	-6.34	20.79	26.36	7.72	-17.76	1.18	-1.47	1	0.04	1	0.04
475.75	-53.55	2.35	-7.41	40.6	32.17	3.31	-10.41	0.58	4.75	0.89	0.97	0.89	0.97
336.34	-50.54	2.06	-6.26	56.58	35.05	1.78	-5.02	0.39	8.18	0.92	0.72	0.92	0.72
264.88	-48.46	2.19	-6.8	63.51	36.06	0.53	5.58	0.22	13.15	0.75	2.45	0.75	2.45

After completion of all the experimentations as per considered experimental matrix, further analysis of the data is required to check the effect of each considered input factor on all the responses. ANOVA is used in Taguchi method to determine the effect of each considered input parameters on the response [174] as well as a brief description is provided in Appendix-III. In Taguchi method, factor response plot is one of the significant plots which shows the effect of all considered levels of each factor involved in processing/testing on the considered output of the system. Factor response plot comprises of X-axis with all the considered factors and Y-axis represents the average value of the response against considered input factor and its level. The factor response plot for present investigation is shown in Fig 5-26. Using factor response plot, the significant influencing input factor(s) as well as their level can be pointed out for each individual output parameter.

Let us consider the engine output parameter or response 'R1', for which the most significant input factor and its level can be observed as 'C4', which means the variation of input factor 'C' have the maximum impact on response 'R1' while other input factors (A, B and D) variation have minor impact on response 'R1', but compared to B and D, input factor A have higher impact on response 'R1'.

And the maximum value of load (input factor C) is the best solution for response 'R1' (i.e. lower BSFC). All the input factors used for analysis of the factors average effect on specific response, and based on the analysis each factor influencing potential for individual response are plotted in Fig 5-26 as well as each input factors intensity of significance of all the input factors for all the cases are tabulated in Table 5-10. Based on the observation from response factor plot the value of each input factor can be decided accordingly for specific response. And these values can be used to find optimal value of specific response, and the computation can be performed using optimal solution formula which can be referred from Appendix-III. The effect of various input factors on specific engine output parameter is tabulated in Table 5-10.
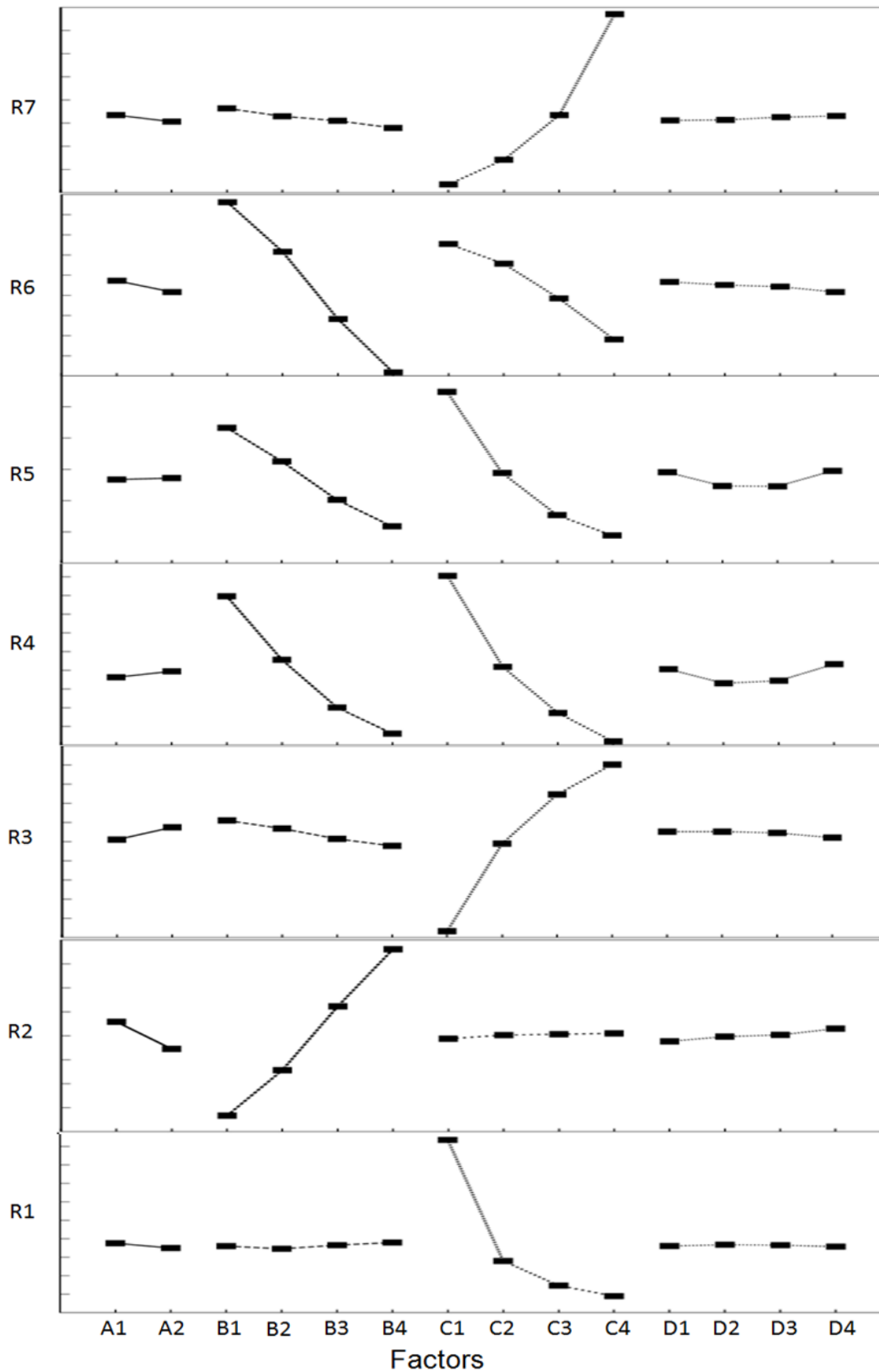
Fig 5-26 Factor response plot for all engine output parameters (R1-BSFC; R2-FP; R3-Mechanical efficiency; R4-sCO; R5-sHC; R6-sNO; R7-Smoke opacity; A, B, C, D are input factors corresponds to engine cylinder, speed, load and CFR)

Table 5-10 Percentage contribution of inputs on output chart

Engine output parameter	Set of inputs	% contribution
BSFC	Engine cylinder	3.74
	Speed	1.33
	Load	94.7
	CFR	0.19
Friction power	Engine cylinder	18.76
	Speed	77.12
	Load	2.27
	CFR	1.78
Mechanical efficiency	Engine cylinder	8.42
	Speed	7.08
	Load	82.12
	CFR	2.37
sCO	Engine cylinder	2.83
	Speed	45.26
	Load	49.79
	CFR	1.97
sHC	Engine cylinder	1.79
	Speed	37.08
	Load	58.27
	CFR	2.78
sNO	Engine cylinder	4.73
	Speed	61.48
	Load	31.67
	CFR	2.02
Smoke opacity	Engine cylinder	3.82
	Speed	4.64
	Load	89.59
	CFR	1.93

The optimization of engine output parameters are performed based on their requirement, as in case of R1 (BSFC) it is expected to be lower. So for that reason, each input factor level selected which gives decreased value of R1 response. So the input factors responsible for lowering BSFC are found as A2-B2-C4-D3 from the analysis, which can be referred in Table 5-11. Using these input factor level values, the optimal value of R1 computed, which came around 254.28, which may be interpreted as BSFC of 254.28 g/kWh can be obtained with coated engine cylinder, speed of 1800 rpm, load of 28 N and 0.23 l/s of CFR. Similarly, for all other responses, optimal value are computed and the details are provided in Table 5-11. Using Taguchi method, the effect of individual factor and their variation on each response was uncovered successfully. But based on the observation of optimization analysis of responses, the input set is varying for each response system.

Table 5-11 Optimization results using standard method

Response	Input set selected	Optimal value	Physical variables
R1	A2-B2-C4-D3	254.28	BSFC
R2	A2-B1-C1-D1	0.74	Friction power
R3	A2-B1-C4-D2	70.53	Mechanical efficiency
R4	A1-B4-C4-D2	9.11	sCO
R5	A1-B4-C4-D2	2.08	sHC
R6	A2-B4-C4-D3	1.07	sNO
R7	A2-B4-C1-D2	2.73	Smoke opacity

In present case, it can be observed that for seven different responses (R1 to R7) there are seven sets of inputs obtained for providing optimal values of each response. As it is not possible to generalize the whole set of inputs to a common input system, this method conveniently gives us the optimization with respect to individual responses. And as per current trend in the automotive and engine industry regarding fuel economy and environmental norms, it is not possible to compromise any engine parameters which involves fuel economy or environmental issues. With such a basis it was decided to provide proper optimization of engine input parameters, so that we can get a balanced response system which is both economical and environmental friendly. To achieve it the multi objective optimization conducted using RSM-GA method is discussed in the next section.

From analysis and optimization results using Taguchi method, it can be observed that overall performance of the coated engine is better than uncoated engine. As coated engine have positive impact on BSFC, Friction power, Mechanical efficiency, specific emission NO and smoke opacity while slight negative impact on specific emissions of carbon monoxide and unburnt hydrocarbons. The negative impact is little bit higher at low loading condition only while at higher loading condition there is negligible difference found between coated engine and uncoated engine regarding specific emission carbon monoxide and unburnt hydrocarbons.

5.4.2 Optimization using RSM-GA method

The optimization of the engine performance parameters was performed in two phases, first phase is for uncoated engine block and the second phase was with the coated engine block. In both the cases same methodology was adopted as explained below:

    a) Considered experimental design matrix – Box Behnken design in RSM

    b) Response surface model – RSM

    c) Transformation function for response models – ANOVA in RSM

    d) Multi-objective optimization – GA

RSM is a statistical technique used for modeling and analysis of any process or method in which several variables influence the response of the system. RSM has been found to be effective in optimizing single objective at a time. Practically the initial requirement of response surface is to choose experimental design, such that an adequately efficient response surface model can be obtained with minimum number of experiments [101]. The main objective is to check the effect of coating on engine performance at optimum engine setting, rather than rigorous experimentation for optimization. So the design of experiment (with least number of experiments) had been chosen to establish relationship between input and response parameters and it was found that Box-Behnken design is one of the suitable designs for the present investigation.

For uncoated engine block

The experimental matrix opted for establishing input-output relation is based on Box-Behnken design as shown in Table 5-12. In which there are three input factors while others are responses. All the response parameter data obtained from the experimental runs based on considered experimental design were used to generate quadratic response surface models. In RSM, the first step is to find the appropriate model approximating function (transformation function) for an apt functional relationship between the set of input factors and the response. In the present investigation a second-order polynomial model is employed to fit the response surfaces of output parameters using input factors namely speed, load and CFR. The transformation function generated for each response using second-order polynomial model were cross checked with the help of Box-Cox plot for its confidence or efficacy. The brief description about Box-Cox plot is given here for better understanding of the method.

Box-Cox plot

This plot represents a potential continuum of transformations that provide a range of opportunities for closely calibrating a transformation to the needs of the data and can be used effectively for objective identification. The form of the Box-Cox transformation is represented as Equation (5-1).

$$y_i^\lambda = \begin{cases} y_i^\lambda & \text{where } \lambda \neq 0; \\ \log_e(y_i) & \text{where } \lambda = 0; \end{cases} \qquad (5-1)$$

After modification, Box-Cox transformation becomes a tool to identify an appropriate exponent (λ-Lambda) for use to transform data into a "normal shape". In order to perform this, the Box-Cox power transformation searches from $\lambda = -5$ to $+5$ until the best value is found.

Table 5-12 Experimental matrix and their responses for uncoated engine

Sl	Input factors			Responses						
	Speed	Load	CFR	BSFC	Friction power	Mechanical Efficiency	sCO	sHC	sNO	Smoke opacity
	rpm	N	l/s	g/kWh	kW	%	g/kWh	g/kWh	g/kWh	%
1	2000	16	0.22	399.4	1.676	50	5.717	0.9914	1.404	5.033
2	2600	16	0.26	431.4	2.6	45.6	2.352	0.4809	0.9284	4.733
3	2000	28	0.26	315.3	1.83	61.58	1.825	0.4093	1.046	11.03
4	2600	4	0.22	1230	2.42	18.37	6.534	1.122	1.036	3.183
5	2600	16	0.18	430.7	2.35	48.11	2.481	0.5073	0.9706	4.733
6	1400	16	0.26	396.3	1.01	53.74	12.1	1.48	1.729	5.933
7	2000	16	0.22	399.4	1.676	50	5.717	0.9914	1.404	5.033
8	2000	28	0.18	314.8	1.61	64.56	1.914	0.3913	1.123	11.03
9	1400	16	0.18	396	0.97	54.74	12.33	1.572	1.752	5.833
10	2000	16	0.22	399.4	1.676	50	5.717	0.9914	1.404	5.033
11	1400	28	0.22	306.1	1.01	67.03	4.057	0.6629	1.39	11.63
12	2000	16	0.22	399.4	1.676	50	5.717	0.9914	1.404	5.033
13	1400	4	0.22	1129	0.98	23.04	36.31	4.563	2.211	3.683
14	2600	28	0.22	295.6	2.53	60.12	0.559	0.2013	0.8302	10.33
15	2000	4	0.18	1132	1.58	20.96	17.55	2.68	1.643	3.283
16	2000	16	0.22	399.4	1.676	50	5.717	0.9914	1.404	5.033
17	2000	4	0.26	1133	1.67	20.06	16.8	2.768	1.555	3.333

Best solution range is plotted in box-cox plot in which abscissa and ordinate are λ and Ln(ResidualSS) where 'λ' indicates the power of the objective to which all data should be raised and 'Ln(ResidualSS)' is the natural logarithm of sum of squares of error residual. The corresponding value of λ is preferred against which Ln(ResidualSS) reported value is low, that confirms the least error in the current transformation function (CTF). The stepwise process of objective identification is as under:

Step 1: Finding transformation/fitting function with n^{th} order polynomial (second order in present case) for each objective with the selection of 'none' option for power transformation

Step 2: Performing check of transformation/fitting function with the help of Box-Cox plot for its best results. If transformation function lies within the 95 % confidence interval (95 % C.I.), no transformation is required, else power transformation law will be applied.

Step 3: Check the transformation/fitting function after applying the power transformation law.

It is performed to establish efficient target response system with respect to input variables, Box-Cox plot for all the objectives namely BSFC, Friction power, Mechanical efficiency, sCO, sHC, sNO and Smoke opacity is shown in Fig 5-27, Fig 5-28, Fig 5-29, Fig 5-30, Fig 5-31, Fig 5-32, and Fig 5-33 respectively.
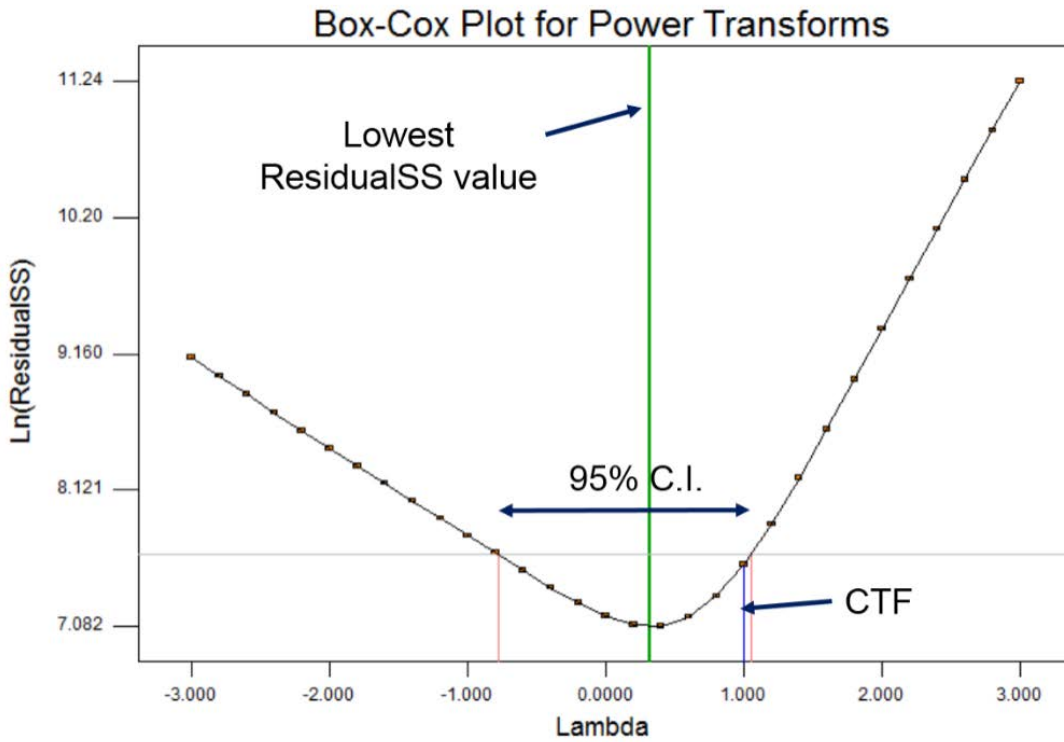
Fig 5-27 Box-Cox Plot of the response BSFC; showing current transformation function lying within 95 % C.I. which indicates the transformation function of response BSFC is reliable
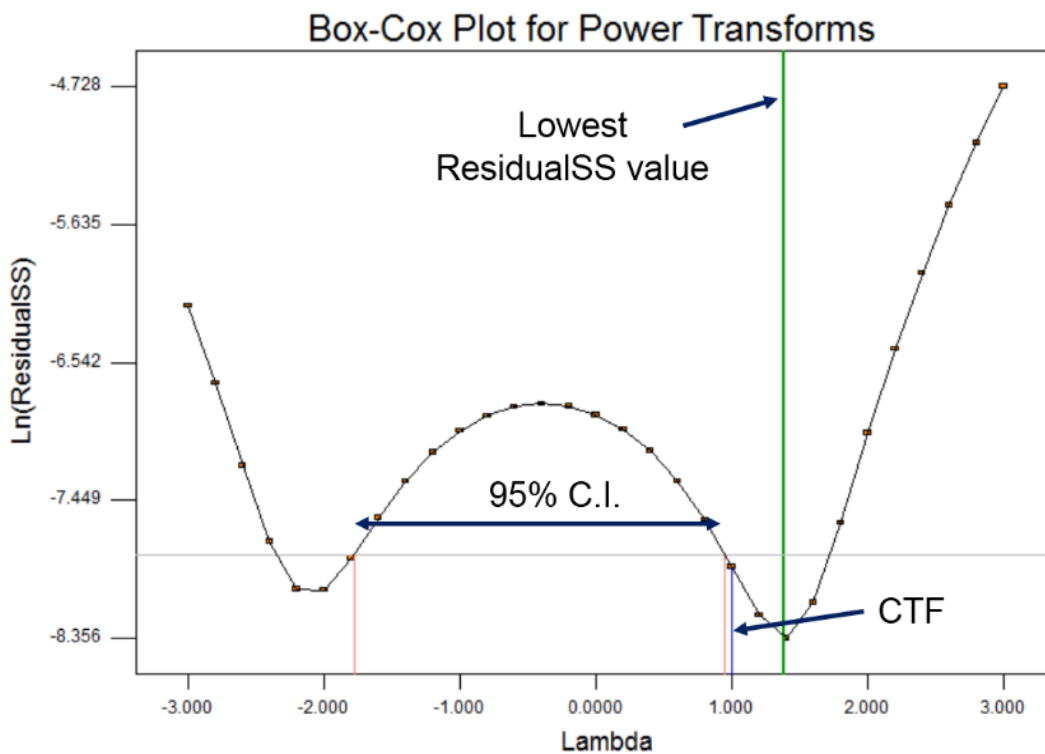
Fig 5-28 Box-Cox Plot of the response friction power; showing current transformation function lying outside 95 % C.I. which indicates that the transformation function of response friction power is not reliable and power transformation law should be applied to make transformation function reliable
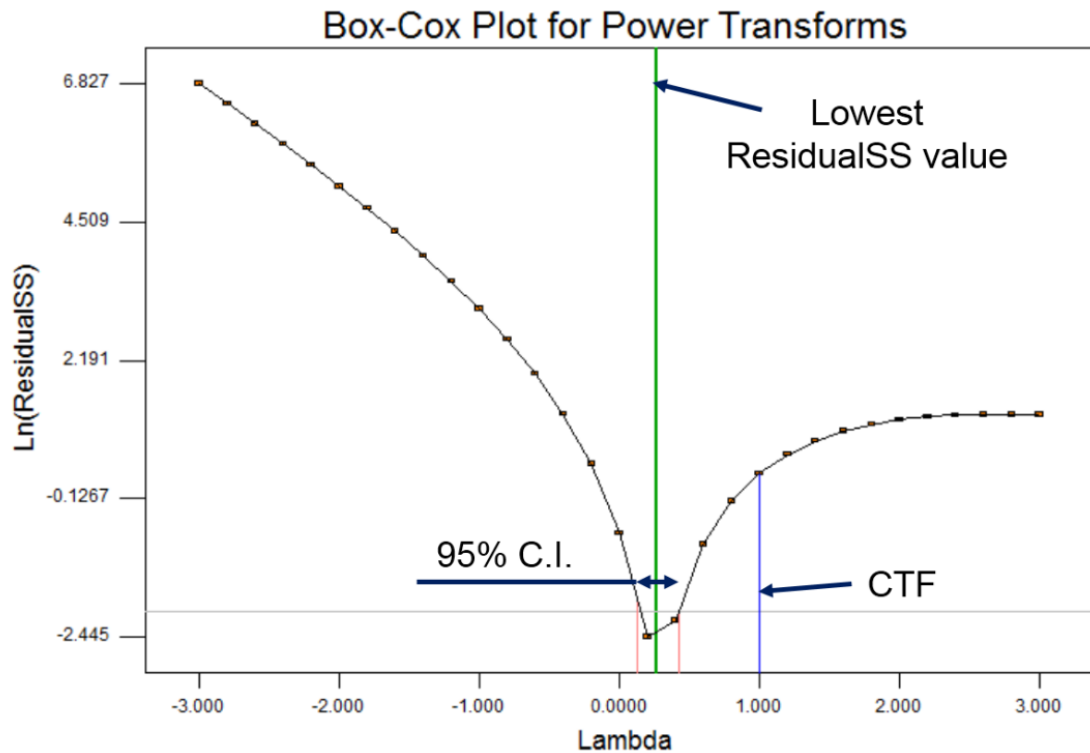
Fig 5-29 Box-Cox Plot of the response mechanical efficiency; showing current transformation function lying far from 95 % C.I. which indicates that the transformation function of response friction power is not reliable and power transformation law should be applied to make transformation function reliable
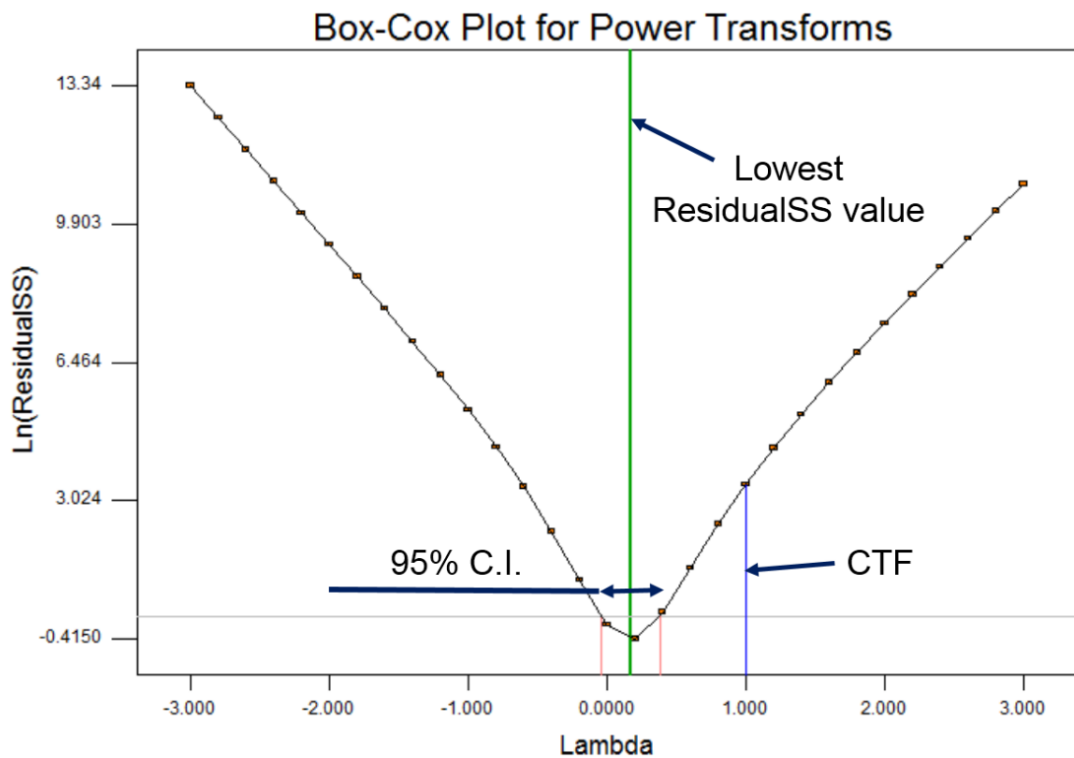
Fig 5-30 Box-Cox Plot of the response sCO; showing current transformation function lying far from 95 % C.I. which indicates that the transformation function of response sCO is not reliable and power transformation law should be applied to make transformation function reliable
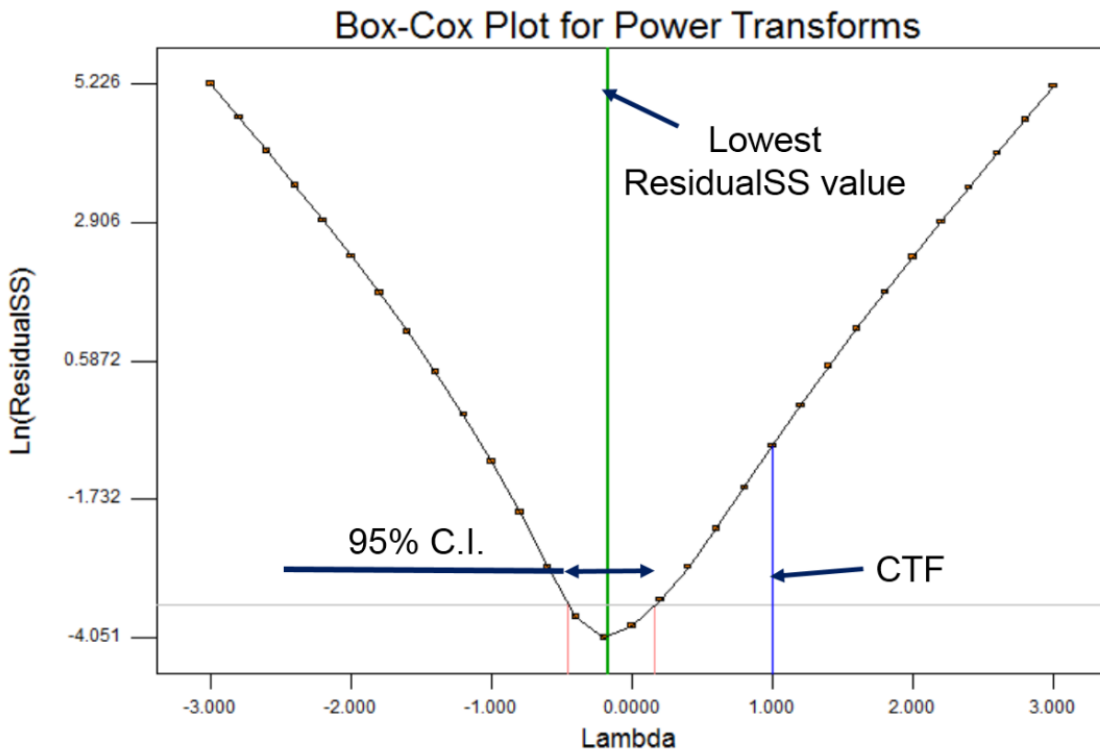
Fig 5-31 Box-Cox Plot of the response sHC; showing current transformation function lying far from 95 % C.I. which indicates that the transformation function of response sHC is not reliable and power transformation law should be applied to make transformation function reliable
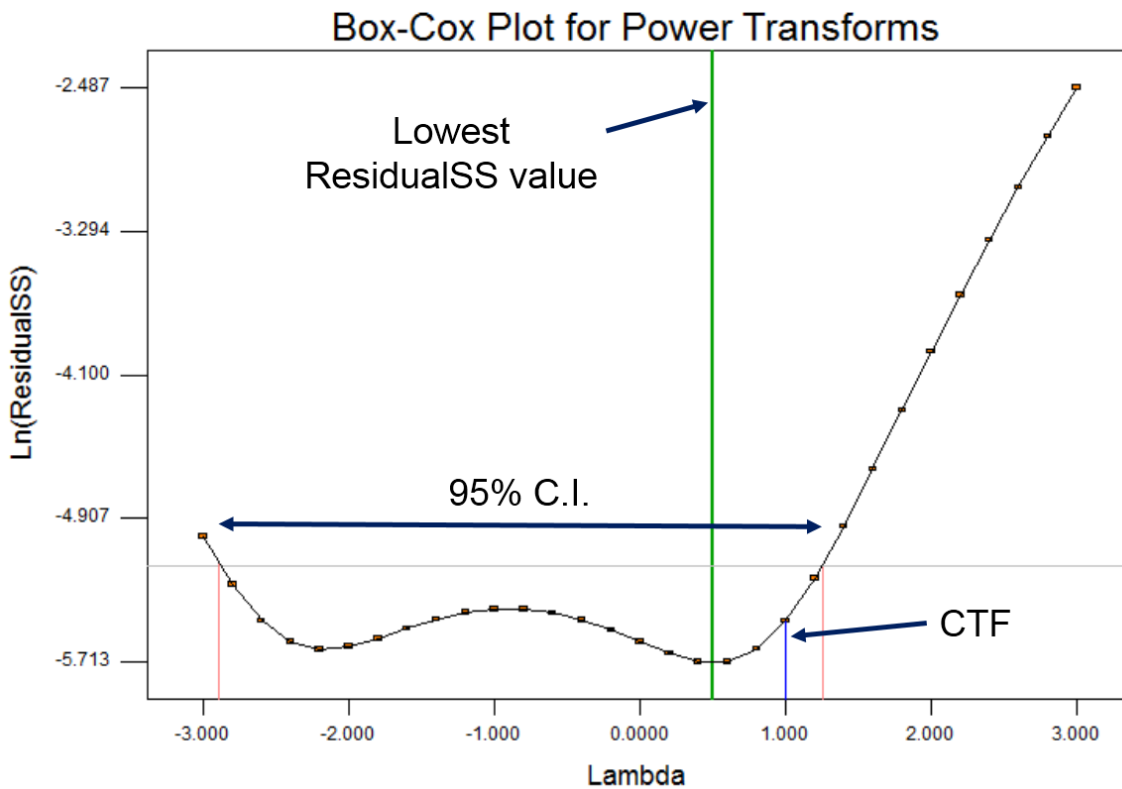
Fig 5-32 Box-Cox Plot of the response sNO; showing current transformation function lying within 95 % C.I. which indicates that the transformation function of response sNO is reliable
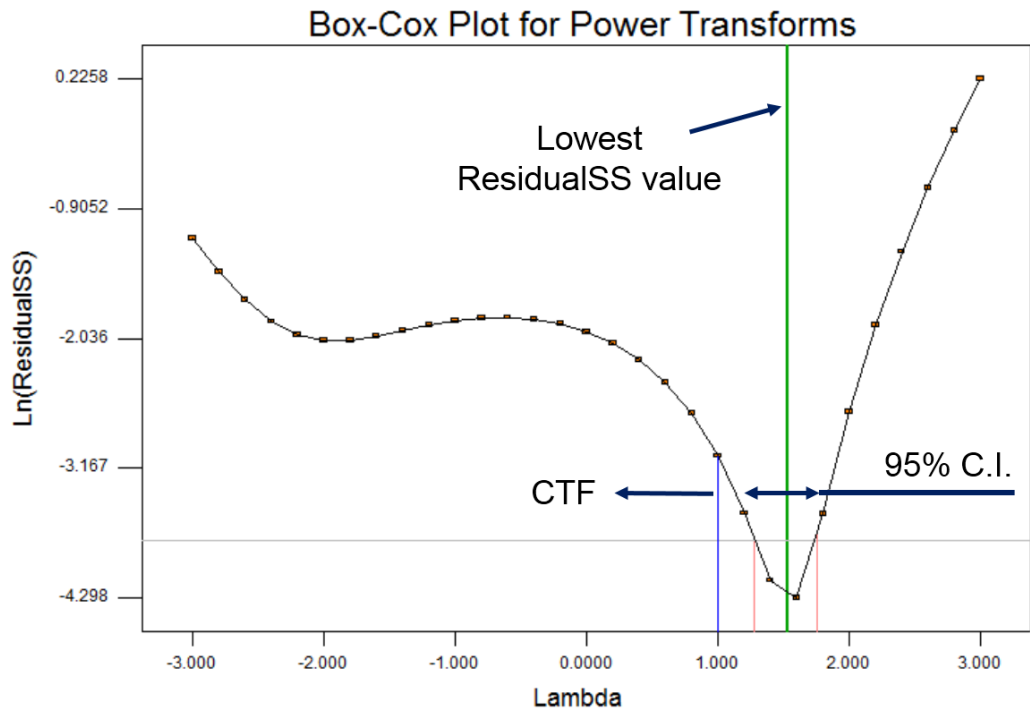
Fig 5-33 Box-Cox Plot of the response smoke opacity; showing current transformation function lying outside 95 % C.I. which indicates that the transformation function of response smoke opacity is not reliable and power transformation law should be applied to make transformation function reliable

In the present investigation as per observations made from Box-Cox plot, power transformation law has been applied for five objectives (responses) namely, Friction power, Mechanical efficiency, sCO, sHC, and Smoke opacity. The accepted mathematical form of RSM response models transformation functions are mentioned in Equation (5-2) which were used for optimization with the aid of GA.

$$
\begin{aligned}
f(1) = {} & 1490 - 75.05E - 03\,x_1 - 99.92\,x_2 + 293.7\,x_3 + 4.23E - 05\,x_1^2 + 2.26\,x_2^2 \\
& - 660.5\,x_3^2 - 3.85E - 03\,x_1x_2 + 3.8E - 03\,x_1x_3 - 0.2121\,x_2x_3 \\[4pt]
f(2) = {} & 1.79 - 1.27E - 03\,x_1 - 31.43E - 03\,x_2 - 6.628\,x_3 + 5.68E - 07\,x_1^2 - 5.69E - 06\,x_2^2 \\
& - 2.059\,x_3^2 + 6.00E - 06\,x_1x_2 + 4.5E - 03\,x_1x_3 + 0.1165\,x_2x_3 \\[4pt]
f(3) = {} & 4.371 - 49.9E - 05\,x_1 + 0.3342\,x_2 - 0.134\,x_3 + 7.65E - 08\,x_1^2 - 58.48E - 04\,x_2^2 \\
& + 3.623\,x_3^2 + 2.76E - 06\,x_1x_2 - 12.06E - 04\,x_1x_3 - 45.85E - 03\,x_2x_3 \\[4pt]
f(4) = {} & 6.18 - 3.21E - 05\,x_1 - 61.18E - 03\,x_2 - 15.05\,x_3 - 2.97E - 07\,x_1^2 - 45.08E - 05\,x_2^2 \\
& + 34.71\,x_3^2 - 9.30E - 06\,x_1x_2 - 35.31E - 05\,x_1x_3 - 20.67E - 04\,x_2x_3 \\[4pt]
f(5) = {} & 2.233 + 36.59E - 05\,x_1 - 0.1049\,x_2 - 1.108\,x_3 - 3.77E - 07\,x_1^2 + 34.01E - 05\,x_2^2 \\
& + 1.726\,x_3^2 + 7.32E - 06\,x_1x_2 + 6.64E - 05\,x_1x_3 + 6.47E - 03\,x_2x_3 \\[4pt]
f(6) = {} & 2.419 - 80.34E - 05\,x_1 - 60.91E - 03\,x_2 + 11.06\,x_3 - 4.64E - 08\,x_1^2 - 13.83E \\
& - 05\,x_2^2 - 26.07\,x_3^2 + 2.14E - 05\,x_1x_2 - 19.97E - 05\,x_1x_3 + 5.36E - 03\,x_2x_3 \\[4pt]
f(7) = {} & 26.55 - 5.58E - 03\,x_1 - 0.4972\,x_2 - 115.4\,x_3 + 1.49E - 06\,x_1^2 + 66.55E - 03\,x_2^2 \\
& + 285.7\,x_3^2 - 17.61E - 05\,x_1x_2 - 3.79E - 03\,x_1x_3 - 0.07105\,x_2x_3
\end{aligned}
\tag{5-2}
$$

where,

$f(1) = BSFC; f(2) = (Friction\ power)^{1.38}; f(3) = (Mechanical\ efficiency)^{0.5};$

$f(4) = ln(sCO); f(5) = ln(sHC); f(6) = sNO; f(7) = (Smoke\ opacity)^{1.5};$

$x1 = Speed; x2 = Load; and\ x3 = CFR$

Significance of the model terms and the precision index value of the individual response model were computed with the help of ANOVA analysis (see Appendix-IV) for uncoated engine block. As per ANOVA analysis the "Adeq Precision" value expresses the signal to noise ratio measurement of the response model, its value being greater than four is indicative of adequate signal for model prediction. All the response models have very high "Adeq Precision" value, which indicate that the models will provide reasonable performance in prediction. The response surface models of all the responses namely BSFC, Friction power, Mechanical efficiency, sCO, sHC, sNO and Smoke opacity are shown in Fig 5-34, Fig 5-35, Fig 5-36, Fig 5-37, Fig 5-38, Fig 5-39, and Fig 5-40, respectively.
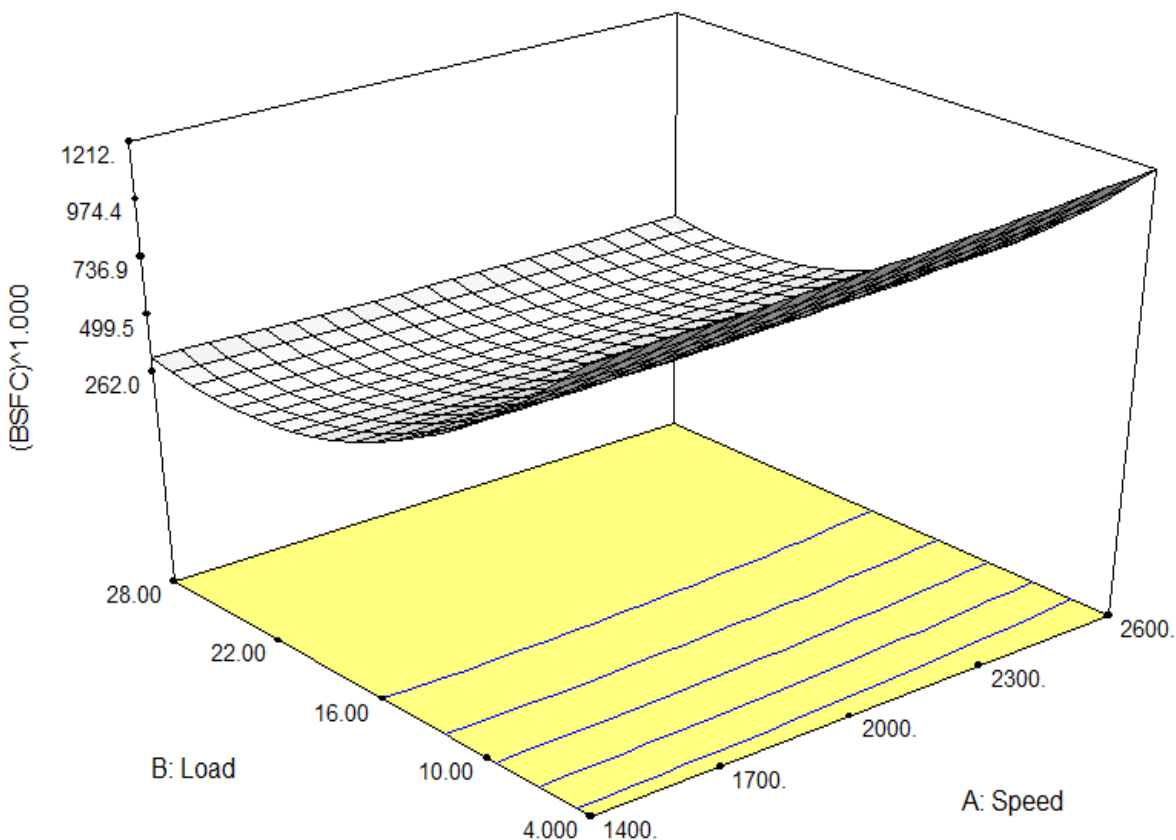
Fig 5-34 Response surface model of the response BSFC (g/kWh); showing significant reduction in BSFC with increase in load
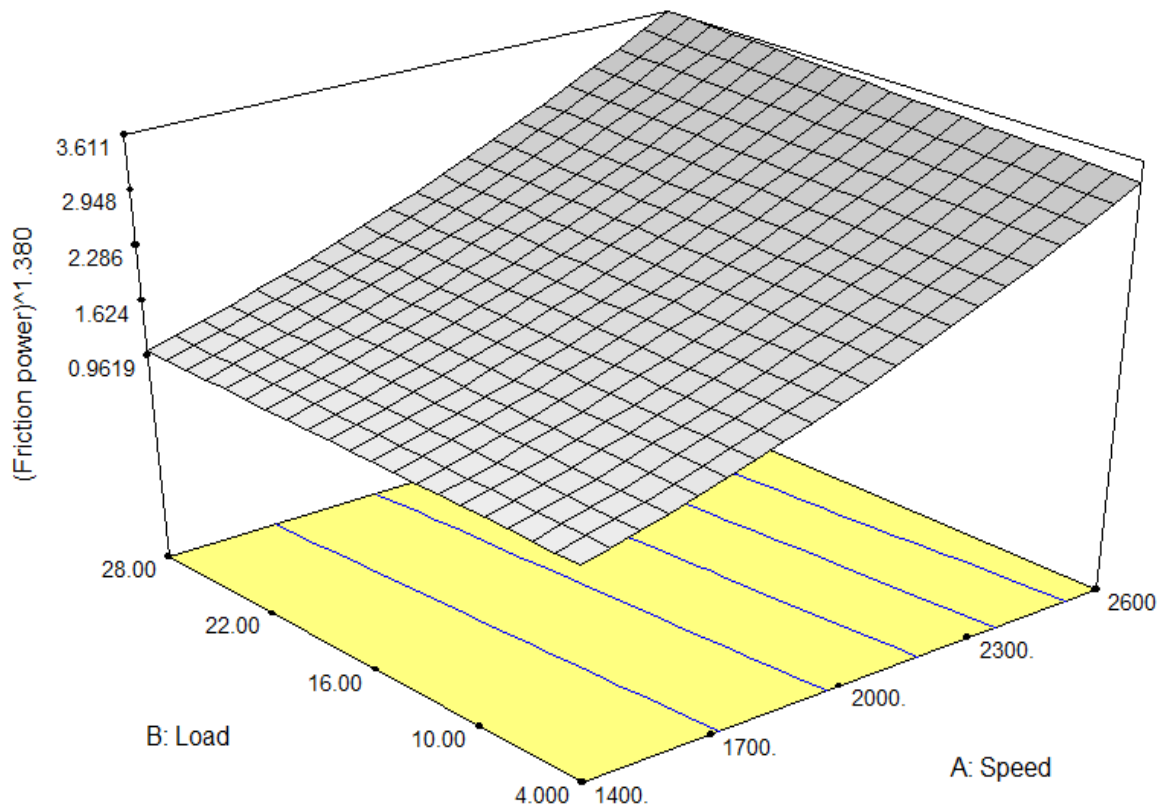
Fig 5-35 Response surface model of the response friction power (kW); showing significant increase in friction power with increase in speed and very little increment with increase in load
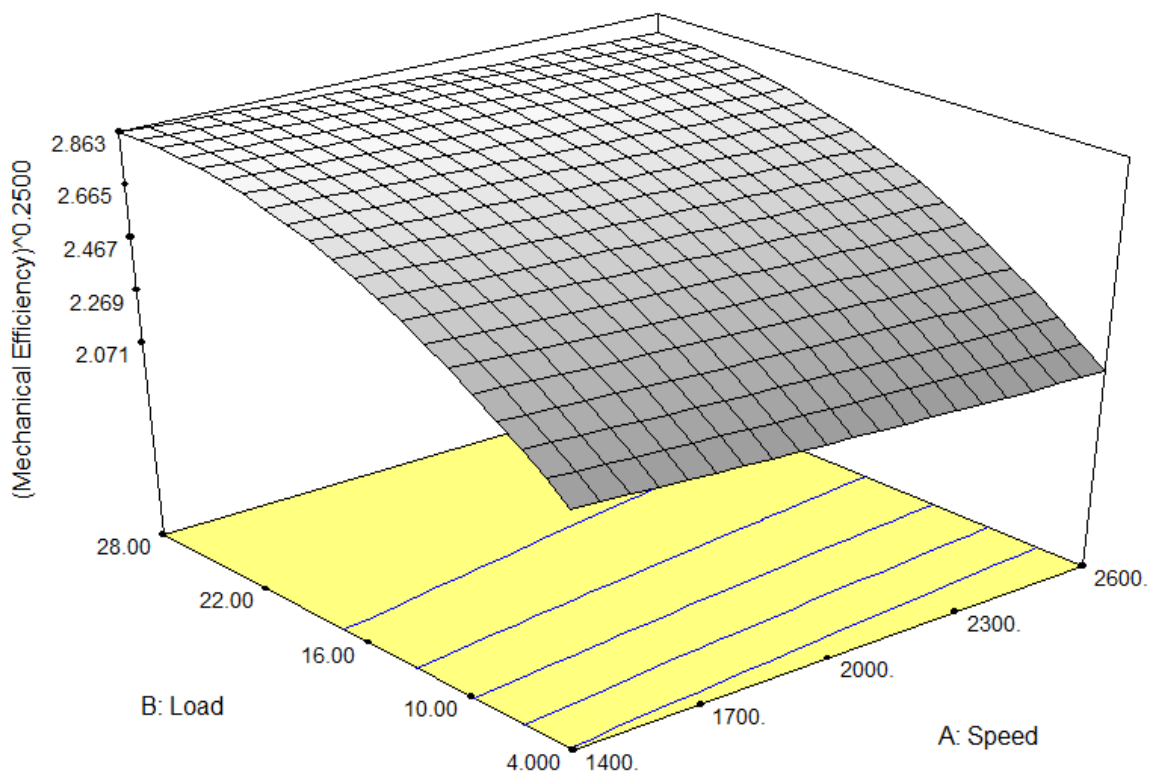
Fig 5-36 Response surface model of the response mechanical efficiency (%); showing significant increase in mechanical efficiency with increase in load and very little decrement with increase in speed
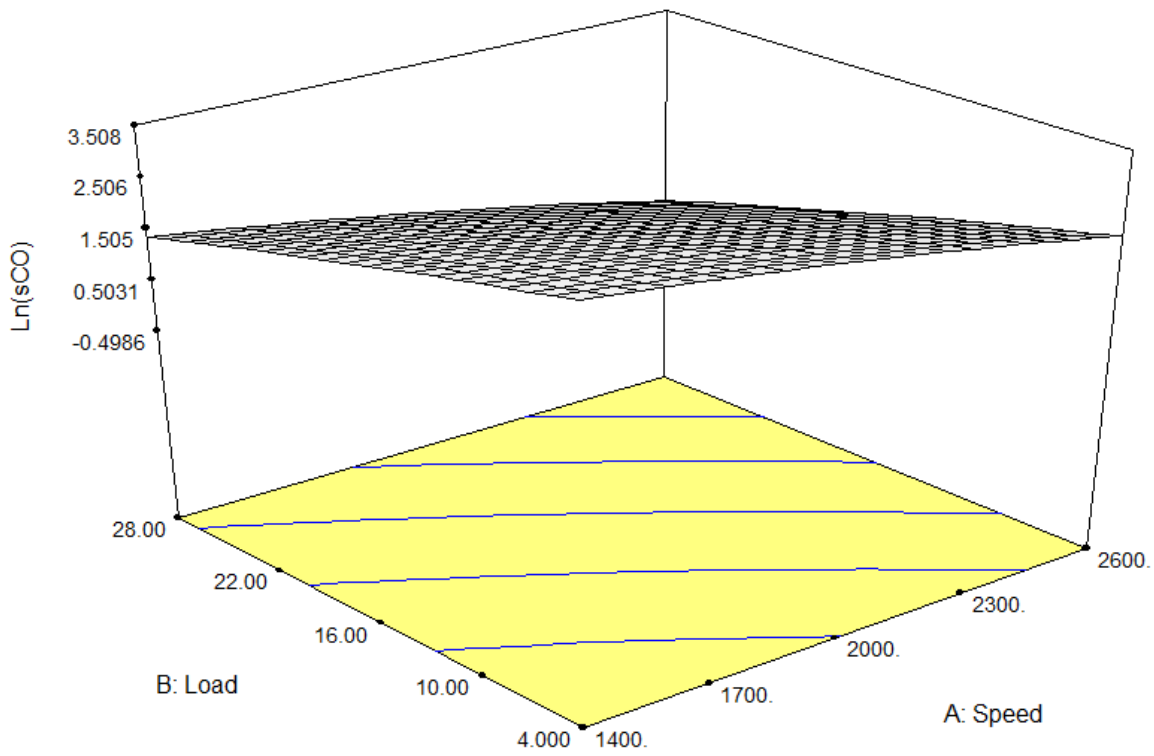
Fig 5-37 Response surface model of the response sCO (g/kWh); showing decrease in sCO with increase in load and speed
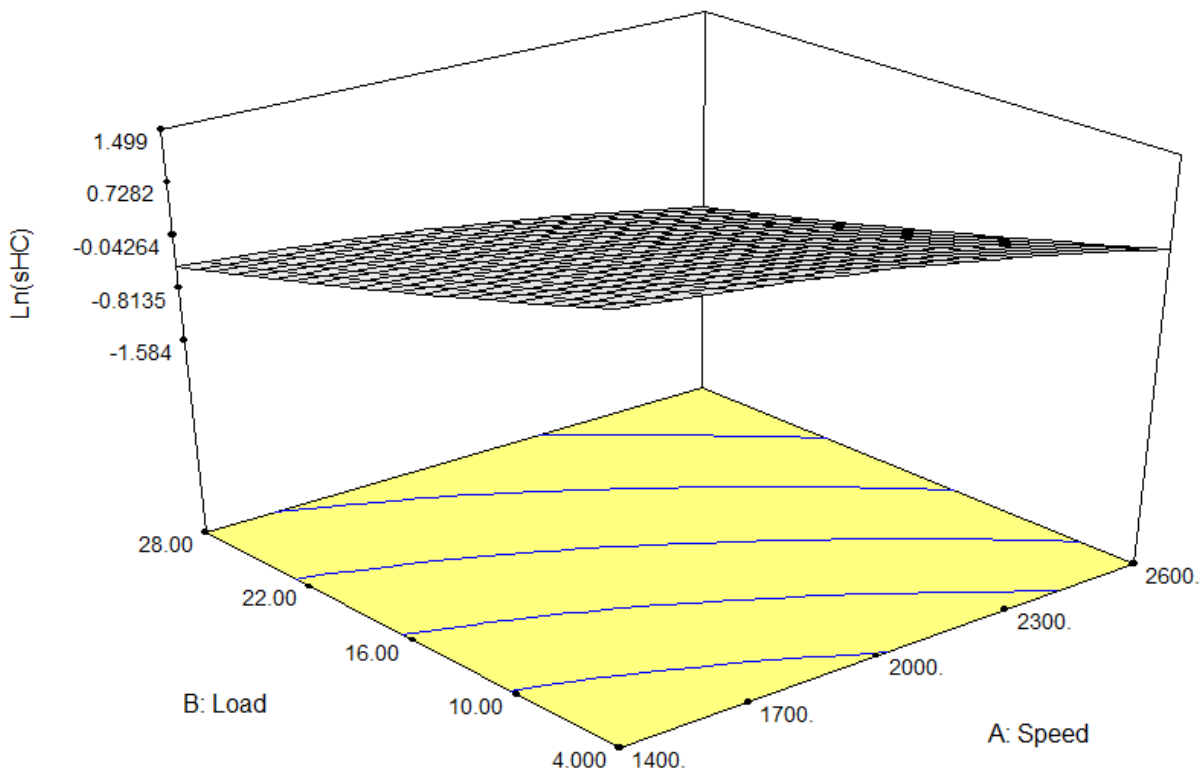
Fig 5-38 Response surface model of the response sHC (g/kWh); showing increase in sHC term with increase in load and speed because of negative power on sHC
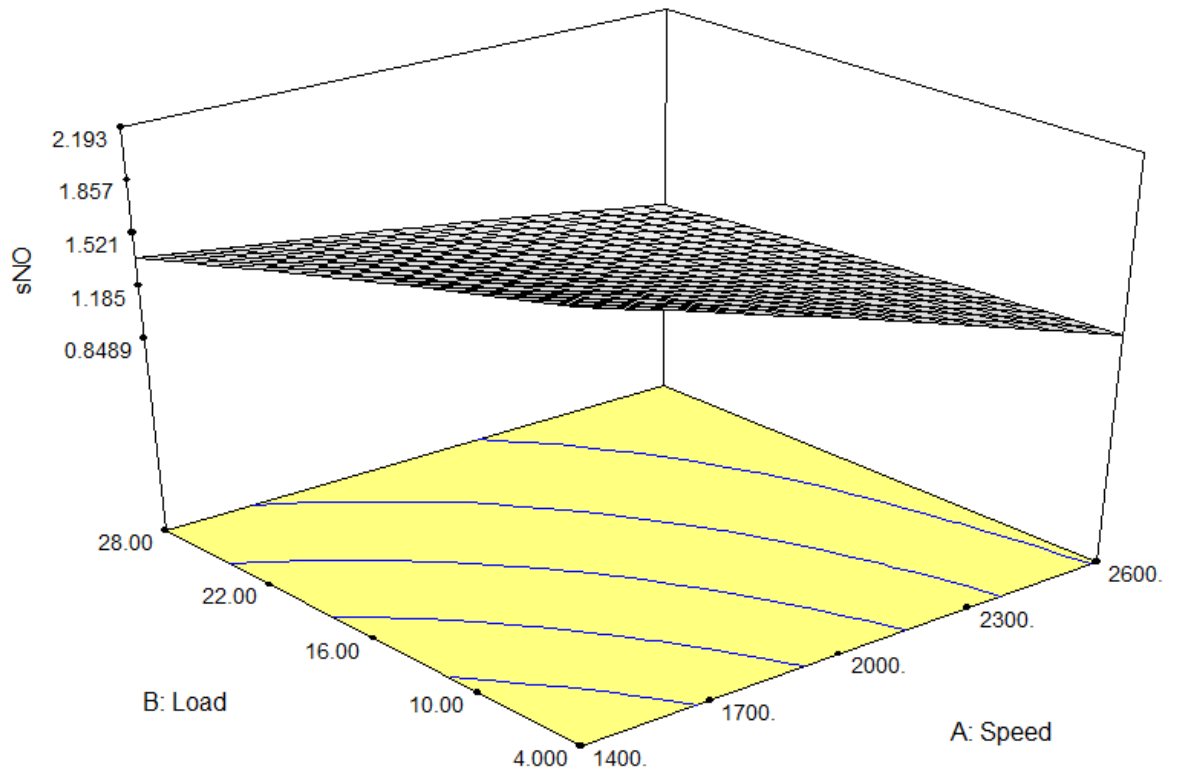
Fig 5-39 Response surface model of the response sNO (g/kWh); showing decrease in sNO with increase in load and speed
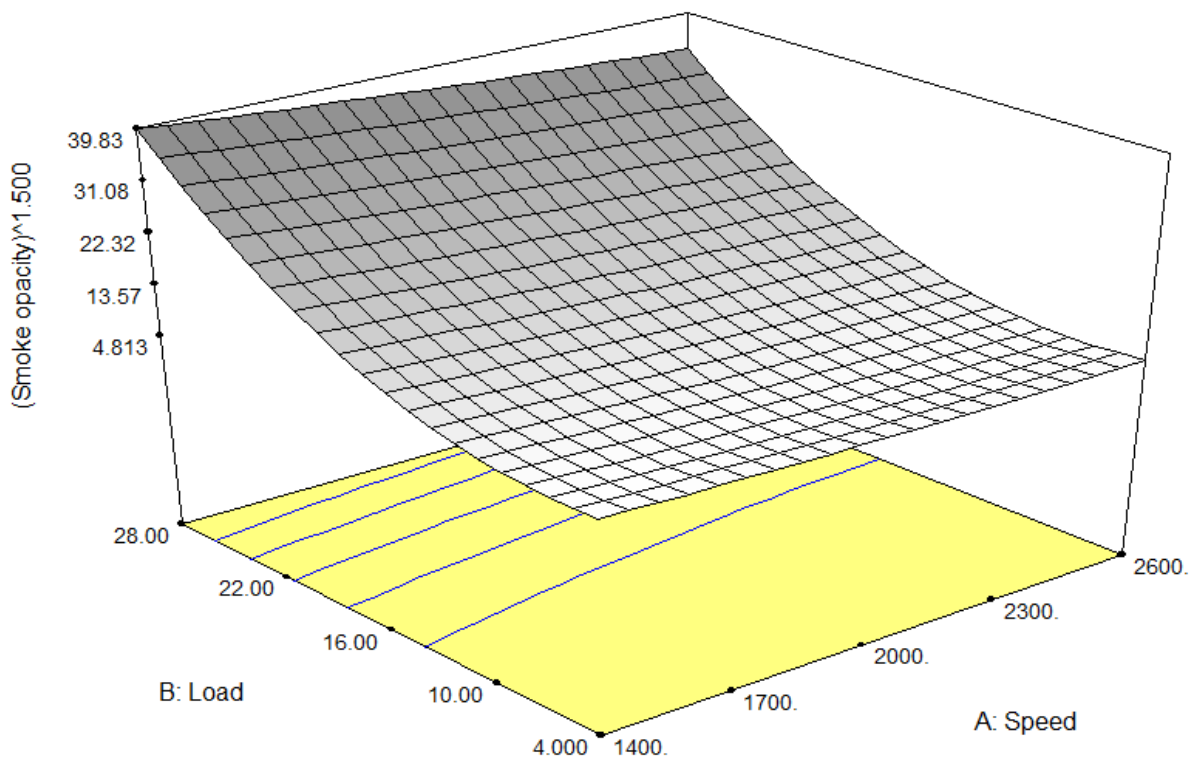
Fig 5-40 Response surface model of the response smoke opacity (%); showing increase in smoke opacity with increase in load and very little decrement with increase in speed

Engine performance optimization using GA for uncoated engine cylinder

In the present investigation GA based multiobjective optimization was performed using Matlab R2012b software platform. GA in Matlab actually performs the search to find a local pareto front for multiple objective functions and mainly concerned with the generation and selection of noninferior solution points. These noninferior solutions are also called pareto optima, so the main goal in GA based multiobjective optimization is constructing the pareto optima. The general functioning step of GA process is presented in Fig 5-41. The algorithm used in Matlab GA command 'gamultiobj' is well described in literature [46].
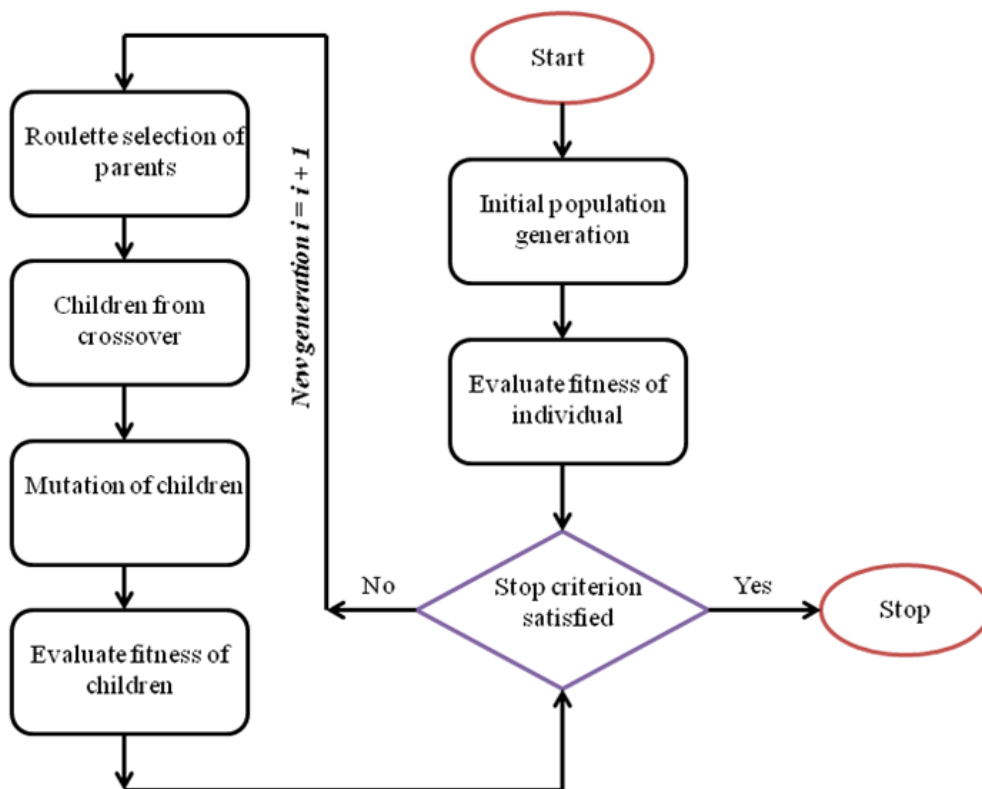
Fig 5-41 Flow chart of genetic algorithm

The quadratic objective functions of all seven responses (refer Equation 5-2) obtained with the aid of RSM were considered for optimization. From the identified seven objective functions, all the functions are to be minimized except Mechanical efficiency function for best engine performance. As multiple objectives are to be optimized simultaneously with different functional constraints it is necessary to understand the process of optimization first. In the present investigation, the considered method is multiple objective optimization using GA (in Matlab R2012b), where all the objectives functional constraint should be function minimization. For proper multiobjective optimization, the Mechanical efficiency function was converted from maximization to minimization function with the help of sign convention.

Upon all objective functions constraint satisfaction, the multiobjective optimization iterative process begins with specific GA parameters (Population=100; Maximum run = 60; Maximum iteration=10000; Mutation probability=0.10; Crossover probability=0.75) and ended with multiple optimal solutions (also called as pareto optimal solutions) as shown in Fig 5-42, which provides range of solutions. But the selection of the best solution is done based on process knowledge.
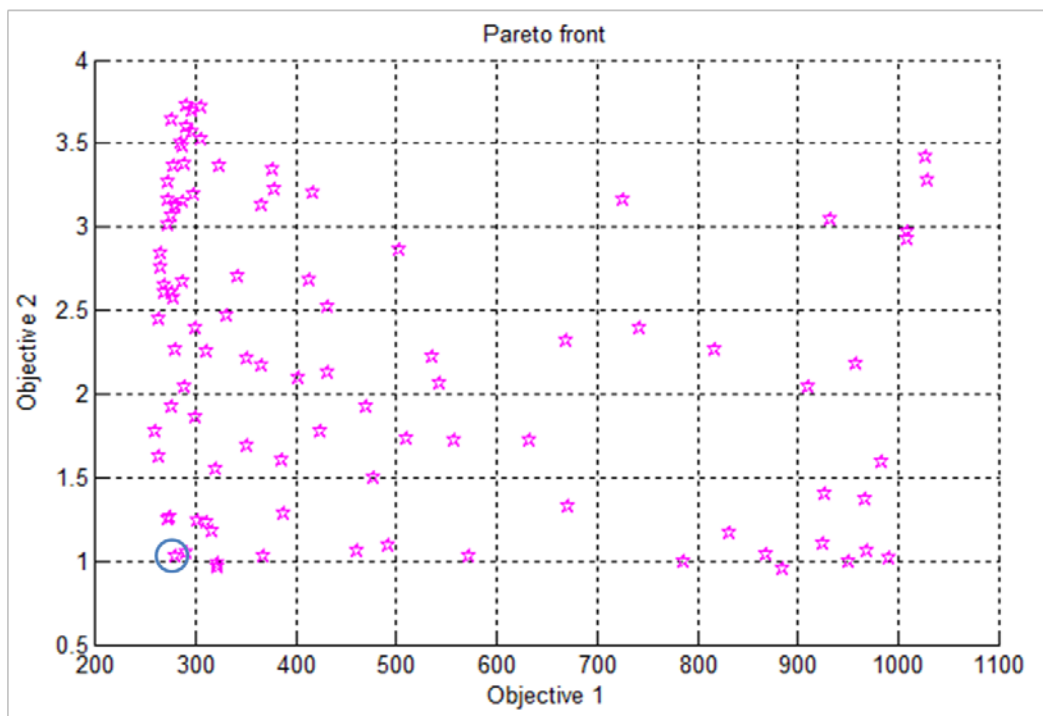
Fig 5-42 Pareto optimal solutions for uncoated engine cylinder; showing multiple optimal points with respect to considered objectives; point encircled shows the selected solution point as that point indicates lower value of both the objectives (1 and 2 for BSFC and friction power respectively)

In the present investigation first and second objectives are BSFC and Friction power which had to be minimized. So to get the optimum results, objective 1 and objective 2 values should be as low as possible which can be pointed out in left bottom corner of the plot, based on these conditions solution point is to be selected from pareto optimal solution plot shown in Fig 5-42, where all points are optimal solution points. But based on our requirement, the encircled point is most suitable optimal solution. The predicted optimization results for selected solution point are presented in Table 5-13. It was observed that with influential variables value of speed = 1420 rpm; load = 21.6 N; and CFR = 0.22 l/s all the responses were optimal.

Table 5-13 Optimized and experimental results comparison

Cases	Influential variables			BSFC	FP	Objectives				
	Speed	Load	CFR			Mechanical efficiency	sCO	sHC	sNO	Smoke opacity
	rpm	N	l/s	g/kWh	kW	%	g/kWh	g/kWh	g/kWh	%
Optimized	1420	21.6	0.22	279.4	1	64	7.39	1	1.6	8.2
Experimental	1420	21.6	0.22	282.51	1.05	62.4	7.85	0.9	1.7	8.6
% Error	--	--	--	1.83	5	2.5	6.22	10	6.25	4.87

Experimental validation of optimization results

Optimized results are validated using conformational experiment, which was carried out on the same DI diesel engine by keeping influential variables value as per the selected result from pareto optimal solutions of optimization run. The corresponding responses parameters (BSFC, Friction power, Mechanical efficiency, sCO, sHC, sNO and Smoke opacity) were measured. Based on the observations of the conformational experiment results, it was found that the optimization results are in good agreement with practical experimentation results as shown in Table 5-13**.** With less than 10 % error of experimental results (for all the responses except sHC) from predicted optimized results, it can be considered that "the predictor model is valid for the considered design space" and the method opted for optimization is effective.

For coated engine block

Similar to uncoated engine block, the experimental matrix opted for optimization is based on Box-Behnken design as shown in Table 5-14 with three inputs and responses considered for study.

Table 5-14 Experimental matrix and their responses for coated engine

	Input factors			Responses						
Sl	Speed	Load	CFR	BSFC	Friction power	Mechanical Efficiency	sCO	sHC	sNO	Smoke opacity
	rpm	N	l/s	g/kWh	kW	%	g/kWh	g/kWh	g/kWh	%
1	2000	4	0.26	1108	1.49	21.95	17.21	2.702	1.483	3.233
2	2000	16	0.22	383.1	1.444	53.72	5.501	0.9538	1.321	4.733
3	2000	4	0.18	1107	1.401	23.02	17.98	2.719	1.568	3.083
4	2600	28	0.22	264.8	2.19	63.52	0.5283	0.2204	0.7535	9.833
5	2000	28	0.26	299.5	1.63	64.28	1.736	0.3894	0.9644	10.63
6	2000	16	0.22	383.1	1.444	53.72	5.501	0.9538	1.321	4.733
7	1400	4	0.22	1112	0.88	25	37.44	4.444	2.087	3.483
8	2000	16	0.22	383.1	1.444	53.72	5.501	0.9538	1.321	4.733
9	2600	16	0.18	377.7	2.049	51.54	2.759	0.4851	0.9696	4.433
10	1400	16	0.18	388.2	0.87	57.42	14.14	1.598	1.762	5.533
11	1400	16	0.26	388.7	0.9	56.59	13.87	1.631	1.739	5.733
12	2600	4	0.22	1154	2.074	20.8	7.72	1.184	0.9953	3.083
13	1400	28	0.22	293.6	0.88	70	5.15	0.6717	1.286	11.13
14	2000	28	0.18	298.6	1.4	67.69	1.821	0.3723	1.037	10.53
15	2000	16	0.22	383.1	1.444	53.72	5.501	0.9538	1.321	4.733
16	2600	16	0.26	378.7	2.345	48.17	2.614	0.4597	0.8874	4.533
17	2000	16	0.22	383.1	1.444	53.72	5.501	0.9538	1.321	4.733

All the response parameters data obtained from the experimental runs based on considered experimental design were used to generate quadratic response surface models. To find the appropriate transformation function for each response, a second-order polynomial model is employed to fit the response surfaces of output parameters using input factors namely speed, load and CFR. Later the transformation function generated for each response using second-order

polynomial model were cross checked with the help of Box-Cox plot for its confidence or efficacy. It is performed to establish efficient target response system with respect to input variables, Box-Cox plot for all the objectives namely BSFC, Friction power, Mechanical efficiency, sCO, sHC, sNO and Smoke opacity are shown in Fig 5-43, Fig 5-44, Fig 5-45, Fig 5-46, Fig 5-47, Fig 5-48, and Fig 5-49, respectively.
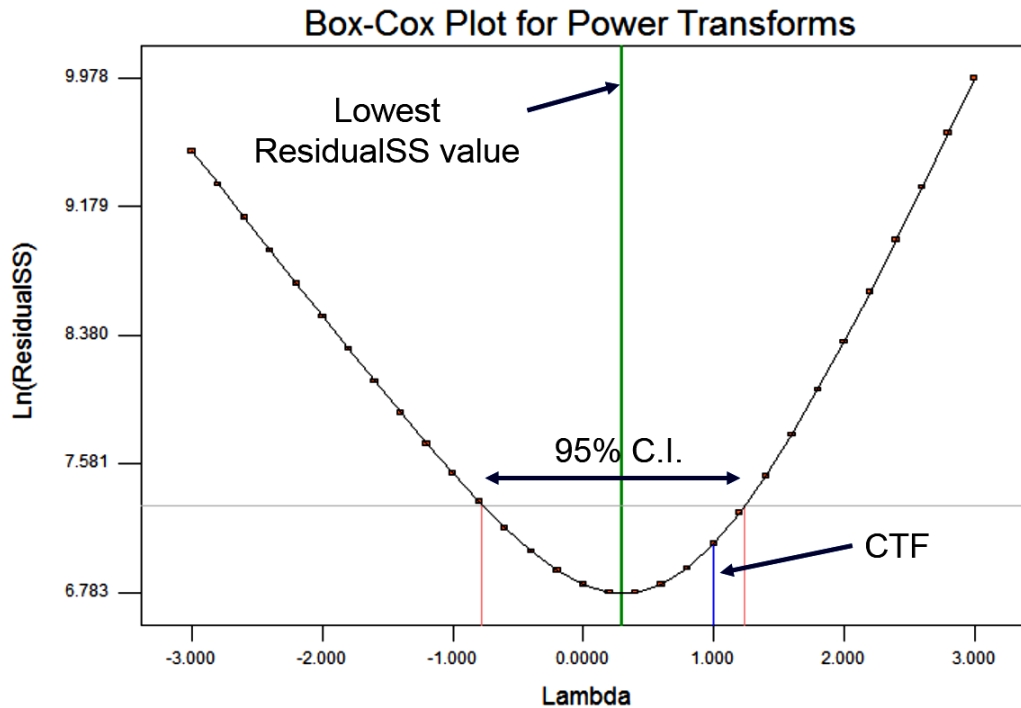
Fig 5-43 Box-Cox Plot of the response BSFC; showing current transformation function lying within 95 % C.I. which indicates the transformation function of response BSFC is reliable
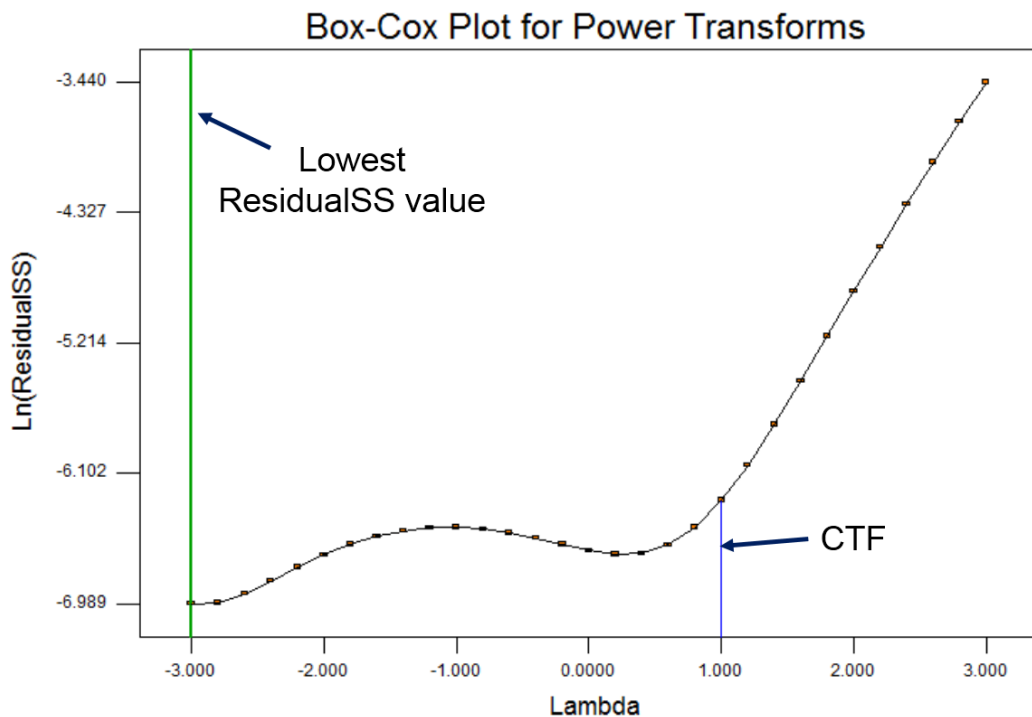
Fig 5-44 Box-Cox Plot of the response friction power; showing current transformation function lying within 95 % C.I. which indicates that the transformation function of response friction power is reliable
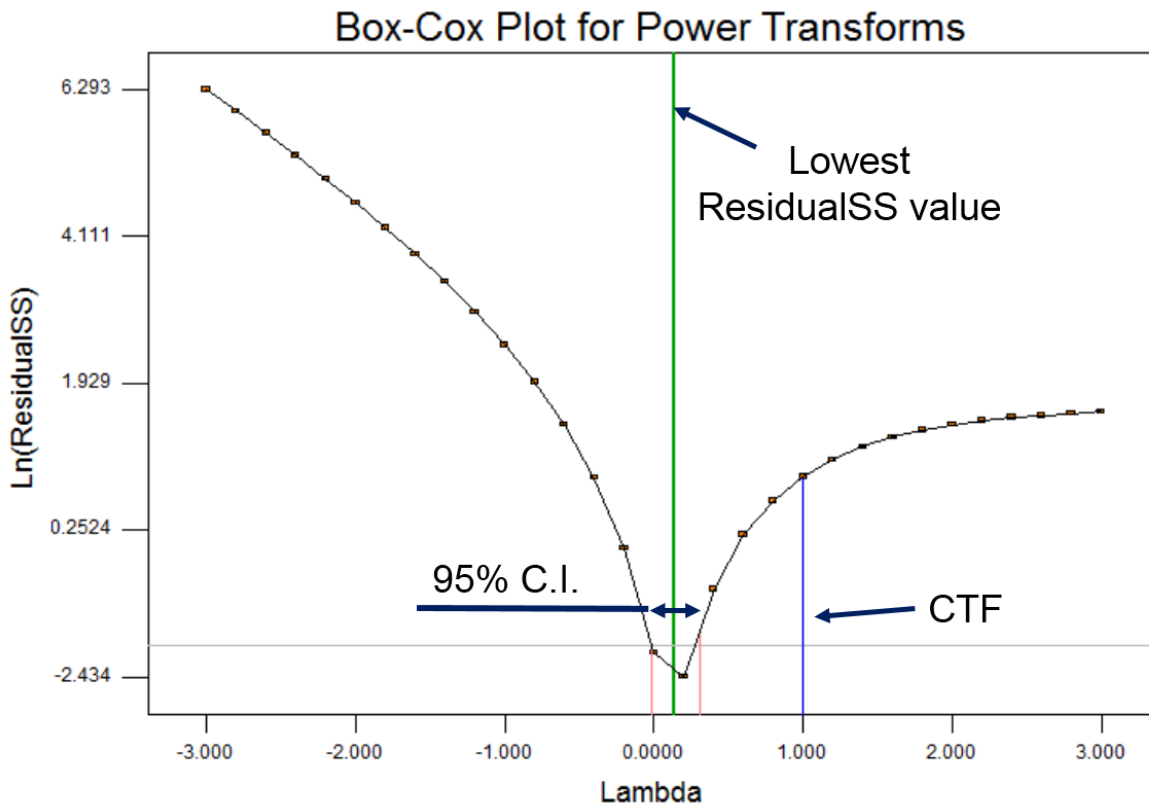
Fig 5-45 Box-Cox Plot of the response mechanical efficiency; showing current transformation function lying far from 95 % C.I. which indicates that the transformation function of response friction power is not reliable and power transformation law should be applied to make transformation function reliable
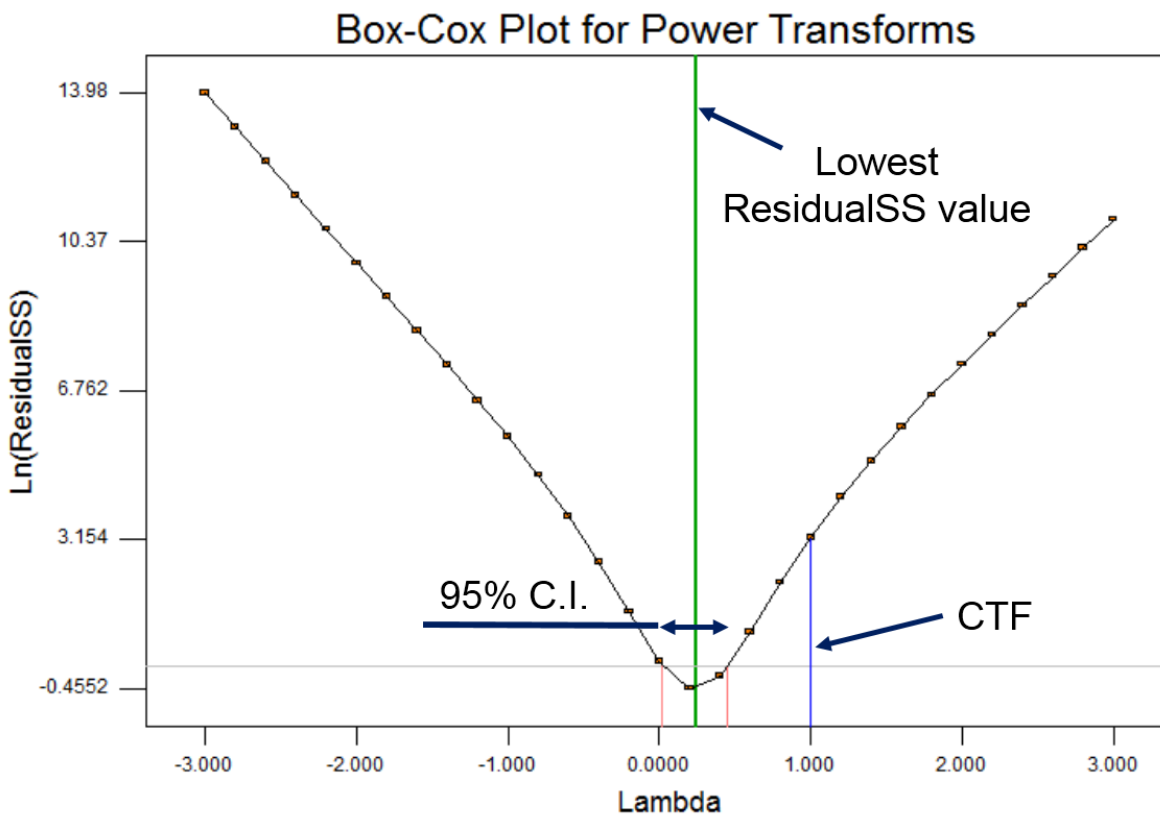
Fig 5-46 Box-Cox Plot of the response sCO; showing current transformation function lying far from 95 % C.I. which indicates that the transformation function of response sCO is not reliable and power transformation law should be applied to make transformation function reliable
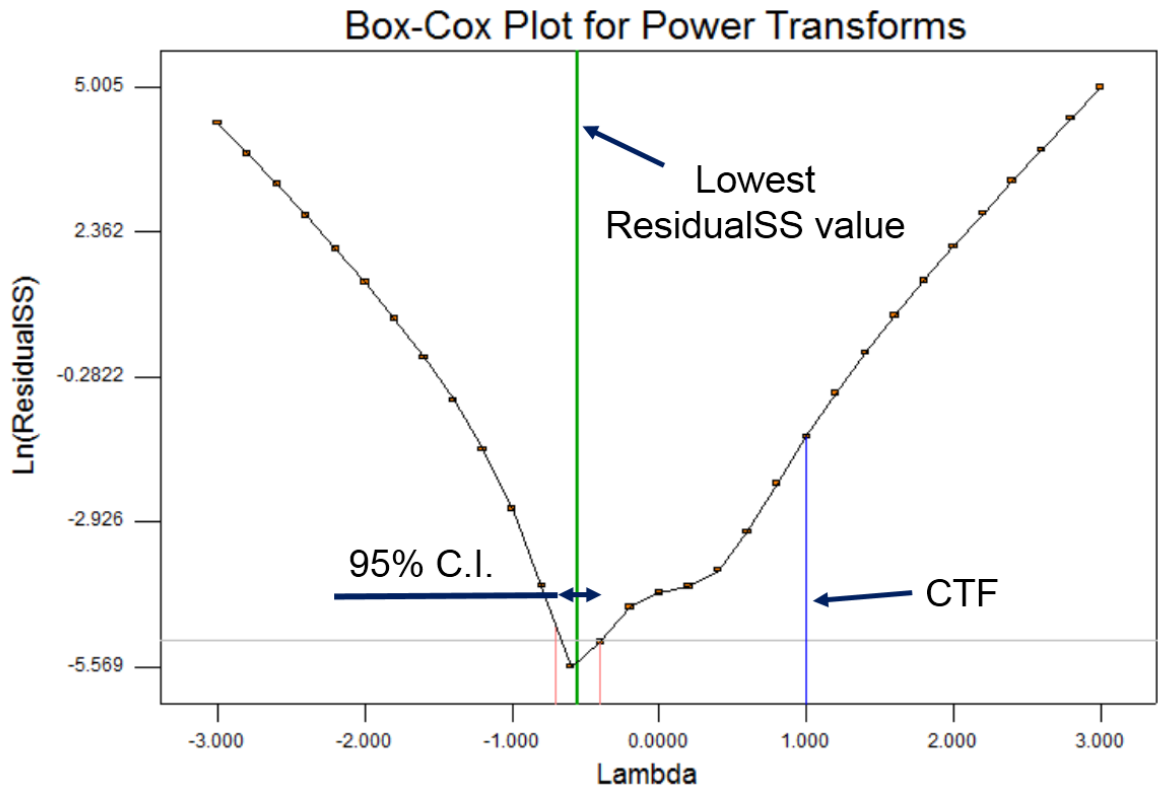
Fig 5-47 Box-Cox Plot of the response sHC; showing current transformation function lying far from 95 % C.I. which indicates that the transformation function of response sHC is not reliable and power transformation law should be applied to make transformation function reliable
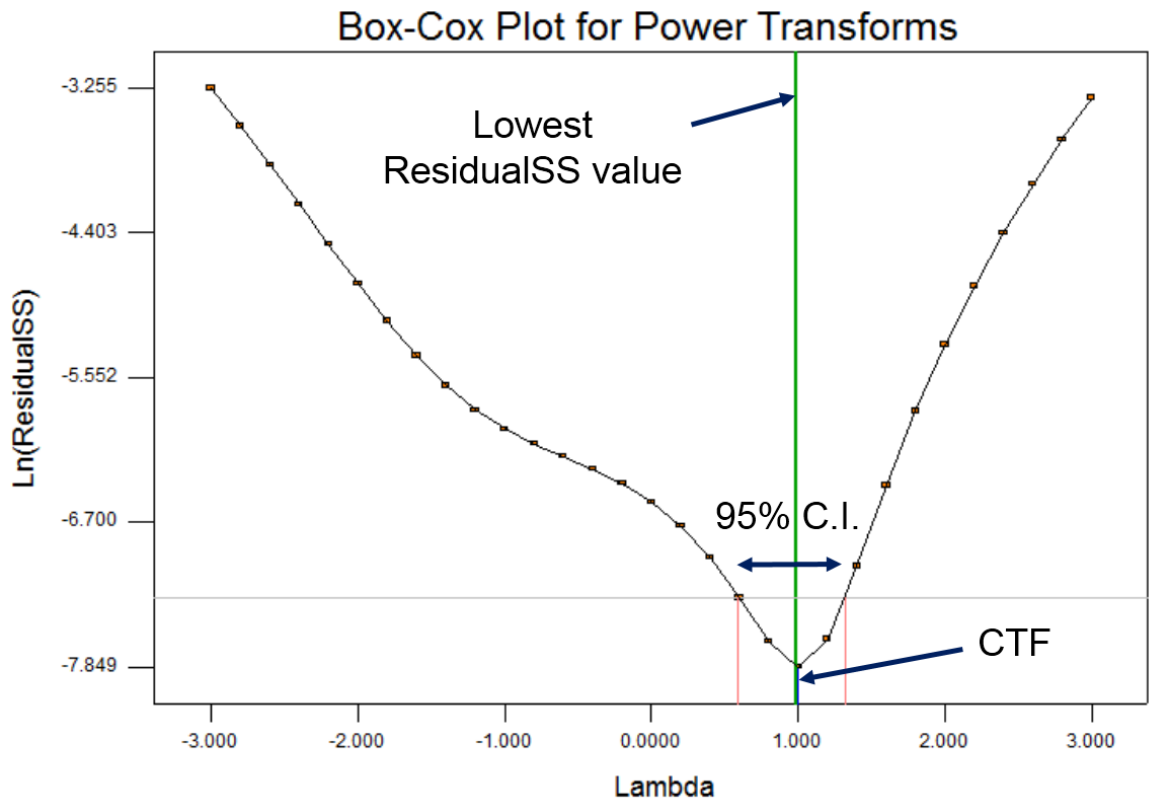
Fig 5-48 Box-Cox Plot of the response sNO; showing current transformation function lying within 95 % C.I. which indicates that the transformation function of response sNO is reliable
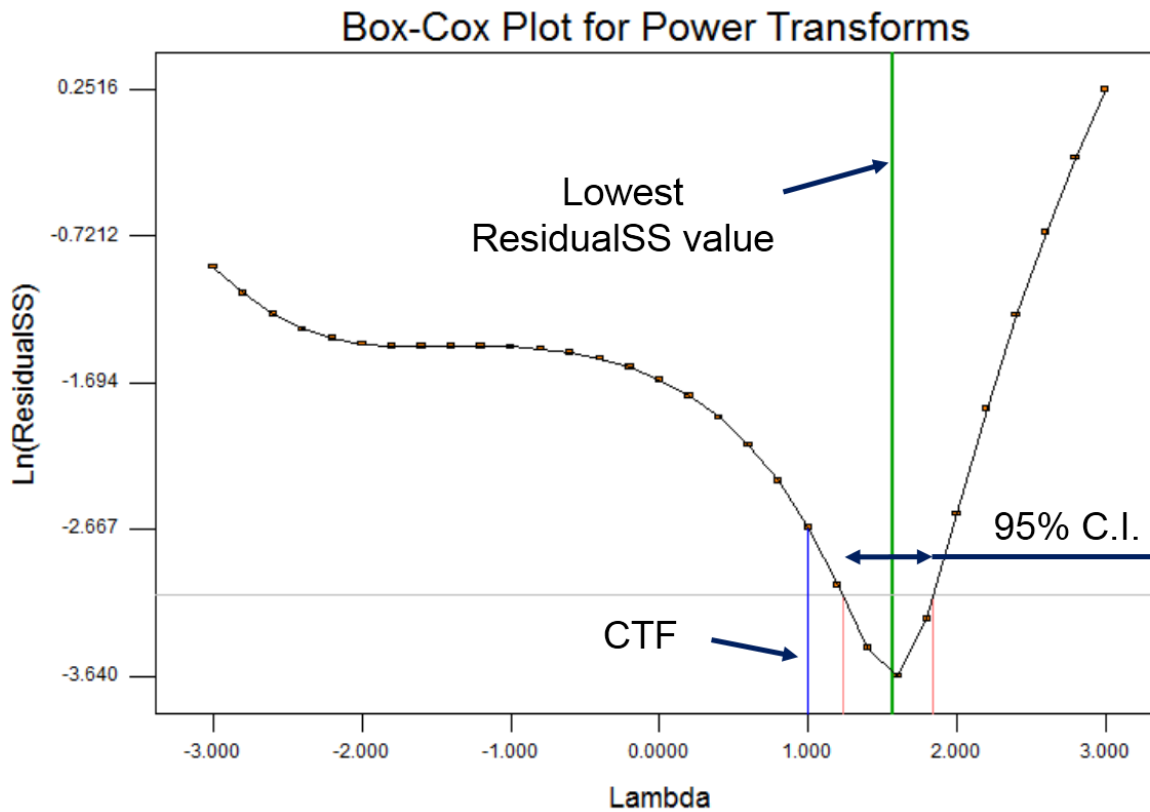
Fig 5-49 Box-Cox Plot of the response smoke opacity; showing current transformation function lying outside 95 % C.I. which indicates that the transformation function of response smoke opacity is not reliable and power transformation law should be applied to make transformation function reliable

As per observations made from Box-Cox plot, power transformation law has been applied for four objectives (responses) namely Mechanical efficiency, sCO, sHC, and Smoke opacity. In Box-Cox plot, CTF indicated the current transformation function for each response without application power transformation law. In case of four objectives Mechanical efficiency, sCO, sHC, and Smoke opacity, the model transformation function falls outside the 95 % C.I. This condition actually represents the poor transformation function of the model, so it has to be rectified with the recommended power transformation law, which can be obtained while using Box-Cox plot tool. Based on application of recommended power transformation law, logarithm of responses was found suitable in the case of Mechanical efficiency and sCO, while in case of sHC the Lambda value of -1/2 found suitable and for Smoke opacity the lambda value of 1.5 providing lowest ResidualSS value. The accepted mathematical form of RSM response models transformation function are mentioned in Equation (5-3) which were used further for optimization with the aid of GA.

$$f(1) = 1408 + 18.47E - 03\ x_1 - 101.1\ x_2 + 388.1\ x_3 + 4.51E - 06\ x_1^2 + 2.232\ x_2^2$$
$$- 876.6\ x_3^2 - 2.46E - 03\ x_1x_2 + 6.16E - 03\ x_1x_3 - 0.2116\ x_2x_3$$

$$f(2) = 2.192 - 28.88E - 05\ x_1 - 21.68E - 03\ x_2 - 14.52\ x_3 + 1.71E - 07\ x_1^2 + 5.26E$$
$$- 06\ x_2^2 + 22.29\ x_3^2 + 4.01E - 06\ x_1x_2 + 27.75E - 04\ x_1x_3 + 73.41E$$
$$- 03\ x_2x_3$$

$$f(3) = 2.608 - 6.61E - 05\ x_1 + 0.1109\ x_2 + 3.4\ x_3 + 6.28E - 09\ x_1^2 - 22.41E - 04\ x_2^2$$
$$- 6.425\ x_3^2 + 3.02E - 06\ x_1x_2 - 55.41E - 05\ x_1x_3 - 20.56E - 04\ x_2x_3$$

$$f(4) = 5.422 - 10.25E - 04\ x_1 - 0.0474\ x_2 + 0.2352\ x_3 - 2.43E - 05\ x_1x_2 - 35.79E$$
$$- 05\ x_1x_3 - 2.07E - 03\ x_2x_3$$

$$f(5) = 1.367 - 74.56E - 05\ x_1 - 36.31E - 04\ x_2 - 4.182\ x_3 + 2.35E - 07\ x_1^2 + 53.75E$$
$$- 05\ x_2^2 + 7.962\ x_3^2 + 1.62E - 05\ x_1x_2 + 49.34E - 05\ x_1x_3 - 19.92E$$
$$- 03\ x_2x_3$$

$$f(6) = 3.692 - 10.55E - 04\ x_1 - 48.98E - 03\ x_2 + 0.1967\ x_3 + 5.00E - 08\ x_1^2 - 40.69E$$
$$- 05\ x_2^2 + 0.2927\ x_3^2 + 1.94E - 05\ x_1x_2 - 62.09E - 05\ x_1x_3 + 61.86E$$
$$- 04\ x_2x_3$$

$$f(7) = 29.05 - 53.92E - 04\ x_1 - 0.4924\ x_2 - 149.1\ x_3 + 1.51E - 06\ x_1^2 + 0.06342\ x_2^2$$
$$+ 369.4\ x_3^2 - 18.14E - 05\ x_1x_2 - 41.09E - 04\ x_1x_3 + 45.9E - 03\ x_2x_3$$

$$(5-3)$$

where,

$f(1) = BSFC;\ f(2) = Friction\ power;\ f(3) = \ln(Mechanical\ efficiency);$

$f(4) = ln(sCO);\ f(5) = (sHC)^{-0.5};\ f(6) = sNO;\ f(7) = (Smoke\ opacity)^{1.5};$

$x1 = Speed;\ x2 = Load;\ and\ x3 = CFR$

  Significance of the model terms and the precision index value of the individual response model are computed with the help of ANOVA analysis and can be referred in Appendix-IV for uncoated engine block. As per ANOVA analysis the "Adeq Precision" value expresses the signal to noise ratio measurement of the response model. Its value greater than four is indicative of adequate signal for model prediction. All the response models have very high "Adeq Precision" value, which indicate that the models will provide reasonable performance in prediction. The response surface models of all the responses namely BSFC, Friction power, Mechanical efficiency, sCO, sHC, sNO and Smoke opacity are shown in Fig 5-50, Fig 5-51, Fig 5-52, Fig 5-53, Fig 5-54, Fig 5-55, and Fig 5-56, respectively.
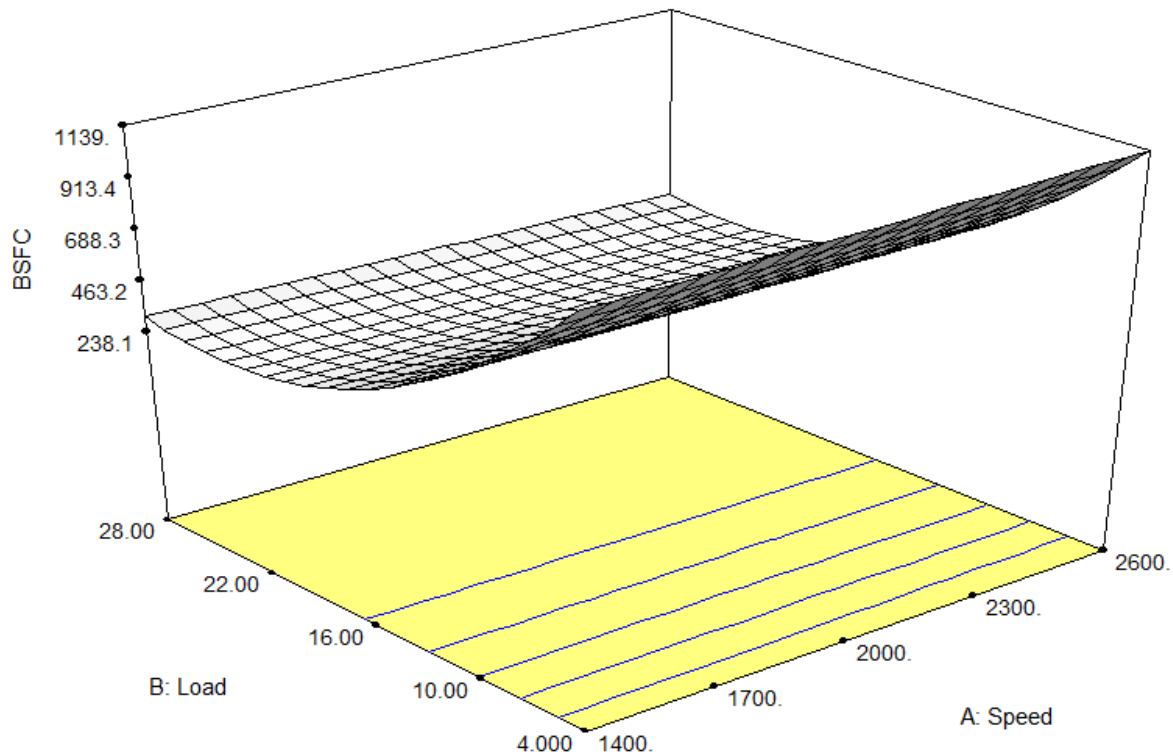
Fig 5-50 Response surface model of the response BSFC (g/kWh); showing significant reduction in BSFC with increase in load
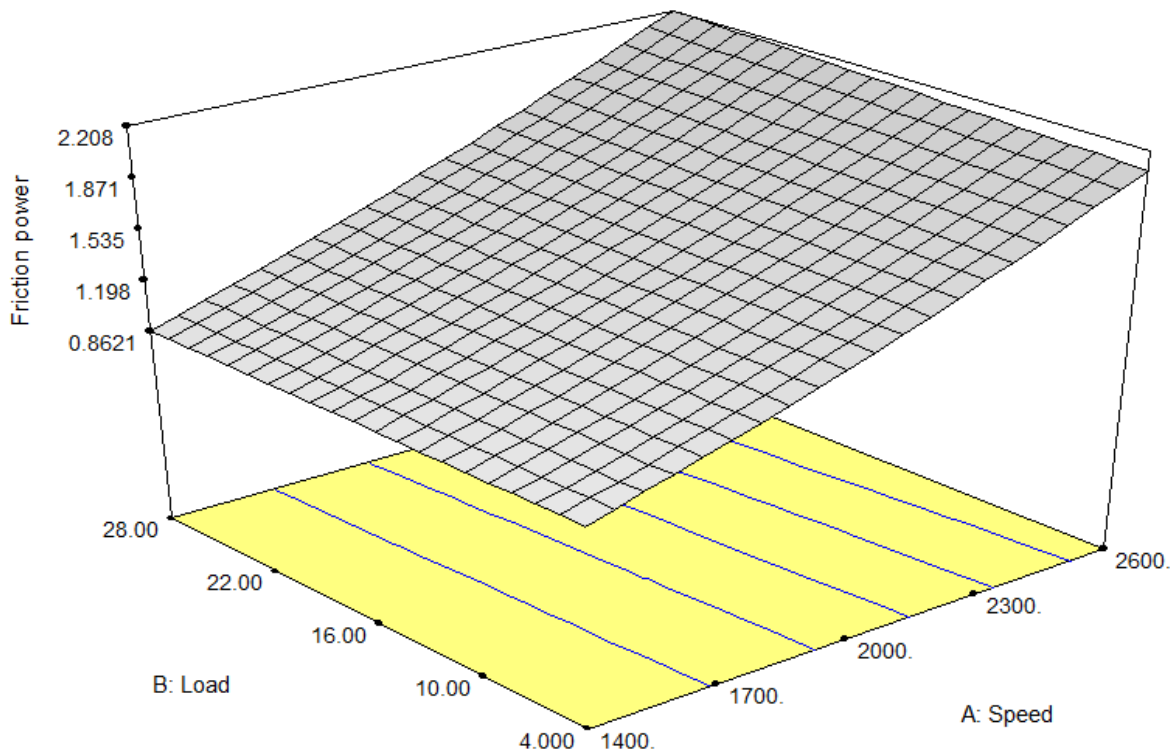
Fig 5-51 Response surface model of the response friction power (kW); showing significant increase in friction power with increase in speed and very little increment with increase in load
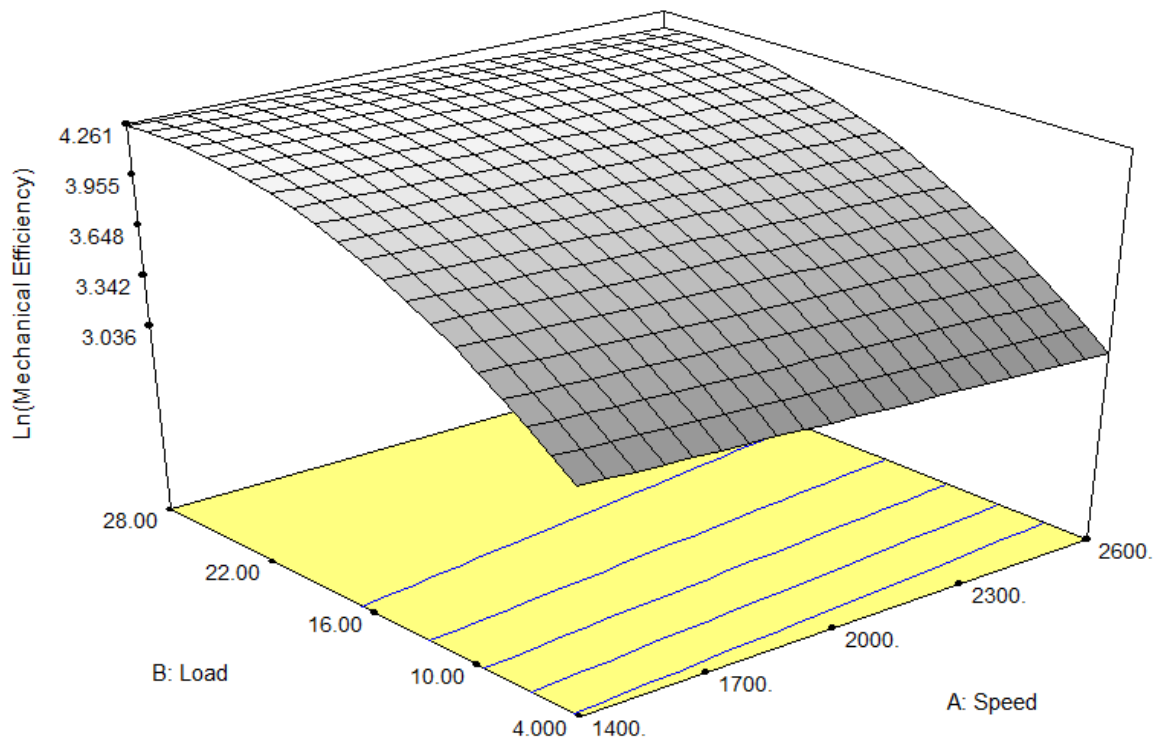
Fig 5-52 Response surface model of the response mechanical efficiency (%); showing significant increase in mechanical efficiency with increase in load and very little decrement with increase in speed
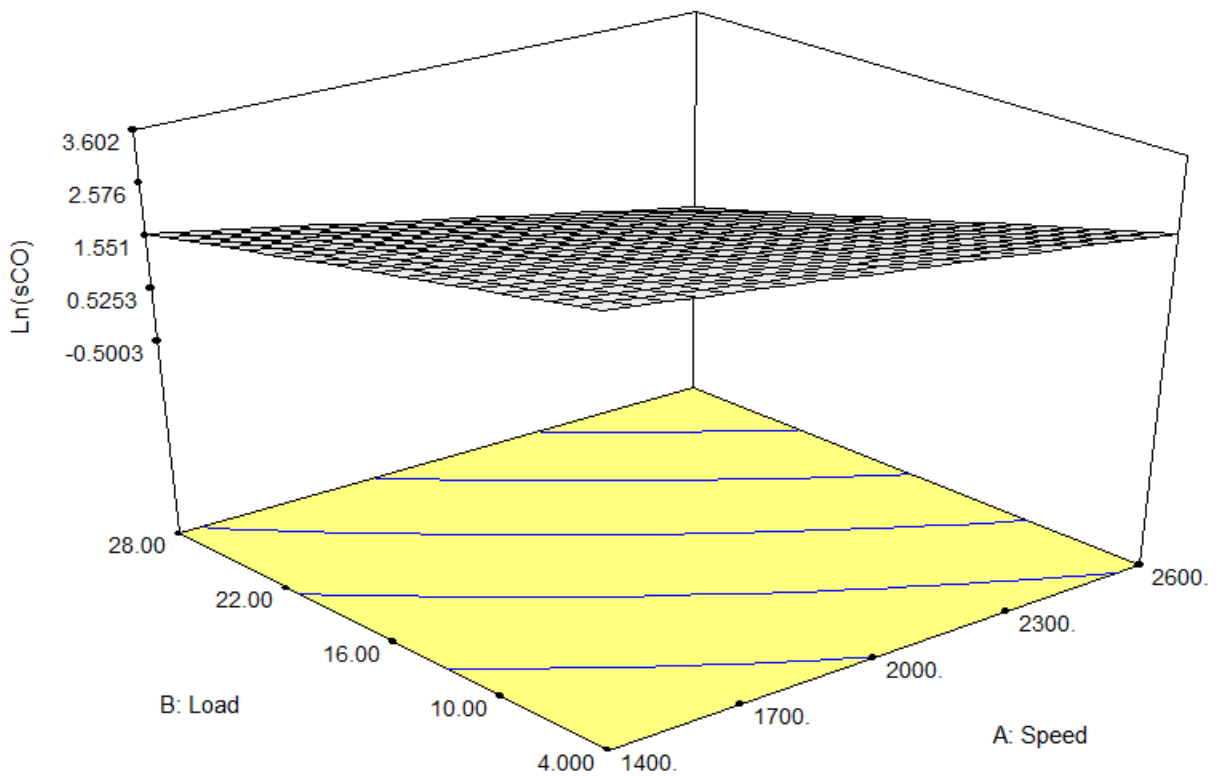
Fig 5-53 Response surface model of the response sCO (g/kWh); showing decrease in sCO with increase in load and speed
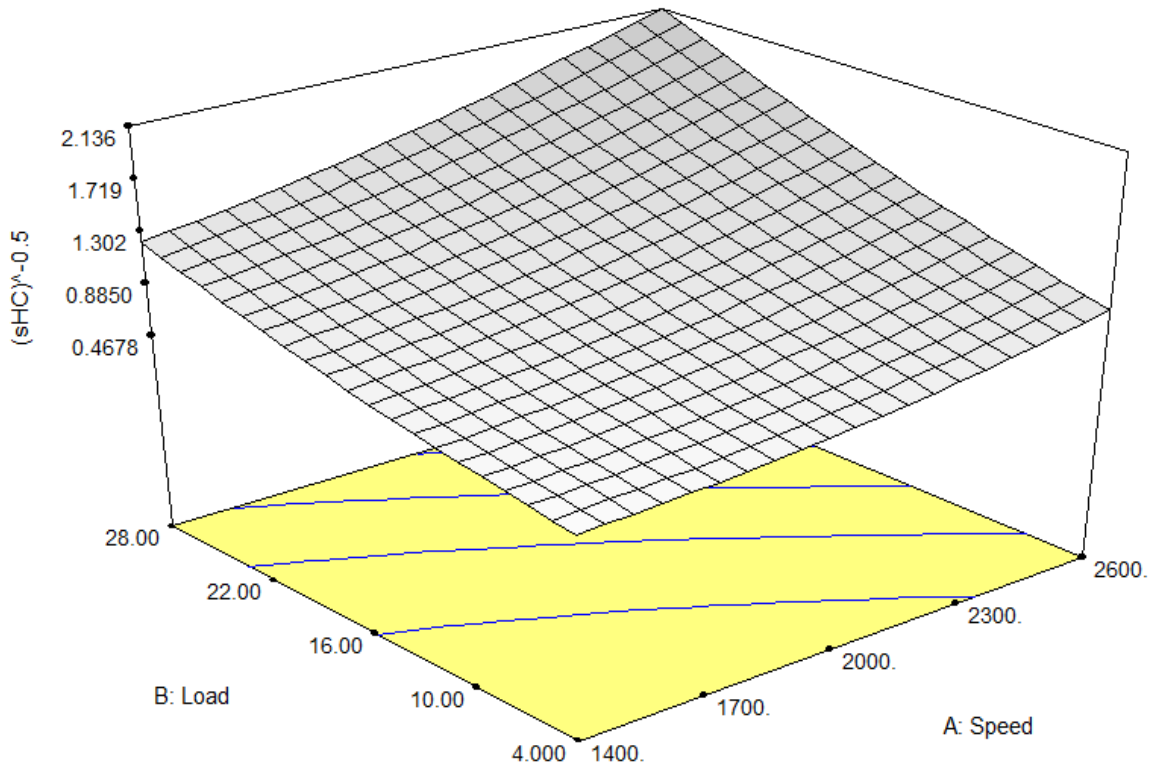
Fig 5-54 Response surface model of the response sHC (g/kWh); showing increase in sHC term with increase in load and speed because of negative power on sHC
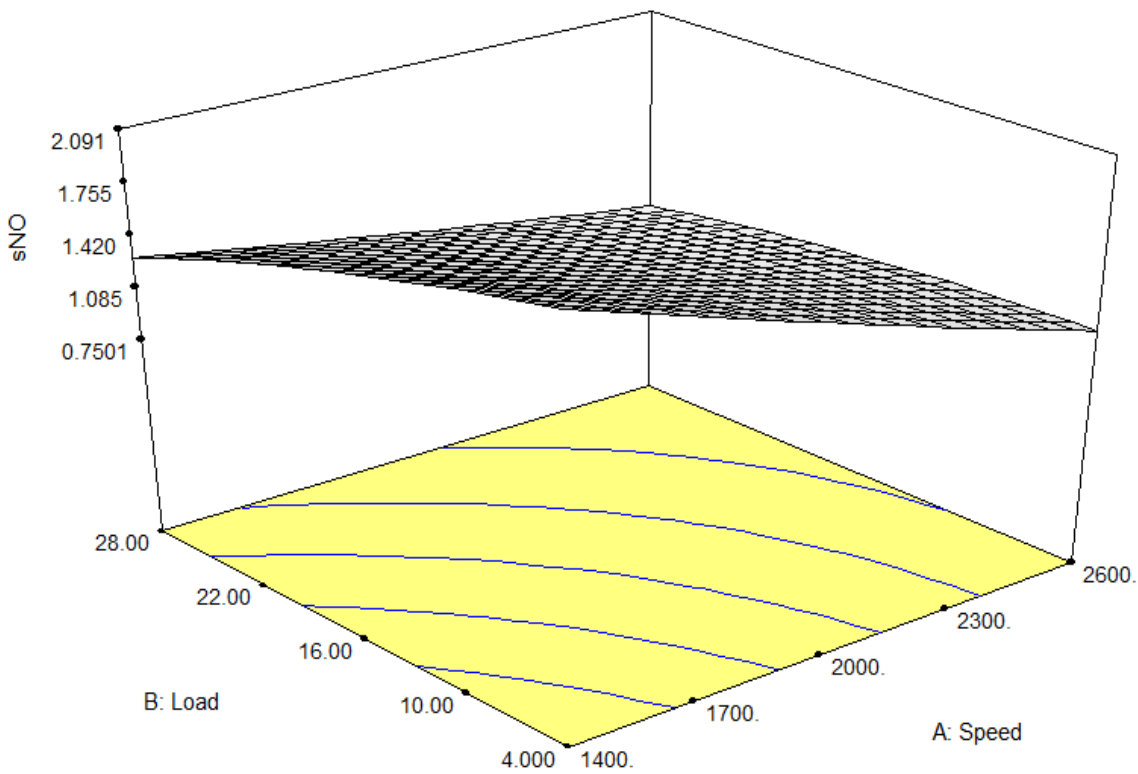
Fig 5-55 Response surface model of the response sNO (g/kWh); showing decrease in sNO with increase in load and speed
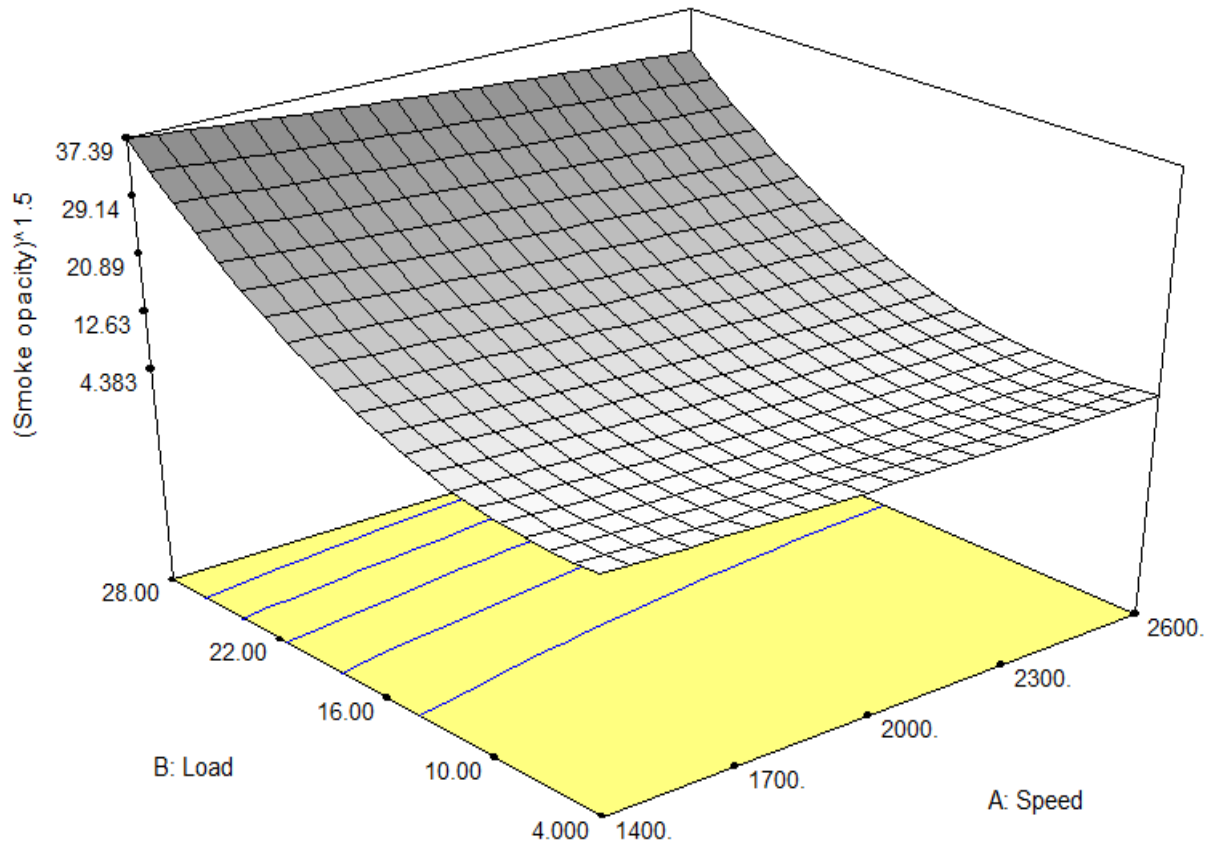
Fig 5-56 Response surface model of the response smoke opacity (%); showing increase in smoke opacity with increase in load and very little decrement with increase in speed

Engine performance optimization for coated engine cylinder

Same methodology was adopted for uncoated engine block, GA based multiobjective optimization was performed for the coated engine block response system. The quadratic polynomial based objective functions of all responses except for the response sCO (as this response was stable with two factor interaction based function) obtained with the aid of RSM are considered for optimization (refer Equation 5-3). Of the seven objective functions, all the functions are to be minimized except Mechanical efficiency function for best engine performance. Upon all objective functions constraint satisfaction, the multiobjective optimization iterative process begins with specific GA parameters (Population=100; Maximum run = 60; Maximum iteration=10000; Mutation probability=0.10; Crossover probability=0.75) and ended with multiple optimal solutions (also called as pareto optimal solutions) as shown in Fig 5-57, which provides range of solutions. The selection of the best solution is done based on process knowledge.
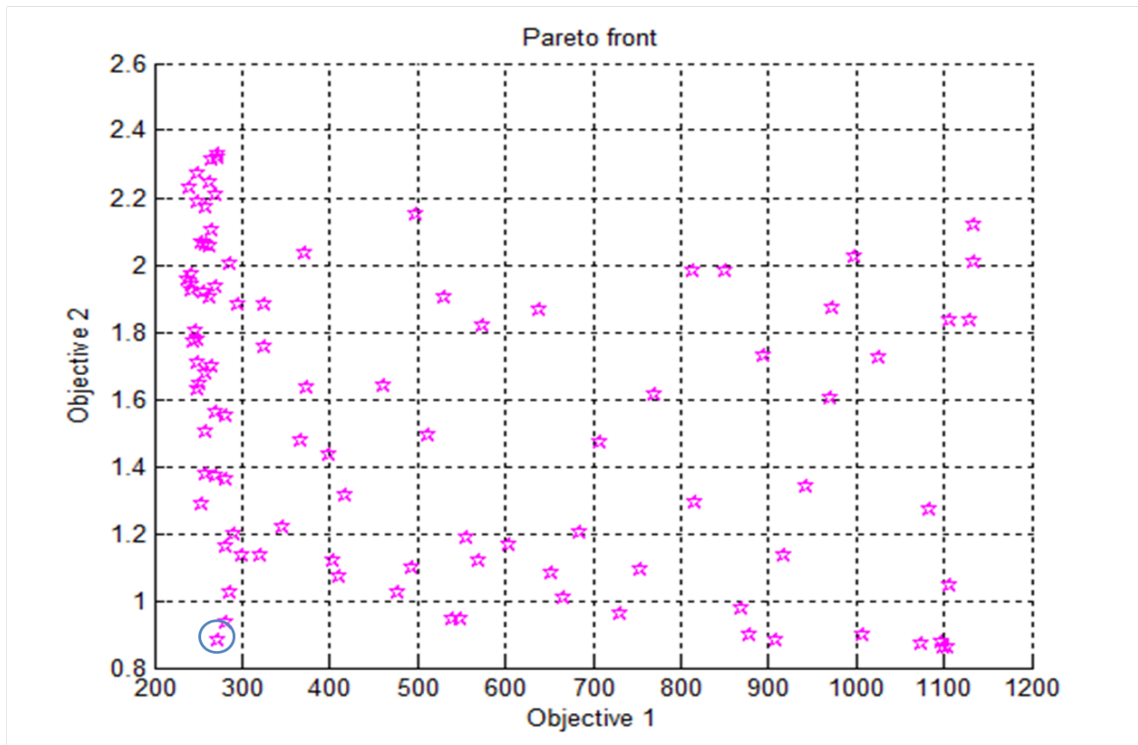
Fig 5-57 Pareto optimal solutions for coated engine cylinder; showing multiple optimal points with respect to considered objectives; point encircled shows the selected solution point as that point indicates lower value of both the objectives (1 and 2 for BSFC and friction power respectively)

The first and second objectives considered are BSFC and Friction power which had to be minimized. So to get the optimum results, objective 1 and objective 2 values should be as low as possible which can be pointed out in left bottom corner of the plot, based on these conditions solution point is to be selected from pareto optimal solution plot shown in Fig 5-57, where all points are optimal solution points. But based on requirement, the encircled point is the most suitable optimal solution. The predicted optimization results for selected solution point are presented in Table 5-15. It was observed that with influential variables value of speed = 1429 rpm; load = 25.7 N; and CFR = 0.22 l/s all the responses were optimal.

Table 5-15 Optimized and experimental results comparison

Cases	Influential variables			Objectives						
	Speed	Load	CFR	BSFC	FP	Mechanical efficiency	sCO	sHC	sNO	Smoke opacity
	rpm	N	l/s	g/kWh	kW	%	g/kWh	g/kWh	g/kWh	%
Optimized	1429	25.7	0.22	272.6	0.9	73.69	6.05	0.69	1.4	9.89
Experimental	1429	25.7	0.22	278.2	0.97	70.32	6.29	0.75	1.35	10.37
% Error	--	--	--	2.05	7.77	4.57	3.96	8.69	3.57	4.85

Experimental validation of optimization results

Optimized results are validated using conformational experiment, which was carried out on same DI diesel engine with coated engine block using diesel fuel by keeping influential variable values as per the selected result from pareto optimal solutions of optimization run. The corresponding

responses parameters (BSFC, Friction power, Mechanical efficiency, sCO, sHC, sNO and Smoke opacity) were measured. Based on the observations of the conformational experiment results, it was found that the optimization results are in good agreement with practical experimentation results as shown in Table 5-15. With less than 10 % error of experimental results for all the responses from predicted optimized results can be considered as "the predictor model is valid for the considered design space" and the method opted for optimization is effective.

5.4.3 Comparative study based on optimization results

Based on optimization results of uncoated engine block and coated engine block, it was found that the predicted value of speed is similar for both the cases, while predicted load is higher for the coated engine block and the coolant flow rate is similar for both the cases. The predicted values of responses at optimum engine setting in case of uncoated engine block was found to be higher for BSFC, Friction power, specific emission CO, HC and NO, and lower for Smoke opacity as compared to coated engine block. The lower value of smoke opacity in case of uncoated engine block may be attributed to the low load condition, which is 21.6 N, while 25.7 N for coated engine block.

The optimized results were validated using experimentation at the optimized setting value generated from optimization procedure. The variation (% error) in the experimental and predicted value is found to be less than 10 % in both cases except for sHC, in the case of uncoated engine block. Generally it can be observed that the percentage error value (Table 5-13 and Table 5-15) are less than 5 % for most of the response cases while it is more than 5 % for few cases such as Friction power and specific emission CO, HC and NO. The engine performance parameters for coated engine block as compared to uncoated engine block when operated at optimized engine setting parameters (speed – 1429 rpm, load – 25.7 N, coolant flow rate – 0.22 l/s), the friction power reduced by ~7.6 %, the BSFC reduced by ~1.5 %, the mechanical efficiency increased by ~12.7 %, sCO reduced by ~19 %, sHC reduced by ~16.6 %, sNO reduced by ~20 % and smoke opacity increased by ~20 %.

Finally it can be concluded that the coated engine block has lower value of BSFC for higher loading conditions with the same or similar speed and coolant flow rate condition as compared to uncoated engine block. The coated engine block gives lesser friction power value, which in turns increases the mechanical efficiency of the engine, as well as the specific emission values for CO, HC and NO, which are lesser compared to the uncoated engine block values. The smoke opacity is higher for coated engine block due to higher loading values from optimization. So overall conclusion can be made that, the coated engine block have certain advantages over uncoated engine block such as lower BSFC, Friction power, specific emission NO and Smoke

opacity and higher Mechanical efficiency against the same input parameters of the engine at higher loading conditions (> 8 N).

5.5 Engine cylinder surface condition after use

Measurement of surface profile of the engine blocks after completion of all the experiments had been done to check the condition of the engine cylinder surface. The results were also compared with those for the engine cylinder of a commercial vehicle. Fig 5-58 shows the used engine cylinder surfaces pointed to the zone where maximum wear of the engine cylinder surface usually occurs. The linear surface profile measurement had been done for all the cases and the result is shown in Fig 5-59. From surface analysis it is confirmed that surface wear at the top of the engine block is inevitable and it will take place continuously with use. The sample of a commercial engine was taken to show the actual condition of the engine block after extensive use. The surface profile measurement had been done after ~800 hrs of use for each case (uncoated and coated engine cylinder). It can be observed that the coated engine cylinder wear is lower than the uncoated engine cylinder. The measured thickness of the maximum wear zone in case of uncoated and coated engine cylinder are ~5.2 µm and ~3.7 µm respectively. Which can be inferred as the coated engine cylinder experiences less wear rate as compared to uncoated engine cylinder.
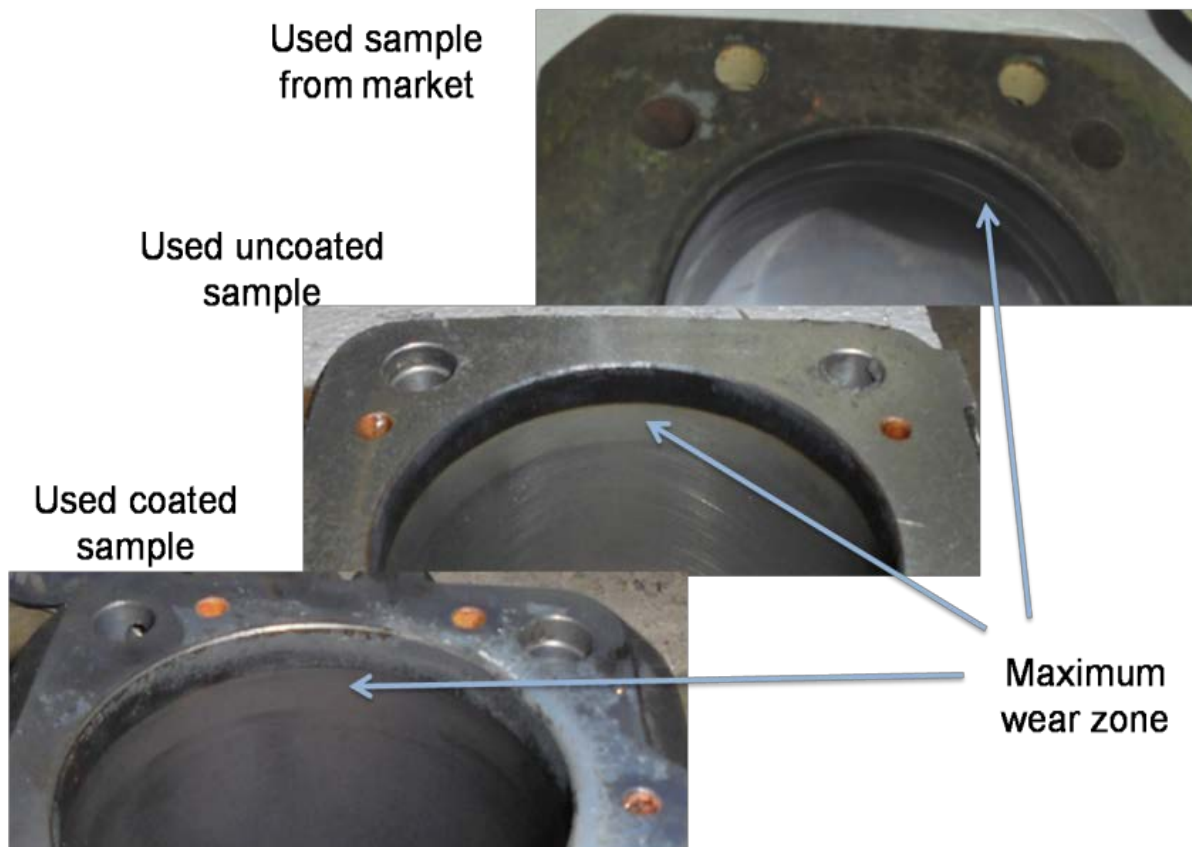
Fig 5-58 Photograph of used engine cylinder (from present investigation and market); showing maximum wear zone in inner surfaces of all the engine cylinder
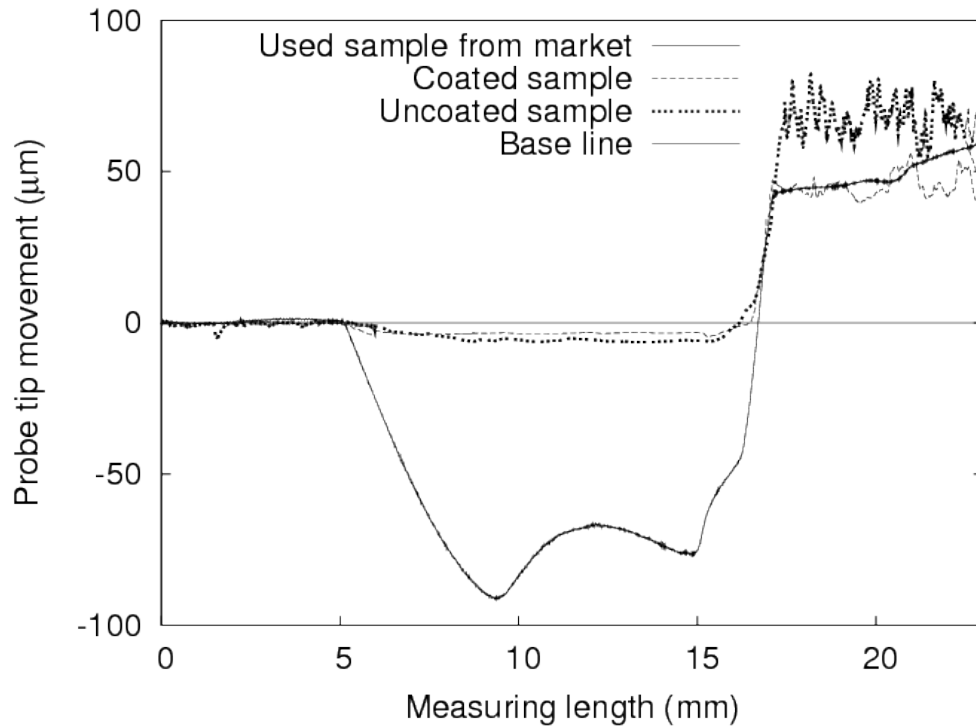
Fig 5-59 Surface profile of coated, uncoated and rejected engine block (from market); where coated and uncoated samples are from present investigation; surface profile measurement confirms that the coated engine cylinder have more wear resistance than uncoated engine cylinder

The surface profile measurement confirmed the effect of reducing friction power which took place due to lowering of coefficient of friction of surface. It is mainly due to the graphite nanoparticles coating. The surface wear is less for coated engine cylinder at maximum wear zone which suggests that the coated nanoparticles are providing wear resistance to the engine cylinder surface.

Based on the present investigation on graphite nanomaterial synthesis, its coating on engine cylinder and the testing of the coated engine cylinder for the enhancement of the engine performance the following conclusions ensue.

1. Graphite was selected as coating material due to its favourable/requisite properties as per the aim of present investigation to coat the IC diesel engine cylinder, and the properties are coating materials compatibility with parent material, coating materials reactivity with engine/lubricating oil, and coating materials reactivity with interacting engine part material (piston/rings).

2. Mechanical milling method with modeling technique was successfully applied to raw graphite of macro size for the preparation of graphite nanopowder. Milling was done at 200 rpm as it was found that milling at a lower rpm reduced contamination. An ANN model is used as a predictive tool to follow the comminution process to optimize the milling duration to achieve a certain average particle size. The TEM result confirms that model prediction for particle size of milled graphite powder is in good agreement with experimental results. It is reported that the milled graphite powder, irrespective of the milling duration has a strain value of 0.54 percent. The residual strains were fully relieved when heat treated at 600°C for one hour. This work affirms that mechanical milling can be an economical approach to process stress-free and contamination-free graphite nanopowder in bulk.

3. Electrophoretic coating was found to be most suitable method for the coating of large scale samples such as engine cylinder. The electrophoretic coatings were performed on small coupons of engine cylinder material first. After confirming all the coating parameters by several hit and trial outcome, the coating of engine block used in a commercial vehicle was performed successfully. In the present coating method electrophoretic electro-chemical cell supplied with a dc voltage of 45-50 V for 10 minutes resulted in better graphite nanoparticles (GNPs) thin film deposition. Coated samples did not have enough adhesive strength between substrate and coating particles (GNPs) after removal of external potential. So to improve bonding, heat treatment of coated sample

performed in inert atmosphere, where coated sample heated from room temperature to 600 ℃, soaked for 1 hr at that temperature and then cooled to room temperature.

The effect of coating was revealed using various characterization techniques. From XRD analysis it was confirmed that the coated surface has dispersion of GNPs throughout. The same was also confirmed using EDS analysis. Hardness measurement results confirmed that the hardness of coated sample is ~13.5 % higher than uncoated sample. While surface coefficient of friction for coated sample was ~38 % lower than that of uncoated sample. The average coating thickness of 5.6 µm obtained after 10 minutes of coating. Nano-graphite coating was responsible for increase in hardness of the coated surface with reduction of surface coefficient of friction.

4. Engine performance testing of small DI compression-ignition engine was conducted on new engines for two cases (1) uncoated engine cylinder and (2) coated engine cylinder in the engine test rig. The characteristics of the engine are found to be quite similar in both the experimental design, which are as follows:

The friction power was found to be ~14 % high for uncoated engine block as compared to that for coated engine block. BSFC was found to decrease with increasing load. The fuel consumption measured for the coated cylinder was found to be 5.6 to 12.5 % less compared to uncoated engine. As the load increases mechanical efficiency of the engine was found to increase. The trend is same for coated and uncoated engine. For coated engine block it was observed that there is 7.5 to 13.5 % enhancement in mechanical efficiency as compared to the uncoated engine.

The specific emission of CO, sCO was observed to decrease as the load increases. And this trend is similar for both uncoated and coated engine blocks. At low load, ~12 % increase in sCO was observed for coated engine block while difference in sCO at higher loads was found to be negligible. Even for sHC a similar trend was observed. At low load, ~6.5 % increase in sHC was observed for coated engine block and the difference at higher loads was found to be negligible. In case of sNO, the decrease in sNO was observed with increase in load. This trend is similar for both uncoated and coated engine blocks with almost constant difference. sNO for coated engine block was observed to be ~10 % lower. Smoke opacity, was observed to increase as the load increases. This trend has been found to be similar for both uncoated and coated engine blocks. It was observed that the smoke opacity was ~5.7 % lower for coated engine block.

5. The optimization of specific engine output parameters are performed based on their requirement. The coated-block engine have positive impact on friction power, BSFC, mechanical efficiency, sNO and smoke opacity while slight negative impact on sCO and sHC. The negative impact is slightly higher at low loading condition only, while at higher loading condition there is negligible variation found between coated engine and uncoated engine regarding sCO and sHC. For seven different responses there are seven sets of input, obtained for providing optimal values of each response. So to address the optimization issue properly multi objective optimization was conducted using RSM-GA method.

   From RSM-GA optimization results of uncoated and coated engine block it was found that the best trade off engine performance parameters value for coated engine block is significantly better as compared to uncoated engine block for almost similar engine setting parameters. The optimized results were validated using experimentation at the optimized setting value generated through optimization procedure. The variation in the experimental and predicted value is found to be less than 10% in both the cases.

   The engine performance parameters for coated engine block as compared to uncoated engine block when operated at optimized engine setting parameters (speed – 1429 rpm, load – 25.7 N, coolant flow rate – 0.22 l/s), the friction power reduced by ~7.6 %, the BSFC reduced by ~1.5 %, the mechanical efficiency increased by ~12.7 %, sCO reduced by ~19 %, sHC reduced by ~16.6 %, sNO reduced by ~20 % and smoke opacity increased by ~20 %.

6. Finally, it can be concluded that the nano-graphite coating can be done on the engine cylinder through chemical route to enhance engine performance. The developed coating method can be applied to any size of cast iron engine block. And applicability of coating process developed in present investigation may be useful in various applications where friction is a major cause of wear such as gear mechanism, heavy loading machineries where a sliding/stationary body rub against another surface etc.

References

[1] Agarwal AK, Gupta T, Kothari A (2011) Particulate emissions from biodiesel vs diesel fuelled compression ignition engine, Renewable and Sustainable Energy Reviews 15, 3278– 3300

[2] Agarwal AK, Rajamanoharan K (2009) Experimental investigations of performance and emissions of Karanja oil and its blends in a single cylinder agricultural diesel engine, Applied Energy 86, 106–112

[3] Agarwal D, Agarwal AK (2007) Performance and emissions characteristics of Jatropha oil (preheated and blends) in a direct injection compression ignition engine, Applied Thermal Engineering 27, 2314–2323

[4] Anand BP, Saravanan CG, Srinivasan CA (2010) Performance and exhaust emission of turpentine oil powered direct injection diesel engine, Renewable Energy 35, 1179-1184

[5] Andrievski RA (2007) Nanostructured superhard films as typical nanomaterials, Surface and Coatings Technology 201, 6112 – 6116

[6] Antisari MV, Montone A, Jovic N (2006) Low energy pure shear milling: a method for the preparation of graphite nano-sheets, Scripta Materialia 55 (11), 1047–1050

[7] Ashok MP, Saravanan CG (2007) Comparing the performance and emission characteristics of the emulsified fuel in DI diesel engine for different injection pressures, SAE paper 2007-01-2127

[8] Assadian M, Shirdar MR, Idris MH, Izman S, Almasi D, Taheri MM, Kadir MRA (2015) Optimisation of electrophoretic deposition parameters in coating of metallic substrate by hydroxyapatite using response surface methodology, Arabian Journal of Science and Engineering 40, 923–933

[9] Assanis DN (1989) Effect of combustion chamber insulation on the performance of a low heat rejection diesel engine with exhaust heat recovery, Heat Recovery Systems & CHP 9 (5), 475-484

[10] Atmanli A, Ileri E, Yuksel B (2014) Experimental investigation of engine performance and exhaust emissions of a diesel engine fueled with diesel-n-butanol-vegetable oil blends, Energy Conversion and Management 81, 312–321

[11] Atmanli A, Yuksel B, Ileri E, Karaoglan AD (2015) Response surface methodology based optimization of diesel-n-butanol cotton oil ternary blend ratios to improve engine performance and exhaust emission characteristics, Energy Conversion and Management 90, 383–394

[12] Balaganesan G, Velmurugan R, Srinivasan M, Gupta NK, Kanny K (2014) Energy absorption and ballistic limit of nanocomposite laminates subjected to impact loading,

International Journal of Impact Engineering 74, 57-66

[13]   Balamurugan T, Nalini R (2014) Experimental study on performance, combustion and emission characteristics of a four-stroke diesel engine using blended fuel, International Journal of Ambient Energy 37 (3), 237-246

[14]   Balani K, Chen Y, Harimkar SP, Dahotre NB, Agarwal A (2007) Tribological Behavior of Plasma Sprayed Carbon Nanotube Reinforced Hydroxyapatite-Coating in Physiological Solution, Acta Biomaterialia 3, 944-951

[15]   Balani K, Harimkar SP, Keshri A, Chen Y, Dahotre NB, Agarwal A (2008) Multiscale wear of plasma sprayed carbon nanotube reinforced aluminum oxide nanocomposite coating, Acta Materialia 56 (20), 5984-5994

[16]   Banhart F (2004) Formation and transformation of carbon nanoparticles under electron irradiation, Philosophical Transactions of the Royal Society of London A 362, 2205–2222

[17]   Bansal RK, Goel AK, Sharma MK (2009) MATLAB and its applications in engineering, Dorling Kindersley (India) Publication under licensees of Pearson Education, 361-389

[18]   Baranescu R, Challen B (1999) Diesel engine reference book, 2nd edition, Butterworth and Heinemann Publishing

[19]   Barber Z (2005) Introduction to materials modelling, Maney publishing, 153-162

[20]   Barberio M, Barone P, Stranges F, Romano A, Xu F, Bonanno A (2013) Carbon nanotubes/metal nanoparticle based nanocomposites: improvements in visible photoluminescence emission and hydrophobicity, Optics and Photonics Journal 3, 34–40

[21]   Barone P, Barberio M, Stranges F, and Xu F (2014) Study of Coating Geometries and Photoluminescence Properties of Metal Nanoparticles/Graphite Composites, Journal of Chemistry, Article ID 204028

[22]   Behera P, Murugan S (2013) Combustion, performance and emission parameters of used transformer oil and its diesel blends in a DI diesel engine, Fuel 104, 147–154

[23]   Bhadeshia HKDH (1999) Neural networks in materials science, ISIJ International 39, 966-979

[24]   Bhandari VB (2014) Machine design data book, McGraw Hill Education (India) Private Limited, 2.1 - 2.6

[25]   Bhusan B (2010) Springer Handbook of Nano-technology, Springer, 3rd edition, 17-1051

[26]   Bilgin A, Durgun O, Sahin Z (2002) The effects of diesel–ethanol blends on diesel engine performance, Energy Sources 24, 431–440

[27]   Billaud D, Balan L, Schneider R, Willmann P (2006) The influence of the synthesis conditions of graphite/tin nanoparticle materials on their electrode electrochemical

performance in Li-ion battery anodes, Carbon 44, 2508–2515

[28] Box GEP, Behnken DW (1960) Some new three level designs for the study of quantitative variables, Technometrics, Vol 2, 455-476

[29] Box GEP, Draper NR (1987) Empirical model building and response surfaces, Wiley

[30] Box GEP, Wilson KB (1951) On the experimental attainment of optimum conditions, Journal of the Royal Statistical Society Series B 13(1), 1–45

[31] Branke J, Deb K, Miettinen K, Slowinski R (2008) Multi-objective optimization: Interactive and evolutionary approaches, Springer Publication, 1-90

[32] Bundy FP (1989) Pressure-temperature phase diagram of elemental carbon, Physica A 156 (1), 169-178

[33] Bundy FP, Bassett WA, Weathers MS, Hemley RJ, Mao HK, Goncharov AF (1996) The pressure-temperature phase and transformation diagram for carbon; Updated through 1994, Carbon 34 (2), 141-153

[34] Buyukkaya E, Cerit M (2007) Thermal analysis of a ceramic coating diesel engine piston using 3-D finite element method, Surface and Coatings Technology 202, 398-402

[35] Cao G (2004) Nanostructures and Nanomaterials - Synthesis, Properties and Applications, Imperial College Press, 7-231

[36] Chakravarti A, Joshi N, Panjiar H (2015) Rainfall Runoff Analysis using Artificial Neural Network, Indian Journal of Science and Technology 8 (14)

[37] Chandrasekharan N, Kamat PV (2001) Assembling Gold Nanoparticles as Nanostructured Films Using an Electrophoretic Approach, Nano Letters 1 (2), 67-70

[38] Chen SX, Low TS, Leow PB (2002) Design optimization of a non-linear magnetic media system using finite element analysis and taguchi method, Compel 21 (2), 223-234

[39] Chen Y, Gerald JF, Chadderton LT, Chaffron L (1999) Nanoporous carbon produced by ball milling, Applied Physics Letters 74 (19), 2782-2784

[40] Chen Y, Li CP, Chen H, Chen Y (2006) One-dimensional nanomaterials synthesized using high-energy ball milling and annealing process, Science and Technology of Advanced Materials 7, 839-846

[41] Chen Y, Samant A, Balani K, Dahotre NB, Agarwal A (2009) Laser Melting of Plasma Sprayed Aluminum Oxide Coatings Reinforced with Carbon Nanotubes, Applied Physics-A: Materials Science & Processing 94 (4), 861-870

[42] Christopher H (2009) The Basics of Crystallography and Diffraction, third ed., Oxford Science Publications, New York

[43]   Ciniviz M, Salman MS, Canli E, Kose H, Solmaz O (2012) Ceramic Coating Applications and Research Fields for Internal Combustion Engines, Ceramic Coatings - Applications in Engineering, Prof. Feng Shi (Ed.), InTech, 195-231

[44]   Cordero-Arias L, Cabanas-Polo S, Gao H, Gilabert J, Sanchez E, Roether JA, Schubert DW, Virtanen S, Boccaccini AR (2013) Electrophoretic deposition of nanostructured-TiO_2/chitosan composite coatings on stainless steel, The Royal Society of Chemistry 3, 11247–11254

[45]   Dahotre NB, Nayak S (2005) Nanocoatings for engine applications, Surface and Coatings Technology 194, 58-67

[46]   Deb K (2001) Multi-objective optimization using evolutionary algorithms, John Wiley & Sons, 1-160

[47]   Deb M, Paul A, Durbadal D, Sastry GRK, Panua RS, Bose PK (2015) An experimental investigation of performance-emission trade off characteristics of a CI engine using hydrogen as dual fuel, Energy 85, 569-585

[48]   Elliott MA, Gerge J. Nebel GL, Rounds FG (1955) The composition of exhaust gases from diesel, gasoline and propane powered motor coaches, Journal of the Air Pollution Control Association 5 (2), 103-108

[49]   Farnoush H, Mohandesi JA, Fatmehsari DH (2013) Effect of particle size on the electrophoretic deposition of hydroxyapatite coatings: a kinetic study based on a statistical analysis, International Journal of Applied Ceramic Technology 10 (1), 87–96

[50]   Ferguson CR, Danieli GA, Heywood JB, Keck JC (1975) Time resolved measurements of exhaust composition and flow rate in a wankel engine, SAE paper 750024

[51]   Fergusson CR (1986) Internal Combustion Engines Applied Thermo Sciences, John Wiley Sons

[52]   Fu ZF, Liu P, Chen XM, Ma JL, Zhang HW (2010) Low-temperature synthesis of $Mg_4Nb_2O_9$ nanopowders by high-energy ball-milling method, Journal of Alloys and Compounds 493, 441–444

[53]   Fugallo G, Cepellotti A, Paulatto L, Lazzeri M, Marzari N, Mauri F (2014) Thermal Conductivity of Graphene and Graphite: CollectiveExcitations and Mean Free Paths, NanoLetters 14, 6109−6114

[54]   Fultz B, Howe J (2002) Transmission electron microscopy and diffractometry of materials, 2nd edition, Springer

[55]   Gabbott P (2007) Principles and applications of thermal analysis, Wiley-Blackwell

[56]   Gaffet E, Caer GL (2004) Mechanical Processing for Nanomaterials, Encyclopedia of Nanoscience and Nanotechnology, Edited by Nalwa HS, Vol 10, 1–39

[57]   Gan YX (2011) Nanofabrication and Nanomanufacturing, Encyclopedia of Nanoscience and Nanotechnology, Edited by Nalwa HS, Vol 17, 145-166

[58]   Ganesan V (2008) Internal combustion engines, Tata McGraw-Hill Education, Technology & Engineering, 446-450

[59]   Gao W, Li Z (2004) Nano-structured alloy and composite coatings for high temperature applications, Materials Research 7 (1), 175-182

[60]   Ghassemali E, Tan MJ, Lim SCV, Jarfors AEW (2012) Friction Factor in a Progressive Microforming Process, Seventh International Conference On MicroManufacturing, Evanston, Illinois, USA

[61]   Ghassemali E, Tan MJ, Wah CB, Lim SCV, Jarfors AEW (2014) Friction effects during open-die micro-forging/extrusion processes: an upper bound approach, Procedia Engineering 81, 1915 – 1920

[62]   Ghorbani HR (2014) A Review of Methods for Synthesis of Al Nanoparticles, Oriental Journal of Chemistry 30 (4), 1941-1949

[63]   Goh CS, Gupta M, Jarfors AEW, Tan MJ, Wei J (2010) Magnesium and Aluminium Carbon Nanotube Composites, Key Engineering Materials 425, 245-261

[64]   Gonca G (2014) Investigation of the effects of steam injection on performance and NO emissions of a diesel engine running with ethanol–diesel blend, Energy Conversion and Management 77, 450–457

[65]   Gurbuz H, Gokkaya H (2010) An evaluation of the effects of coating with thermal barrieron engine performance in diesel engine, Technology 13 (1), 49-57

[66]   Hage DS, Carr JR (2010) Analytical chemistry and quantitative analysis, Prentice Hall, 571-590

[67]   Hazar H, Ozturk U (2011) The effects of Al_2O_3-TiO_2 coating in a diesel engine on performance and emission of corn oil methyl ester, Renewable Energy 35, 2211-2216

[68]   Hejwowski T, Weronski A (2002) The effect of thermal barrier coatings on diesel engineperformance, Vacuum 65, 427-432

[69]   Heywood JB (2011) Internal Combustion Engine Fundamentals, Tata McGraw-Hill

[70]   Hulwan DB, Joshi SV (2011) Performance, emission and combustion characteristic of a multicylinder DI diesel engine running on diesel–ethanol–biodiesel blends of high ethanol content, Applied Energy 88, 5042–5055

[71]   Ilkilic C, Aydın H (2011) Fuel production from waste vehicle tires by catalytic pyrolysis and its application in a diesel engine, Fuel Process. Technol. 92, 1129-1135

[72]   Iscan B (2015) Application of ceramic coating for improving the usage of cottonseed oil in a diesel engine, Journal of the Energy Institute 89 (1), 150-157

[73]   Islam MS , Ahmed AS, Islam A, Aziz SA, Xian LC, Mridha M (2014) Study on Emission and Performance of Diesel Engine Using Castor Biodiesel, Journal of Chemistry, Vol 2014, Article ID 451526

[74]   Jain AK, Mao J (1994) Nueral networks and pattern recognition *in* computational intelligence: Imitating life, IEEE Press, 194-212

[75]   Jain P, Mandal T, Prakash P, Garg A, Balani K (2013) Electrophoretic Deposition of Nanocrystalline Hydroxyapatite on Ti6Al4V/TiO2 Substrate, Journal of Coatings Technology and Research 10 (2), 263-275

[76]   Jiang DE, Carter EA (2003) Carbon dissolution and diffusion in ferrite and austenite from first principles, Physical Review B 67, 214103

[77]   Johansson S, Nilsson PH, Ohlsson R, Rosen BG (2011) Experimental friction evaluation of cylinder liner/piston ring contact, Wear 271, 625-633

[78]   Kamo R (1987) Adiabatic diesel-engine technology in future transportation, Energy 12 (10/11), 1073-1080

[79]   Kandasamy MMK, Thangavelu M (2009) Investigation on the Performance of Diesel Engine Using Various Bio Fuels and the Effect of Temperature Variation, Journal of Sustainable Development 2 (3), 176-182

[80]   Kelly BT, Walter Jr. PL (1970) Theory of thermal expansion of a graphite crystal in the semi-continuum model, Carbon 8, 211 – 226

[81]   Keshri A, Balani K, Bakshi SR, Singh V, Laha T, Seal S, Agarwal A (2009) Structural Transformation in Carbon Nanotubes During Thermal Spray Processing, Surface and Coatings Technology 203 (16), 2193-2201

[82]   Kim BG, Sang KC, Chung HS, Lee JJ, Saito F (2002) Grinding characteristics of crystalline graphite in a low-pressure attrition system, Powder Technology 126 (1), 22–27

[83]   Kirupasankar S, Gnanamoorthy R, Velmurugan R (2010) Effect of apparent area, load, and filler content on sliding friction characteristics of polymer nanocomposites, Proceedings of the Institution of Mechanical Engineers, Part J: Journal of Engineering Tribology 224 (2), 133-138

[84]   Kreyszig E (2006) Advance engineering mathematics, 9th Edition, John Wiley & Sons Publication, 955-965

[85]   Kumar M, Singh H, Singh N, Chavan NM, Kumar S, Joshi SV (2015) Development of Erosion-Corrosion-Resistant Cold-Spray Nanostructured Ni-20Cr Coating for Coal-Fired Boiler Applications, Journal of Thermal Spray Technology 24 (8), 1441–1449

[86] Kumar M, Singh H, Singh N, Joshi RS (2015) Erosion–corrosion behavior of cold-spray nanostructured Ni–20Cr coatings in actual boiler environment, Wear 332-333, 1035–1043

[87] Lin DC, Wang GX, Srivatsan TS, Al-Hajri M, Petraroli M (2003) Influence of titanium dioxide nanopowder addition on microstructural development and hardness of tin–lead solder, Materials Letters 57 (21), 3193-3198

[88] Lin SS, Patterson DJ (1993) Piston/Ring Assembly Friction Modeling By Similarity Analysis, SAE Paper 930794

[89] Lin W, Xi X, Yu C (2009) Research of silver plating nano-graphite filled conductive adhesive, Synthetic Metals 159, 619-624

[90] Louda P (2007) Applications of thin coatings in automotive industry, Journal of Achievements in Materials and Manufacturing Engineering 24 (1), 51-56

[91] Ma C, Ma C, Wang J, Wang H, Shi J, Song Y, Guo Q, Liu L (2014) Exfoliated graphite as a flexible and conductive support for Si-based Li-ion battery anodes, Carbon 72, 38–46

[92] Mack JJ, Viculis LM, Ali A, Luoh R, Yang G, Hahn HT (2005) Graphite nanoplate reinforcement of electrospun polyacrylonitrilenano-fibers, Advanced Materials 17 (1), 77–80

[93] Majewski WA, Khair MK (2006) Diesel emissions and their control, SAE International Paper, 1007680-06740

[94] Makhlouf ASH, Tiginyanu I (2011) Nanocoatings and Ultra-Thin Films: Technologies and Applications, Woodhead Publishing Limited, 3-112

[95] Martyr AJ, Plint MA (2007) Engine Testing Theory and Practice, Third edition, Butterworth-Heinemann, 21-422

[96] McCulloh WS, Pitts W (1943) A logical calculus of ideas immanent in nervous activity, Bulletin of Mathematical Bio-physics 5, 115-133

[97] Michalski J, Wos P (2011) The effect of cylinder liner surface topography on abrasive wear of piston-cylinder assembly in combustion engine, Wear 271, 582-589

[98] Misra RD, Murthy MS (2011) Performance, emission and combustion evaluation of soapnut oil–diesel blends in a compression ignition engine, Fuel 90, 2514–2518

[99] Mohiuddin K, Mao J (1994) A comparative study of different classifiers for hand-printed character recognition, Pattern Recognition in Practice IV, Elsevier Science, 437-448

[100] Montgomery DC (1999) Experimental design for product and process design and development, Journal of the Royal Statistical Society D 48, 159-177

[101] Montgomery DC (2001) Design and analysis of experiments, 5th edition, John Willey and Sons, 427-500

[102] Montgomery DC, Runger GC (1999) Applied statistics and probability for engineers, 2nd edition, Wiley

[103] Morgan WC (1972) Thermal expansion coefficients of graphite crystals, Carbon 10, 73-79

[104] Murugananth M (2002) Design of welding alloys creep and toughness, PhD Thesis, University of Cambridge, 46-55

[105] Myers RH, Montgomery DC (1995) Response surface methodology: Process and product optimization using designed experiments, Wiley

[106] Nagatsu M, Yoshida T, Mesko M, Ogino A, Matsuda T, Tanaka T, Tatsuoka H, Murakami K (2006) Narrow multi-walled carbon nanotubes produced by chemicalvapor deposition using graphene layer encapsulated catalytic metal particles, Carbon 44, 3336-3341

[107] Nalwa HS, Ed. (2004) Encyclopedia of Nanoscience and Nanotechnology, Vol 1, American Scientific Publishers

[108] Nayak S, Reister L, Dahotre NB (2004) Instrumented Indentation Characterization of Laser-Remelted A319Al Alloy, Journal of Materials Research 19 (1), 202-207

[109] Nesbitt JA (2000) Thermal modeling of various thermal barrier coatings in a high heat flux rocket engine, Surface and Coatings Technology 130, 141-151

[110] Nguyen KB, Dan T, Asano I (2014) Combustion, performance and emission characteristics of direct injection diesel engine fueled by Jatropha hydrogen peroxide emulsion, Energy 74, 301-308

[111] Obert EF (1973) Internal Combustion Engines and Air Pollution, 3rd edition, Intex Educational Pub

[112] Ohring M (2012) Materials science of thin films – Deposition and structure, Second edition, Academic press, Elsevier, 95-347

[113] Oner C, Hazar H, Nursoy M (2009) Surface properties of CrN coated engine cylinders, Materials and Design 30, 914-920

[114] Oprescu E-E, Dragomir RE, Radu E, Radu A, Velea S, Bolocan I, Stepan E, Rosca P (2014) Performance and emission characteristics of diesel engine powered with diesel–glycerol derivatives blends, Fuel Processing Technology 126, 460–468

[115] Ozer C, Ismet C, Nazım U (2004) Effects of ethanol addition on performance and emissions of a turbocharged indirect injection Diesel engine running at different injection pressures, Energy Conversion and Management 45, 2429–2440

[116] Ozturk E (2015) Performance, emissions, combustion and injection characteristics of a diesel engine fuelled with canola oil-hazelnut soapstock biodiesel mixture, Fuel Processing Technology 129, 183–191

[117] Palash SM, Kalam MA, Masjuki HH, Arbab MI, Masum BM, Sanjid A (2014) Impacts of NO_x reducing antioxidant additive on performance and emissions of a multi-cylinder diesel engine fueled with Jatropha biodiesel blends, Energy Conversion and Management 77, 577–585

[118] Panjiar H, Gakkhar RP, Daniel BSS (2014) Modeling mechanical milling process for synthesis of graphite nanoparticles and their characterization, Advanced Materials Research 922, 586-591

[119] Panjiar H, Gakkhar RP, Daniel BSS (2015) Strain-free graphite nanoparticle synthesis by mechanical milling, Powder Technology 275, 25-29

[120] Pant P (2004) Dislocation interactions in thin films, Cornell University

[121] Pant P, Baker SP (2003) Strain Relaxation by Dislocation Arrays in Thin Films, MRS Proceedings 779, W5.25

[122] Pant P, Schwarz KW, Baker SP (2003) Dislocation interactions in thin FCC metal films, Acta Materialia 51, 3243–3258

[123] Park S, Kim H, Choi B (2009) Emission characteristics of exhaust gases and nanoparticles from a diesel engine with biodiesel-diesel blended fuel (BD20), Journal of Mechanical Science and Technology 23, 2555-2564

[124] Patel KD, El-Fiqi A, Lee HY, Singh RK, Kim DA, Lee HH, Kim HW (2012) Chitosan–nanobioactive glass electrophoretic coatings with bone regenerative and drug delivering potential, Journal of Materials Chemistry 22, 24945

[125] Patil KR, Thipse SS (2015) Experimental investigation of CI engine combustion, performance and emissions in DEE–kerosene–diesel blends of high DEE concentration, Energy Conversion and Management 89, 396–408

[126] Patil S, Kuiry SC, Seal S (2004) Nanocrystalline ceria imparts better high-temperature protection, Proceedings of the Royal Society of London A 460, 3569-3587

[127] Patterson DJ, Henein NA (1972) Emissions from Combustion Engines and Their Control, Ann Arbor Science Publishers

[128] Paulmier T, Bell JM, Fredericks PM (2007) Deposition of nano-crystalline graphite films by cathodic plasma electrolysis, Thin Solid Films 515, 2926-2934

[129] Piao Y, Han DJ, Seo TS (2014) Highly Conductive Graphite Nanoparticle Based Enzyme Biosensor for Electrochemical Glucose Detection, Sensors and Actuators B 194, 454–459

[130] Pierson HO (1993) Handbook of Carbon, Graphite, Diamond and fullerenes: Properties, Processing and Applications, Noyes Publications, New Jersey, 3-70

[131] Pilusa TJ, Mollagee MM, Muzenda E (2012) Reduction of vehicle exhaust emissions from diesel engines using the whale concept filter, Aerosol and Air Quality Research 12, 994–1006

[132] Prabhu S, Vinayagam BK (2009) Nanocoatings for Engine Application, International Journal of Nanotechnology and Applications 3 (1), 17-28

[133] Prakash SK, Singh H, Panjiar H, Manhas S, Daniel BSS (2012) Application of Graphene Oxide and TiO_2 in the fabrication of Dye sensitized solar cells module by electrode modification, Advanced Materials Research 585, 255-259

[134] Pulkrabek WW (1997) Engineering Fundamentals of the Internal Combustion Engine, Prentice Hall, New Jersey

[135] Rahaei MB, Yazdani R, Kazemzadeh A, Ebadzadeh T (2012) Mechanochemical synthesis of nanoTiC powder by mechanical milling of titanium and graphite powders, Powder Technology 212, 369-376

[136] Raheman H, Jena PC, Jadav SS (2013) Performance of a diesel engine with blends of biodiesel (from a mixture of oils) and high-speed diesel, International Journal of Energy and Environmental Engineering 4:6

[137] Rakopoulos CD, Antonopoulos KA, Rakopoulos DC, Hauntalos DT, Giakoumis EG (2006) Comparative performance and emissions study of a direct injection Diesel engine using blends of Diesel fuel with vegetable oils or bio-diesels of various origins, Energy Conversion and Management 47, 3272–3287

[138] Rakopoulos CD, Rakopoulos DC, Hountalas DT, Giakoumis EG, Andritsakis EC (2008) Performance and emissions of bus engine using blends of diesel fuel with bio-diesel of sunflower or cottonseed oils derived from Greek feedstock, Fuel 87, 147–157

[139] Rakopoulos DC, Rakopoulos CD, Giakoumis EG, Dimaratos AM, Kyritsis DC (2010) Effects of butanol-diesel fuel blends on the performance and emissions of a high-speed DI diesel engine, Energy Conversion and Management 51, 1989–1997

[140] Ramu P, Saravanan CG (2009) Effect of ZrO_2-Al_2O_3 and SiC coating on diesel engine to study the combustion and emission characteristics, SAE paper 2009-01-1435

[141] Ramu P, Saravanan CG (2009) Investigation of combustion and emission characteristics of a diesel engine with oxygenated fuels and thermal barrier coating, Energy & Fuels 23, 653–656

[142] Rao CNR, Muller A, Cheetham AK (2004) Chemistry of nanomaterials: Synthesis, properties and applications, Wiley-VCH, 4-250

[143] Rao VDN, Kabat DM, Rose R, Yeager D, Leong DY (1997) Material Systems for Cylinder Bore Applications - Plasma Spray Technology, SAE Paper 970023

[144] Rao VDN, Kabat DM, Yeager D, Lizotte B (1997) Engine studies of solid film lubricant coated pistons, SAE Paper 970009

[145] Reimer L (1993) Transmission electron microscopy: Physics of image formation and microanalysis, 3rd edition, Springer-Verlag

[146] Resitoglu IA, Altinisik K, Keskin A (2015) The pollutant emissions from diesel-engine vehicles and exhaust after treatment systems, Clean Technologies and Environmental Policy 17, 15–27

[147] Ross PJ (1987) Taguchi techniques for quality engineering, McGraw-Hill

[148] Roy MM, Wang W, Alawi M (2014) Performance and emissions of a diesel engine fueled by biodiesel–diesel, biodiesel–diesel-additive and kerosene–biodiesel blends, Energy Conversion and Management 84, 164–173

[149] Roy R (2001) Design of Experiments Using the Taguchi Approach, John Wiley & Sons

[150] Roy R (2009) A primer on the taguchi method, Second edition, Society of Manufacturing Engineers

[151] Saito Y, Yoshikawa T, Okuda M, Fujimoto N, Yamamuro S, Wakoh K, Sumiyama K, Suzuki K, Kasuya A, Nishina Y (1993) Iron particles nesting in carbon cages grown by arc discharge, Chemical Physics Letters 212, 379-383

[152] Sankaranarayanan S, Menon H, Srivatsan TS, Almajid A, Gupta M (2014) Ball Milled (Titanium Plus Nickel) Additions to Enhance Compressive Response of Pure Magnesium, Twenty-third International Conference on Processing and Fabrication of Advanced Materials, Indian Institute of Technology Roorkee, Vol 2

[153] Santner JS, Goodrich GM (2006) Iron alloys, Casting source directory-engineered casting solutions, 17-22

[154] Saraswati TE, Ogino A, Nagatsu M (2012) Plasma-activated immobilization of biomolecules onto graphite-encapsulated magnetic nanoparticles, Carbon 50, 1253-1261

[155] Saraswati TE, Ogino A, Nagatsu M (2013) Surface Modification of Graphite-Encapsulated Iron Compound Magnetic Nanoparticles by Radio Frequency Inductively-Coupled Plasma for Biomolecules Immobilization, MAKARA Journal of Technology series 17 (3), 138-144

[156] Saraswati TE, Tsumura S, Nagatsu M (2014) High-efficiency plasma surface modification of graphite-encapsulated magnetic nanoparticles using a pulsed particle explosion technique, Japanese Journal of Applied Physics 53, 010205

[157] Sarma SD, Anand M (2013) Capabilities and Governance of Nanotechnology in the Developing World: Insights from India, The Energy and Resources Institute, 41 – 60

[158] Sayin C (2010) Engine performance and exhaust gas emissions of methanol and ethanol–diesel blends, Fuel 89, 3410–3415

[159] Sayin C, Canakci M (2009) Effects of injection timing on the engine performance and exhaust emissions of a dual-fuel diesel engine, Energy Convers Manage 50, 203–213

[160] Schobert HH (1990) The chemistry of hydrocarbon fuels. England: Butterworth–Heinemann Ltd

[161] Searle SR (1987) Linear models for unbalanced data, Wiley

[162] Sengupta R, Bhattacharya M, Bandyopadhyay S, Bhowmick AK (2011) A review on the mechanical and electrical properties of graphite and modified graphite reinforced polymer composites, Progress in Polymer Science 36, 638-670

[163] Sepeur S, Goedicke S, Breyer C (2009) Nanotechnology-High temperature protection, European Coatings Journal 9, 34-37

[164] Shanthi M, Gupta M, Jarfors AEW, Tan MJ (2011) Synthesis, characterization and mechanical properties of nano alumina particulate reinforced magnesium based bulk metallic glass composites, Materials Science and Engineering A 528, 6045–6050

[165] Shen TD, Ge WQ, Wang KY, Quan MX, Wang JT, Wei WD, Koch CC (1996) Structural disorder and phase transformation in graphite produced by ball milling, Nanostructured Materials 7 (4), 393–399

[166] Shin SE, Choi HJ, Hwang JY, Bae DH (2015) Strengthening behavior of carbon/metal nanocomposites, Scientific Reports 5, 16114

[167] Shpilevsky EM, Zhdanok SA, and Schur DV (2011) Carbon Nanomaterials in Clean Energy Hydrogen Systems - II, NATO Science for Peace and Security Series C: Environmental Security 2, edited by S.Yu. Zaginaichenko et al., Springer Science+Business Media

[168] Singh H, Prakash SK, Panjiar H, Daniel BSS (2012) Synthesis of TiO_2 film for Dye-sensitized solar cells, Advanced Materials Research 585, 284-288

[169] Singh SB, Bhadeshia HKDH, MacKay DJC, Carey H, Martin I (1998) Neural network analysis of steel plate processing, Ironmaking and steelmaking 25 (5), 355-365

[170] Singla MK, Singh H, Chawla V (2011) Thermal Sprayed CNT Reinforced Nanocomposite Coatings – A Review, Journal of Minerals & Materials Characterization & Engineering 10 (8), 717-726

[171] Spindt RS (1965) Air-fuel ratios from exhaust gas analysis, SAE paper 650507

[172] Sun G, Li X, Yan H, Qiu J, Zhang Y (2008) Production of nanosized graphite powders

from natural graphite by detonation, Carbon 46, 476–481

[173] Taguchi G (1987) System of experimental design, Unipub Kraus Intl. Publications

[174] Taguchi G, Chowdhury S, Wu Y (2005) Taguchi's quality engineering handbook, John Wiley & Son's Inc., 1525-1617

[175] Tang J, Zhao W, Li L, Falster AU, Simmons Jr. WB, Zhou WL, Ikuhara Y, Zhang JH (1996) Amorphization of graphite induced by mechanical milling and subsequent crystallization of the amorphous carbon upon heat treating, Journal of Materials Research 11 (3), 733-738

[176] Taylor CF (1985) The Internal Combustion Engine in Theory and Practice, 2nd Edition, MIT Press

[177] Taymaz I (2007) The effect of thermal barrier coatings on diesel engine performance, Surface and Coatings Technology 201, 5249-5252

[178] Taymaz I, Cakir K, Gur M, Mimaroglu A (2003) Experimental investigation of heat losses in a ceramic coated diesel engine, Surface and Coatings Technology 169 – 170, 168–170

[179] Thakur SK, Srivatsan TS, Gupta M (2007) Synthesis and mechanical behaviour of carbon nanotube–magnesium composites hybridized with nanoparticles of alumina, Materials Science and Engineering: A 466 (1), 32-37

[180] Thomas V, Mohan YM, Mary G, Bajpai M, Bajpai SK (2011) Synthesis of Silver nanomaterials and their antibacterial applications, Encyclopedia of Nanoscience and Nanotechnology, Edited by Nalwa HS, Vol 24, 187-205

[181] Tovell JF (1984) Ceramics and the reciprocating internal combustion engine, Materials & Design 5, 215-220

[182] Truhan JJ, Qu J, Blau PJ (2005) A rig test to measure friction and wear of heavy duty diesel engine   piston rings and cylinder liners using realistic lubricants, Tribology International 38, 211-218

[183] Umer A, Naveed S, Ramzan N, Rafique MS (2012) Selection of a suitable method for the synthesis of copper nanoparticles, Nano: brief reports and reviews 7 (5), 1230005

[184] Uzun A, Cevik I, Akcil M (1999) Effects of thermal barrier coating on a turbocharged diesel engine performance, Surface and Coatings Technology 116-119, 505-507

[185] Velmurugan R, Balaganesan G, Gupta NK (2013) Impact Loading on Glass/Epoxy Composite Laminates with Nano Clay, Key Engineering Materials 535, 72-75

[186] Venkateswara RP, Veeresh BA (2013) Performance and Emission Characteristics of Diesel Engine Using Waste Fried (Groundnut) Oil Methyl Ester – Diesel Blends, The IUP Journal of Mechanical Engineering 6 (2), 5-14

[187] Wang YJ, Lo TY, Wu CH, Liu DM (2013) Electrophoretic coating of amphiphilic chitosan colloids on regulating cellular behavior, Journal of the Royal Society Interface 10, 20130411

[188] Welham NJ, Berbenni V, Chapman PG (2003) Effect of extended ball milling on graphite, Journal of Alloys and Compounds 349, 255–263

[189] Welham NJ, Williams JS (1998) Extended milling of graphite and activated carbon, Carbon 36 (9), 1309–1315

[190] Wen C, Jin ZH, Guan JQ, Li X, Zhou G, Lin JD (2002) Nano-graphite synthesized by explosive detonation, Rare Met M 6 (33), 628–631

[191] Wen C, Jin ZH, Liu XX, Sun DY, Li X, Zhou G (2006) Synthesis of diamond using nano-graphite and Fe powder under high pressure and high temperature, Materials Letters 60, 3507–3510

[192] Westlund A (2009) Measuring and Predicting Transient Diesel Engine Emissions, Ph.D. Thesis, KTH Stockholm, Sweden

[193] Wisser M (2006) Graphite and carbon powders for electrochemical applications, Journal of Power Sources 156 (2), 142–150

[194] Workie B, McCandless BE, Gebeyehu Z (2013) Electrophoretic deposition of aluminum nitride from its suspension in acetylacetone using iodine as an additive, Journal of Chemistry, Vol 2013, Article ID 489734

[195] Wu CF, Hamada M (2000) Experiments: planning, analysis, and parameter design optimization, Wiley – Interscience

[196] Xia Y, Yan H, Facchetti A (2013) Carbonaceous nanomaterial-based thin-film transistors, United States Patent US20130048949A1

[197] Xie M, Lee CH, Wang J, Yap YK, Bruno P, Gruen D, Singh D, Routbort J (2010) Induction annealing and subsequent quenching: Effect on the thermoelectric properties of boron- doped nanographite ensembles, Review of Scientific Instruments 81, 043909, 1-6

[198] Xing-Cia L, Yang JG, Zhang WG, Huang Z (2004) Effect of Cetane number improver on heat rate and emissions of high speed diesel engine fuelled with ethanol–diesel blend fuel, Fuel 83, 2013–2020

[199] Xue J, Grift TE, Hansen AC (2011) Effect of biodiesel on engine performances and emissions. Renewable Sustainable Energy Review 15, 1098–1116

[200] Yadav TP, Yadav RM, Singh DP (2012) Mechanical milling: a top down approach for the synthesis of nanomaterials and nanocomposites, Nanoscience and Nanotechnology 2 (3), 22-48

[201] Yang Y, Qu L, Dai L, Kang TS, Durstock M (2007) Electrophoresis coating of titanium dioxide on aligned carbon nanotubes for controlled syntheses of photoelectronic nanomaterials, Advanced Materials 19, 1239–1243

[202] Yoshimitsu T (1987) Internal combustion engine cylinder liner coatings, United States Patent US4706616

[203] Zazula JM (1997) On graphite transformations at high temperature and pressure induced by absorption of the LHC beam, LHC Project Note 78/97, 1-15

[204] Zhang HY, Wang HQ, Chen GH (2006) A new kind of conducting filler-graphite nanosheets, Plastics 35 (4), 42–45

[205] Zhaoping X, Siqin C (2010) Prototype testing and analysis of a novel internal combustion linear generator integrated power system, Applied Energy 87 (4), 1342–1348

[206] Zheng WG, Wong SC, Sue HJ (2002) Transport behavior of PMMA/expanded graphite nano-composites, Carbon 43 (25), 6767–6773

APPENDIX-I

Engine details

The complete details of the IC engine used in present investigation are furnished below, which is a vertical, single cylinder, water cooled, compression ignition, 4-stroke, high speed diesel engine.

Table A-I Engine details

Sl	Engine component	Description/Value	Unit
1	Type	Diesel, 4-stroke engine	
2	Make/manufacturer	Greaves cotton	
3	Model	G 600 W II	
4	Material	Gray cast iron	
5	No. of Cylinder(s)/ Configuration	1/ In-line	
6	Capacity	611	cc
7	Firing order	Single cylinder	
8	Bore	92	mm
9	Stroke	92	mm
10	Rated compression ratio	18:1	
11	Rated HP @ 3000rpm	11	
12	Rating (Any)	CMVR[a]	
13	Dry weight	75	Kg
14	Fuel type used	Diesel or heavy fuel	
15	Dimensions (l X w X h)	379 X 477 X 683	mm
16	Maximum rated speed	3000	rpm
17	Maximum torque	32 Nm @ 1600-1800 rpm	Nm
18	SFC (rated)	210	gm/bhp/hr
19	Lubricating oil consumption	0.006	Kg/hr
20	Oil sump capacity	1.75	L
21	Clearance length	0.8 – 1.0	mm
22	Max. output/Cylinder	8.1	kW/cylinder
23	Max. brake mean effective pressure (max. BMEP)	5.3	bar
24	Max. output	8.1	kW

[a] – from company (http://www.gsgnet.net/c/c.aspx/GRE002/productspecs)
[b] – from lab analysis
CMVR – Automotive rating: For intermittent duty at variable speed and variable load.

APPENDIX-II

Uncertainty analysis

Uncertainty analysis deals with assessing the measurement uncertainty in physical experiments. Usually experiments are designed to estimate the numerical value of a physical variable, or to define the effect of independent variable will be affected by errors (like instrumentation, presence of confounding effects, methodology, and so on). Experimental uncertainty evaluations are needed in physical experiments to assess the confidence in the results.

Uncertainty analysis was performed using Kline and McClintock's method described by Doebelin and Holman [a,b]. The instruments detail used in the present investigation are given in Table AII-1. Each value measurements done three times in present investigation, and errors in various terms were determined by applying widely known method of evaluation, which is a standard method as well reported by Sahin et al. and Behera et al. [c,d].

Table AII-1 Instruments detail used for the measurements of engine parameter

Instrument	Measurement	Range	Accuracy	Remark
Speed sensor in dynamometer	Speed	0-17000 rpm	±10 rpm	---
Load cell in dynamometer	Torque	0-33 Nm	±0.05 Nm	Permissible torque is lower than the maximum value cited here, but the experiments were conducted up to 32 Nm safely at lower speed (≤1800 rpm)
Burette	Fuel consumption	0-100 cc	±0.2 cc	---
Pressure transducer	Cylinder pressure	0-200 bar	±1 bar	---
Crank angle encoder	Crank angle	---	±1	---
Exhaust gas analyzer	CO, HC, NO, O_2, and CO_2	---	---	Details furnished in Table 3-6
Smoke meter	Smoke opacity	0-100%	---	Details furnished in Table 3-7
Temperature sensor	Exhaust gas temperature	0-1200 ℃	±1 ℃	---
Gas chromatograph	H_2 in exhaust	0-0.5 cc	±5%	---
Stop watch	Time for fuel consumption	---	±0.1 s	---

a. Doebelin EO (1990) Measurement Systems: Application and Design, McGraw-Hill, 54-71

b. Holman JP (2003) Experimental Methods for Engineers, McGraw-Hill, 50-61

c. Sahin Z, Tuti M , Durgun O (2014) Experimental investigation of the effects of water adding to the intake air on the engine performance and exhaust emissions in a DI automotive diesel engine, Fuel 115, 884–895

d. Behera P, Murugan S (2013) Combustion, performance and emission parameters of used transformer oil and its diesel blends in a DI diesel engine, Fuel 104, 147–154

An example is presented here for better understanding, let us try to determine uncertainty in the computed results on the basis of primary measurements uncertainties. Suppose the result Y is a function of the independent variables $a_1, a_2, a_3, ..., a_n$. Thus

$$Y = Y(a_1, a_2, a_3 ...., a_n) \qquad \text{(AII-1)}$$

Let u_y be the uncertainty in the result and $u_1, u_2, u_3..., u_n$ be the uncertainties in the independent variable. Then the corresponding uncertainty u_y in Y is given by

$$u_y = \left[\left(\frac{\partial Y}{\partial a_1}u_1\right)^2 + \left(\frac{\partial Y}{\partial a_2}u_2\right)^2 + \left(\frac{\partial Y}{\partial a_3}u_3\right)^2 ... + \left(\frac{\partial Y}{\partial a_n}u_n\right)^2\right]^{1/2} \qquad \text{(AII-2)}$$

The uncertainty of the calculations such as BP, IP, v_f, and v_a are performed in present investigation, while here the detailed description of one of the parameter (BP) uncertainty analysis furnished for clear understanding of the method, which is as follows.

For computing BP, following equation can be used

$$BP = \frac{2*\pi*N*T}{60} \qquad \text{(Refer Equation 3-21)}$$

where, N is the speed (rpm), and T is torque (Nm). And the uncertainties associated with these independent variables are as follows:

$u_N = 10$ rpm; $u_T = 0.05$ Nm   (Refer Table AII-1)

The uncertainty in BP value is computed by applying Equation (AII-2), the various terms involved are:

$$\frac{\partial BP}{\partial N} = \frac{2*\pi*T}{60}$$

$$\frac{\partial BP}{\partial T} = \frac{2*\pi*N}{60}$$

$u_N = 10$ rpm

$u_T = 0.05$ Nm

Thus, the uncertainty in the BP (u_{BP}) is

$$u_{BP} = \left[\left(\frac{\partial BP}{\partial N}u_N\right)^2 + \left(\frac{\partial BP}{\partial T}u_T\right)^2\right]^{1/2} \qquad \text{(AII-3)}$$

Let us consider an experimental run with N = 1400 rpm, and T = 2 Nm, then the computed value of uncertainty in BP is equals to 7.6235 W. Which can also be represented in % as per the following method.

The nominal BP value can be computed using Equation 3-21 with respect to above considered value of N and T. The BP value obtained is 293.215 W, so the percentage uncertainty can be computed using following equation:

$$\% \ uncertainty = \frac{u_{BP}}{BP} * 100 \qquad\qquad (AII\text{-}4)$$

And the % uncertainty in BP found to be 2.599%.

The uncertainties associated with derived parameters of engine testing in Phase-I and Phase-II is given in Table AII-2 and AII-3.

Table AII-2 Uncertainties in the derived parameters of engine testing in Phase-I

Sl.	Derived parameters	Uncertainty (%)
1	BP	0.52 – 2.6
2	IP	0.91 – 2.39
3	v_f	2.51 – 2.66
4	v_a	0.65 – 2.27

Table AII-3 Uncertainties in the derived parameters of engine testing in Phase-II

Sl.	Derived parameters	Uncertainty (%)
1	BP	0.58 – 1.17
2	IP	0.76 – 2.05
3	v_f	2.51 – 2.80
4	v_a	0.91 – 4.54

APPENDIX-III

Analysis of variance (ANOVA)

ANOVA is probably the most useful technique in the field of statistical inference. This section provide the details of ANOVA used in two different methods as follows:

1. **Taguchi method**
2. **RSM technique**

The description of the terms used in ANOVA is represented in clear manner hereunder for both the methods:

1. Taguchi method

There are several terms used in ANOVA whose detailed description can be referred in literature (Roy 2009), which are as follows:

C.F. – Correction factor

e – Error (experimental)

n – Number of trials

r – Number of repetitions

F – Variance ratio

f – Degrees of freedom

f_e - Degrees of freedom of error

f_T – Total Degrees of freedom of error

P – Percent contribution

T – Total sum (of results)

S – Sum of squares

S_T – Total variation

S' – Pure sum of squares

V – Mean squares (variance)

Consider three factors namely A, B, and C having some levels, and Y_i is the output for ith run. The following terms are necessary to carry out ANOVA:

a) Total number of trials (n)

   $n = n1 + n2 + \ldots.+ nL$

b) Degrees of freedom (DOF)

   DOF of data concerning a factor equals one less than the number of levels.

   f_A = number of levels of A – 1   (similarly for other factors)

   Total DOF becomes $(f_T) = n*r – 1$

   The DOF for error variance is: $f_e = f_T – f_A – f_B – f_C$

c) S_T = Sum of squares of all trial run results – C.F.

   $S_T = (Y_1{}^2 + Y_2{}^2 + \ldots. + Y_i{}^2) – C.F.$

   Where, $C.F. = T^2/n$

   and $T = (Y_1 + Y_2 + Y_3 + \ldots. + Y_i)$

d) Average effects of all factors:

   $A'_1 = (Y_1 + Y_2)/2$ (similarly for other factors/levels)

e) Variance:

   $V_A = S_A/f_A$ (for A and similarly for other factors)

   $V_e = S_e/f_e$ (for error terms)

f) Variance ratio:

   $F_A = V_A/ V_e$ (for A and similarly for other factors)

   $F_e = V_e/ V_e = 1$

g) Total variance of each factor is:

   $S_A = A_1{}^2/N_{A1} + A_2{}^2/N_{A2} – C.F.$ (Similarly for factors B and C)

   $S_e = S_T - (S_A + S_B + S_C)$

h) Percent influence

   $P_A = (S_A \times 100)/ S_T$ (Similarly for factors B and C)

   $P_e = (S_e \times 100)/ S_T$

i) Performance at optimum condition (Y_{opt})

   $Y_{opt} = T/n + (A'_s – T/n) + (B'_s – T/n) + (C'_s – T/n)$ (For 3 factors A,B and C)

2. RSM technique

The terms used in ANOVA under RSM are as follows:

i.   Source of variation – Factors and their derivatives (treatments), error and total.

ii.   SS – Sum of squares

iii.   DOF – Degree of freedom

iv.   MS – Mean square

v.   a – Levels of treatments

vi.   n – Replicates of responses

vii.   N – Total number of experiments

viii. F-value – Statistical hypothesis value

ix.   P-value – The smallest level of significance that would lead to rejection of the statistical hypothesis. P-value corresponds to smallest tail area probability and type of hypothesis.

Computation of following terms are necessary to perform ANOVA for each source of variation, whose detailed description can be referred in literature (Montgomery 2001):

a) SS

$$SS_{treatments} = n \sum_{i=1}^{a} (\bar{y}_{ia} + \bar{y}_{ga})^2$$

$$SS_{total} = \sum_{i=1}^{a} \sum_{j=1}^{n} (y_{ij} + \bar{y}_{ga})^2$$

$$SS_{error} = SS_{total} - SS_{treatments}$$

where,

$\bar{y}_{ia}$ – average of the observations under ith treatment

$\bar{y}_{ga}$ – grand average of all the observations

y_{ij} – ijth observation

b) DOF

$$DOF_{treatments} = a - 1$$

$$DOF_{error} = N - a$$

$$DOF_{total} = N - 1$$

c) MS

$$MS_{treatments} = \frac{SS_{treatments}}{a - 1}$$

$$MS_{error} = \frac{SS_{error}}{N - a}$$

d) F-value

$$F - value = \frac{MS_{treatments}}{MS_{error}}$$

Apart from these basic terms of ANOVA, some additional useful terms are described hereunder which are the indicator of the precision of the RSM model.

1. Standard deviation (Std. Dev.)

$$Std. Dev. = \sqrt{MS_{error}}$$

2. Coefficient of variation (C.V.)

$$C.V. = \left(\frac{\sqrt{MS_{error}}}{\bar{y}}\right) * 100$$

   Where, $\bar{y}$ is mean of the response variable

3. R-Squared (R^2)

$$R^2 = \frac{SS_{model}}{SS_{total}}$$

4. Adjusted R^2 (R^2_{Adj})

$$R^2_{Adj} = 1 - \frac{\left(SS_{error}/DOF_{error}\right)}{\left(SS_{total}/DOF_{total}\right)}$$

5. Predicted R^2 (R^2_{Pred})

$$R^2_{Pred} = 1 - \frac{PRESS}{SS_{total}}$$

where *PRESS* is Prediction Error Sum of Squares, the PRESS statistic is a measure of how well the model will predict new data. A model with a small value of PRESS indicates that the model is likely to be a good predictor.

6. Adequate precision (Adeq Precision)

$$Adeq\ Precision = \frac{PR_{max} - PR_{min}}{PR_{Avg\ Std.Dev.}}$$

where PR_{max} is maximum predicted response, PR_{min} is minimum predicted response, and $PR_{Avg\ Std.Dev.}$ is average standard deviation of all the predicted responses.

The term "Adeq Precision" measures the signal to noise ratio. Its value more than four usually indicate that the model will provide reasonable performance in prediction, as the number 'four' indicates that the signal is four times the noise in model prediction.

APPENDIX-IV

ANOVA Table of the response models using RSM

The ANOVA results obtained for both the conditions (for uncoated and coated engine block) are tabulated here for reference. There are seven responses considered in present investigation for both the cases, which are BSFC, Friction power, Mechanical efficiency, sCO, sHC, sNO and Smoke opacity.

1) For uncoated engine block

   A. BSFC

Table AIV-1 ANOVA Table for BSFC model

Source	Sum of Squares	DF	Mean Square	F-Value	Prob > F
Model	1.90E+06	9	2.11E+05	772.8	< 0.0001
A	3194	1	3194	11.71	0.0111
B	1.44E+06	1	1.44E+06	5275	< 0.0001
C	0.6864	1	0.6864	0.002517	0.9614
A^2	975.5	1	975.5	3.577	0.1005
B^2	4.46E+05	1	4.46E+05	1636	< 0.0001
C^2	4.703	1	4.703	0.01725	0.8992
AB	3074	1	3074	11.27	0.01212
AC	0.03329	1	0.03329	0.000122	0.9915
BC	0.04145	1	0.04145	0.000152	0.9905
Residual	1909	7	272.7		
Total	1.90E+06	16			

Table AIV-2 Precision index data of BSFC model

Std. Dev.	16.51	R-Squared	0.999
Mean	559.3	Adj R-Squared	0.9977
C.V.	2.953	Pred R-Squared	0.9839
PRESS	3.05E+04	Adeq Precision	72.03

B. Friction power

Table AIV-3 ANOVA Table for Friction power model

Source	Sum of Squares	DF	Mean Square	F-Value	Prob > F
Model	12.97	9	1.441	1.56E+04	< 0.0001
A	12.54	1	12.54	1.36E+05	< 0.0001
B	0.04177	1	0.04177	452.4	< 0.0001
C	0.1416	1	0.1416	1533	< 0.0001
A^2	0.1761	1	0.1761	1907	< 0.0001
B^2	2.83E-06	1	2.83E-06	0.03065	0.866
C^2	4.57E-05	1	4.57E-05	0.495	0.5044
AB	0.007472	1	0.007472	80.92	< 0.0001
AC	0.04661	1	0.04661	504.8	< 0.0001
BC	0.01251	1	0.01251	135.4	< 0.0001
Residual	0.000646	7	9.23E-05		
Total	12.97	16			

Table AIV-4 Precision index data of Friction power model

Std. Dev.	0.009609	R-Squared	1
Mean	2.134	Adj R-Squared	0.9999
C.V.	0.4503	Pred R-Squared	0.9992
PRESS	0.01034	Adeq Precision	376.1

C. Mechanical efficiency

Table AIV-5 ANOVA Table for Mechanical efficiency model

Source	Sum of Squares	DF	Mean Square	F-Value	Prob > F
Model	26.92	9	2.991	1.53E+04	< 0.0001
A	0.4939	1	0.4939	2526	< 0.0001
B	23.39	1	23.39	1.20E+05	< 0.0001
C	0.03637	1	0.03637	186	< 0.0001
A^2	0.003196	1	0.003196	16.35	0.004913
B^2	2.986	1	2.986	1.53E+04	< 0.0001
C^2	0.000141	1	0.000141	0.7234	0.4232
AB	0.001575	1	0.001575	8.055	0.02511
AC	0.003351	1	0.003351	17.14	0.004351
BC	0.001938	1	0.001938	9.91	0.0162
Residual	0.001369	7	0.000196		
Total	26.92	16			

Table AIV-6 Precision index data of Mechanical efficiency model

Std. Dev.	0.01398	R-Squared	0.9999
Mean	6.691	Adj R-Squared	0.9999
C.V.	0.209	Pred R-Squared	0.9992
PRESS	0.0219	Adeq Precision	365.2

D. sCO

Table AIV-7 ANOVA Table for sCO model

Source	Sum of Squares	DF	Mean Square	F-Value	Prob > F
Model	16.44	9	1.827	401	< 0.0001
A	6.02	1	6.02	1322	< 0.0001
B	10.32	1	10.32	2266	< 0.0001
C	0.00336	1	0.00336	0.7375	0.4189
A^2	0.04807	1	0.04807	10.55	0.01409
B^2	0.01774	1	0.01774	3.895	0.08903
C^2	0.01299	1	0.01299	2.851	0.1352
AB	0.01794	1	0.01794	3.937	0.08763
AC	0.000287	1	0.000287	0.06308	0.8089
BC	3.94E-06	1	3.94E-06	0.000865	0.9774
Residual	0.03189	7	0.004555		
Total	16.47	16			

Table AIV-8 Precision index data of sCO model

Std. Dev.	0.06749	R-Squared	0.9981
Mean	1.689	Adj R-Squared	0.9956
C.V.	3.996	Pred R-Squared	0.969
PRESS	0.5102	Adeq Precision	77.4

E. sHC

Table AIV-9 ANOVA Table for sHC model

Source	Sum of Squares	DF	Mean Square	F-Value	Prob > F
Model	10.04	9	1.115	333.5	< 0.0001
A	2.941	1	2.941	879.6	< 0.0001
B	6.999	1	6.999	2094	< 0.0001
C	0.000161	1	0.000161	0.04807	0.8327
A^2	0.07757	1	0.07757	23.2	0.001929
B^2	0.0101	1	0.0101	3.02	0.1258
C^2	3.21E-05	1	3.21E-05	0.009608	0.9247
AB	0.01111	1	0.01111	3.324	0.111
AC	1.02E-05	1	1.02E-05	0.003037	0.9576
BC	3.86E-05	1	3.86E-05	0.01153	0.9175
Residual	0.0234	7	0.003343		
Total	10.06	16			

Table AIV-10 Precision index data of sHC model

Std. Dev.	0.05782	R-Squared	0.9977
Mean	-0.04812	Adj R-Squared	0.9947
C.V.	-120.2	Pred R-Squared	0.9628
PRESS	0.3744	Adeq Precision	69.53

F. sNO

Table AIV-11 ANOVA Table for sNO model

Source	Sum of Squares	DF	Mean Square	F-Value	Prob > F
Model	2.017	9	0.2241	377.6	< 0.0001
A	1.375	1	1.375	2317	< 0.0001
B	0.5292	1	0.5292	891.6	< 0.0001
C	0.006662	1	0.006662	11.22	0.01225
A^2	0.001173	1	0.001173	1.977	0.2025
B^2	0.00167	1	0.00167	2.814	0.1373
C^2	0.007325	1	0.007325	12.34	0.009821
AB	0.09461	1	0.09461	159.4	< 0.0001
AC	9.19E-05	1	9.19E-05	0.1549	0.7056
BC	2.65E-05	1	2.65E-05	0.04463	0.8387
Residual	0.004155	7	0.000594		
Total	2.021	16			

Table AIV-12 Precision index data of sNO model

Std. Dev.	0.02436	R-Squared	0.9979
Mean	1.367	Adj R-Squared	0.9953
C.V.	1.783	Pred R-Squared	0.9671
PRESS	0.06648	Adeq Precision	71.91

G. Smoke opacity

Table AIV-13 ANOVA Table for Smoke opacity model

Source	Sum of Squares	DF	Mean Square	F-Value	Prob > F
Model	2276	9	252.9	1.09E+04	< 0.0001
A	31.19	1	31.19	1338	< 0.0001
B	1843	1	1843	7.91E+04	< 0.0001
C	0.03128	1	0.03128	1.342	0.2847
A^2	1.205	1	1.205	51.7	0.000179
B^2	386.7	1	386.7	1.66E+04	< 0.0001
C^2	0.8797	1	0.8797	37.74	0.000471
AB	6.432	1	6.432	276	< 0.0001
AC	0.03309	1	0.03309	1.42	0.2722
BC	0.004652	1	0.004652	0.1996	0.6685
Residual	0.1631	7	0.02331		
Total	2276	16			

Table AIV-14 Precision index data of Smoke opacity model

Std. Dev.	0.1527	R-Squared	0.9999
Mean	16.27	Adj R-Squared	0.9998
C.V.	0.9384	Pred R-Squared	0.9989
PRESS	2.61	Adeq Precision	293

2) For coated engine block

    A. BSFC

Table AIV-15 ANOVA Table for BSFC model

Source	Sum of Squares	DF	Mean Square	F-Value	Prob > F
Model	1.82E+06	9	2.02E+05	1187	< 0.0001
A	6.444	1	6.444	0.03781	0.8513
B	1.38E+06	1	1.38E+06	8105	< 0.0001
C	1.629	1	1.629	0.009559	0.9249
A^2	11.11	1	11.11	0.0652	0.8058
B^2	4.35E+05	1	4.35E+05	2553	< 0.0001
C^2	8.283	1	8.283	0.0486	0.8318
AB	1256	1	1256	7.369	0.03
AC	0.08745	1	0.08745	0.000513	0.9826
BC	0.04126	1	0.04126	0.000242	0.988
Residual	1193	7	170.4		
Total	1.82E+06	16			

Table AIV-16 Precision index data of BSFC model

Std. Dev.	13.06	R-Squared	0.9993
Mean	534.5	Adj R-Squared	0.9985
C.V.	2.443	Pred R-Squared	0.9895
PRESS	1.91E+04	Adeq Precision	86.54

    B. Friction power

Table AIV-17 ANOVA Table for Friction power model

Source	Sum of Squares	DF	Mean Square	F-Value	Prob > F
Model	3.395	9	0.3772	1416	< 0.0001
A	3.286	1	3.286	1.23E+04	< 0.0001
B	0.00809	1	0.00809	30.37	0.000896
C	0.05208	1	0.05208	195.5	< 0.0001
A^2	0.01588	1	0.01588	59.62	0.000114
B^2	2.42E-06	1	2.42E-06	0.009077	0.9268
C^2	0.005357	1	0.005357	20.11	0.00285
AB	0.00333	1	0.00333	12.5	0.009524
AC	0.01775	1	0.01775	66.62	< 0.0001
BC	0.004967	1	0.004967	18.65	0.003488
Residual	0.001865	7	0.000266		
Total	3.397	16			

Table AIV-18 Precision index data of Friction power model

Std. Dev.	0.01632	R-Squared	0.9995
Mean	1.49	Adj R-Squared	0.9987
C.V.	1.095	Pred R-Squared	0.9912
PRESS	0.02983	Adeq Precision	117.2

C. Mechanical efficiency

Table AIV-19 ANOVA Table for Mechanical efficiency model

Source	Sum of Squares	DF	Mean Square	F-Value	Prob > F
Model	2.797	9	0.3108	3.64E+04	< 0.0001
A	0.03785	1	0.03785	4427	< 0.0001
B	2.31	1	2.31	2.70E+05	< 0.0001
C	0.004133	1	0.004133	483.4	< 0.0001
A^2	2.15E-05	1	2.15E-05	2.518	0.1566
B^2	0.4384	1	0.4384	5.13E+04	< 0.0001
C^2	0.000445	1	0.000445	52.05	0.000175
AB	0.001885	1	0.001885	220.5	< 0.0001
AC	0.000707	1	0.000707	82.75	< 0.0001
BC	3.90E-06	1	3.90E-06	0.4559	0.5212
Residual	5.98E-05	7	8.55E-06		
Total	2.797	16			

Table AIV-20 Precision index data of Mechanical efficiency model

Std. Dev.	0.002924	R-Squared	1
Mean	3.828	Adj R-Squared	1
C.V.	0.07637	Pred R-Squared	0.9997
PRESS	0.000957	Adeq Precision	540.6

D. sCO

Table AIV-21 ANOVA Table for sCO model

Source	Sum of Squares	DF	Mean Square	F-Value	Prob > F
Model	17.23	6	2.871	333.5	< 0.0001
A	6.406	1	6.406	744	< 0.0001
B	10.69	1	10.69	1242	< 0.0001
C	0.003379	1	0.003379	0.3925	0.545
AB	0.1219	1	0.1219	14.16	0.003705
AC	0.000295	1	0.000295	0.03428	0.8568
BC	3.95E-06	1	3.95E-06	0.000459	0.9833
Residual	0.0861	10	0.00861		
Total	17.31	16			

Table AIV-22 Precision index data of sCO model

Std. Dev.	0.09279	R-Squared	0.995
Mean	1.725	Adj R-Squared	0.992
C.V.	5.378	Pred R-Squared	0.9749
PRESS	0.4339	Adeq Precision	68.89

E. sHC

Table AIV-23 ANOVA Table for sHC model

Source	Sum of Squares	DF	Mean Square	F-Value	Prob > F
Model	3.004	9	0.3338	1976	< 0.0001
A	0.9052	1	0.9052	5360	< 0.0001
B	1.984	1	1.984	1.17E+04	< 0.0001
C	1.47E-06	1	1.47E-06	0.008696	0.9283
A^2	0.03008	1	0.03008	178.1	< 0.0001
B^2	0.02522	1	0.02522	149.3	< 0.0001
C^2	0.000683	1	0.000683	4.046	0.08418
AB	0.05411	1	0.05411	320.4	< 0.0001
AC	0.000561	1	0.000561	3.32	0.1112
BC	0.000366	1	0.000366	2.165	0.1846
Residual	0.001182	7	0.000169		
Total	3.005	16			

Table AIV-24 Precision index data of sHC model

Std. Dev.	0.013	R-Squared	0.9996
Mean	1.106	Adj R-Squared	0.9991
C.V.	1.175	Pred R-Squared	0.9937
PRESS	0.01892	Adeq Precision	167.4

F. sNO

Table AIV-25 ANOVA Table for sNO model

Source	Sum of Squares	DF	Mean Square	F-Value	Prob > F
Model	1.986	9	0.2207	3959	< 0.0001
A	1.336	1	1.336	2.40E+04	< 0.0001
B	0.5475	1	0.5475	9821	< 0.0001
C	0.008549	1	0.008549	153.3	< 0.0001
A^2	0.001362	1	0.001362	24.43	0.00167
B^2	0.01446	1	0.01446	259.3	< 0.0001
C^2	9.24E-07	1	9.24E-07	0.01657	0.9012
AB	0.07822	1	0.07822	1403	< 0.0001
AC	0.000888	1	0.000888	15.93	0.005249
BC	3.53E-05	1	3.53E-05	0.6325	0.4526
Residual	0.00039	7	5.58E-05		
Total	1.987	16			

Table AIV-26 Precision index data of sNO model

Std. Dev.	0.007467	R-Squared	0.9998
Mean	1.302	Adj R-Squared	0.9996
C.V.	0.5734	Pred R-Squared	0.9969
PRESS	0.006244	Adeq Precision	234.1

G. Smoke opacity

Table AIV-27 ANOVA Table for Smoke opacity model

Source	Sum of Squares	DF	Mean Square	F-Value	Prob > F
Model	2013	9	223.7	4831	< 0.0001
A	28.72	1	28.72	620.3	< 0.0001
B	1616	1	1616	3.49E+04	< 0.0001
C	0.4596	1	0.4596	9.927	0.01614
A^2	1.245	1	1.245	26.89	0.001273
B^2	351.2	1	351.2	7586	< 0.0001
C^2	1.471	1	1.471	31.77	0.000785
AB	6.827	1	6.827	147.5	< 0.0001
AC	0.03889	1	0.03889	0.8401	0.3899
BC	0.001942	1	0.001942	0.04194	0.8436
Residual	0.3241	7	0.0463		
Total	2013	16			

Table AIV-28 Precision index data of Smoke opacity model

Std. Dev.	0.2152	R-Squared	0.9998
Mean	15.13	Adj R-Squared	0.9996
C.V.	1.422	Pred R-Squared	0.9974
PRESS	5.185	Adeq Precision	195.2

List of publications

1. Himanshu Panjiar, RP Gakkhar, BSS Daniel (2015) Strain-free graphite nanoparticle synthesis by mechanical milling, Powder Technology, Vol 275, 25-29

2. Himanshu Panjiar, RP Gakkhar, BSS Daniel (2014) Modeling mechanical milling process for synthesis of graphite nanoparticles and their characterization, Advanced Materials Research Vol 922, 586-591

3. Himanshu Panjiar, Jyoti Pinjarkar, BSS Daniel, RP Gakkhar (2016) Performance and exhaust emission optimization of small DI compression ignition engine using response surface methodology and genetic algorithm (under review)

4. Himanshu Panjiar, BSS Daniel, RP Gakkhar (2016) Graphite nanoparticles coating can address friction in small DI compression-ignition engine (under preparation)

5. Himanshu Panjiar, BSS Daniel, RP Gakkhar (2016) Effect of nano-graphite coating on small DI compression-ignition engines specific emissions and smoke (under preparation)

6. Himanshu Panjiar, RP Gakkhar, BSS Daniel (2013) Modeling Mechanical Milling Process for Synthesis of Graphite Nanoparticles and their Characterization, THERMEC 2013, Las Vegas, USA

7. Himanshu Panjiar, RP Gakkhar, BSS Daniel (2013) Synthesis of Graphite Nanoparticles by Mechanical Milling Using ANN, PM-13, Pune

8. Himanshu Panjiar, BSS Daniel (2011) Nanomaterials for high temperature application of internal combustion diesel engine, Cochin Nano - 2011, Cochin

9. Ankit Chakravarti, Nitin Joshi, Himanshu Panjiar (2015) Rainfall Runoff Analysis using Artificial Neural Network, Indian Journal of Science and Technology, Vol 8(14)

10. Shejale Kiran Prakash, Harjeet Singh, Himanshu Panjiar, Sanjeev Manhas, BSS Daniel (2012) Application of Graphene Oxide and TiO2 in the fabrication of Dye sensitized solar cells module by electrode modification, Advanced Materials Research 585, 255-259

11. Harjeet Singh, Shejale Kiran Prakash, Himanshu Panjiar, BSS Daniel (2012) Synthesis of TiO2 film for Dyesensitized solar cells, Advanced Materials Research 585, 284-288

12. Shejale Kiran Prakash, Himanshu Panjiar, BSS Daniel, Sanjeev Manhas (2012) Application of Graphene Oxide and TiO2 in the fabrication of solar cell module by electrodes modification, Nanosolar 2012, Kochi